Multimessenger Astrophysics of Pulsars in Extreme Mass Ratio Systems

Tom Kimpson

Thesis submitted for the degree of

Doctor of Philosophy (PhD)

of

University College London

Mullard Space Science Laboratory
Department of Space and Climate Physics
University College London

February 2021

I, Tom Kimpson, confirm that the work presented in this thesis is my own. Where information has been derived from other sources, I confirm that this has been indicated in the thesis.

Abstract

The detection of a millisecond pulsar (MSP) in a short, relativistic orbit around a massive astrophysical black hole - such as those found in the Galactic centre or in the centre of Globular clusters - would allow for precision tests of fundamental physics and astrophysics in the gravitational strong-field regime.

The radio timing signals from these systems are subject to a slew of non-linear, relativistic and astrophysical effects. Therefore, in order to both detect these systems, and use them as a natural, precision apparatus for scientific tests, it is essential to be able to model the theoretical signal in a way that is applicable to the strong-field regimes that these systems inhabit. The development of such a relativistic timing framework is the primary focus of this thesis. This formulation can then self-consistently and accurately calculate the timing signal in the gravitational strong-field from an MSP in a general orbit around a supermassive or intermediate mass black hole.

In the latter part of the thesis I explore the prospects for detecting gravitational wave signals from these MSP Extreme Mass Ratio Systems. The observation of gravitational radiation in conjunction with the electromagnetic pulsar radio signal would enable multimessenger astronomy of the gravitational strong-field. Finally I explore the signature of beyond-GR effects in the pulsar timing signal via a modification of the black hole quadrupole moment.

Impact Statement

The impact of the research presented in this thesis falls into 3 broad categories:

1. **Impact on the detection of astrophysical pulsars and search methods**
   Whilst the detection of pulsars in the Galactic centre or the centre of globular clusters is a major scientific goal, despite many previous searches we have not yet detected any pulsars from these central regions. This research establishes that whilst increased sensitivity of the next generation of radio facilities is key, higher-order relativistic effects will mean that current search algorithms (e.g. Fourier search) may not be sufficiently sophisticated to detect the signals from these systems. By providing the ability to construct accurate, strong-field synthetic data, this work lays the foundation for the development of more advanced search algorithms and an accurate assessment of current search methods.

2. **Impact on the use of MSP systems for tests of strong-field fundamental physics**
   It is essential to be able to model the expected theoretical signal from a strong-field MSP Extreme Mass Ratio System accurately, both to enable accurate estimates of the utility of MSPs as a precision probe of fundamental physics and in order to provide an accurate basis for comparison with observation. Typically, analysis of strong-field fundamental physics with MSP systems is undertaken via the post-Keplerian framework. This work highlights that for MSPs in Extreme Mass Ratio Systems, these approximate modelling methods may not be appropriate for strong field regimes, given the range of relativistic effects that can influence the sig-

nal. In turn, this enables the the construction of sufficiently advanced timing models that can be applied to real strong-field astrophysical data and the exploration of beyond-GR effects.

3. **Impact on precision multimessenger astrophysics in the strong-field regime**
   Astronomical observations of the strong gravitational-field are very difficult. Despite the potential for compounded scientific return, there have been few strong-field systems with which one would expect to be able to make multimessenger observations; BH-NS mergers as detected by LIGO being the notable exception. This work raises another potential avenue for multimessenger astronomy via the simultaneous observations of both radio electromagnetic and gravitational radiation from an MSP during its orbit around a massive black hole. Given the precision with which measurements can be made with pulsar timing, this is a unique route for precision multimessenger astronomy to probe general relativity in the non-linear regime.

Acknowledgements

In the same way that it takes a village to raise a child, it takes a company of people to create a scientist. Consequently, in order to try to thank everyone, the following acknowledgements are undeservedly brief. Firstly I would like to thank my primary supervisor Professor Kinwah Wu for his deep scientific understanding and fundamental insight combined with an infectious enthusiasm and passion as a teacher and scientific mentor. This is a unique combination of traits and I will be forever grateful to have had him as my supervisor. Secondly, I am deeply indebted to my supervisor Professor Silvia Zane for always being on-hand to offer her technical expertise, scientific counsel and unwavering support. Additionally I would also like to thank Professor Daisuke Katawa and Professor Mark Cropper and for their kindness and encouragement, as well as dependably filling the roster on our seminar pub trips. I would also like to extend a special thanks to Professor Michela Mapelli and Dr. Mario Spera who gave me my first taste of what scientific research was really like. Their enthusiasm and generosity over an Italian summer in 2015 has been formative in my life.

I extend my sincere thanks to the inhabitants of office 158 - Ellis, Jennifer, Brian, Yichao and Ziri - for creating a fun and open environment in which to bounce around difficult concepts. I also thank my friends at MSSL for making my time here so enjoyable as well as the entire astrophysics group more broadly for providing an immensely friendly and warm environment in which to work. Thanks also to my housemates and fellow 2016 cohort Jo, Lloyd and Jack for providing much needed option to either switch-off or vent at the end of the day. I thank my family for their love and support and for making my visits home so enjoyable and bubbly. Finally, I wish to thank Lucy who has put up with me for a long time, despite my refusal to get a dog.

Contents

List of Figures

List of Tables

Lists of Acronyms and Symbols

a	black hole spin parameter
B	magnetic field strength
$\bar{B}$	radiation beam vector pulsar
BH	Black Hole
c	speed of light
d_θ	angular distance
ds	spacetime interval
$d\Sigma$	3-volume hypersurface element
d_t	pulsar timing distance
DM	dispersion measure
e	orbital eccentricity
$e_{(\mu)}$	tetrad basis
e_μ	vector basis
E	energy
FAST	Five Hundred Metre Aperture Spherical Telescope
$F^{\mu\nu}$	electromagnetic field tensor
$\mathcal{F}^\mu$	Dixon force
$\tilde{F}^{\mu\nu}$	electromagnetic field tensor dual
$f_{\mu\nu}$	polarization bivector
$g_{\mu\nu}$	covariant metric tensor $(-,+,+,+)$
G	gravitational constant
$\hbar$	reduced Planck constant
H	Hamiltonian
i	orbital inclination w.r.t observer

$\mathcal{I}$	moment of inertia
I	pulse intensity
IMBH	Intermediate Mass Black Hole
J^{μ}	4-current density
k^{μ}	wave 4 vector
KAGRA	Kamioka Gravitational Wave Detector
$K^{\mu\nu}$	Killing tensor
$\mathcal{K}$	Kretschman curvature scalar
l^{μ}	metric principal null vector
(a)LIGO	(Advanced) Laser Interferometer Gravitational-Wave Observatory
LISA	Laser Interferometer Space Antenna
L_z	z projection of angular momentum
m	pulsar mass
m_e	electron mass
M	BH mass
MSP	Millisecond Pulsar
$\mathcal{R}_M$	Moller Radius
$M_{\odot}$	solar mass
n	refractive index
NS	Neutron Star
n^{μ}	metric principal null vector
$\hat{O}$	line of sight vector between observer and BH
p^{μ}	4 momentum
$\mathcal{P}$	orbital semi-latus rectum
PSR	pulsar
P_s	pulsar spin period
P	orbital period
q	binary mass ratio
q_e	electron charge
Q	general BH quadrupole parameter
Q_C	Carter Constant

Q_K	Kerr BH quadrupole parameter
r_g	gravitational radius
r_h	radial harmonic coordinate
r_s	Schwarzchild radius
r_+	event horizon of Kerr BH
r_-	Cauchy horizon of Kerr BH
$R_\odot$	solar radius
$R_{\mu\nu\alpha\beta}$	Riemann curvature tensor
R_n	3D rotation matrix about axis n
s	spin scalar
SKA	Square Kilometre Array
s^μ	spin vector
$s^{\mu\nu}$	spin dipole tensor
$\bar{S}$	spin axis vector pulsar
ToA	Time of Arrival
t	coordinate time
$T^{\mu\nu}$	energy momentum tensor
$\mathcal{T}^{\mu\nu}$	Dixon torque
u^μ	4 velocity
v	orbital 3-velocity
v_g	group velocity
v_p	phase velocity
w	angular beam width
x^μ	4 position
z^μ	worldline
γ	time dilation parameter
${\Gamma^\gamma}_{\mu\nu}$	Christoffel connections
δ^μ_γ	Kronekar delta
Δ	Boyer Lindquist variable
Δ_R	Roemer delay
Δ_S	Shapiro delay
Δ_E	Einstein delay

ϵ	gravitational field strength
$\epsilon^{\mu\nu\alpha\beta}$	Levi-Cevita psuedo-tensor
$\theta_{\rm spin}$	spin axis angle
Θ	observer latitude angle
ι	orbital inclination
λ	spin curvature coupling parameter
ν	frequency
$\nu_{\rm obs}$	observed frequency
ξ	spacetime curvature parameter
ξ^{μ}	Killing vector
σ	stellar velocity dispersion
Σ	BL variable
τ	proper time variable
τ_c	characteristic pulsar age
τ_{GW}	gravitational wave timescale
τ_s	scattering timescale
$\phi_{\rm spin}$	spin axis angle
Φ	observer azimuthal angle
χ	pulsar beam phase
ψ	polar angle of radiation beam w.r.t spin axis
ω	angular frequency
ω_p	plasma frequency
$\tilde{\omega}$	pitch angle

Chapter 1

Introduction

1.1 Overview

In this work I develop a general relativistic pulsar (PSR) timing model and apply it to investigate the theoretical time-frequency signal from a pulsar in orbit around a massive ($> 10^3 M_\odot$) black hole (BH). A PSR-BH system would be a unique laboratory for testing both astrophysics and fundamental physics in an extreme parameter space; consequently they are prime targets for the next generation of radio instrumentation. The intense strong-field curvature of these systems means that weak-field approximations that are typically employed no longer hold and so this work is carried out in a fully covariant general relativistic framework.

I use a general relativistic ray tracing method to determine the trajectory of light around a spinning black hole. The formulation is covariant and so naturally accounts for all relativistic and gravitational features (e.g. relativistic Doppler/frequency shift, gravitational lensing, gravitational redshift etc.) I further include the effects of an astrophysical plasma on the light ray geodesic, such that the ray path becomes chromatic. I describe the spin-orbital dynamics of a spinning PSR on a background curved spacetime going beyond the geodesic approximation and accounting for the dynamical influence of the PSR spin on the background spacetime (‘spin-curvature coupling’). Such an approach then consistently describes the dynamical and spin evolution of the PSR, including relativistic precession and nutation of the PSR spin axis.

The core focus of this thesis is the development of a pulsar time-frequency ($t - \nu$) framework applicable to the gravitational strong-field. With the PSR orbital dynamics and the light ray trajectory specified, I develop an algorithmic pipeline to combine these two ingredients so as to generate fully relativistic and frequency-dependent photon time of arrivals (ToAs). The orbital dynamics effectively provide time-varying boundary conditions for the PSR light ray, accounting for the PSR beamed emission, beam phase and relativistic aberration. This formulation can then self-consistently and accurately calculate the $t - \nu$ signal from a pulsar, in an arbitrary orbit in the gravitational strong-field around an astrophysical BH, accounting for both relativistic and astrophysical effects.

With this timing framework in hand I go on to explore explicitly the influence of relativistic and astrophysical effects on the timing signal (ToA, pulse profile, intensity, Fourier spectrum) from a strong-field radio PSR. This includes the effects related to relativistic spin-orbital dynamics of a spinning pulsar around a spinning BH, e.g. spin coupling, curvature coupling, and time dilations (gravitomagnetic, relativistic, gravitational), spin axis precession and nutation, gravitational lensing, gravitational and relativistic time dilation and dispersions in both time and space.

I compare the relativistic timing model with the commonly used post-Keplerian model when applied to PSR in gravitational strong field environments such as the Galactic Centre and the centre of stellar clusters. I further extend the description of the spin-orbital dynamics for a spinning BH with an arbitrary mass quadrupole and determine the strong-field relativistic signatures. Finally, I use a numerical kludge approach to calculate the gravitational burst waveforms from PSR-BH systems in the Galactic centre or the centre of globular clusters and explore the prospects for multimessenger observations of these systems.

1.2 Pulsars

When a main-sequence star exhausts its energy supply and is unable to power nuclear fusion, it undergoes a core collapse. For stars of intermediate mass ($8 - 20 M_{\odot}$), the collapse is halted by the neutron degeneracy pressure. The result is a compact object (radius ~10 km) with a stellar mass, composed entirely of neutrons; a neutron star (NS). Main-sequence stars have dipolar magnetic fields, due to the motion of conducting plasma acting like a dynamo. During the collapse, the magnetic flux is conserved due to Gauss' Law. Consequently, since the stellar radius decreases from $\sim R_{\odot} \rightarrow \mathcal{O}(10 \text{ km})$, NSs have typically have strong magnetic fields, on the order of $10^8 - 10^{13}$ G (Lyne & Graham-Smith 2012). Some NSs, known as magnetars, have exceptionally strong fields strengths of the order $\sim 10^{14} - 10^{15}$ G, likely due to dynamo amplification during the core collapse (Raynaud et al. 2020). The magnetic dipole axis is typically misaligned with respect to the spin axis resulting in rotating beams of radiation which are seen as 'pulses' in the radio band of the electromagnetic spectrum whenever the beam intersects with the observer's line of sight. Neutron stars for which these rotating radiation beams are observed are therefore known as (radio) pulsars. The NSs emission is not limited to the radio band; thanks to multiwavelength observations, nowadays a vast zoo of NSs are observed at different energy bands, from optical, through X-ray to gamma ray. The various classes include rotation-powered pulsars (RPP), magnetars, X-ray dim isolated NS, accretion-powered NS (including the X-ray burster sub-class) and central compact objects (Harding 2013; Kaspi 2018). For the purposes of this work, we will be concerned only with the RPP class, which we will simply refer to as pulsars.

Whilst the conservation of magnetic flux ensures that pulsars have strong magnetic fields, the conservation of angular momentum during the collapse means that pulsars spin exceptionally quickly, with spin periods on the order of a few seconds or less. Their rapid spin, stellar mass and compact radius all conspire to make pulsars gyroscopically stable rotators. Although pulsars are exceptionally stable, their spin period, P_{s}, is not entirely constant owing to the loss of energy due to electromagnetic radiation from the magnetic dipole. The rate of period change, $\dot{P}_{\rm s}$, is typically small, of order 10^{-15}, and the measurement of this period derivative allows us to make an approximate estimate of the 'characteristic age' of the pulsar

$$\tau_c = \frac{P_{\rm s}}{2\dot{P}_{\rm s}} \ , \tag{1.1}$$

under the assumption that $\dot{P}$ is constant over over the star's lifetime. The surface magnetic field strength is related to the spin period and the spin-down rate as

$$B = \left(\frac{3c^3 I}{8\pi^2 R^6} \right) \sqrt{\frac{P_{\rm s}\dot{P}_{\rm s}}{[s]}} \ , \tag{1.2}$$

and so in c.g.s units, for a canonical pulsar with moment of inertia $I = 10^{45}$g cm and radius $R = 10^6$cm,

$$\frac{B}{[G]} = 3.2 \times 10^{19} \sqrt{\frac{P_{\rm s}\dot{P}_{\rm s}}{[s]}} \ . \tag{1.3}$$

We can distinguish two populations of pulsars, determined explicitly by their periods and period derivatives and implicitly by their evolutionary histories (see Fig 1.1). Canonical pulsars (CP) have periods on the order of a few seconds (the longest period NS radio pulsar is PSR J0250+5854, with $P_s \sim 23.5$ s, Tan et al. 2018) whilst those pulsars with shorter spin periods, on the order of milliseconds are correspondingly known as millisecond pulsars (MSP); the fastest recorded MSP is PSR J1748-2446 with a spin frequency of 714 Hz (Hessels et al. 2006). CP are the younger of the two populations with $\tau_c \sim 10^4$ years and are directly formed via the stellar collapse mechanism. Consistent with this origin they are typically found to lie close to the Galactic plane and are associated with supernova remnants. Due to the decay of the spin period, eventually the NS is not spinning fast enough to power the radiation mechanism; CP typically 'go dark' at $\tau_c \sim 10^6$ years (Manchester 2015). However, CPs go on to ultimately serve as the progenitors for MSPs; old dead CP can be 'spun up' through the accretion of matter and angular momentum from a binary companion. This resurrection process results in much greater spin frequencies. Consistent with this conception, MSPs are commonly found as members of a binary system in regions of high stellar density.

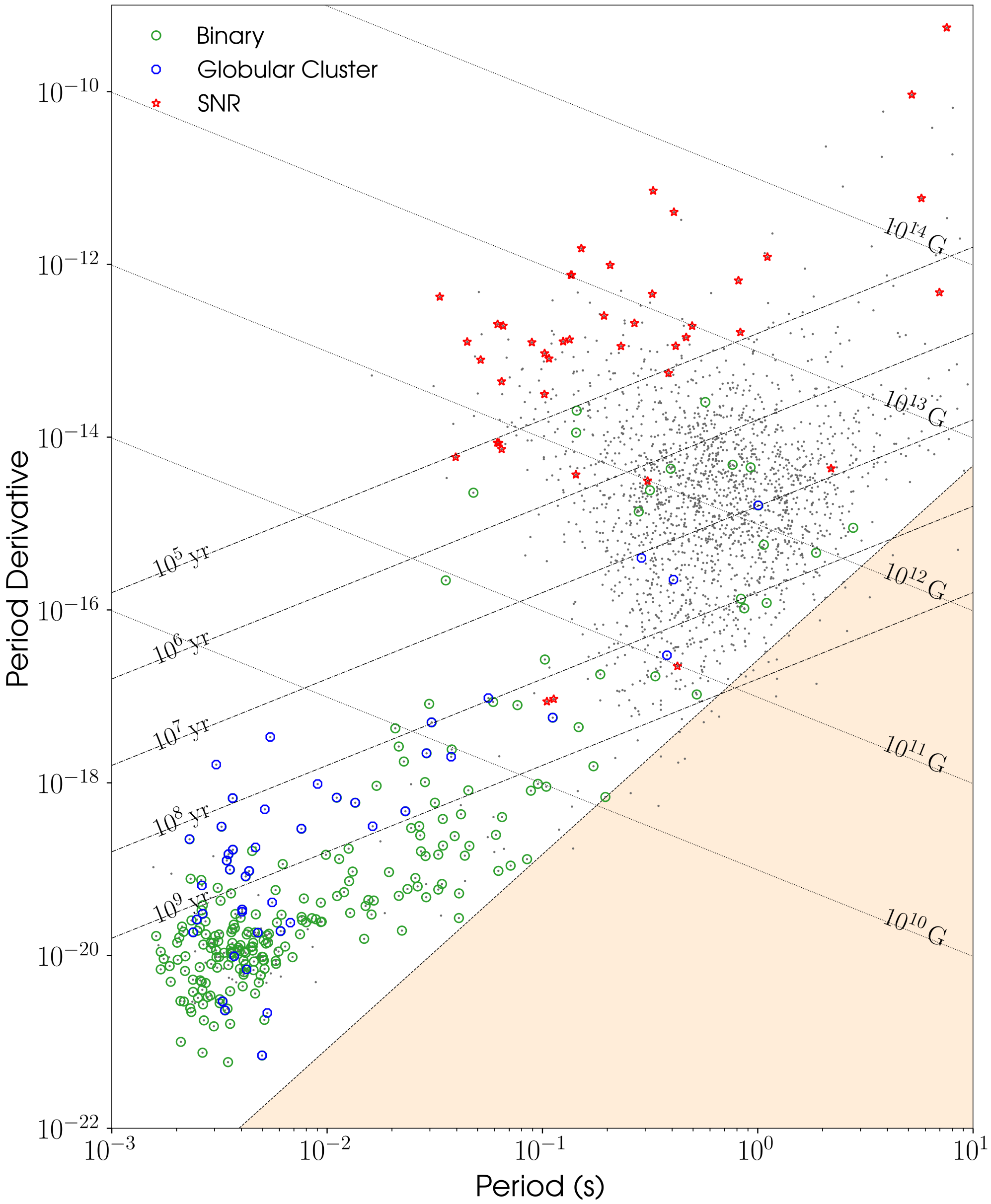

Fig. 1.1: The distribution of radio pulsars in the $P_\mathrm{s} - \dot{P}_\mathrm{s}$ space. PSRs with binary companions are labelled with a green circle around them, those in globular clusters with a blue circle, whilst those with supernovae association are shown by the red star. There is a clear bimodality in the pulsar population; those with spin periods of ~ 1 s and those with millisecond periods. This figure made use of the psrqpy package (Pitkin 2018) and the ANTF pulsar catalogue (Manchester et al. 2005).

1.3 Black Holes

For sufficiently massive stars ($\gtrsim 20M_\odot$) the neutron degeneracy pressure is insufficient to halt the stellar collapse. The infall continues to form a massive, compact and dark object: an astrophysical black hole (BH). BHs which directly result from this stellar collapse mechanism typically have masses in the range $3 - 100M_\odot$ and form a distinct class known as stellar-mass black holes. Evidence for the existence of these astrophysical objects is available via both both electromagnetic and gravitational observations. On the electromagnetic side, observations of X-ray binaries suggest accretion onto some compact object with a mass beyond that allowed for a NS (see e.g. Remillard & McClintock 2006; Tomsick et al. 2015). In addition, the detection of gravitational radiation from ground based interferometers (e.g. LIGO/VIRGO), evidences the existence of inspiralling binary BHs (e.g. Abbott et al. 2016, 2017b; The LIGO Scientific Collaboration et al. 2020).

In addition to the stellar-mass class, there also exists a population of supermassive BHs, with typical masses $\gtrsim 10^6 M_\odot$, up to the maximum detected mass of $4 \times 10^{10} M_\odot$ (Mehrgan et al. 2019). These beasts lurk in the centre of galaxies, including our own Milky Way. Observations of the population of S-stars in Galactic centre - in particular the relativistic S2 star - indicate that there lies a central dark object with mass $\sim 4 \times 10^6 M_\odot$ (Gravity Collaboration et al. 2018a,b). This massive object is coincident with the Sgr A* radio source, the origin of which is thought to be due to accretion onto the central BH. Radio observations confine this source to be exceptionally compact (Doeleman et al. 2008) whilst the VLBI observations of Sgr A* flaring events are also consistent with the hypothesis of a supermassive BH (Gravity Collaboration et al. 2018b). The existence of extragalactic supermassive black holes at the centre of galaxies is established via observations of AGN (which are thought to be powered by accretion onto a central black hole, see Lu et al. 2019, for a recent review and references therein), radio observations of megamaser disks (Greene et al. 2010; van den Bosch et al. 2016), dynamical evidence (Filippenko & Ho 2003), tidal disruption flaring events (Burrows et al. 2011) and reverberation mapping (Campitiello et al. 2019). The formation of supermassive BHs remains an open question, but they are expected to be formed hierarchically from smaller 'seed' BHs in relation to the evolution of their host galaxy (Volonteri 2010). As a result of this coevolution of supermassive BHs and their host environments, there is an empirical relation between the central BH mass and the velocity dispersion of stars in that galaxy, the so called '$M - \sigma$ relation' (Gültekin et al. 2009).

Given the theoretical mechanism of hierarchical formation of supermassive BHs from smaller seed BHs, it seems natural that there should exists BHs of intermediate mass $\sim 10^2 - 10^5 M_\odot$ that bridge the gap between the stellar and supermassive classes. However, only very recently has the first and only intermediate mass BHs (IMBH) been definitively detected (The LIGO Scientific Collaboration et al. 2020). Observations of X-ray emission from globular clusters led to the first suggestion that globular clusters could host central BHs of intermediate mass (Silk & Arons 1975; Colbert & Miller 2006; Lin et al. 2018), whilst extrapolation to the low-mass end of the 'M-σ relation' (Ferrarese & Merritt 2000; Gebhardt et al. 2000) also suggests that that stellar clusters such as globular clusters or dwarf galaxies should host IMBHs (Sadoun & Colin 2012; Graham & Soria 2019). Consilient, suggestive yet tentative evidence for IMBHs is put forth via observational radiative accretion signatures (Ulvestad et al. 2007, e.g.), stellar kinematics (e.g. Gebhardt et al. 2002; van der Marel & Anderson 2010; Feldmeier et al. 2013), integral field spectroscopy (Lützgendorf et al. 2013) and pulsar timing observations (Perera et al. 2017; Kızıltan et al. 2017a). However some evidence for IMBH is contested (e.g. Miller-Jones et al. 2012; Baumgardt 2017; Freire et al. 2017) and definitive 'smoking-gun' evidence for IMBH at the centre of stellar clusters is still lacking. See Mezcua (2017) for a full review of the observational evidence for IMBHs.

The existence of astrophysical BHs, that is, the existence of massive, compact dark physical objects is then well established. However it remains an open and deep question as to whether these astrophysical BHs are also *mathemat-*

ical BHs, that is a BH which is a solution to the Einstein field equations. Whether astrophysical BHs are described by Einsteinian General Relativity is an essential question in the foundations of astrophysics and fundamental physics and one to which we will return at the end of this chapter.

1.4 Pulsar - Black Hole Systems

The environments surrounding supermassive or intermediate mass BHs have exceptionally high stellar densities; within the central parsec of the Milky Way there are expected to be $\sim 10^7 - 10^8$ stars, whilst the centres of globular clusters have core number densities $\sim 10^4$ pc^{-3}. As a consequence, the effects of dynamical friction and mass segregation cause heavy objects, like pulsars, to sink towards more central radii. Within these central regions, two-body scattering drives these compact objects onto eccentric orbits. Pulsars can obtain compact, relativistic orbits around the central BH without being tidally disrupted on account of their high densities. Such systems in which an approximately stellar mass PSR, (mass m) orbits a much more massive BH (mass M) are known as Extreme/Intermediate Mass Ratio Binaries (E/IMRBs) and will be the main focus of this thesis. EMRBs refer to systems with a mass ratio $q = M/m \gtrsim 10^6$, whilst IMRBs have $q \sim 10^3 - 10^5$.

On account of the high stellar densities, large molecular complexes and the known population of young massive stars and stellar remnants, there is expected to be a large population of neutron stars in the Galactic Centre (Genzel et al. 2010; Fragione et al. 2018; Kim & Davies 2018). However, despite extensive surveys (Johnston et al. 2006; Macquart et al. 2010; Bates et al. 2011), until 2013 no pulsar had been detected within ~ 25 parsecs of Sgr A*. Both Sgr A* and OH/IR Galactic centre stars exhibit extreme angular broadening (Frail et al. 1994; Sjouwerman et al. 2002) indicating that the Galactic centre must be a region of high radio scattering (Lazio & Cordes 1998). The dearth of pulsar detections was then attributed to this extreme scattering in the Galactic centre. To avoid radio pulsar observations being hindered by scattering requires observations at higher radio frequencies, ν, since scattering causes a smearing of the pulsar pulse profile on a timescale $\tau_s \propto \nu^{-4}$, where the exponent can be derived by taking the interstellar medium as a homogeneous Kolmogorov spectrum or measured empirically. However, pulsars have steep radio spectra making detections at high frequencies similarly challenging. The situation changed in 2013 with the detection of the magnetar, PSR J1745-29 at a projected distance from Sgr A* of ~ 0.1 pc (Kennea et al. 2013; Mori et al. 2013). Surprisingly, measurements of this magnetar indicate that scattering towards the Galactic centre is in-fact relatively benign and previous surveys should have been able to detect pulsars from this region. Moreover, since the (radio-emitting) magnetar itself is a rare astrophysical object it further suggests that there should be a large NS population. This paradox - 'the missing pulsar problem' - led to suggestions that there are few pulsars in the Galactic centre (Chennamangalam & Lorimer 2014) along with conjectures that that magnetars are preferentially formed (Dexter & O'Leary 2014) or that NSs are destroyed by dark matter (Bramante & Linden 2014). Whilst these solutions remain possibilities, perhaps simpler explanations exist; it was subsequently noted that if the Galactic centre population was composed primarily of MSPs, then previous surveys would be insensitive to this population (Macquart & Kanekar 2015; Rajwade et al. 2017). The Galactic Centre is a region of high stellar density, enabling spin-up of old dead CPs to MSPs via frequent close interactions. Indeed, in dense globular clusters - where radio observations are less hampered by scattering - MSPs comprise a significant fraction of the globular cluster pulsar population (Camilo & Rasio 2005; Ransom 2008). Some notable clusters are Terzan 5 with 37 MSPs (Cadelano et al. 2018a) and 47 Tucanae which is known to host 25 pulsars, all of which have spin periods less than 8ms (Freire et al. 2017). More broadly, of the 145 currently known pulsars in globular clusters, 136 have $P_{<50}$ ms ($\sim$ 94% of the population, Manchester et al. 2005; Pitkin 2018). This suggests that in regions of high stellar density with frequent two-body interactions the pulsar spin period distribution can be significantly modified, and the Galactic centre is known to be orders of magnitude more dense than the Globular clusters in which the large MSP populations are observed. As noted in Macquart & Kanekar (2015), the formation rate of Low Mass X-ray Binaries (LMXBs), which act as the spin-up progenitors of MSPs, is approximately proportional to the square of the stellar density. Consequently many more LMXBs (and hence binary pulsars) would be expected in the Galactic center compared to globular clusters. Indeed, the the Galactic Centre is observed to host an overabundance of X-ray transients which are attributed to LMXBs (Muno et al. 2005; Hailey & Mori 2017; Generozov et al. 2018). In addition the leading explanation for the Fermi γ-ray excess at the Galactic centre (Ackermann et al. 2017) is a point source MSP population (Fragione et al. 2018). Consequently, it seems reasonable, if not likely, that the NS population at the Galactic centre is dominated by MSPs. In addition to the Galactic centre, if the centre of globular clusters do host IMBHs then these regions would be expected to form MSP-IMBH binaries.

1.5 Scientific potential

The gyroscopic stability of pulsars allows them to be used as precision, free-falling celestial clocks. Indeed, the precision with which pulsar periods can be measured rivals that of the best atomic clocks e.g. PSR J1748-2446ad is measured to have a spin period $P_s = 5.757451924362137$ (Verbiest et al. 2008), i.e. a measurement to a precision of 1 part in 10^{16}. The basis of pulsar timing is the measurement of the frequency-dependent pulse time of arrival (ToA). Given this $t - \nu$ signal, a model is constructed which maps the emission time in the pulsar frame to the ToA in the observer's frame. The difference between the observed timing signal and the theoretical modelled signal is described by the timing residuals. Errors in the timing model lead to systematic variability in the residuals. In this way radio pulsar timing observations allow high-precision measurements to be made of the intrinsic properties of the pulsar and host system (e.g. Liu et al. 2011; Desvignes et al. 2016; Lazarus et al. 2016; Liu et al. 2018).

Whilst the first detection of an MSP-E/IMRB system would be an important discovery in and of itself, such a system would also provide a powerful and unique laboratory - accessible via radio timing - with which to investigate key questions in astrophysics and fundamental physics. Indeed, for this reason the detection of a pulsar-BH system has been dubbed the ‘holy grail’ of astrophysics (Faucher-Giguère & Loeb 2011). From the perspective of fundamental physics, MSP-E/IMRBs would enable precision tests of general relativity (GR) in the gravitational strong-field (see e.g. Liu et al. 2012; Psaltis et al. 2016). GR has already passed a long series of experimental tests (Will 2014). In the modern era, these include measurements of the gravitational frequency shift as measured by Cassini (Bertotti et al. 2003), geodetic and Lense-Thirring precession of Gravity Probe B in Earth-orbit (Everitt et al. 2015), orbital decay of the Hulse-Taylor binary due to gravitational wave emission (Weisberg et al. 1981), precision tests of the equivalence principle to 1 part in 10^{14} (Nobili & Anselmi 2018), gravitational lensing measurements with Hipparcos (Froeschle et al. 1997) and Gaia (Krone-Martins et al. 2018), tests in binary pulsar systems (Lorimer 2008), gravitational redshift of stars at the Galactic centre (Gravity Collaboration et al. 2018a; GRAVITY Collaboration et al. 2020) and the direct detection of gravitational radiation from coalescing binary BH-BH and NS-NS systems (Abbott et al. 2016, 2017a,b). GR has passed all of these tests with flying colours.

Despite this success there remain open questions in GR: the existence of singularities in matter densities and spacetime curvature at the centre of BHs and at the origin of the universe (Pachner 1970), the non-uniqueness of the Einstein-Hilbert action (Psaltis 2008), as well as the spacetime dynamics of spinning objects (Obukhov et al. 2009; d’Ambrosi et al. 2015; Plyatsko & Fenyk 2016). In particular all existing electromagnetic observations have occurred in a region where the gravitational field strength is relatively weak. The strength of the gravitational field is quantified by the parameter ϵ,

$$\epsilon = \frac{GM}{rc^2} \, , \tag{1.4}$$

for mass M and separation r. Whilst this parameter has an intuitive interpretation, being proportional to the classical Newtonian gravitational potential, geometric theories of gravity such as GR deal not with potentials but curvatures. The spacetime curvature is defined via the parameter ξ

$$\xi = \frac{GM}{r^3c^2} \; . \tag{1.5}$$

Together these two parameters define a 2-space over which to quantify the strength of the gravitational field. As can be seen from Fig. 1.2, the bulk of existing tests of GR have primarily probed the weak-field regime, where $\epsilon \lesssim 10^{-6}, \xi_c \lesssim 10^{-28}$. In contrast, for a MSP in a 0.1 year orbit around the Galactic centre, with eccentricity $e = 0.9$, as it passes through periapsis it will probe a potential $\epsilon \sim 0.01$ and be traveling at an orbital velocity of $\sim 0.15c$. The unique nature of radio pulsar timing would then allow for system parameters to be determined with a remarkable precision: for a pulsar in a 0.3 year period orbit around Sgr A*, measuring the set of post-Keplerian parameters allows the mass and spin to be determined to a precision of 10^{-5} and 10^{-3}, respectively, assuming a modest timing precision of 100 μs (Liu et al. 2012). At shorter orbital radii or increased timing precisions relativistic effects would become more pronounced, potentially allowing for more precise tests and probing deeper into the strong-field regime.

Tests of fundamental physics with MSP-E/IMRBs are directly complementary with alternative methods. Stellar optical interferometric astrometry of the Galactic centre population of S-stars, in particular the 16-year orbit S2, has been used to measure the gravitational and relativistic redshift and shown to be inconsistent with Newtonian mechanics (Gravity Collaboration et al. 2018a,b). Whilst the development of more advanced instruments with increased sensitivities may allow the detection of fainter stars on more relativistic orbits, there is no evidence that such stars exist and it seems likely that they would be tidally disrupted. In contrast pulsars as compact objects can attain highly relativistic orbits without tidal disruption and so probe stronger gravitational fields. Moreover, as noted in Bower et al. (2019), milli-arsecond astrometry of the Galactic centre has a lengthscale precision of,

$$L_{\text{astrometry}} \sim 8.33 \, d_\theta[\text{kpc}] \sim 8\text{AU} \tag{1.6}$$

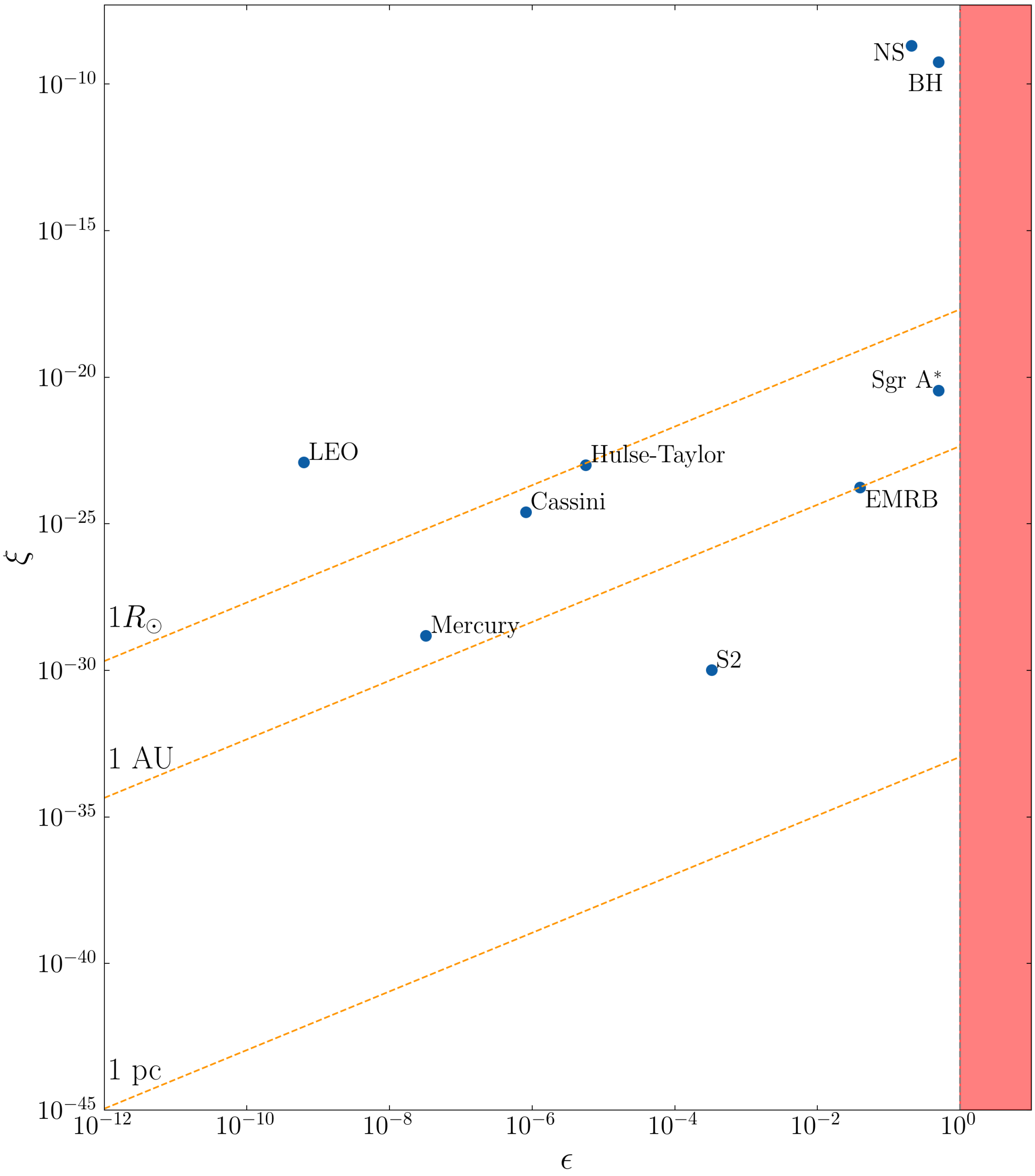

Fig. 1.2: The gravitational field strength parameter space in terms of the gravitational potential $\epsilon = GM/rc^2$ and the spacetime curvature $\xi = GM/r^3c^2$. The parameter space probed by different GR tests is shown. 'LEO' refers to the experiments in Low Earth Orbit, e.g. Gravity Probe B and MICROSCOPE. The EMRB system is taken to be a $P = 0.1$ year, $e = 0.9$ system in the Galactic centre. The mass of the Sgr A* BH is taken to be $4 \times 10^6 M_\odot$, whilst we set the 'BH' to have mass $10M_\odot$ and take the 'NS' to have mass $1.4M_\odot$, radius 10 km. The curvatures and potentials are calculated assuming point sources and at periapsis separation. The red region denotes the below horizon regime and the dashed orange lines show the relevant lengthscales. The potential and curvature strengths for dark matter and dark energy are too small to be shown on this chart.

whilst pulsar timing with timing precision $\sim \mu$s has,

$$L_{\text{pulsar}} \sim c d_t \sim 2 \times 10^{-9} \text{AU} \tag{1.7}$$

and so MSP timing ultimately offers more precise tests of GR.

Very long baseline interferometry (VLBI) with the Event Horizon Telescope (EHT) enables radio imaging on the scale of the supermassive BH event horizon (Ricarte & Dexter 2015). For a BH surrounded by some emission region such as an accretion disk, observations of the 'shadow' that result from gravitational lensing and photon capture then allow for parameter estimation of the central BH. This method has been applied to the supermassive BH at the centre of the elliptical galaxy M87 and was able to determine the mass to a precision of $\sim 10\%$ (Event Horizon Telescope Collaboration et al. 2019). Determination of further parameters such as the spin have not yet been possible, nor have observations of the Galactic centre due to scattering, but these challenges may be over come in the future as the instrumentation is further developed. EHT observations are a complementary method to PSR timing for strong field tests, with their own set of systematics, since the measurements made by EHT require a sufficiently advanced modelling and understanding of the accretion flow and jet behaviour.

Moving beyond the electromagnetic messenger channel, gravitational wave astronomy is now a routine practice following the first BH-BH detections in 2016 (Abbott et al. 2016). Ground based detectors such as LIGO/Virgo are able to determine the constituent BH masses to a precision $\mathcal{O}(10\%)$ in the dynamical strong field and offer definitive proof of the existence of astrophysical BHs. However, in their current inception it is difficult to do precision parameter estimation. Again this situation may be improved with the development of advanced versions (aLIGO, aVirgo, KAGRA) and 3rd generation ground based detectors (Einstein Telescope). Ground based detectors are noise limited to frequencies greater than $\sim 1 - 10$ Hz (Chaibi et al. 2016). The future generation of space-based detectors such as LISA (Baker et al.

2019) will open up the mHz gravitational wave regime and new population of sources. Directly related to MSP-E/IMRBs are the Extreme Mass Ratio Inspirals, the descendants of general EMRBs. Via gravitational wave observations one can expect to measure the redshifted mass to a precision $10^{-6} - 10^{-3}$ and spin to $10^{-5} - 10^{-3}$ and the quadrupole moment to $\sim 10^{-3}$ (Barack & Cutler 2007). However waveform modelling issues in EMRIs do remain (e.g. Barack & Pound 2019), whilst to determine the intrinsic BH mass - rather than the luminosity mass - requires accurate measurements of the source distance. Moreover, since gravitational wave observations naturally probe the dynamical spacetime pulsars would be more sensitive to modifications of GR which affect only the stationary part of the spacetime, since they would not be subject to the same confusion noise. Whilst MSPs are primarily expected to be detected in the radio, as they pass through periapsis they may emit a burst of gravitational radiation. This in turn would allow for strong-field multimessneger astronomy. The detection of this coincident gravitational radiation is a question we will return to in Chapter 6.

The essential goal of MSP-E/IMRB timing from the perspective of fundamental physics is precision measurements of the key parameters of the central BH: the mass M, spin S, and the quadrupole moment Q. If these parameters can be determined to sufficient precision it would open a vast array of opportunities and questions in fundamental physics. The Cosmic Censorship Conjecture (Penrose 1979) requires that all singularities are hidden behind event horizons. Since the event horizon radius for a spinning BH is

$$r_h^{\pm} = 1 \pm \sqrt{1 - a^2} \ , \tag{1.8}$$

the Cosmic Censorship Conjecture imposes a requirement on the BH spin parameter that,

$$a \equiv \frac{c}{G} \frac{S}{M^2} \leq 1 \ . \tag{1.9}$$

A measurement of a of a BH is then a direct challenge to GR, with $a > 1$ testing our understanding of the nature of spacetime and gravity. The No

Hair Theorem (Israel 1967) states that uncharged astrophysical black holes are completely characterized by their lowest order multipole moments (M, S), and all higher order moments (e.g. Q) can be expressed as a function of the lower moments. The quadrupole moment of an astrophysical BH must then satisfy,

$$\frac{c^4}{G^2}\frac{Q}{M^3} = -a^2 \; . \tag{1.10}$$

By measuring the mass, spin and quadrupole of an astrophysical BH these foundational issues in GR can then be definitively answered. Via PSR timing at the Galactic centre, the Cosmic Censorship Conjecture and the No Hair Theorem can then be possibly tested to $\leq 1\%$ precision (see e.g. Kramer et al. 2004; Liu et al. 2012; Liu et al. 2014; Wex & Kopeikin 1999; Eatough et al. 2015). By extension, the nature of the central massive compact object can also be investigated, i.e. whether the Kerr solution is a true astrophysical solution (the 'Kerr Hypothesis' Bambi 2011) or if parametrized deviations from the Kerr solution exist (so called 'bumpy' black holes, Yagi & Stein 2016), or even whether the massive central compact object is some more exotic object like a boson star (Kleihaus et al. 2012). Pulsar timing of EMRBs can also be used to test alternative theories of gravity such as scalar-tensor theories (Liu et al. 2014), search for quantum gravitational effects (Yagi & Stein 2016; Estes et al. 2017) and constrain the cosmological constant (Iorio 2018). From an astrophysical perspective, radio timing of MSP-E/IMRBs can be used to precisely determining the mass of black holes at the centre of Local Group galaxies and globular clusters in order to constrain the low end of the $M - \sigma$ relation (Ferrarese & Merritt 2000), establishing the existence or otherwise of otherwise of intermediate mass black holes (Singh et al. 2014), solve the Fermi GeV excess (Ackermann et al. 2017), explore the properties of ultra-dense matter (Fonseca et al. 2019), the nature of dark matter (Siegel et al. 2007) as well as properties of the interstellar medium and the nature of magnetic fields and the stellar formation hisotry at the centre of stellar clusters. Moreover, E/IMRBs in turn serve as progenitors of the extreme-mass-ratio-inspiral (EMRI) gravitational-wave sources, a major class of targets for the future LISA observations (Gair et al. 2010, 2017; Babak et al. 2017). Evidently there is then a huge scientific return from the disovery and timing of a strong-field MSP-E/IMRB

1.5.1 Challenges

Precision astronomy in strong-field environments remains a hugely challenging enterprise. In order realise the scientific potential of MSP-E/IMRBs, it is essential to be able to model the expected $t - \nu$ radio timing signal. The requirements for such a model are twofold. Firstly, being able to accurately model the theoretical signal is vital to inform the detection of these systems. As discussed the lack of pulsar detections in the centre of stellar clusters is likely due to insufficient sensitivity of current instrumentation to detect a MSP population. The current timing precision for slow pulsars is limited by irregularities of the pulsar's spin (e.g. Lyne et al. 2010), which is difficult to be improved by an increase in telescope sensitivity. However, the timing residuals for most MSPs are still dominated by system white noise (e.g. Verbiest et al. 2009), which can be greatly decreased by the increased instantaneous gain of the future telescopes. Even with the increased facilities and instrumentation performance, the detection of relativistic timing signals remains a non-trivial task. It is known for example that highly accelerated pulsars must be search for using computationally expensive 'acceleration searches', in order to correct the received signal for the motion of the pulsar (Adámek et al. 2019). As we move into the strong-field regime of the Galactic centre and consider relativistic systems, one must also consider a further series of effects which will influence the received pulsar signal, which fall into two broad classes:

1. Effects which influence the geodesic followed by a radio pulsar light ray while traveling through a curved space–time. This includes gravitational light bending, gravitational and relativistic time dilation, relativistic Doppler frequency shift, velocity-induced intensity boost, and dispersion induced by the interaction of the radio signal with line-of-sight material.

2. Effects related to the relativistic orbital dynamics and spin precession of a spinning pulsar around a spinning BH, e.g. spin couplings, cur-

vature couplings, associated time dilation (gravitomagnetic, relativistic, gravitational) and relativistic aberration.

It remains an open question whether current pulsar search algorithms are sufficiently sophisticated when applied to these strong-field signals.

The second requirement for a strong-field pulsar timing model is in order to use MSP-BH binaries as precision astrophysical laboratories. As discussed, with these systems we can make precision measurements in an extreme parameter space. However typically in pulsar system the intrinsic system parameters are inferred by fitting a set of 'post-Keplerian' parameters to the timing signal. The framework is derived only for weak gravitational fields and its applicability to strong-field regimes remains unclear. In order to use MSP-E/IMRBs as a precision fundamental physics laboratory a proper theoretical framework - applicable to strong field regimes and allowing unambiguous predictions to be made and compared with observations - is paramount.

Throughout this work we adopt the natural units, with $c = G = \hbar = 1$, and a $(-, +, +, +)$ metric signature. Unless otherwise stated, a c.g.s. gaussian unit system is used in the expressions for electromagnetic properties of matter. With these units, the gravitational radius of the black hole $r_{\rm g}$ is simply $= M$ and the corresponding Schwarzschild radius $r_{\rm s}$ is $2M$, where M is the black-hole mass. We will adopt a normalization that the black-hole mass is unity. A comma denotes partial derivative (e.g. ${x^{\nu}}_{,\mu} = \partial_{\mu} x^{\nu}$), and a semicolon denotes covariant derivative (e.g. ${x^{\nu}}_{;\mu} = Dx^{\nu}/d\mu = \partial_{\mu} x^{\nu} + {\Gamma^{\nu}}_{\mu\gamma} x^{\gamma}$).

Chapter 2

Propagation of Electromagnetic Radiation in Curved Spacetime

The first step in constructing a relativistic pulsar timing solution is being able to determine the geodesic motion of the emitted photons as they travel between the pulsar and the observer. In the strong gravitational field these spacetime trajectories are generally non-trivial, and are determined by both the mass and spin of the central BH. Moreover, the line of sight between the observer and a pulsar is in reality not a vacuum. Instead photons will generally propagate through a plasma due to the contribution from the interstellar medium (ISM), stellar winds, accretion disks etc. The combination of vacuum gravitational effects and chromatic line of sight effects will have a marked influence on the pulsar timing signal.

This Chapter introduces the mathematical techniques for computing the propagation of light in the strong gravitational field of a rotating (Kerr) black hole. I first introduce the properties of the Kerr spacetime and then derive the vacuum equations of motion via a Hamiltonian formalism. I then go on to modify the vacuum equations to account for the presence of astrophysical plasma. The set of differential equations defining the propagation of light can then be solved numerically.

2.1 Kerr Spacetime

BHs form from a gravitational collapse. Since astrophysical objects invariably posses some degree of angular momentum, and this momentum is conserved during the collapse, astrophysical BHs are expected to be rotating. Conversely, whilst it is theoretically possible for BHs to have electric charge, in astrophysical scenarios it is expected that any charge would be rapidly neutralised by the surrounding medium. The solution to the Einstein Field Equations for a rotating, uncharged BH is given by the Kerr solution (Kerr 1963) where in Boyer-Lindquist coordinates (t, r, θ, ϕ) the metric interval is

$$\mathrm{d}s^2 = g_{tt}\mathrm{d}t^2 + 2g_{t\phi}\mathrm{d}t\mathrm{d}\phi + g_{rr}\mathrm{d}r^2 + g_{\theta\theta}\mathrm{d}\theta^2 + g_{\phi\phi}\mathrm{d}\phi^2 \ , \tag{2.1}$$

where the covariant terms are

$$g_{tt} = -\left(1 - \frac{2r}{\Sigma}\right) \ , \tag{2.2}$$

$$g_{rr} = \frac{\Sigma}{\Delta} \ , \tag{2.3}$$

$$g_{\theta\theta} = \Sigma \ , \tag{2.4}$$

$$g_{\phi\phi} = \frac{\sin^2\theta}{\Sigma}\left[\left(r^2 + a^2\right)^2 - \Delta a^2 \sin^2\theta\right] \ , \tag{2.5}$$

$$g_{t\phi} = -\frac{2ar\sin^2\theta}{\Sigma} \ , \tag{2.6}$$

with $\Sigma(r, \theta) = r^2 + a^2\cos^2\theta$, $\Delta(r) = r^2 - 2r + a^2$, and the spin parameter $a = S/M^2$ for BH spin S and mass M. The contravariant terms are defined via, $g_{\mu\nu}g^{\nu\gamma} = \delta^{\mu}_{\gamma}$ such that,

$$g^{tt} = \frac{-g_{\phi\phi}}{\Delta\sin^2\theta} \ , \tag{2.7}$$

$$g^{rr} = \frac{1}{g_{rr}} \ , \tag{2.8}$$

$$g^{\theta\theta} = \frac{1}{g_{\theta\theta}} \ , \tag{2.9}$$

$$g^{\phi\phi} = \frac{-g_{tt}}{\Delta \sin^2 \theta} \ , \tag{2.10}$$

$$g^{t\phi} = \frac{g_{t\phi}}{\Delta \sin^2 \theta} \ . \tag{2.11}$$

The Boyer-Lindquist coordinates are oblate spheroidal coordinates; the radial coordinate r can be understood as a spin-modified analogue of the standard spherical polar radius, whilst θ, ϕ are the polar and azimuthal coordinates respectively. In the zero mass limit the metric reduces to flat Minkowski space and the relation between the Boyer Lindquist and the usual Cartesian/rectangular coordinates is made explicit:

$$x = m \sin\theta \cos\phi \ , \tag{2.12}$$

$$y = m \sin\theta \sin\phi \ , \tag{2.13}$$

$$z = r \cos\theta \ , \tag{2.14}$$

where $m = \sqrt{r^2 + a^2}$, and the inverse transform is simply defined algebraically as,

$$r = \sqrt{\frac{w + \sqrt{w^2 + 4a^2 z^2}}{2}} \ , \tag{2.15}$$

$$\theta = \arccos\left(\frac{z}{r}\right) \ , \tag{2.16}$$

$$\phi = \arctan 2(y, x) \ , \tag{2.17}$$

where $w = x^2 + y^2 + z^2 - a^2$. The Kerr metric has two singular regions when working in Boyer-Lindquist coordinates. The first occurs when $\Delta(r) = 0$. This condition in turn describes two singular horizons,

$$r_{\pm} = 1 \pm \sqrt{1 - a^2} \ . \tag{2.18}$$

The positive solution r_+ describes the BH event horizon; the past causal boundary of future null infinity. More physically this can be thought of as the region within which the escape velocity is greater than the speed of light.

The negative solution r_- is the Cauchy Horizon; whilst the radial tangent vector becomes timelike for $r < r_+$ after passing the Cauchy Horizon it again becomes spacelike. In the zero spin limit, $r_+ = 2$ - the Schwarzschild radius - and $r_- = 0$ - the BH singularity. The relevant geometry is presented in Fig. 2.1. The second singular region occurs when $\Sigma(r,\theta) = 0$ which corresponds to a equatorial circular ring of radius a. Evidently in the zero-spin limit this reduces to the BH singularity. It is important to note that this ring singularity is a true curvature singularity, a property of the spacetime itself. This can be seen since the Kretschman curvature scalar is defined as,

$$\begin{aligned}\mathcal{K} &\equiv R^{\mu\nu\alpha\beta}R_{\mu\nu\alpha\beta} \\ &= \frac{48M^2\left(2r^2-\Sigma\right)\left(\Sigma^2-16r^2a^2\cos^2\theta\right)}{\Sigma^6} \ ,\end{aligned} \tag{2.19}$$

which is clearly singular at $\Sigma = 0$. Conversely, the $\Delta = 0$ singularities are only coordinate singularities and can be removed by an appropriate change of coordinates, for example to Kerr-Schlid ‘Horizon penetrating coordinates’ (Debney et al. 1969)

The Kerr spacetime possesses two Killing vectors ξ^t, ξ^ϕ, related to temporal and axial diffeomorphisms of the vacuum metric. A general Killing vector ξ^μ satisfies Killing’s equation:

$$\xi^{(\mu;\nu)} = 0 \ . \tag{2.20}$$

The inner product of a Killing tensor ξ^μ with a tangent vector p_μ is conserved along a geodesic, i.e. if $K = \xi^\mu p_\mu$ then $\dot{K} = 0$, where “$\cdot$” denotes differentiation with respect to an affine parameter. The temporal Killing vector is associated with the conservation of energy, whilst the azimuthal Killing vector is related to the components of the angular momentum along the black hole spin axis:

$$E = -\xi^t p_t \ , \tag{2.21}$$

$$L_z = \xi^\phi p_\phi \ . \tag{2.22}$$

In addition, the Kerr spacetime admits a rank-2 Killing tensor

$$K^{\mu\nu} = 2\Sigma l^{(\mu}n^{\nu)} + r^2 g^{\mu\nu} \ , \tag{2.23}$$

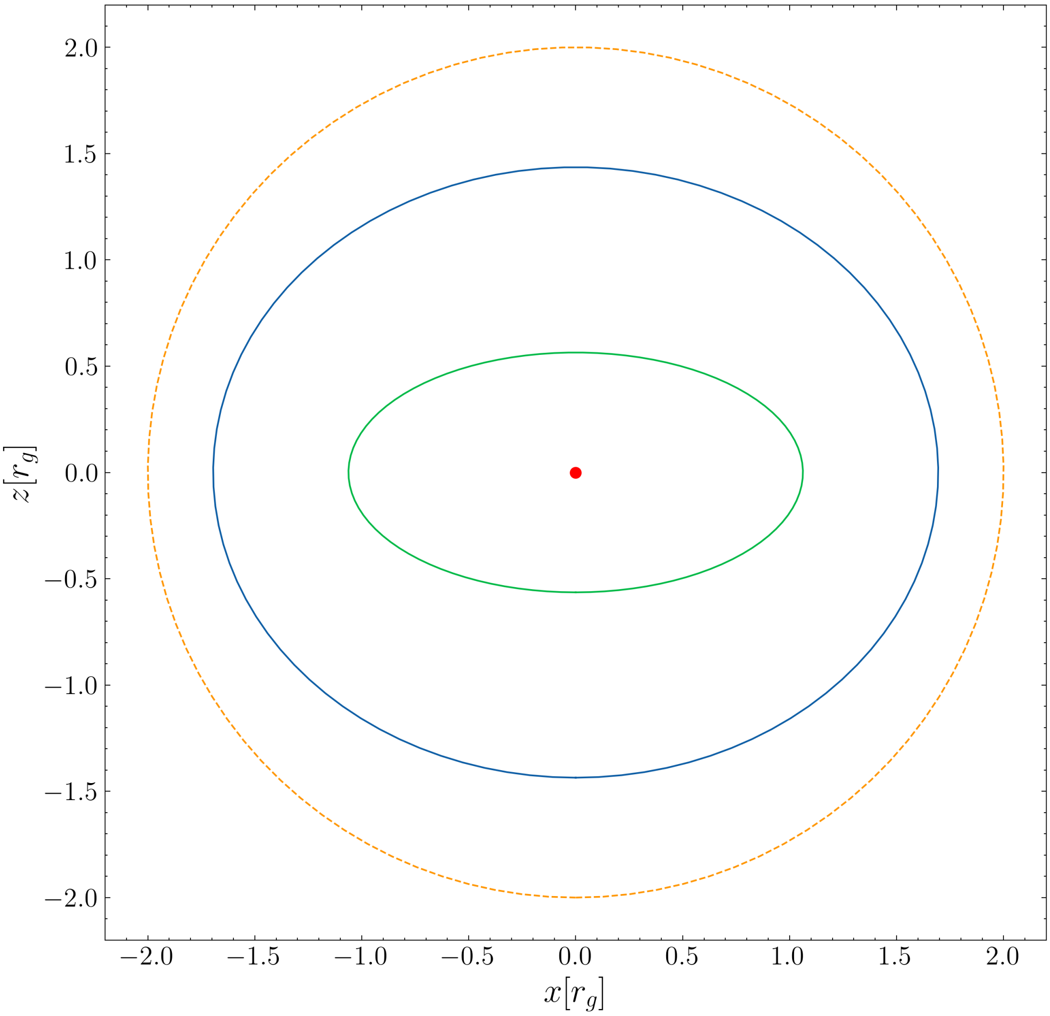

Fig. 2.1: Event horizon geometry in the $x - z$ plane. The dashed orange line is the event horizon on the zero spin (a=0) limit. The solid blue and green lines denote the outer and inner ($r_{\pm}$) horizons for a spinning BH with $a = 0.9$. As the spin parameter is turned down from $a = 0.9$ to $a = 0$, the outer radius (r_+) tends towards the dashed orange line, whilst the inner radius (r_-) collapses to the central singularity.

where l^μ, n^ν are the principal null vectors of the metric

$$l^\mu = \left(\frac{r^2+a^2}{\Delta}, 1, 0, \frac{a}{\Delta}\right) \ , \tag{2.24}$$

$$n^\nu = \left(\frac{r^2+a^2}{2\Sigma}, -\frac{\Delta}{2\Sigma}, 0, \frac{a}{2\Sigma}\right) \ , \tag{2.25}$$

and a Killing tensor obeys the higher order generalisation of Eq. 2.20

$$\nabla^{(\gamma} K^{\mu\nu)} = 0 \ . \tag{2.26}$$

This Killing tensor is related to a further conserved quantity - the Carter Constant (Q_C) (Carter 1968). Unlike the energy and angular momentum, the exact physical understanding of the Carter constant remains unclear (De Felice & Preti 1999; Rosquist et al. 2009).

2.2 Propagation in vacuum

Electromagnetic phenomena are generally described by Maxwell's equations, which have the covariant form in vacuum

$$\nabla_\mu F^{\mu\nu} = 4\pi J^\nu \ , \tag{2.27}$$

$$\nabla_\mu \tilde{F}^{\mu\nu} = 0 \ , \tag{2.28}$$

where J^μ is the divergence free 4-current density and $F^{\mu\nu}$ is the electromagnetic (Faraday) field tensor, defined with respect to the potential as,

$$F^{\mu\nu} = 2\nabla_{[\mu} A_{\nu]} \ , \tag{2.29}$$

whilst the dual to this tensor is

$$\tilde{F}^{\mu\nu} \equiv \epsilon^{\mu\nu\alpha\beta} F_{\alpha\beta}/2 \ , \tag{2.30}$$

and $\epsilon^{\mu\nu\alpha\beta}$ is the Levi-Cevita psuedo-tensor. By taking the covariant derivative of Eq. 2.27 in conjunction with the Bianchi identity Eq. 2.28, one can arrive at a general wave equation

$$\Box F_{\mu\nu} + 2R_{\mu\alpha\nu\beta} F^{\alpha\beta} + R^\alpha_\mu F_{\nu\alpha} - R^\alpha_\nu F_{\mu\alpha} = 0 \ , \tag{2.31}$$

where $R_{\mu\alpha\nu\beta}$ is the Riemann curvature tensor, $R_{\mu\nu} = R^{\alpha}_{\mu\alpha\nu}$ and we have set $J^{\nu} = 0$ i.e. charge-free space. This wave equation generally describes how electromagnetic waves behave in a gravitational field, i.e. general relativistic optics. Since the gravitational lengthscale is much longer than the wavelength we can employ the geometrical optics (eikonal) approximation and take the field tensor to have a slowly varying amplitude and a rapidly varying phase (e.g. Dolan 2018):

$$F_{\mu\nu} = \mathcal{A} f_{\mu\nu} e^{i\omega\Phi} \ , \tag{2.32}$$

where A is the wave amplitude, $f_{\mu\nu}$ the polarization bivector, Φ the phase and ω an order parameter which can be understood as the frequency. If we define the wavevector as a gradient,

$$k_{\mu} = \nabla_{\mu}\Phi \ , \tag{2.33}$$

then

$$-\omega^2 k^c k_c f_{ab} + i\omega \left[\left(2k^c \mathcal{A}_{;c} + k^c_{;c}\mathcal{A} \right) f_{ab} + \mathcal{A} k^c f_{ab;c} \right] + O\left(\omega^0\right) = 0 \ . \tag{2.34}$$

By comparing terms of equivalent order in ω it can be seen that

$$k^{\mu} k_{\mu} = 0 \ , \tag{2.35}$$

i.e. the wavevector is null. This implies that the wavevector satisfies the geodesic equation

$$\frac{d^2 x^{\mu}}{ds^2} + \Gamma^{\mu}_{\alpha\beta} \frac{dx^{\alpha}}{ds} \frac{dx^{\beta}}{ds} = 0 \tag{2.36}$$

The problem for the evolution of the light wave is then reduced to the evolution of a particle, i.e. a photon, along rays, where rays are curves which are orthogonal to surfaces of constant phase.

Rather than directly integrating the geodesic equation, it is more elegant and straightforward to determine the light ray propagation via a Hamiltonian formulation. The covariant form of the Hamiltonian is

$$H(x^{\mu}, p_{\nu}) = \frac{1}{2} g^{\mu\nu} p_{\mu} p^{\nu} \ , \tag{2.37}$$

where x^μ are the coordinate variables and p_ν the conjugate 4-momenta. The corresponding equations of motion, Hamilton's equations, are then

$$\dot{x^\mu} = \frac{\partial H}{\partial p_\mu} , \ \ \dot{p}_\mu = -\frac{\partial H}{\partial x^\mu} \ . \tag{2.38}$$

As discussed, $\dot{p}_t$ and $\dot{p}_\phi$ are constant related to symmetries of the spacetime. For the Kerr metric, the remaining equations are:

$$\begin{align}
\dot{t} &= E + \frac{2r(r^2+a^2)E - 2arL_z}{\Sigma\Delta} \ ; \tag{2.39}\\
\dot{r} &= \frac{p_r\Delta}{\Sigma} \ ; \tag{2.40}\\
\dot{\theta} &= \frac{p_\theta}{\Sigma} \ ; \tag{2.41}\\
\dot{\phi} &= \frac{2arE + (\Sigma - 2r)L_z \csc^2\theta}{\Sigma\Delta} \ ; \tag{2.42}\\
\dot{p}_\theta &= \frac{1}{2\Sigma}\left[-2a^2E^2\sin\theta\cos\theta + 2L_z^2\cot\theta\csc^2\theta\right] \ ; \tag{2.43}\\
\dot{p}_r &= \frac{1}{\Sigma\Delta}\big[-\kappa(r-1) + 2r(r^2+a^2)E^2 - 2aEL_z\big] \tag{2.44}\\
&\quad - \frac{2p_r^2(r-1)}{\Sigma} \ ; \tag{2.45}
\end{align}$$

where

$$\kappa = p_\theta^2 + E^2a^2\sin^2\theta + L_z^2\csc^2\theta \ , \tag{2.46}$$

is an effective recasting of the Carter constant:

$$\kappa = Q_C + L_z^2 + a^2E^2 \ . \tag{2.47}$$

2.2.1 Initial Conditions

In order to solve the above set of differential equations numerically it is necessary to specify the initial conditions of the photon ray (i.e. the initial x^μ, p_μ) and the associated constants of the motion. One can choose to integrate either 'forwards' (i.e. from pulsar to observer) or 'backwards' (from observer to pulsar) in time, since the metric is explicitly time independent. We now examine each of these approaches.

Forward Ray Tracing

Forwards ray tracing is the intuitive interpretation of firing a photon ray from source to observer. In this case the spacetime coordinates, the origin of the ray x^μ, can be freely chosen to coincide with the location of the source. The initial variable momenta terms p_r, p_θ ultimately specify the initial direction of the ray. We want to be able describe this initial ray orientation in terms of a polar angle with respect to the BH spin axis, $\theta_{\rm ray}$ and and azimuthal angle with respect to the BH x-axis, $\phi_{\rm ray}$. To achieve this, we can first write the Cartesian components of the ray velocity as,

$$V^i = \dot{x}^i = \begin{pmatrix} \dot{x} \\ \dot{y} \\ \dot{z} \end{pmatrix} = \begin{pmatrix} \sin\theta_{\rm ray}\cos\phi_{\rm ray} \\ \sin\theta_{\rm ray}\sin\phi_{\rm ray} \\ \cos\theta_{\rm ray} \end{pmatrix} \ . \tag{2.48}$$

We can then transform into Boyer-Lindquist coordinates by the transformation of a general contravariant vector,

$$V^\mu = \frac{\partial x^\mu}{\partial x^\nu} V^\nu \ , \tag{2.49}$$

such that explicitly:

$$\dot{r} = \frac{m}{\Sigma}\Big(r\sin\theta\cos\phi\sin\theta_{\rm ray}\cos\phi_{\rm ray} + r\sin\theta\sin\phi\sin\theta_{\rm ray}\sin\phi_{\rm ray} + m\cos\theta\cos\theta_{\rm ray}\Big) \ , \tag{2.50}$$

$$\dot{\theta} = \frac{m}{\Sigma}\Big(\cos\theta\cos\phi\sin\theta_{\rm ray}\cos\phi_{\rm ray} + \cos\theta\sin\phi\sin\theta_{\rm ray}\sin\phi_{\rm ray} - \frac{r}{m}\sin\theta\cos\theta_{\rm ray}\Big) \ , \tag{2.51}$$

$$\dot{\phi} = \frac{1}{m\sin\theta}\Big(-\sin\phi\sin\theta_{\rm ray}\cos\phi_{\rm ray} + \cos\phi\sin\theta_{\rm ray}\sin\phi_{\rm ray}\Big) \ . \tag{2.52}$$

By rearranging Eqs. 2.40,2.41, this specifies p_θ, p_r in terms of $\theta_{\rm ray}, \phi_{\rm ray}$. The constants E and $L_{\rm z}$ $(-p_t, p_\phi)$ can be expressed in terms of the $x^i, \dot{x}^i$ components by rearranging the Hamiltonian and equations of motion as:

$$E^2 = (\Sigma - 2r)\left(\frac{\dot{r}^2}{\Delta} + \dot{\theta}^2\Sigma\right) + \Delta\dot{\phi}^2\sin^2\theta \ ; \tag{2.53}$$

$$L_z = \frac{(\Sigma\Delta\dot{\phi} - 2arE)\sin^2\theta}{\Sigma - 2r} \ . \tag{2.54}$$

Backward Ray Tracing

For backwards ray tracing we integrate from the observer towards the BH. The observer has a coordinate system $\mathbf{x}'$ where the z' axis is aligned with the BH singularity. The coordinates of the observer image plane are then x', y'. The centre of this image plane is at $r_{\rm obs}$, $\theta_{\rm obs}$ defined with respect to the BH coordinate system. Since the Kerr metric is axisymmetric, generally we can set $\phi_{\rm obs} = 0$. The observer distance $r_{\rm obs}$ is chosen so as to be sufficiently large such that the observer's grid can be considered as a Euclidean grid with zero curvature, and all rays are perpendicularly incident on this grid. Throughout this work we set the observer grid at $r_{\rm obs} = 10^4\, r_{\rm g}$. We can approximate the deviation from Minkowski spacetime via the Kretschman scalar (Eq. 2.19), which in the limit of large r $(= r_{\rm obs})$,

$$\mathcal{K} \sim \frac{48}{r^6} \sim 10^{-24} \,, \tag{2.55}$$

which is much smaller than typical numerical precision and so we are well-justified as taking the observer plane as Euclidean.

Given the coordinates of the ray on the observer's image plane, we can transform to the BH coordinate system $(\mathbf{x}' \to \mathbf{x})$ as follows: (Pu et al. 2016)

1. Rotate clockwise by $(\pi - \theta_{\rm obs})$ about the x'-axis $(R_{x'})$
2. Rotate clockwise by $(2\pi - \phi_{\rm obs})$ about the z'-axis $(R_{z'})$.
3. Reflect in the plane $y' = x'$ $(A_{y'=x'})$.
4. Translate $\mathbf{x}'$ so that the origins of both coordinate systems coincide $(T_{x' \to x})$

The net transformation is then

$$\mathbf{x} = A_{y'=x'} R_{z'} R_{x'} \mathbf{x}' + T_{x' \to x} \tag{2.56}$$

$$= \begin{pmatrix} \mathcal{D}(y', z') \cos\phi_{\rm obs} - x' \sin\phi_{\rm obs} \\ \mathcal{D}(y', z') \sin\phi_{\rm obs} + x' \cos\phi_{\rm obs} \\ (r_{obs} - z') \cos\theta_{\rm obs} + y' \sin\theta_{\rm obs} \end{pmatrix} \tag{2.57}$$

$$\mathbf{x} = \Lambda \mathbf{x}' \tag{2.58}$$

where $\mathcal{D} = (\sqrt{r_{\text{obs}}^2 + a^2} - z')\sin\theta_{\text{obs}} - y' \cos\theta_{\text{obs}}$. Subsequently transforming from Cartesian to Boyer-Lindquist coordinates completely defines the initial x^μ. Since each ray arrives perpendicular to the image plane, $\dot{\mathbf{x}}' = (0, 0, 1)$ and so the velocity components in the black hole frame (the backwards ray tracing equivalent of Eq. 2.48) is

$$\dot{\mathbf{x}} \quad = \dot{\Lambda}\mathbf{x}' + \Lambda\dot{\mathbf{x}}' = \begin{pmatrix} -\sin\theta_{\text{obs}}\cos\phi_{\text{obs}} \\ -\sin\theta_{\text{obs}}\sin\phi_{\text{obs}} \\ -\cos\theta_{\text{obs}} \end{pmatrix} . \tag{2.59}$$

Converting to Boyer-Lindquist coordinates gives expressions for $(\dot{r}, \dot{\theta}, \dot{\phi})$ in the black hole frame:

$$\dot{r} = -\frac{-r\mathcal{R}\sin\theta\sin\theta_{\text{obs}}\cos\Phi + \mathcal{R}^2\cos\theta\cos\theta_{\text{obs}}}{\Sigma} , \tag{2.60}$$

$$\dot{\theta} = \frac{r\sin\theta\cos\theta_{\text{obs}} - \mathcal{R}\cos\theta\sin\theta_{\text{obs}}\cos\Phi}{\Sigma} , \tag{2.61}$$

$$\dot{\phi} = \frac{\sin\theta_{\text{obs}}\sin\Phi}{\mathcal{R}\sin\theta} , \tag{2.62}$$

where $\mathcal{R} = \sqrt{r^2 + a^2}$ and $\Phi = \phi - \phi_{\text{obs}}$. Specifying p_r, p_θ, E, L_z then proceeds as in the forward ray tracing case. An example backwards ray tracing integration for a spinning BH is presented in Fig. 2.2.

2.3 Propagation in a plasma

The previous discussion applied to a vacuum spacetime. However, for astrophysical applications we are typically operating not in a vacuum, but in some kind of plasma, whether this is due to the interstellar medium, stellar winds or accretion disks. We consider a cold, unmagnetized plasma. The geometrical derivation of light propagation in a dispersive medium was first outlined by Synge (1960) who showed that the phase velocity of a wave, relative to an observe with 4-velocity u^μ is,

$$v_p^2 = \frac{p_\mu u^\mu}{p_\nu u^\nu + \frac{p_\alpha p^\alpha}{p_\beta u^\beta}} . \tag{2.63}$$

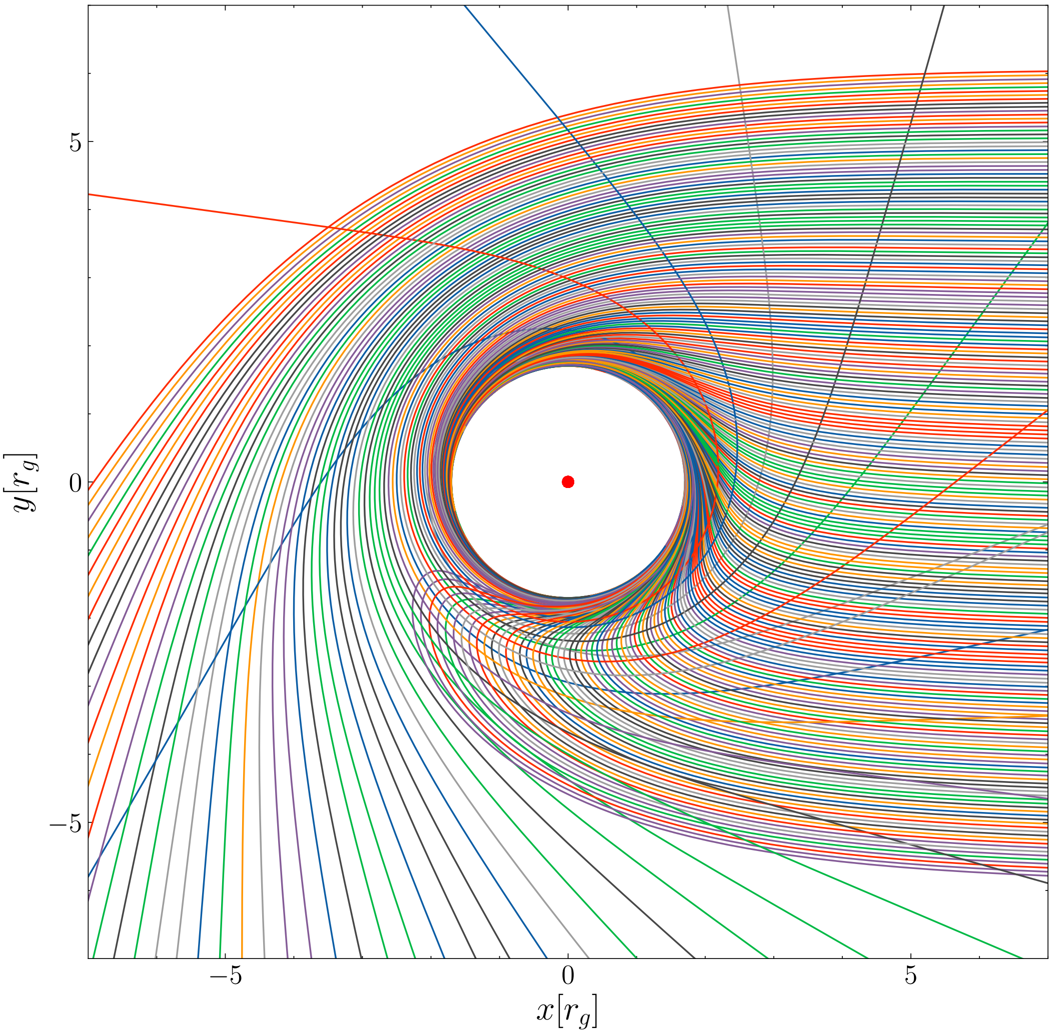

Fig. 2.2: Backwards ray tracing in the equatorial plane around a Kerr BH with spin parameter $a = 0.9$. The rays originate in the distant positive x direction. The gravitational lensing of photon geodesics and the frame dragging due to the BH spin is clearly visible.

Since the refractive index of a medium n is the reciprocal of the phase speed then,

$$n^2 = 1 + \frac{p_\mu p^\mu}{(p_\nu u^\nu)^2} \ . \tag{2.64}$$

It follows that the Hamiltonian is then,

$$H(x^\mu, p_\mu) = \frac{1}{2}\left[g^{\mu\nu}p_\mu p_\nu - (n^2-1)(p_\alpha u^\beta)^2\right] \ . \tag{2.65}$$

Now, since the scalar product of the momentum is related to the plasma frequency

$$p_\mu p^\mu = -\omega_p^2 \ , \tag{2.66}$$

it follows that the Hamiltonian can be written in a neat form as,

$$H(x^\mu, p_\mu) = \frac{1}{2}\left[g^{\mu\nu}p_\mu p_\nu + \omega_\mathrm{p}^2(x^\mu)\right] = 0 \ . \tag{2.67}$$

Rather than a macroscopic, geometrical approach, the same result can also be derived via a microscopic electromagnetic method (e.g. Broderick & Blandford 2003). From Eq. 2.67 it can be seen that all of the plasma interactions are contained in the plasma frequency term, where

$$\omega_p^2(x^\mu) = \frac{4\pi q_e^2}{m_e} n_e(x^\mu) \ , \tag{2.68}$$

and q_e is the charge on the electron, m_e the electron mass and $n_e(x^\mu)$ the number density profile of the plasma. If the number density does not evolve in time and is independent of ϕ (axisymmetric) then $\omega_\mathrm{p}^2 = \omega_\mathrm{p}^2(r,\theta)$, then the Hamiltonian remains axisymmetric and stationary and the associated conserved quantities E, L_z remain constant. Naturally the photon rest mass remains null ($H = 0$). However we have lost the Carter constant, which depends explicitly on the separability of the Hamiltonian into its coordinate variables. To illustrate, consider the explicit form of Eq. 2.67 for the Kerr metric:

$$-\frac{E^2}{\Delta}\left[(r^2+a^2)^2 - \Delta a^2 \sin^2\theta\right] + \frac{4arEL_z}{\Delta} + p_r^2\Delta + p_\theta^2 + \frac{L_z^2}{\sin^2\theta}\left(1 - \frac{a^2\sin^2\theta}{\Delta}\right) + r^2\omega_\mathrm{p}^2(r,\theta) + a^2\cos^2\theta\,\omega_\mathrm{p}^2(r,\theta) = 0 \ , \tag{2.69}$$

Evidently it is impossible to separate this expression into r, θ terms, due to the cross terms introduced by ω_p^2. Conversely when $\omega_p = 0$ (the vacuum case) this expression can be separated, the Carter constant defined and the previous equations derived. The underlying physics can be elucidated by comparing the ‘plasmic-Hamiltonian’, Eq. 2.67, with the Hamiltonian of a massive particle (mass m) travelling through a vacuum.

$$H = g^{\mu\nu} p_\mu p_\nu + m^2 \ . \tag{2.70}$$

The plasma frequency effectively plays the role of a particle mass in a vacuum spacetime. For a uniform plasma distribution, ω_p is a constant and hence the Hamiltonian is separable. Otherwise, the photon essentially acquires an effective mass which varies during its propagation in the plasma. To proceed we define a specific form of ω_p^2 such that the Hamiltonian recovers its separability:

$$\omega_\mathrm{p}^2 = \frac{4\pi e^2}{m_e} \frac{f(r) + g(\theta)}{\Sigma} \ . \tag{2.71}$$

This form describes a stationary and axisymmetric plasma distribution with independent radial and polar dependence through the additive contribution by the two terms $f(r)$ and $g(\theta)$. Although this particular form restricts the description of general density distributions, it retains certain desirable properties from the perspective of astrophysical modelling, as with an appropriate choices of $f(r)$ and $g(\theta)$ we may describe the key features of an axisymmetric plasma, such as inverse radial dependence, dominance of radial terms at large radii, maximal value in equatorial plane, etc. Going forward, we adopt this particular functional form of ω_p in our demonstrative calculations.

The properties of astrophysical plasma near the Sgr A* BH has been probed by the polarisation of the emission (Agol 2000; Quataert & Gruzinov 2000), the spectra at millimeter - centimeter wavelengths (Narayan et al. 1995; Falcke et al. 1998; Marrone et al. 2007) and the size of the emission region (Özel et al. 2000; Doeleman et al. 2008). Based on these observations it is possible to construct a semi-analytical model for the plasma at the Galactic centre as (Broderick & Loeb 2005; Broderick et al. 2009):

$$n_e = n_e^0 \left(\frac{r c^2}{GM} \right)^{-1.1} \ , \tag{2.72}$$

where the best fit normalisation parameter to the model is $n_e^0 = 3.5 \times 10^7 \mathrm{cm}^{-3}$ (Broderick et al. 2011). Similar models and normalisations are commonly used in the literature (Mościbrodzka et al. 2009; Psaltis 2012). Such a density profile can then be described by our separable form by setting $f(r) = r^{0.9}$, $g(\theta) = 0$.

Adopting the form of ω_p^2 as given by Eq. 2.71 the Hamiltonian regains its separability and we can proceed analogously to the vacuum case to derive the equations of motion. The coupled set of differential equations 2.39 - 2.45 is modified from the vacuum case as,

$$\dot{t} = E + \frac{2r(r^2+a^2)E - 2arL_z}{\Sigma\Delta} \; ; \tag{2.73}$$

$$\dot{r} = \frac{p_r \Delta}{\Sigma} \; ; \tag{2.74}$$

$$\dot{\theta} = \frac{p_\theta}{\Sigma} \; ; \tag{2.75}$$

$$\dot{\phi} = \frac{2arE + (\Sigma - 2r)L_z \csc^2\theta}{\Sigma\Delta} \; ; \tag{2.76}$$

$$\dot{p}_\theta = \frac{1}{2\Sigma}\left[-Cg(\theta)_{,\theta} - 2a^2E^2 \sin\theta\cos\theta + 2L_z^2 \cot\theta\csc^2\theta\right] \; ; \tag{2.77}$$

$$\dot{p}_r = \frac{1}{\Sigma\Delta}\Big[-\kappa_\omega(r-1) + 2r(r^2+a^2)E^2 - 2aEL_z \tag{2.78}$$

$$- \frac{Cf(r)_{,r}\Delta}{2} - C(r-1)f(r)\Big] \tag{2.79}$$

$$- \frac{2p_r^2(r-1)}{\Sigma} \; ; \tag{2.80}$$

where $C = 4\pi q_e^2/m_e$ and we reproduce the full set for completeness. Now, κ_ω is the plasma equivalent of κ and is defined,

$$\kappa_\omega = p_\theta^2 + E^2a^2\sin^2\theta + L_z^2\csc^2\theta + a^2\omega_\mathrm{p}^2\cos^2\theta \; . \tag{2.81}$$

This is effectively a new Carter constant applicable to plasmic - Kerr spacetimes. The angular momentum is unchanged from the vacuum case, whilst the energy is now given by,

$$E^2 = (\Sigma - 2r)\left(\frac{\dot{r}^2}{\Delta} + \dot{\theta}^2\Sigma + \frac{\omega_p^2}{\Sigma}\right) + \Delta\dot{\phi}^2\sin^2\theta \; . \tag{2.82}$$

Ray tracing in a vacuum is frequency independent. Conversely, when ray tracing through a plasma we must specify the frequency of the ray. In GR, frequency is observer dependent:

$$\nu = p_\alpha u^\alpha \ , \tag{2.83}$$

gives the frequency of a ray with 4 momenta p_μ as measured by an observer moving with 4-velocity u^α. For the purposes of observational astronomy, we want to be able to specify the observation frequency i.e. the frequency measured by a distant observer ν_{obs}, which is related to the energy at infinity as $E = 2\pi\nu_{\text{obs}}$. For a given initial position (r, θ, ϕ), E is determined by the ray velocity components $\dot{r}, \dot{\theta}, \dot{\phi}$ via Eq. 2.82. The problem then becomes how to set the initial $\dot{r}, \dot{\theta}, \dot{\phi}$ such that we can specify the observation frequency of the ray. In the vacuum case the ray geodesic is independent of the value of E and we set the ray velocity to have unit magnitude for simplicity. Conversely in the plasma case we want to be able to set the magnitude of the ray velocity E',

$$V^i = E' x^i \ , \tag{2.84}$$

such that the energy at infinity E is related to a specific observation frequency. By rearranging Eq. 2.82 it can be shown that E' can be specified relative to the observed ray energy (frequency) as,

$$(E')^2 = \frac{E^2 - \omega_p^2 + 2r\omega_p^2/\Sigma}{(\Sigma - 2r)\left[\dot{r}^2/\Delta + \dot{\theta}^2\right] + \Delta \sin^2\theta \dot{\phi}^2} \ , \tag{2.85}$$

where $\dot{r}, \dot{\theta}, \dot{\phi}$ are the components of the unit vector of the ray velocity as specified by Eqs. 2.60 - 2.62 and Eqs. 2.50 - 2.52.

The introduction of the plasma frequency term means that our ray tracing is now chromatic and the rays are subject to dispersion in both time and space. In classical electromagnetism the group velocity of an electromagnetic wave with angular frequency ω and wavenumber k propagating through a plasma is,

$$v_g = \frac{\partial \omega}{\partial k} = \sqrt{1 - \frac{\omega_p^2}{\omega^2}} \tag{2.86}$$

It follows that the time taken, Δt, for this EM wave to propagate a distance D along a path ds is

$$\Delta t = \int_0^D \frac{ds}{v_g} = \frac{1}{c}\int_0^D \left(1 - \frac{\omega_p^2}{\omega^2}\right)^{-0.5} ds \ . \tag{2.87}$$

Performing a Taylor expansion to first order and using the definition of ω_p^2 (Eq. 2.68) then gives,

$$\Delta t = \frac{D}{c} + \frac{2\pi q_e^2}{m_e c\omega}\int_0^D n(s) ds \ , \tag{2.88}$$

where $n(s)$ is the plasma number density profile along the path. We can then see that generally EM waves are delayed with respect to the vacuum case (D/c) by a frequency-dependent time delay. The plasmic Hamiltonian naturally describes the general relativistic analogue of this effect. In addition to a dispersion in time, the combination of high spacetime curvature and a dispersive plasma also induces a dispersion in space whereby rays of different frequencies follow different spatial paths (Fig. 2.3). This can be considered as a relativistic equivalent of a dispersive prism; in the classical case the rays are bent according to Snell's Law as the refractive index of the medium changes at the boundary of the prism. In the relativistic astrophysical case, the index of refraction is changing continuously as it tracks the plasma density distribution whilst the strong-field curvature causes gravitational lensing of the light rays which in turn acts as an effective refraction. The consequence of the introduction of a plasma into the vacuum spacetime is that is that rays of different frequencies will not follow the same spacetime trajectory; the light geodesics are now chromatic. The implications for pulsar timing in the gravitational strong field will be discussed in later chapters.

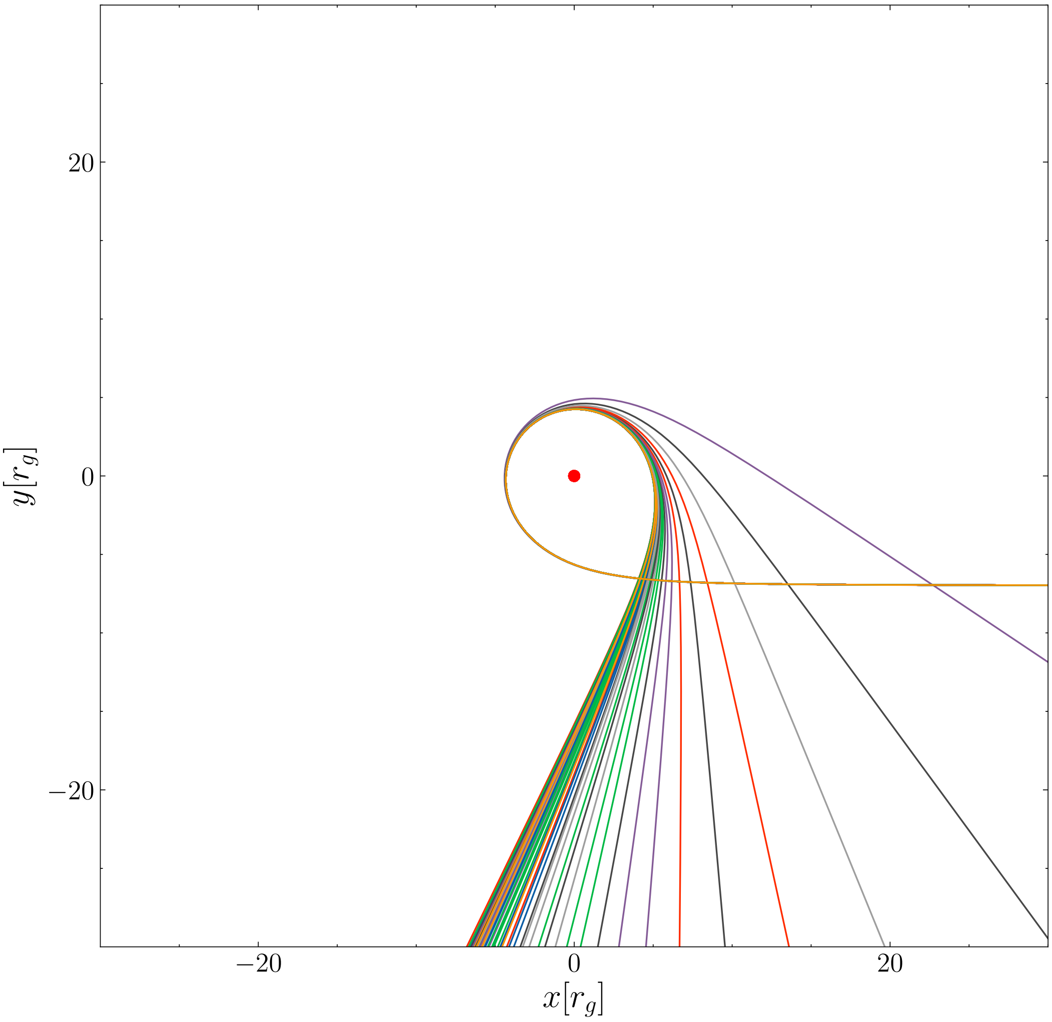

Fig. 2.3: Spatial dispersion induced in the rays propagating through a plasma on a Kerr background geometry with a maximal BH spin parameter $a = 0.998$. The rays have radio frequencies as measured by the observer between 0.18 and 6 GHz, where the less strongly lensed purple line represents the lowest frequency. We use the plasma density model as given by Eq. 2.72 and set the normalisation parameter to $n_e^0 = 3.5 \times 10^7$ cm^{-3}. All rays start on the observers image plane with $(x', y') = (-7, 0)$, and the observer is at $\theta_{\rm obs} = \pi/2$ such that the rays propagate in the equatorial plane.

Chapter 3

Relativistic Spin Orbital Dynamics

The most basic approximation in GR is that of a test particle which has no spin, no internal structure and is not subject to self-force effects. Such a particle then directly follows a geodesic of the spacetime metric. However, real astrophysical objects are not in actuality test particles and to obtain an accurate description of their dynamics, higher-order effects must be considered. This is particularly important for modelling fast spinning pulsars in the gravitational strong field; the spin of the pulsar itself will modify the background spacetime and so generally such objects will not follow geodesics of the Kerr metric. In addition to an accurate description of the dynamical behaviour (i.e. position, velocity, momenta) for pulsars it is equally important to establish the spin evolution; since pulsar emission is not isotropic but beamed at some angle from the spin axis, the evolution of the spin axis will directly imprint on the observed signal. In this Chapter we establish how a spinning particle behaves in a gravitational field. The determination of the equations of motion will then allow us to describe the spin-orbital dynamics of a millisecond pulsar orbiting a massive spinning black hole. We follow the methods outlined by Mathisson (Mathisson 1937), Papetrou (Papapetrou 1951) and Dixon (Dixon 1974), commonly referred to as the MPD framework.

3.1 Constructing the gravitational skeleton

Given a pulsar with some energy momentum tensor $T^{\mu\nu}$, the spin-orbital dynamics are completely specified by Einstein's Field Equations. However, such a solution is computationally intractable and the problem then becomes how to approximate this behaviour such that it becomes tractable, whilst still retaining the astrophysical complexity, subtlety and nuance that we are interested in. The energy momentum tensor can be expressed as an infinite sum of multipole moments - the gravitational skeleton - with respect to some reference worldline $z^\mu(\tau)$, as measured by an observer with 4-velocity u^μ (Dixon 1974)

$$\int_{\Sigma(z,u)} T^{\mu\nu}\delta x^{\alpha_1}\dots\delta x^{\alpha_n}\sqrt{-g}d\Sigma_\nu \ , \tag{3.1}$$

where $\delta x^\alpha = x^\alpha - z^\alpha$ (i.e. deviation from the worldline) for a system of Riemann normal coordinates x^α. The integration takes place over a spacelike hypersurface $\Sigma(z,u)$ which is generated by all geodesics at the point z^α which are orthogonal to u^μ. It follows that $d\Sigma$ is the 3-volume element of the hypersurface and $d\Sigma_\gamma = -n_\gamma d\Sigma$ where n_γ is the unit normal to $\Sigma(z,u)$.

The equations of motion of the pulsar are defined by

$$T^{\mu\nu}{}_{;\nu} = 0 \ . \tag{3.2}$$

The two lowest order moments are the 0th mass moment, encoded in the 4-momentum p^μ and the 1st dipole moment, given by the spin tensor $s^{\mu\nu}$:

$$p^\alpha \equiv \int_{\Sigma(z,u)} T^{\alpha\beta}d\Sigma_\beta \ , \tag{3.3}$$

$$S^{\alpha\beta} \equiv 2\int_{\Sigma(z,u)} x^{[\alpha}T^{\beta]\mu}d\Sigma_\gamma \ . \tag{3.4}$$

It follows from the conservation law that,

$$\frac{Dp^\mu}{d\tau} = -\frac{1}{2}R^\mu_{\nu\alpha\beta}u^\nu s^{\alpha\beta} + \mathcal{F}^\mu \ , \tag{3.5}$$

$$\frac{Ds^{\mu\nu}}{d\tau} = p^\mu u^\nu - p^\nu u^\mu + \mathcal{T}^{\mu\nu} \ , \tag{3.6}$$

where the Dixon force $\mathcal{F}^\mu$ and the Dixon torque $\mathcal{T}^{\mu\nu}$ are determined by moments higher than the dipole and $D/d\tau$ denotes a covariant derivative with respect to the proper time along the PSR worldline.

3.2 Spin Supplementary Condition

The system of equations specified by Eqs. 3.5, 3.6 is not determinate, since there exist more unknowns than equations. This is related to the uncertainty in choosing a reference world line for the multipole expansion of $T^{\mu\nu}$. A natural choice of a representative point of the bulk motion of the body is the centre of mass. However in GR the centre of mass of a spinning body is not invariant. It is therefore necessary to specify a spin supplementary condition (SSC) which renders the system of equations determinate. This is equivalent to choosing an observer with respect to which the centre of mass (centroid) is defined. For this work we adopt the Tulczyjew-Dixon (TD) condition,

$$s^{\mu\nu}p_{\nu} = 0 \ , \tag{3.7}$$

(Tulczyjew 1959; Dixon 1964). This is equivalent to choosing the centre of mass as measured in the zero 3-momentum frame. In this case, by contracting Eq. 3.6 with u^{μ} the momentum can be written as

$$p^{\alpha} = \frac{1}{m}\left(M^2 u^{\alpha} + S^{\alpha\beta}\frac{Dp_{\beta}}{d\tau}\right) \ , \tag{3.8}$$

where we have neglected terms greater than the dipole. From this we can see that the momentum and velocity are not generally parallel due to the presence of the orthogonal component $S^{\alpha\beta}p_{\beta;\tau}$. This term is known as the 'hidden momentum' (Filipe Costa & Natário 2014). The nomenclature references the fact that in our frame the 3-momentum is zero, yet the particle centroid is not as rest; there exists some additional momentum hidden in the particle. This hidden momentum term is defined by the SSC and can be considered as a choice of gauge. Other SSC choices do exist, e.g. Frenkel-Mathisson-Pirani condition, $s^{\alpha\beta}u_{\beta} = 0$ (Frenkel 1926; Mathisson 1937; Pirani 1956), which specifies the centroid measured by a comoving observer. The question then naturally arises as to how the choice of SSC affects the spin-orbital dynamics? Different choices of SSC correspond to different choices of the body worldline. The set of all potential worldlines forms a worldtube. In the extreme mass ratio limit, the minimal worldtube is always contained within the convex hull of the worldtube of the body (Filipe Costa & Natário 2014). Consequently different choices of SSC describe different but equivalent motions. The choice of the TD condition is advantageous since it specifies a unique worldline; i.e. for a given $T^{\mu\nu}$ there is only one $z^\alpha(\tau)$ such that the SSC holds. This contrasts with e.g. the FMP condition; there are infinitely many worldlines such that $s^{\alpha\beta}u_\beta = 0$.

In the limit of extreme mass ratio $m \ll M$ and since the pulsar radius $r_{\rm PSR} \ll$ gravitational lengthscale r_g, the lowest order moments dominate over the higher order moments and so we can neglect all terms greater than the dipole ($\mathcal{F}^\mu = 0, \mathcal{T}^{\mu\nu} = 0$). When combined with the TD condition this leads to intuitive conserved quantities; firstly the dynamical mass

$$m^2 = -p^\mu p_\mu \ , \tag{3.9}$$

is conserved:

$$\frac{dm}{d\tau} = \frac{1}{m p_\mu u^\mu} \frac{Dp_\nu}{d\tau} p_\mu \frac{DS^{\mu\nu}}{d\tau} = 0 \ . \tag{3.10}$$

Secondly, by contracting the spin tensor to obtain the spin vector,

$$s_\mu = -\frac{1}{2m} \epsilon_{\mu\nu\alpha\beta} p^\nu s^{\alpha\beta} \ , \tag{3.11}$$

$$s^{\mu\nu} = \frac{1}{m} \epsilon^{\mu\nu\alpha\beta} p_\alpha s_\beta \ , \tag{3.12}$$

we can define a spin scalar s:

$$s^2 = s^\mu s_\mu \ . \tag{3.13}$$

This quantity is also conserved via the TD condition:

$$\frac{ds^2}{d\tau} = 2 s_{\mu\nu} p^{[\mu} u^{\nu]} = 0 \ . \tag{3.14}$$

3.3 Equations of motion

As discussed, all the possible wordlines, contingent on choice of SSC, exist within the minimal worldtube. The radius of this worldtube (the radius of the disk of all possible centroids) is the Moller Radius (Möller 1949)

$$R_{\rm M} = \frac{s}{m} \ . \tag{3.15}$$

Now, since $m \ll M$ and the $R_{\mathrm{M}} \ll r_{\mathrm{PSR}}$ the pole-dipole terms are much stronger than the dipole-dipole terms,

$$\left(\frac{p^\mu}{m} - u^\mu\right) \sim \frac{M R_{\mathrm{M}}^2}{r^3} \propto 1 \tag{3.16}$$

(Chicone et al. 2005). Therefore, to first order the 4-velocity and 4 momentum are parallel, i.e. $p^\mu \approx m u^\mu$. The equations of motion then become,

$$\frac{Du^\mu}{d\tau} = -\frac{1}{2m} R^\mu_{\nu\alpha\beta} u^\nu s^{\alpha\beta} \ , \tag{3.17}$$

$$\frac{Ds^{\mu\nu}}{d\tau} \approx 0 \ , \tag{3.18}$$

(Chicone et al. 2005; Mashhoon & Singh 2006). The complete set of coupled differential equations for the evolution of the momentum, spin and position vectors is then (Singh 2005; Mashhoon & Singh 2006; Singh et al. 2014)

$$\frac{dp^\alpha}{d\tau} = -\Gamma^\alpha_{\mu\nu} p^\mu u^\nu + \lambda \left(\frac{1}{2m} R^\alpha_{\beta\rho\sigma} \epsilon^{\rho\sigma}{}_{\mu\nu} s^\mu p^\nu u^\beta\right) \ , \tag{3.19}$$

$$\frac{ds^\alpha}{d\tau} = -\Gamma^\alpha_{\mu\nu} s^\mu u^\nu + \lambda \left(\frac{1}{2m^3} R_{\gamma\beta\rho\sigma} \epsilon^{\rho\sigma}{}_{\mu\nu} s^\mu p^\nu s^\gamma u^\beta\right) p^\alpha \ , \tag{3.20}$$

$$\frac{dx^\alpha}{d\tau} = -\frac{p^\delta u_\delta}{m^2} \left[p^\alpha + \frac{1}{2} \frac{\lambda(s^{\alpha\beta} R_{\beta\gamma\mu\nu} p^\gamma s^{\mu\nu})}{m^2 + \lambda(R_{\mu\nu\rho\sigma} s^{\mu\nu} s^{\beta\sigma}/4)}\right] \ . \tag{3.21}$$

Here we have set the affine parameter to be the proper time such that $u^\mu u_\mu = -1$ and those terms which arise due to the dynamics interaction of the pulsar spin with the background curvature ('spin-curvature coupling') are tagged via the λ parameter. Spin-curvature coupling is included when $\lambda = 1$ and excluded when $\lambda = 0$.

3.3.1 Initial Conditions

The equations of motion are written in a covariant form and so are applicable to a general metric $g_{\mu\nu}$. For our purposes we will specialise to the Kerr metric, since we want to describe the dynamics of a spinning pulsar around a spinning black hole. To complete the set up and solve these equations the initial values of each of the 4-vectors x^μ, p^μ, s^μ must first be specified.

The initial spacetime coordinates x^μ are fairly inconsequential and can be almost freely chosen. Since the spacetime is stationary and axisymmetric we generally set $t(\tau=0)=\phi(\tau=0)=0$. The initial r and θ coordinates can be set subject to the constraints imposed by the orbital configuration. The initial spin 4-vector is determined by the polar and azimuthal spin angles $\theta_{\rm spin}$, $\phi_{\rm spin}$. The spin angles are in turn defined locally in the particle tetrad frame such that the background is Minkowskian and Cartesian coordinate basis can be used. In the coordinate basis, the spin angles are related to the spatial components of the spin 4-vector $s^i=(s^1,s^2,s^3)$ as,

$$s^1 = S\sin\theta_{\rm spin}\cos\phi_{\rm spin} \ , \tag{3.22}$$

$$s^2 = -\frac{S\cos\theta_{\rm spin}}{r} \ , \tag{3.23}$$

$$s^3 = -\frac{S\sin\theta_{\rm spin}\sin\phi_{\rm spin}}{r\sin\theta} \ , \tag{3.24}$$

where S is the magnitude of the spin spatial vector:

$$S = 2\pi\frac{\mathcal{I}}{P_{\rm s}} \ , \tag{3.25}$$

and $\mathcal{I}$ is the moment of inertia of the spinning body. The temporal s^0 term is then simply calculated by noting that the SSC can be expressed as,

$$p^\mu s_\mu = 0 \ . \tag{3.26}$$

In order to determine the initial conditions of the momenta p^μ, the massless geodesic equations Eq. 2.39 - 2.45 can be recast to an equivalent form for massive particles ($p_\mu p^\mu=-1$) such that,

$$p^t = \frac{m}{\Sigma}\left[\frac{r^2+a^2}{\Delta}P - a\left(aE\sin^2\theta - L_z\right)\right] \ , \tag{3.27}$$

$$p^r = \pm\frac{m}{\Sigma}\sqrt{R} \ , \tag{3.28}$$

$$p^\theta = \pm\frac{m}{\Sigma}\sqrt{\Theta} \ , \tag{3.29}$$

$$p^\phi = \frac{m}{\Sigma}\left[\frac{a}{\Delta}P - aE + \frac{L_z}{\sin^2\theta}\right] \ , \tag{3.30}$$

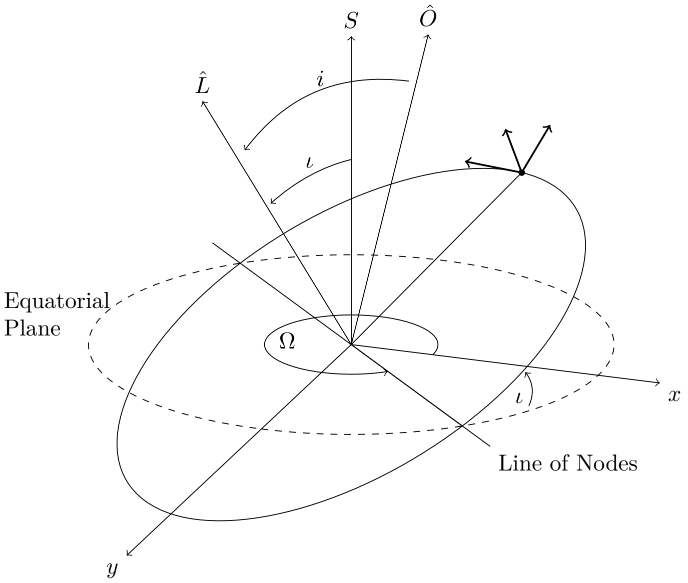

Fig. 3.1: The coordinate system and orbital elements used to define the MSP motion. The orbital plane is inclined by an angle ι with respect to the BH equatorial plane - i.e. the $\theta = \pi/2$ plane about the BH spin axis. The inclination of the orbit with respect to the observer's line of sight is given by i and the longitude of the ascending node as Ω, where we have set the positive $x-$axis as the reference direction.

where

$$R = \left[\left(r^2 + a^2\right) E - aL_z\right]^2 - \Delta\left[r^2 + \left(L_z - aE\right)^2 + Q\right] \ , \tag{3.31}$$

$$\Theta = Q - \left[\left(1 - E^2\right) a^2 + \frac{L_z^2}{\sin^2\theta}\right]\cos^2\theta \ , \tag{3.32}$$

$$Q = P - E\left(r^2 + a^2\right) - aL_z \ . \tag{3.33}$$

As discussed, in Kerr geometry E, L_z and Q are conserved quantities. For astronomical purposes it is useful to map these constants to classical orbital parameters. In this way we can specify the sort of Keplerian orbit that we want to describe. In particular, the E, L_z, Q can be mapped to the orbital elements $\mathcal{P}, e, \iota$, the semi-latus rectum, eccentricity and inclination respectively. The semi-latus rectum and the eccentricity are effectively a reparameterization in turn of the apsidal approaches (periapsis distance, r_p, and apoapsis, r_a),

$$r_p = \frac{\mathcal{P}}{1+e} \ ; \ r_a = \frac{\mathcal{P}}{1-e} \ , \tag{3.34}$$

whilst the inclination angle ι is defined,

$$\cos\iota = \frac{L_z}{\sqrt{Q + L_z}} \ . \tag{3.35}$$

We also define i - as distinct from ι- as the inclination of the orbit with respect to the observer, i.e.

$$\cos i = \hat{L}_z \cdot \hat{O} \tag{3.36}$$

and $\hat{O}$ is the line of sight unit vector between the observer and the BH. The observer is at some distant radius with polar and azimuthal coordinates $\theta_{\text{obs}}, \phi_{\text{obs}}$ respectively. The relevant geometry is described in Fig 3.1. It will also prove useful to define θ_{min} as the minimum polar angle acquired by the orbiting body ($= \pi/2 - \iota$). The mapping between conserved quantities and orbital parameters can be derived by requiring that at $r = r_a, r_p$,

$$\dot{r} = 0 \implies R(r) = 0 \ , \tag{3.37}$$

whilst at $\theta = \theta_{\text{min}}$

$$\dot{\theta} = 0 \implies \Theta(\theta) = 0 \ . \tag{3.38}$$

Solving these equations to find the roots allows the mapping to be defined (Schmidt 2002; Barausse et al. 2007) as

$$E = \sqrt{\frac{\kappa\rho + 2\epsilon\sigma - 2D\sqrt{\sigma\left(\sigma\epsilon^2 + \rho\epsilon\kappa - \eta\kappa^2\right)}}{\rho^2 + 4\eta\sigma}} \ , \tag{3.39}$$

$$L_z = -\frac{g_1 E}{h_1} + \frac{D}{h_1}\sqrt{g_1^2 E^2 + \left(f_1 E^2 - d_1\right) h_1} \ , \tag{3.40}$$

$$Q = z_- \left[a^2\left(1 - E^2\right) + \frac{L_z^2}{1 - z_-}\right] \ , \tag{3.41}$$

where

$$z_- = \sin^2\iota \tag{3.42}$$

and $D = \pm 1$ denotes prograde and retrograde orbits. In turn, the functions are defined as,

$$f(r) \equiv r^4 + a^2\left[r(r+2) + z_-\Delta\right], \tag{3.43}$$

$$g(r) \equiv 2ar \ , \tag{3.44}$$

$$h(r) \equiv r(r-2) + \frac{\Delta z_-}{1-z_-} \ , \tag{3.45}$$

$$d(r) \equiv \Delta \left(r^2 + a^2 z_-\right) \ , \tag{3.46}$$

and for the eccentric orbits considered in this work,

$$(f_1, g_1, h_1, d_1) = f(r_p), g(r_p), h(r_p), d(r_p) \ , \tag{3.47}$$

$$(f_2, g_2, h_2, d_2) = f(r_a), g(r_a), h(r_a), d(r_a) \ , \tag{3.48}$$

and

$$\kappa \ \ \equiv d_1 h_2 - d_2 h_1 \ , \tag{3.49}$$

$$\varepsilon \ \ \equiv d_1 g_2 - d_2 g_1 \ , \tag{3.50}$$

$$\rho \ \ \equiv f_1 h_2 - f_2 h_1 \ , \tag{3.51}$$

$$\eta \ \ \equiv f_1 g_2 - f_2 g_1 \ , \tag{3.52}$$

$$\sigma \ \ \equiv g_1 h_2 - g_2 h_1 \ . \tag{3.53}$$

This mapping between conserved quantities and orbital elements is exactly accurate for geodesic motion. However, as mentioned the spin couplings ensure that the motion of a spinning particle in a gravitational field is non-geodesic. However, these corrections to the orbital elements are typically small and we take this mapping as a decent approximation to model the sort of orbits we are interested in. An MSP with particular orbital parameters $\mathcal{P}, e$ will have a corresponding semi-major axis $\mathcal{A} = \mathcal{P}/(1-e^2)$. As a shorthand we will sometimes refer not to the system semi-major axis, but instead to the orbital period P where the two are related via Kepler's 3rd law, $P^2 \propto \mathcal{A}^3$. We use this only as a convenient re-parameterization with the understanding that this relation only hold exactly in the weak-field, zero-spin limit and that generally the orbital period will be different due to contributions from BH spin.

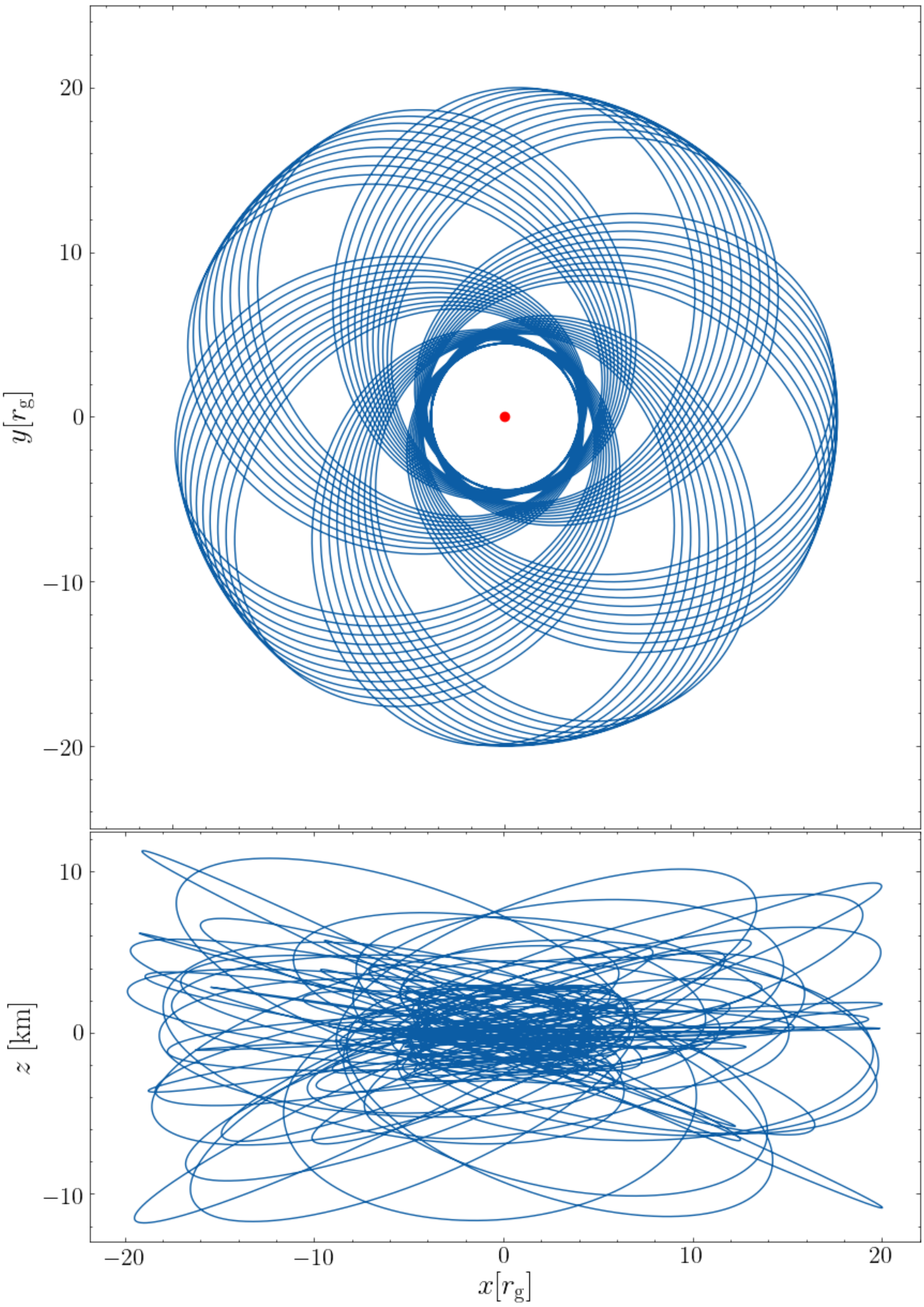

Fig. 3.2: The spin-orbital dynamics of a MSP with semi-major axis $20r_\mathrm{g}$ and eccentricity $e = 0.8$ over 30 orbits, around a BH with a maximal spin parameter $a = 0.998$. The pulsar is initialised in the orbital plane with $\iota = 0$, $\theta_\mathrm{spin} = \phi_\mathrm{spin} = \pi/4$. Due to the presence of spin-curvature coupling, the MSP does does not remain in the plane $z = 0$ but exhibits additional vertical motions.

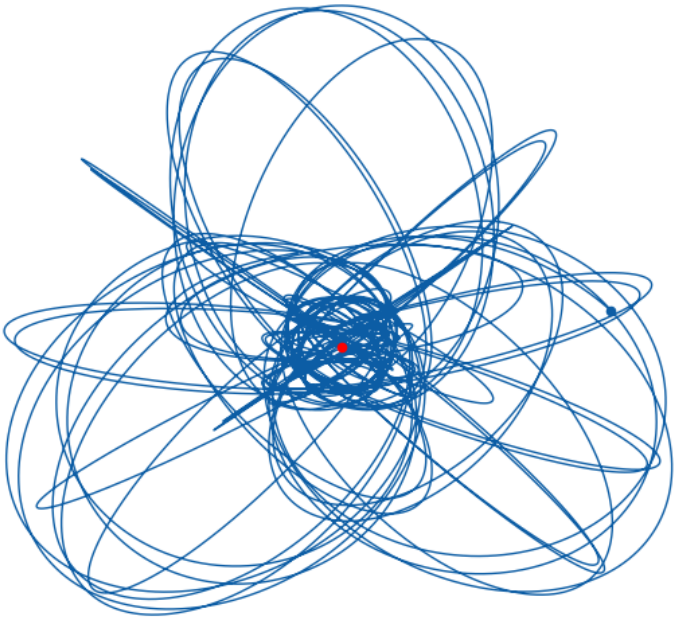

Fig. 3.3: As Fig. 3.2 but with $\iota = 35\,\mathrm{deg}$ and plotted in 3 dimensions. The initial momentum is orientated $p^r \cos\eta$, $p^\phi \sin\eta$ where $\eta = \pi/4$. The lengthscale is $\mathcal{O}(10) r_g$.

Chapter 4

Strong Field Pulsar Timing

We now have the two ‘ingredients’ of a relativistic timing model; we can accurately describe the dynamical and spin evolution of a spinning MSP around a spinning BH and also determine the behaviour of a light ray as it travels on a curved spacetime through an astrophysical plasma between the pulsar and observer. The problem then becomes how to combine these two effects so as to create a consistent model for the MSP $t - \nu$ signal. There are two obvious ways to do this. The first way is perhaps the most intuitive: we use the MSP orbital dynamics as an initial condition for the pulsar light beams and integrate the ray forwards in time. Whilst this method is an option it is computationally wasteful since it involves integrating many geodesics that do not hit the observer’s image plane. Instead we will use here a backwards-in-time approach and integrate rays from the observer to the pulsar. We then go on to explore the influence of a variety of relativistic effects on the timing signal.

4.1 Constructing the timing signal

The characteristic observational feature of a pulsar compared to a normal star is the beamed, anisotropic radiation. We describe this radiation beam, $\bar{B}$, by a rotating vector model where the radiation beam rotates about the spin axis $\bar{S}$. The radiation beam is at some polar angle ψ and azimuthal angle (i.e. the beam phase) χ with respect to the spin axis. The MPD orbital dynamics equations describe the evolution of the MSP centre of mass, the spatial components of which we label x^i. To take account of the beamed emission, we want to transform from the centre of mass to the 'radiation point', $x^i_{\rm B}$, which lies in the direction $\bar{B}$ at a radius $R_{\rm PSR}$. The spin axis orientation is described by the polar and azimuthal angles $\theta_{\rm spin}$, $\phi_{\rm spin}$. These angles are defined as,

$$\theta_{\rm spin} = \arctan(\sqrt{(S^x)^2 + (S^y)^2}, S^z) \ , \tag{4.1}$$

$$\phi_{\rm spin} = \arctan(S^y, S^x) \ , \tag{4.2}$$

the Cartesian components of which are related to the spin vector coordinate components (Eqs. 3.22 - 3.24) as

$$S^x = s^1 \sin\theta\cos\phi + s^2 r\cos\theta\cos\phi - s^3 r\sin\theta\sin\phi \ , \tag{4.3}$$

$$S^y = s^1 \sin\theta\sin\phi + s^2 r\cos\theta\sin\phi + s^3 r\sin\theta\cos\phi \ , \tag{4.4}$$

$$S^z = s^1 \cos\theta - s^2 r\sin\theta \ . \tag{4.5}$$

It follows that we can transform $x^i \rightarrow x^i_{\rm B}$ as

$$x^i_{\rm B} = R_z(\phi_{\rm spin}) R_y(\theta_{\rm spin}) R_{\rm PSR} \begin{bmatrix} \sin(\psi)\cos(\chi) \\ \sin(\psi)\sin(\chi) \\ \cos(\psi) \end{bmatrix} + x^i \ , \tag{4.6}$$

where R_z and R_y are 3-dimensional rotation matrices about the coordinate z and y axes respectively:

$$R_z(\phi_{\rm spin}) = \begin{pmatrix} \cos\phi_{\rm spin} & -\sin\phi_{\rm spin} & 0 \\ \sin\phi_{\rm spin} & \cos\phi_{\rm spin} & 0 \\ 0 & 0 & 1 \end{pmatrix} \tag{4.7}$$

$$R_y(\theta_{\rm spin}) = \begin{pmatrix} \cos\theta_{\rm spin} & 0 & \sin\theta_{\rm spin} \\ 0 & 1 & 0 \\ -\sin\theta_{\rm spin} & 0 & \cos\theta_{\rm spin} \end{pmatrix} \tag{4.8}$$

Typically, ψ is set to be some constant angle corresponding to the case where the latitude of the radiation beam does not evolve with respect to the spin axis. The beam phase $\chi = 2\pi\tau/P_\mathrm{s}$, for pulsar spin period P_s and proper time τ. The spin angles are naturally time dependent i.e. $\theta_\mathrm{spin} = \theta_\mathrm{spin}(\tau)$, $\phi_\mathrm{spin} = \phi_\mathrm{spin}(\tau)$ and are related to the precession and nutation of the spin axis with their evolution described by the MPD formalism.

4.1.1 Ray Tracing as a Boundary Value Problem

For each integration timestep on the PSR orbit, we want to find the ray which intersects with x^i_B. The problem of finding an intersection is a two point boundary value problem; we know the desired final boundary value, i.e. the radiation point x^i_B, and we want to find the initial boundary value, i.e. the values of the image plane coordinates x', y'. The ray then traces between these two limits. We solve this problem numerically using a shooting method (Press et al. 1992). The ray tracing is effectively a black box function $f(x', y', x^i_B)$ which takes some initial coordinates (x', y') and a target point x^i_B and returns the minimal distance along the ray from the target value, ds. We want to minimize $ds = f(x', y', x^i_B)$, to within some tolerance by varying the initial conditions x', y'. There are multiple methods by which to optimize a black box (or derivative free) function, including Nelder–Mead simplex methods (Nelder & Mead 1965), Generalized Pattern Search (Torczon 1997) and Mesh Adaptive Direct Search Algorithms (Audet & Dennis 2006). See Rios & Sahinidis (2009) for a full review of blackbox optimisation methods. Multiple algorithms were trialled and their performance assessed; it was soon discovered that despite the computational overhead of calculating gradients numerically, the additional information and improvement in performance outweighed the expense, allowing gradient based methods were to outperform the derivative-free methods for our particular problem. The adjustment of x', y' therefore proceeds via a non-linear conjugate gradient descent algorithm (Fletcher & Reeves 1964; Press et al. 1992), where the descent direction at each step is conjugate to the previously computed directions. The conjugate direction vector $\mathbf{h}_j$, is updated at each iteration step j as,

$$\mathbf{h}_{j+1} = \mathbf{g}_{j+1} + \gamma_j \mathbf{h}_j \ , \tag{4.9}$$

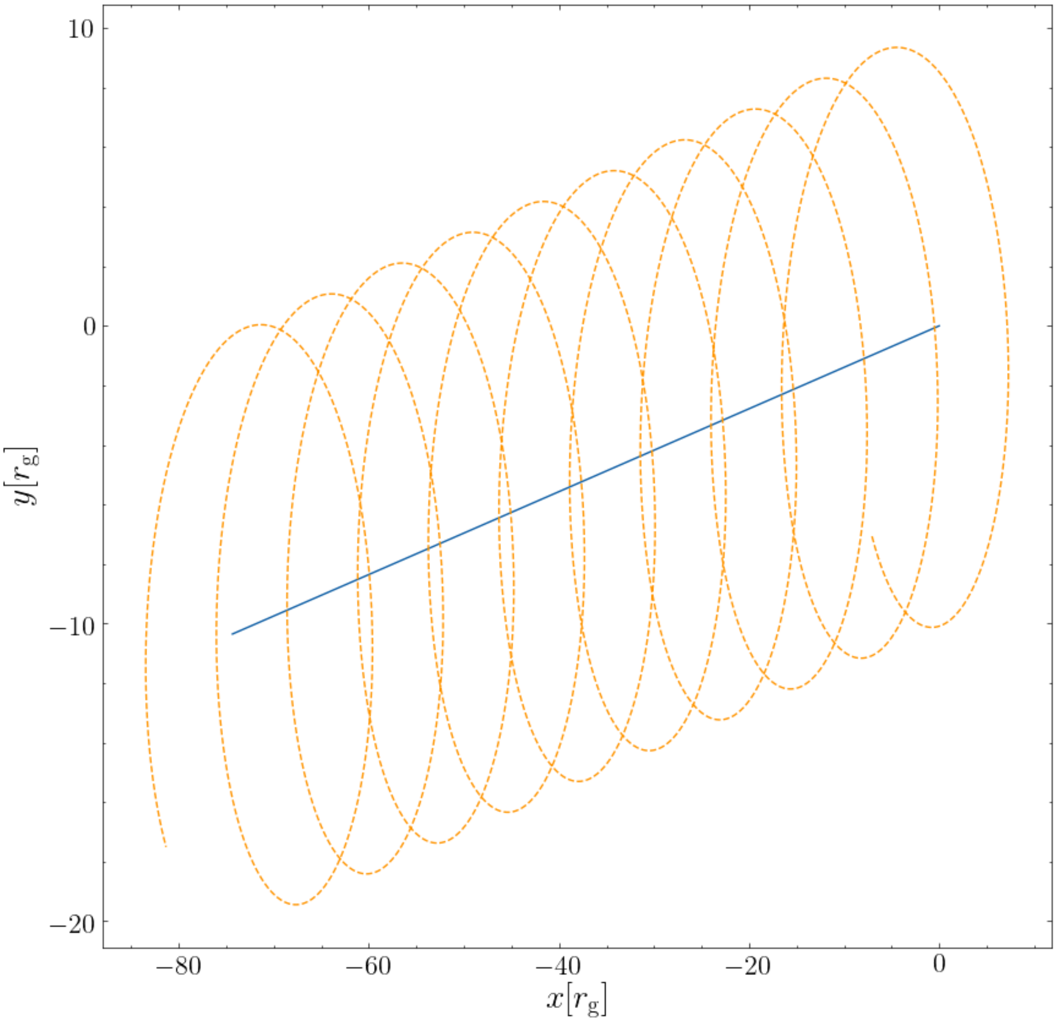

Fig. 4.1: The rotating vector model describing the pulsar's radiation point (x^i_B, orange dashed line) relative to the motion of the centre of mass of the pulsar (blue solid line) over 10 spin periods. Whilst the pulsar centre of mass follows a straight line over this orbital segment, the radiation point rotates about this line segment. The MSP spin axis is aligned with the coordinate z direction and $\psi = \pi/2$. The orbital segment is at $r \sim$ semi-major axis of an equatorial $P = 0.1$ year Galactic centre orbit

where $\mathbf{g}_j = -\nabla f(x'_j, y'_j)$ and

$$\gamma_j = \frac{\mathbf{g}_{j+1} \cdot \mathbf{g}_{j+1}}{\mathbf{g}_j \cdot \mathbf{g}_j} \ , \tag{4.10}$$

(Fletcher & Reeves 1964; Press et al. 1992). Now, since the analytical form of $ds = f(x', y', x_B^i)$ is unknown, the gradients necessary for the optimization,$\mathbf{g}_j$, are evaluated numerically via the difference quotient. The variables x', y' are then updated at each iteration as,

$$\mathbf{x}_{j+1} = \mathbf{x}_j + \delta_j \mathbf{h}_j \ , \tag{4.11}$$

for vector $\mathbf{x}'_j = (x', y')$ and where δ_j is the variable stepsize. The choice of stepsize is determined via an inexact line search, where δ_j is required to satisfy the Wolfe conditions (Wolfe 1971):

$$f(\mathbf{x}_j + \delta_j \mathbf{h}_j) \leq f(\mathbf{x}_j) + c_1 \delta_j \mathbf{h}_j^T \nabla f(\mathbf{x}_j) \tag{4.12}$$

$$-\mathbf{h}_j^T \nabla f(\mathbf{x}_j + \delta_j \mathbf{h}_j) \leq -c^2 \mathbf{h}_j^T \nabla f(\mathbf{x}_j) \tag{4.13}$$

where $0 < c_1 < c_2 < 1$. Following Nocedal & Wright (2006), we take $c_1 = 10^{-4}$ and $c_2 = 0.1$. Together these two conditions provide upper and lower bounds on permissible values of the stepsize, ensuring that f (via the first condition) and the slope (via the second) both decrease sufficiently.

The use of non linear conjugate gradient over a more vanilla optimization approach such as a basic gradient descent algorithm is advantageous since for particular values of x_{B}^i the distance function $f(x', y', x_B^i)$ takes the form of an ill-conditioned narrow valley. In such an environment, gradient steepest descent becomes inordinately slow, since the direction of steepest descent is not, in general, in the direction of the minimum and the algorithm instead follows a 'criss-cross' pattern, oscillating between the sides of the valley. By moving in directions which are conjugate to the previous directions this issue is avoided. The algorithm exhibits dependable and fast convergence and for this work we set the tolerance such that the function has been minimized and an intersection is declared when $ds < 0.3$ m which corresponds to a light travel time of 1 ns. In natural units, for a BH of mass $4 \times 10^6 M_\odot$ this is a lengthscale of $\sim 5 \times 10^{-11} r_{\rm g}$.

4.1.2 Pitch angle and transformation to the comoving frame

Once an intersection with the radiation point is found, in order to determine if the beam is seen by a distant observer it is necessary to calculate the pitch angle $\tilde{\omega}$, i.e. the angle of the photon ray relative to the normal to the stellar surface, n^i, at the point $x^i_{\rm B}$. All the calculations for the orbital dynamics and the ray tracing take place in the global coordinate frame and so the pitch angle is also that measured in the coordinate frame. However the physical angle that determines whether the beam will be visible to an observer is the angle as measured in the orthonormal tetrad frame comoving (with 4-velocity u^μ) with the star, $\hat{\omega}$. Due to relativistic aberration these two angles are not the same, $\tilde{\omega} \neq \hat{\omega}$. In order to calculate the pitch angle we must first transform to the comoving tetrad basis $e_{(\nu)}$. The transformation for general covariant (v_μ) and contravariant (v^μ) vectors is

$$v_{(\mu)} = e^{\nu}_{(\mu)} v_\nu \; ; \; v^{(\mu)} = e^{(\mu)}_{\nu} v^\nu \tag{4.14}$$

and indices with braces denote the comoving basis, which is locally flat such that $v^{(\mu)} = \eta^{(\mu)(\nu)} v_{(\nu)}$. In the tetrad frame the 4-velocity is simply $e_{(t)}$. The three remaining tetrads can then be constructed via a Gram Schmidt orthonormalistaion procedure (e.g. Krolik et al. 2005; Kulkarni et al. 2011; Shcherbakov & Huang 2011; Dexter 2016) such that the complete set is given by:

$$e^{\mu}_{(t)} = u^\mu \ , \tag{4.15}$$

$$e^{\mu}_{(r)} = \frac{1}{N_r}\left(u_r u^t, -u_t u^t - u_\phi u^\phi, 0, u_r u^\phi\right) \ , \tag{4.16}$$

$$e^{\mu}_{(\theta)} = \frac{1}{N_\theta}\left(u_\theta u^t, u_\theta u^r, 1 + u_\theta u^\theta, u_\theta u^\phi\right) \ , \tag{4.17}$$

$$e^{\mu}_{(\phi)} = \frac{1}{N_\phi}\left(u_\phi, 0, 0, -u_t\right) \ , \tag{4.18}$$

where,

$$N_r^2 = -g_{rr}(u_t u^t + u_\phi u^\phi)(1 + u_\theta u^\theta) \ , \tag{4.19}$$

$$N_\theta^2 = -g_{\theta\theta}(1 + u_\theta u^\theta) \ , \tag{4.20}$$

$$N_\phi^2 = -(u_t u^t + u_\phi u^\phi)\Delta \sin^2\theta \ , \tag{4.21}$$

and the inverse terms can be determined via the orthonormality condition $e^\alpha_{(\beta)} e^{(\gamma)}_\alpha = \delta^{(\gamma)}_{(\beta)}$ such that:

$$e^{(t)}_\mu = -u_\mu \ , \tag{4.22}$$

$$e^{(r)}_\mu = \frac{1}{N_r}\left(u_r u_t, -g_{rr}\left(u_t u^t + u_\phi u^\phi\right), 0, u_r u_\phi\right) \ , \tag{4.23}$$

$$e^{(\theta)}_\mu = \frac{1}{N_\theta}\left(u_\theta u_t, u_\theta u_r, g_{\theta\theta}\left(1 + u_\theta u^\theta\right), u_\theta u_\phi\right) \ , \tag{4.24}$$

$$e^{(\phi)}_\mu = \frac{-\Delta \sin^2\theta}{N_\phi}\left(u^\phi, 0, 0, -u^t\right) \ . \tag{4.25}$$

The pitch angle in the comoving frame is then

$$\hat{\omega} = \arccos\left(\frac{n^{(i)} k_{(i)}}{|n||k|}\right) \ . \tag{4.26}$$

Once $\hat{\omega}$ has been determined, we declare an observation if $\hat{\omega} < \omega_c$ where ω_c is some critical angle, e.g. the pulsar jet opening angle. The variation in the pitch angle over 3 rotations of a millisecond pulsar is illustrated in Fig. 4.2, for pitch angle calculated in both the global ($\tilde{\omega}$) and comoving ($\hat{\omega}$) frames. The observer is at $\Theta = \pi/4$, $\Phi = 0$ and the beam latitude angle is $\chi = \pi/4$. The pulsar is in the equatorial plane at r = semi-major axis of a ~ 0.1 year orbit of the Galactic centre. Initially the MSP spin axis is aligned with the BH (vertical z) spin axis such that $\theta_{\rm spin} = \phi_{\rm spin} = 0$. In this case the pitch angle in the global frame oscillates between $\tilde{\omega} = 0, \pi/2$, whilst in the comoving frame the periodicity of the oscillations is the same, but $\hat{\omega}$ is shifted in both time and amplitude with respect to $\tilde{\omega}$. If the pulsar spin axis is inclined by an angle $\theta_{\rm spin} = \pi/12$, the same general behaviour is exhibited, but the amplitude of the oscillations in $\tilde{\omega}$ is reduced since the radiation beam is shifted away from the observer's line of sight.

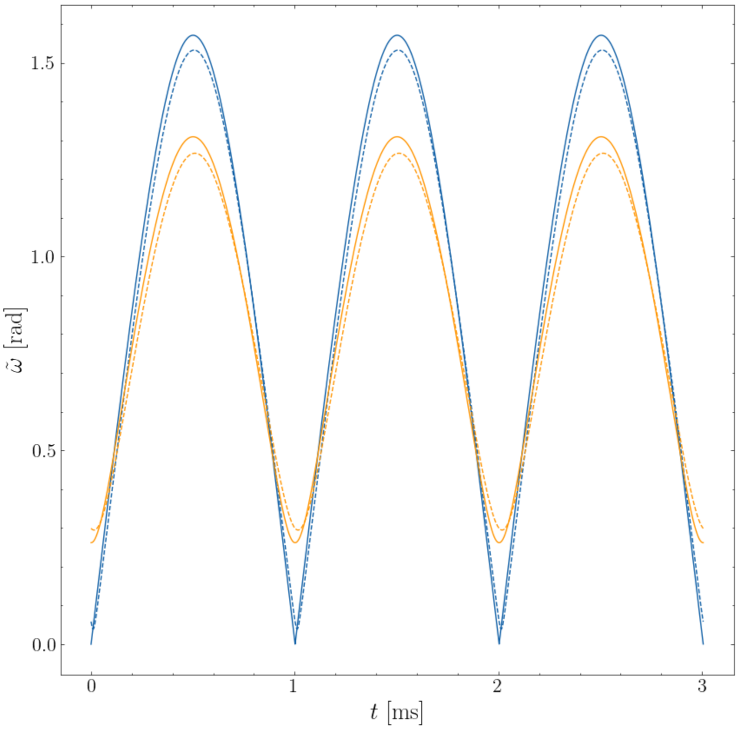

Fig. 4.2: The evolution of the pitch angle for a MSP in both the coordinate ($\tilde{\omega}$, solid lines) and comoving ($\hat{\omega}$, dashed) frames. The MSP is at $r = 800 r_{\rm g} (=$ semi-major axis) of an $e = 0.8$, equatorial orbit about a BH with $M_{\rm BH} = 4 \times 10^6 M_\odot, a = +0.9$. The orientation of the spin axis is set at $\theta_{\rm spin} = 0$ (blue) and $\theta_{\rm spin} = \pi/12$ (orange). The distant observer is at $\Theta = \pi/4$, $\Phi = 0$ and the latitude of the radiation beam with respect to the pulsar spin axis is $\chi = \pi/4$. For $\theta_{\rm spin} = 0$, the pitch angle oscillates between 0 and $\pi/2$, and is shifted vertically and horizontally (time/amplitude) upon transformation to the comoving frame. Inclination of the spin orientation to $\theta_{\rm spin} = \pi/12$ reduces the amplitude of the oscillations since the observer's line of sight is now permanently shifted away from the beam direction.

4.2 Application: Relativistic effects

We have established the framework for determining the pulsar ray path and orbital dynamics, along with the algorithm to find the intersection of the ray and calculate the pitch angle. We can now apply this framework to investigate the impact of the convolution of relativistic and astrophysical effects on the signal from a PSR in an E/IMRB, in particular the photon time of arrival and time-frequency profile.

Investigating the strong field timing signal necessitates specifying the BH mass and spin parameters - i.e. setting the background spacetime. Regarding the BH mass, we will consider two representative cases; a supermassive BH and an IMBH. In the supermassive case, the BH mass will be set at $4.31 \times 10^6 M_\odot$, in keeping with the estimated mass of the Galactic centre BH (Gillessen et al. 2009). For IMBH, we set $M = 2.2 \times 10^3 M_\odot$, which is the purported mass of the IMBH at the centre of the globular cluster 47 Tucanae (Perera et al. 2017). If the next generation of radio telescopes allow for the detection of extragalactic E/IMRBs then there may be systems with BH masses intermediary or greater than these values (Wrobel et al. 2018). Nevertheless, we take these two mass values as representative of the sorts of systems we are interested in. Indeed, the Galactic centre and the centre of globular clusters remain the prime hunting grounds for MSP-E/IMRBs and this is where we focus out attention. There remains considerable uncertainty in the spin parameter of astrophysical BHs. Astrophysical measurements of the nearest BH candidate, Sgr A*, range from $0.44 - 0.996$ (Aschenbach 2010; Kato et al. 2010; Dokuchaev 2014). The determination of the spin of BHs other than Sgr A* have been possible via continuum fitting and iron lines measurements, and again cover a wide range from $-0.2 < a < 0.98$ (see Table 1 of Bambi et al. 2016). Going forward we set $a = +0.6$ as our canonical value, and explore the wider parameter range where relevant.

4.2.1 Relativistic spin orbital dynamics

Treating the pulsar as a rigid spinning object and accounting for the associated spin couplings causes substantial variation in the pulsar orbital dynamics compared to the Newtonian or even geodesic case. In addition to the spin-orbit (gravitomagnetic) and spin-spin couplings, the interaction of the pulsar spin with the background spacetime (spin-curvature coupling) causes an additional acceleration in the pulsar dynamics. This effects is most clear when considering a pulsar initialised in the equatorial plane of the BH ($\theta = \pi/2$), with initial conditions chosen such that, in the geodesic or Newtonian cases, it would continue to orbit in this plane, i.e. $\iota = 0$. When spin curvature coupling is 'switched off', $\lambda = 0$, the motion is geodesic and the pulsar remains in the plane. Conversely, when $\lambda = 1$ there is a marked vertical motion; these dynamical effects will naturally influence the pulse ToA. This is illustrated in Fig 4.3 for a MSP with semi-major axis = 100 r_g, $e = 0.2$, $\iota = 0$ around a supermassive black hole ($M = 4 \times 10^6 M_\odot$, $a = 0.6$). The spin orientation is initially set to $\theta_{\rm spin} = \pi/4$, $\phi_{\rm spin} = 0$. The observer is at $\Theta = \pi/4$, and we integrate for 60 orbits. By turning on spin curvature coupling an additional time delay is observed on the order of 10μs. The vertical motions and hence the time delay are observed to be independent of the BH mass, for a system with the same orbital radius in corresponding natural units. This suggests, as also noted in Singh et al. (2014), that this effect will be more apparent for systems with lower mass black holes since the vertical motion becomes a greater fraction of the gravitational lengthscale. Naturally this effect will also be increased for fast spinning pulsars and high inclination observers. There is also a strong dependence on the orbital velocity. Take the same MSP-EMRB system as in Fig 4.3, but modify the semi major axis to $825 r_{\rm g}$ and the eccentricity to $e = 0.9$. In this case then the periapsis approach is approximately the same as before, $\sim 80 r_{\rm g}$. The orbital velocity can be approximated via the Keplerian expression:

$$v^2 \propto \left(\frac{2}{r} - \frac{1}{a}\right) \tag{4.27}$$

It follows that at periapsis this pulsar with a longer orbital period is moving much faster. As a consequence, the magnitude of the vertical displacement is enhanced and the time delay is on the order $100\mu s$ (see Fig. 4.4). Timing variations of this size are readily detectable with pulsar timing techniques with the next generation of radio telescopes; 10 minute integrations of millisecond pulsars at GHz frequencies should achieve a ToA precision of the order $10 - 100$ ns with both SKA and FAST (Liu et al. 2011; Hobbs et al. 2014; Stappers et al. 2018). Furthermore, any variation in the light travel time due to the orbital dynamics will be further compounded by the impact of additional factors (e.g. time dispersion, time dilation, spin axis precession etc., see subsequent sections).

An accurate description of the MSP orbital dynamics is essential, since the apparent or observed pulse frequency is related to the intrinsic frequency as,

$$\nu_{\text{obs}} = \frac{p_\alpha u^\alpha|_{\text{observed}}}{p_\alpha u^\alpha|_{\text{intrinsic}}} \nu_{\text{intrinsic}} \ . \tag{4.28}$$

In order to determine the Doppler shift accurately, one must therefore have an appropriate description of the PSR velocity (see Sec. 4.2.4). The complex orbital dynamics of a spinning pulsar around a spinning black hole will also naturally influence both the acceleration and the change in acceleration (i.e. jerk) of the pulsar, depending on the orbital and observer configuration. Highly accelerated systems - the most scientifically interesting systems from the perspectives of testing GR - are difficult to search for when the integration time is comparable to the orbital period since the line of sight velocity is not constant over an integration period. Assuming the acceleration to be constant, the changing velocity of the pulsar causes the signal to drift into multiple frequency bins, with the number of bins drifted,

$$N_{\text{drift}} \propto a_0 T^2 \ , \tag{4.29}$$

for constant line-of-sight acceleration a_0 and integration time T. Search algorithms can correct for this effect (‘acceleration searches’), but the correction is typically computationally intensive. Spin-curvature coupling can cause additional acceleration as measured by the observer, depending on the line of sight, and will influence the number of frequency bins drifted. Furthermore, in the presence of spin-curvature dynamics the assumption of constant acceleration may need modification, since in highly relativistic regimes the jerk may

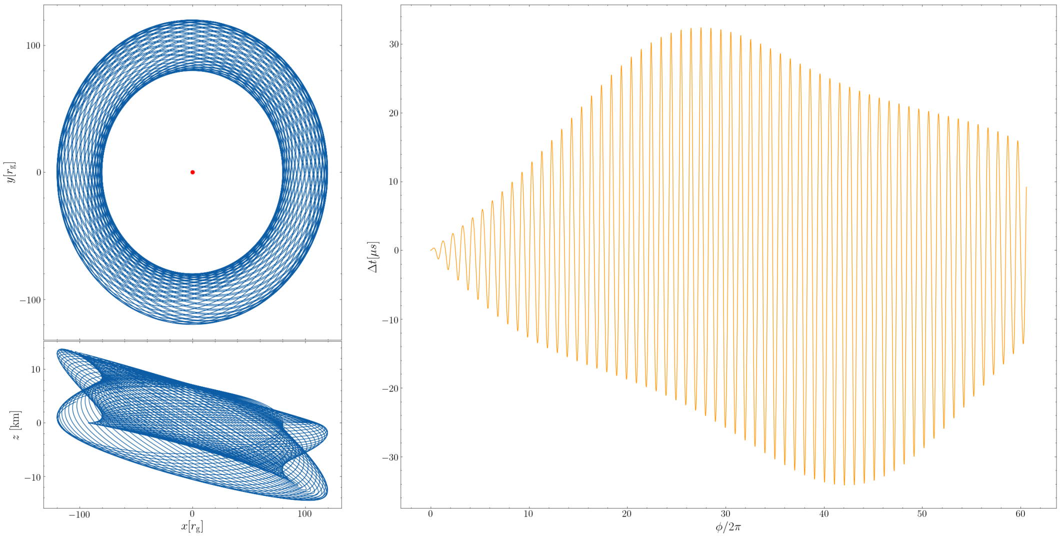

Fig. 4.3: The modulation in the photon arrival time (right panel) between the $\lambda = 0$ and $\lambda = 1$ spin curvature couplings, along with the associated orbital dynamics (left panels). We consider a Galactic centre system with semi major axis $= 100 r_g$ and $e = 0.2$ over 60 orbits. The observer is at $\Theta = \pi/4$ and the initial spin axis angle is $\theta_{\rm spin} = \pi/4$. Timing variations on the order of a few 10's of μs are observed.

be non-negligible. In this case the number of frequency bins drifted becomes time dependent,

$$N_{\rm drift} \propto (a_0 + j_0 t) T^2 \ , \tag{4.30}$$

at time t with jerk j_0, which may introduce additional complications in searching for highly relativistic systems.

4.2.2 Spin precession and nutation

Generally the MSP spin axis is not aligned with the orbital angular momentum axis. As a consequence, the spin vector s^μ evolves with time and the spin axis exhibits precession ($\partial_\tau \phi_{\rm spin}$) and nutation ($\partial_\tau \theta_{\rm spin}$). In a Newtonian description, given a binary system with masses m_1, m_2, the spin vector $\mathbf{s}_1$ evolves as (Kidder 1995),

$$\dot{\mathbf{s}}_1 = \frac{1}{r^3} \left[(\mathbf{L} \times \mathbf{s}_1) \left(2 + \frac{3\, m_1}{2\, m_2} \right) - \mathbf{s}_1 \times \mathbf{s}_2 + 3\, (\hat{\mathbf{n}} \cdot \mathbf{s}_2)\, (\hat{\mathbf{n}} \times \mathbf{s}_1) \right] \ , \tag{4.31}$$

where $\hat{\mathbf{n}}$ is the unit vector between the two bodies and $\mathbf{L}$ is the usual orbital angular momentum. The first term ($\mathbf{L} \times \mathbf{s}_1$) describes the spin-orbit coupling and the other terms describe the spin-spin couplings. In a relativistic context,

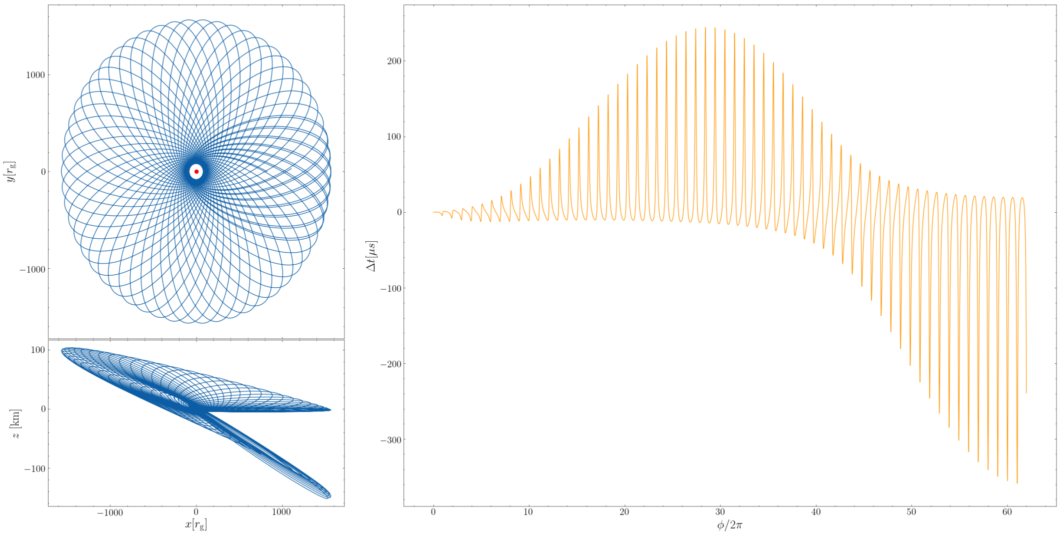

Fig. 4.4: As Fig. 4.3 but for semi major axis $= 825r_{\rm g}$ and $e = 0.9$. The increased orbital velocity at periastron leads to a greater degree of vertical motion. The photon timing modulations are increased accordingly to $\mathcal{O}(0.1)$ ms.

the effect of a vector carried by an orbiting body in a curved spacetime is due to a combination of geodetic (de Sitter) and Lense-Thirring precession (i.e. gravitomagentic frame dragging). This dynamical evolution of the spin, along with the effects due to the coupling of the MSP spin itself are all naturally described by the MPD framework (see e.g. Fig 4.5).

The evolution of the MSP spin axis influences the observed timing signal in two key ways. The first is via the coupling between the pulsar spin vector and the dynamical motion of the pulsar i.e. the orbital motion and spin evolution are interdependent. This is the effect we studied in the previous section, 4.2.1. The second is via the relation between the spin axis orientation and the pulsar beam direction as measured by the distant observer. It is this point we will explore in this subsection. The orientation of the spin axis as described by the precession and nutation angles, in conjunction with relativistic aberration induced by the transform to the comoving frame, work to influence the observability of the pulsar signal, the pulse profile (e.g. Rafikov & Lai 2006) and the pulse arrival time. The precession and nutation of the spin axis causes the radio beam direction $\bar{B}$ to shift relative to the observer's line of sight, i.e. the pitch angle

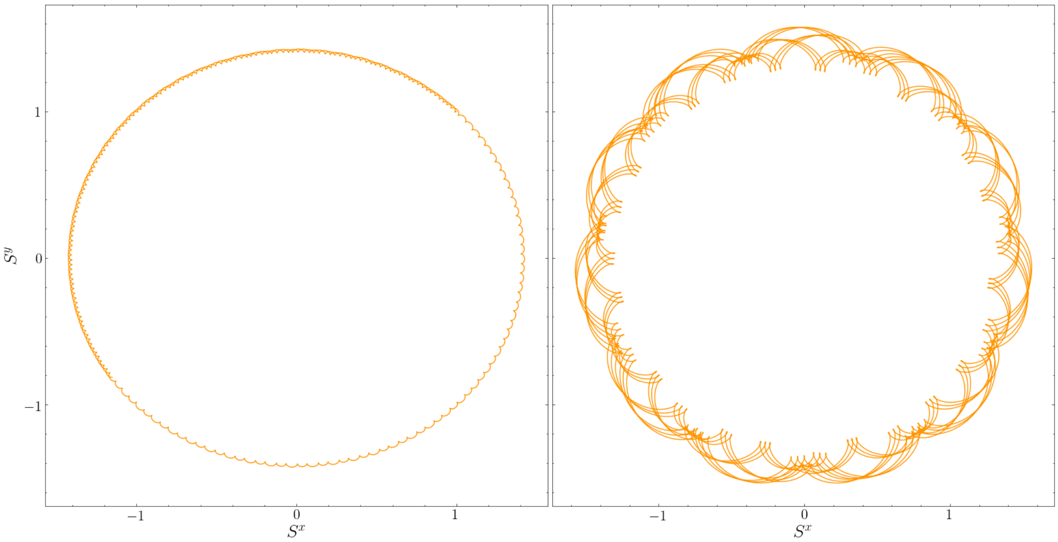

Fig. 4.5: The S^x, S^y projection (Eqs. 4.3,4.4) of the spin axis orientation for a MSP with semi major axis $= 100r_{\rm g}$, $\iota = 0$ orbiting an IMBH with $a = +0.6$ over 100 orbits. The left panel is for $e = 0.1$, the right panel for $e = 0.9$. The initial orientation is $\theta_{\rm spin} = \pi/4$, $\phi_{\rm spin} = 0$. The values of $S^{x,y}$ have been normalised with respect to their initial values. The precession of the spin axis and the smaller nutation perturbations about this precession are clearly visible with greater magnitude oscillations for more eccentric orbits which are more relativistic and probe an increasingly curved spacetime.

$\hat{\omega}$ is modified. The time centre of the pulse profile naturally occurs when the pitch angle is at a minimum, $\partial_\tau \hat{\omega}(\theta_{\rm spin}, \phi_{\rm spin}, \psi, \chi) = 0$. This time centre is analogous to the photon ToA, subject to a ray tracing mapping. We therefore have the condition that the pulse arrival time occurs when then beam phase $\chi(\tau)$ obtains some critical value χ_c, at which $\partial_\tau \omega = 0$. Generally, we can find the minimum of $\tilde{\omega}$ via a full numerical solution as outlined in the previous subsections (see e.g. Fig. 4.2). To illustrate the influence of spin precession on the timing solution more broadly we here employ an approximate semi-analytical solution to calculate $\partial_\tau \tilde{\omega}$ (i.e. neglecting relativistic aberration). We label the observer direction by the vector $\bar{O}$. This vector can be considered as the vector which is tangent to the asymptote that converges at the observer in a flat spacetime. The pitch angle between the pulsar radiation beam vector and the observer vector is then defined via,

$$\cos \tilde{\omega} = \bar{B} \cdot \bar{O} \tag{4.32}$$

for normalised unit vectors $\bar{B}, \bar{O}$. Since the pulsar spin timescale (~ 1 ms) is much shorter than the precession and nutation timescales of the spin axis, we can employ a two timescale approximation and neglect the evolution of $\theta_{\rm spin}, \phi_{\rm spin}$ over the MSP rotation period. Solving $\partial_\tau \tilde{\omega}(\chi_c) = 0$ generally is conceptually straightforward to calculate, but exceptionally algebraically complicated and so we do not reproduce it here. Taking the specific case with polar angle of the radiation beam with respect to the spin axis is $\psi = \pi/4$, and the observer is at $\Theta = \pi/4, \Phi = 0$ then then the critical phase angle is:

$$\chi_c = \arccos \left[\frac{\cos \phi_{\rm spin} \cos \theta_{\rm spin} - \sin \theta_{\rm spin}}{N_\chi} \right] \tag{4.33}$$

where

$$N_\chi = \sqrt{\cos^2 \phi_{\rm spin} \cos^2 \theta_{\rm spin} + \sin^2 \phi_{\rm spin} + \sin^2 \theta_{\rm spin} - \cos \phi_{\rm spin} \sin 2\theta_{\rm spin}} \,. \tag{4.34}$$

From this equation we can see that both the precession ($\phi_{\rm spin}$) and the nutation ($\theta_{\rm spin}$) contribute to the critical phase angle. The extra phase angle than must be traversed in order to reach the centre of the pulse profile, $\delta \chi_c$, will directly influence the observed pulse frequency. In this way, variations in the spin axis can directly imprint on the pulsar timing solution. A difference in the critical phase value is related to a timing delay as,

$$\Delta t = \frac{P_s}{2\pi} \delta \chi_c \tag{4.35}$$

for MSP spin period P_s. The pulse timing delay due to the time evolution of the pulsar spin axis is shown in Figure 4.6 for an eccentric MSP-IMRB with semi-major axis $= 200 r_{\rm g}$. The timing delay due to the shift in the centre of the pulse profile is of the order 100 μs, with rapid variations as the pulsar passes through periapsis, and with greater magnitude shifts for more eccentric orbits. After ~ 5 orbital phases the time delay for a MSP with $e = 0.9$ accumulates to $\sim 300 \mu$s. When passing through periapsis, in addition to a rapid shift in Δt, there is also a small oscillatory feature (inset plot of Fig. 4.6) due to the rapid change in both $\theta_{\rm spin}$ and $\phi_{\rm spin}$.

In addition to the orientation of the spin axis causing a timing shift, it will also influence the shape of the pulse profile. Whilst the dominant contribution to the Δt is due to the spin precession, the nutation of the spin axis will also cause a shift in the observed pulse width. If the pulsar beam has half opening angle γ, then the edges of the emission cone as seen by the observer occur when $\omega = \pm \gamma$, at beam phase χ_1, χ_2, with the two roots corresponding to where the observer's vector enters and leaves the pulse cross section. The angular beam width is simply,

$$w = \chi_1 - \chi_2 \tag{4.36}$$

Since the precession does not meaningfully affect the beam width, we can set $\phi_{\rm spin}, \dot{\phi}_{\rm spin}$ and solve explicitly for the beam width:

$$w = 2 \cos^{-1} \left(\frac{1.41 \cos \gamma \csc \psi - \cos \theta_{\rm spin} \cot \psi - \sin \theta_{\rm spin} \cot \psi}{\cos \theta_{\rm spin} - \sin \theta_{\rm spin}} \right) \tag{4.37}$$

where we have specified the observer to be at $\Theta = \pi/4$ (again, a general solution is computationally straightforward to calculate, but algebraically complicated and so we do not reproduce it in full here). The evolution of the pulse width is shown in Fig 4.7 for the same MSP-IMRB considered above

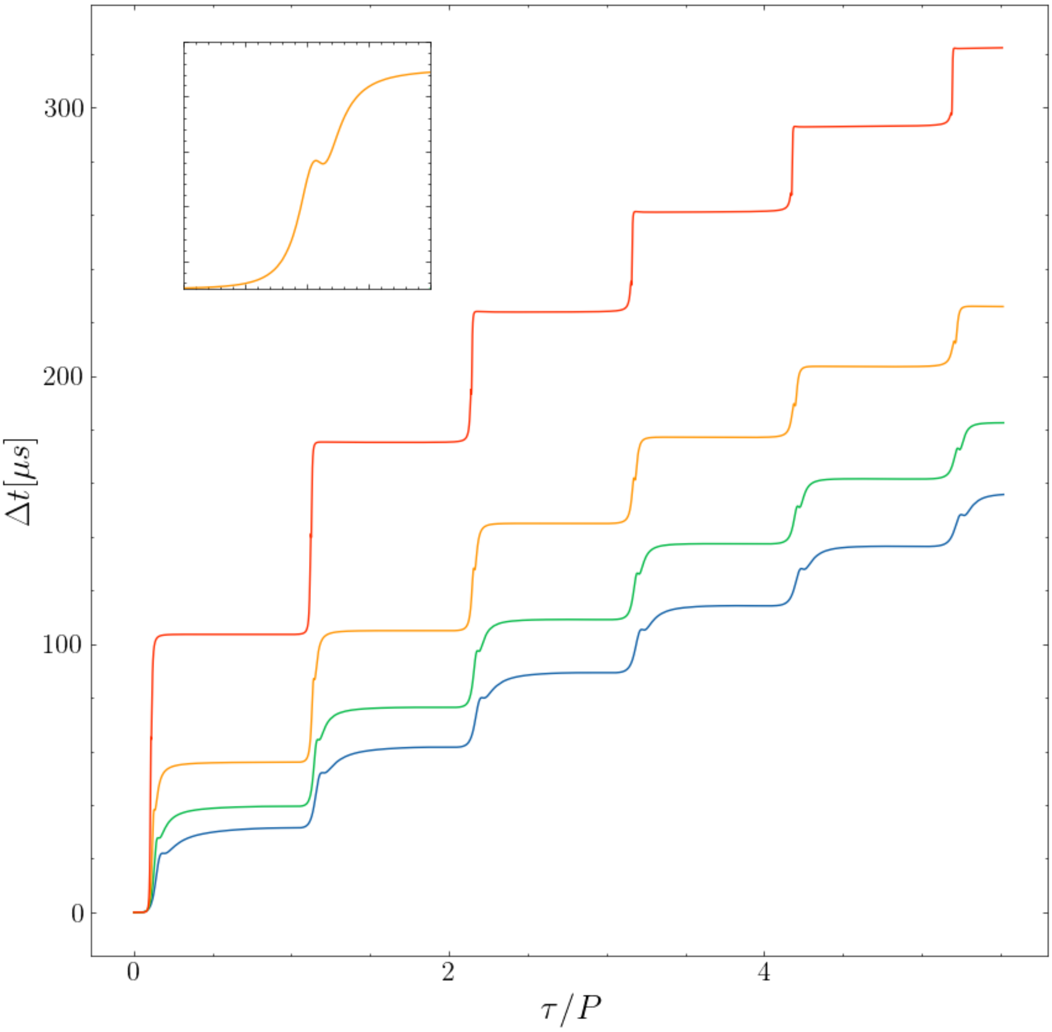

Fig. 4.6: Timing delay due to the shift in the arrival time of the centroid of the pulse profile as a result of the precession and nutation of the MSP spin axis. The MSP has spin period $P_s = 1$ ms, semi-major axis $= 200r_\mathrm{g}$ and eccentricities $e = 0.6, 0.7, 0.8, 0.9$ (blue, green, orange, red lines respectively). The BH has an intermediate mass of $M = 2.2 \times 10^3 M_\odot$ and spin parameter $a = 0.6$. The observer is located at $\Theta = \pi/4, \Phi = 0$ and the pulsar beam is at a polar angle of $\pi/4$ with respect to the spin axis. Initially, $\theta_\mathrm{spin} = \pi/6$ and $\phi_\mathrm{spin} = 0$. The inset plot shows an enhanced view of the small oscillatory feature due to the rapid change in the precession and nutation angles.

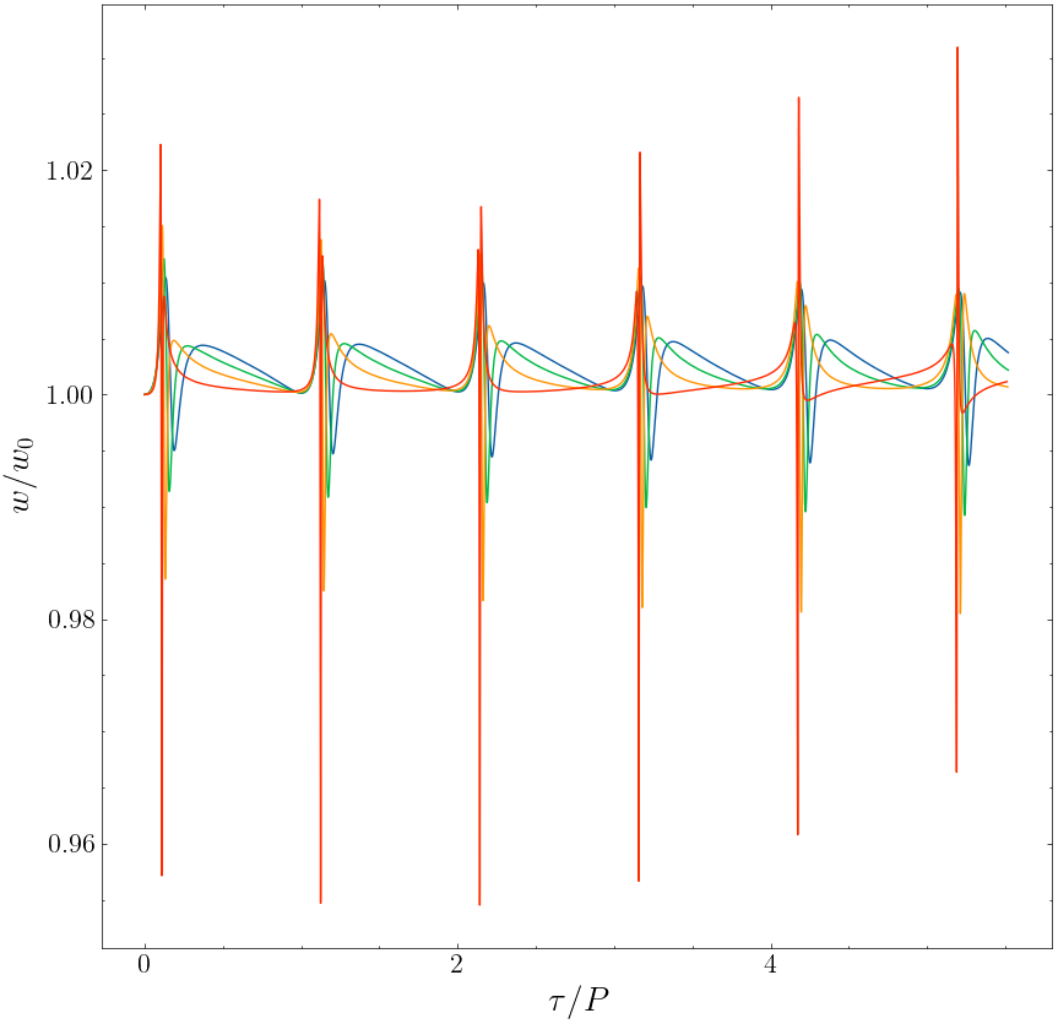

Fig. 4.7: Modulation of the observed pulsar beam width for a MSP-IMRB with the same system parameters as Fig. 4.6. For high eccentricities ($e = 0.9$) the pulse width changes by up to $\sim 4\%$, whilst for more mild eccentricities the changes is reduced: when $e = 0.6$, w/w_0 is of order 1 %.

(i.e. Fig. 4.6). The beam width varies on the order of a few %, with rapid variations close to periapsis. Those systems with greater eccentricities again experience a greater shift in the observed pulse width due to the increased strength of relativistic effects. Rather than a longer timescale, semi-analytical approach, we can also examine the pulse profile and the impact of the nutation angle using the full numerical solution on shorter timescales. Figure 4.8 illustrates the change in the pitch angle evolution $\tilde{\omega}$ for a MSP with different initial values of θ_{spin}. We arbitrarily define the angular beam width as the phase subtended when $\tilde{\omega}$ varies from 20 deg, through the minimum and back to 20 deg. Since the orientation of the spin axis affects the effective latitude on the radiation cone with which the line of sight intersects, the pulse width exhibits a clear variation with the orientation of the spin axis. The pulse width can be considered as a proxy for the observed pulse duration, and so nutation of the spin axis over the course of the pulsar's orbit will directly influence the time over which a pulse is observable. Again, as the nutation angle increases, the amplitude of $\hat{\omega}$ is also reduced since the radiation beam is shifted further from the observer's line of sight. In addition, the centre of the pulse profile - the time at which $\hat{\omega}$ is at its minimum - is shifted on account of relativistic aberration. If we consider $\tilde{\omega}$ instead of $\hat{\omega}$ the minima occur at the same time, with no variation based on $\theta_{\rm spin}$. Analogous to the time delay induced by the precession, the shift in the minima of $\tilde{\omega}$ due to aberration also causes a shift in the pulse arrival time. For this system and observer parameters, the pulse arrival time is delayed by $\sim 30\mu s$ when the polar spin angle is shifted from $\theta_{\rm spin} = \pi/6$ to $\theta_{\rm spin} = \pi/12$. Evidently then, whilst the centroid shift is primarily due to the precession angle evolution, the change in nutation angle in conjunction with relativistic aberration can also cause a shift in the timing solution. Notably, for variations of sufficient magnitude the spin axis variation would be so severe that the minimum of ω would be greater than the beam opening angle. This corresponds in Fig. 4.8 to a $\tilde{\omega} - t$ profile which does not cross the horizontal grey dashed line. Consequently for some orbital configurations, this oscillation will leave the pulsar beam invisible at certain times (e.g. Istomin 1991). The pulsar signal would consequently be intermittent, leading to additional complications in search observations and any consistent timing model.

In addition to the MSP spin vector evolution influencing the pulse shape and arrival times, it can also influence the pulse intensity. Approximating the pulsar beam as a Lambertian surface, precession of the spin axis will cause variations in the pulse intensity dI as,

$$dI \propto \sin(\hat{\omega}) d\hat{\omega}. \tag{4.38}$$

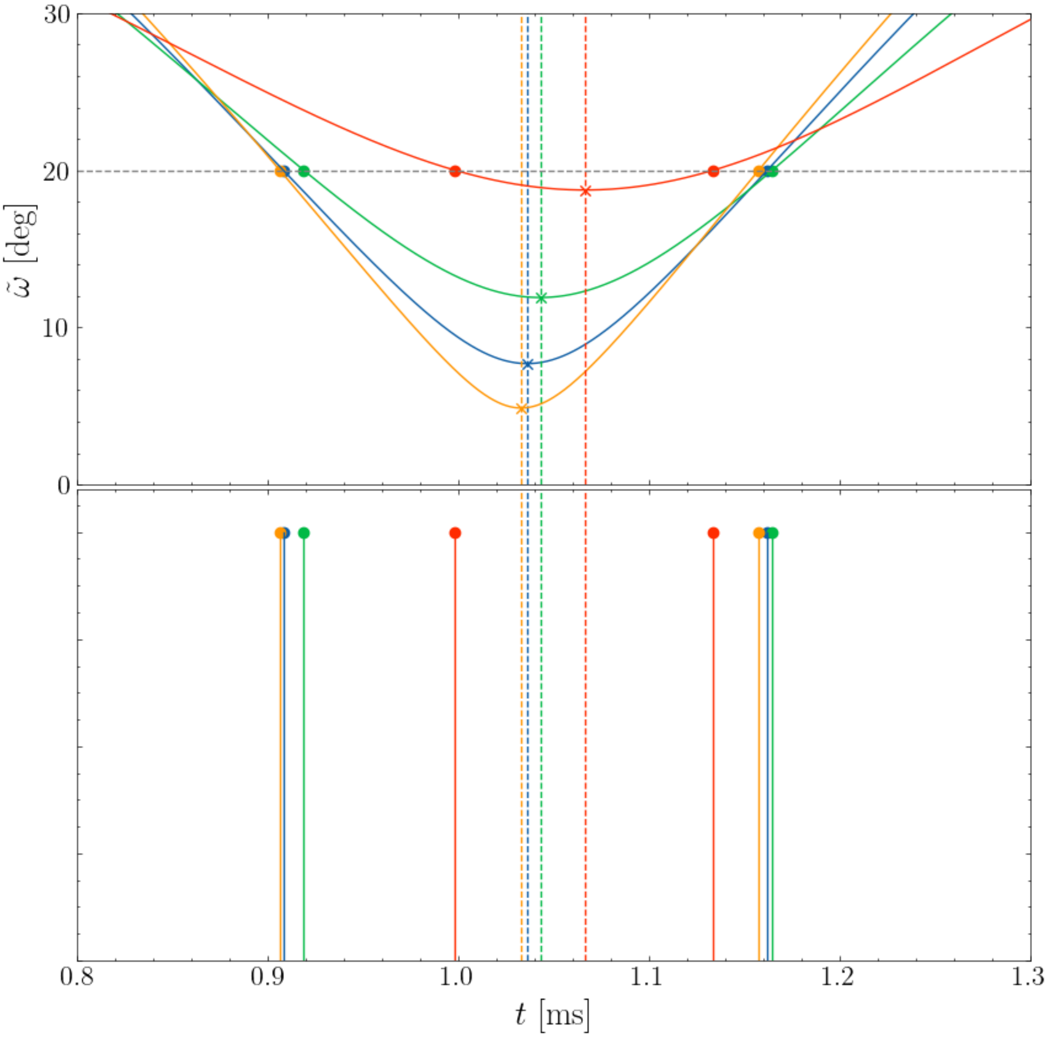

Fig. 4.8: *Top panel:* Change in the pitch angle as the pulsar beam rotates, at nutation angles $\theta_{\rm spin} = \pi(1/12, 1/10, 1/8, 1/6)$. The observer is at $\Theta = \pi/4$, and the beam angle with respect to the spin axis is $\psi = \pi/6$. As $\theta_{\rm spin}$ changes, the minimum of $\tilde{\omega}$ increases, and the beam width decreases since the line of sight now intersects more sharply with the beam. The centroid of the pulse is shifted on account of relativistic aberration. *Bottom panel:* Time at which the pitch angle crosses the grey dashed line, defining the beam width.

Consequently, the precession of the spin axis can directly affect the observed intensity. Clearly this is an oversimple approximation and to correctly determine the pulse intensity also accounting for scattering, absorption and Doppler boosting would require covariant general relativistic radiative transfer (e.g. Younsi et al. 2012) along the geodesics determined via the framework presented in this work. However, the Lambertian approximation serves as a adequate first order estimate to inspect the influence of spin precession on the pulse intensity. Considering the system described in Fig. 4.8, the minimum of $\tilde{\omega}$ is $\sim 5\,\mathrm{deg}$ when $\theta_{\mathrm{spin}} = \pi/12$ and $\sim 18\,\mathrm{deg}$ when $\theta_{\mathrm{spin}} = \pi/6$, which corresponds to a relative intensity shift of $\sim 5\%$ under the Lambertian approximation.

In summary, in addition to the orbital dynamics, spin precession can then also affect the pulse width (and hence duration), the pulse ToA due to the relativistic centroid shift and the observed pulse intensity. The precision that can be achieved with pulsar timing is a function of both the pulse intensity and the sharpness of the pulse profile, and so an accurate description of these quantities is key for realistic assessment of the prospects of the detection of a PSR-EMRB. Variations in the pulse profile width may provide a method to determine the PSR spin behaviour (e.g. Rafikov & Lai 2006) or even test the Cosmic censorship Conjecture (Kocherlakota et al. 2019). For very compact orbits or periastron passages, the timescale of spin orientation variation can severely shorten, causing rapid changes in the pulse profile (width, intensity, ToA). Corrections for this change in the overall pulse profile shape will be necessary for both long term timing and - if the timescale of spin axis oscillation is comparable to the observation integration time - initial detection.

4.2.3 Gravitational Lensing

The notion of a geodesic, i.e. a straight line in curved spacetime, means that the spatial path of a light ray propagating in the gravitational strong field can be bent due to the spacetime curvature. Gravitational lensing by Sgr A* has been considered for emission for S-stars close to the Galactic centre (Bozza & Mancini 2009; Bin-Nun 2010; Bozza & Mancini 2012) as observed by

Very Large Telescope optical interferometer instrumentation (e.g. GRAVITY, Gravity Collaboration et al. 2017). The magnitude of the astrometric shift that results from gravitational bending is naturally dependent on the configuration of the system (i.e. relative alignment of source, lens, observer. See e.g. Bozza & Mancini 2012, for a description of the relevant angles and geometry). For the S-stars, at alignment angles of $\sim 35^{\circ}$, the expected astrometric shift is of order 30μas, whilst the contribution of post-Newtonian and spin corrections to gravitational bending are expected to appear at $\sim 5\mu$as, below current interferometric instrumental sensitivity (Bozza & Mancini 2012).

The light ray from a MSP-E/IMRB can also be lensed due to the gravitational field of the central massive BH. This was considered in the analytical case for a Schwarzschild black hole in Wang et al. (2009a,b). Gravitational lensing in a Kerr spacetime is naturally included in the ray tracing set up described in Sec. 2 which accounts for contributions from both the BH mass and spin. Gravitational lensing directly influences the MSP timing signal in a number of ways. Firstly, since the spatial trajectory of the ray is modified compared to the radial path of a flat Minkowski spacetime, this will induce additional timing variations. These variations in turn are modulated over the course of the MSP orbit since the degree of gravitational lensing is strongly correlated with how close the light beam passes to the BH; changes in the relative observer - BH - PSR orientation over the course of the orbital then directly change the degree of gravitational lensing (see e.g. Fig. 4.9) and hence the relative time delay (Fig. 4.10). Furthermore, gravitational lensing allows the observer to receive multiple pulses; in addition to the primary pulse that undergoes little or no lensing, as the MSP continues to rotate it is possible that the beam is lensed in such a way that the observer receives a secondary highly bent ray (Fig. 4.9). ‘Higher order’ pulses (i.e. those which circle the central BH more than once) are possible (see e.g. Wang et al. 2009b) but for the purposes of this work we only consider the primary and secondary pulses, since the intensity of higher order pulses is naturally low. Clearly these strong bending effects are most prominent when the pulsar is on the far side of the black hole, but due to the BH spin the ray can undergo lensing even for near side emission. For certain orbital configurations, the pulsar 'primary' pulses may be invisible, and instead the pulsar is only visible via the strongly bent 'secondary' pulses. Whether strong bending of pulsar rays will occur astrophysically is highly dependent on both the system orbital configuration and the observer viewing angle, with the maximal bending occurring when the pulsar lies close to the central black hole and on the far side with respect to the observer. Analysis from Stovall et al. (2012) suggests that with current radio observation facilities, the probability of detecting strong bent pulsar beams is small but non-negligible, whilst future radio facilities such as SKA, should be able to detect strongly bent beams from multiple pulsars, despite secondary pulses expected to be fainter compared to their primary counterparts. Moreover, this analysis is focused towards the Galactic centre where there are complications due to scattering which decreases the detection probability. Observations of MSP-IMRBs in globular clusters where scattering is less problematic further increases the chances of observing strongly bent beams. Furthermore, in estimating a probability Stovall et al. (2012) take as a prototypical model a pulsar at $r = 10^4 r_{\rm g}$. Taking this as the semi-major axis, this gives a Keplerian period of $\sim$ 4 years. At such radii, the degree of strong deflection is rather small. Consequently if an observer receives the primary beam it will also receive the secondary beams. However, for pulsars with shorter orbital periods or at more compact orbital radii (e.g. at periapsis of some eccentric orbit) the probability of observing a strongly deflected beam would be increased. Extending the considered pulsar population to include not just pulsars of the Milky Way, but also nearby globular clusters would also increase this rate. Moreover, the large baselines offered by future radio interferometers like SKA will enable $\sim \mu$as astrometry (Fomalont & Reid 2004; Smits et al. 2011). This provides a complementary pathway to timing for identifying secondary rays.

Our relativistic timing framework is naturally able to account for both these primary and secondary rays on the final timing signal. Gravitational lensing of both the primary and secondary rays will influence the signal not only due to a difference and modulated spatial path, but also due to the different gravitational and relativistic time dilation, relativistic energy shift (see Sec. 4.2.4) and subject to different to temporal and spatial dispersion (Sec. 4.2.5). Moreover, the period of the primary and secondary rays is not generally the same, introducing an additional Fourier frequency, whilst the time delay between the primary and secondary pulses is also modulated over the course of the orbit (Fig. 4.10).

4.2.4 Gravitational and relativistic time dilation

For a pulsar in a strong-field environment, one must account for general relativistic effects influencing the rate at which the pulsar clock is observed to tick. There are two effects to consider here. The first is gravitational time dilation; clocks run slower in potential wells. The second is the relativistic Doppler shift induced by the motion of the pulsar. Both these effects will influence the observer radio signal; an apparent modulation in the observed pulsar period where the intrinsic pulsar rotation frequency is different to that recorded by some distant observer. This effect can be quantified as,

$$\gamma = \frac{\nu_{\text{intrinsic}}}{\nu_{\text{observed}}} = \frac{p_\alpha u^\alpha|_{\text{emitted}}}{p_\alpha u^\alpha|_{\text{observed}}} \ . \tag{4.39}$$

Note that this quantity is frame-invariant - for simplicity and we choose to evaluate it in the global coordinate frame. The magnitude of γ varies periodically over the course of a pulsar's orbit as the 4-velocity u^α changes due to the pulsar's motion and the ray 4-momentum p_α changes due to gravitational redshift (e.g. Fig. 4.11). Consequently the modulation will be greatest for eccentric orbits where the orbital velocity is changing most severely and more compact orbits which probe stronger gravitational fields. As we have seen, due to gravitational lensing it it possible for an observer to receive both primary and secondary rays. Since these secondary rays traverse a different spacetime path to the primary rays, the evolution of γ over the course of the orbit is flattened compared to the primary rays. Therefore not only will secondary rays arrive at a different time from the primary rays, but the modulation in the ticks as recorded by the secondary rays will differ from the primary rays.

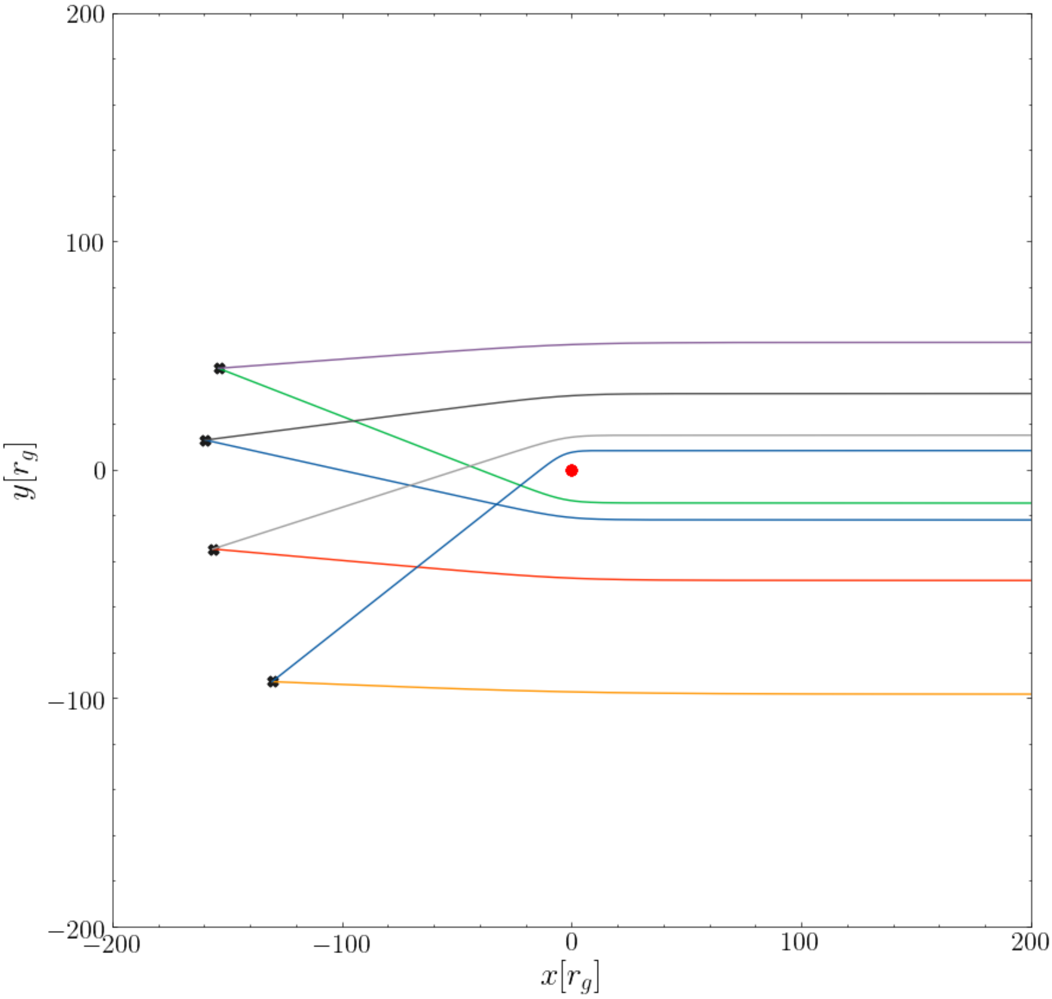

Fig. 4.9: Gravitational lensing of light rays in a vacuum by a BH with $a = +0.6$. The dark grey crosses show the emission points, i.e. the pulsar. For each emission point there are two rays which reach the distant observer (at $\Theta_{\rm obs} = \pi/2$, $\Phi_{\rm obs} = 0$); a primary ray which is subject to a lesser degree of gravitational lensing and a secondary ray which undergoes significant lensing. The time delay between the primary and secondary rays is modulated over the course of the orbit. Each different colored line represents a ray with different coordinates on the observer's image plane.

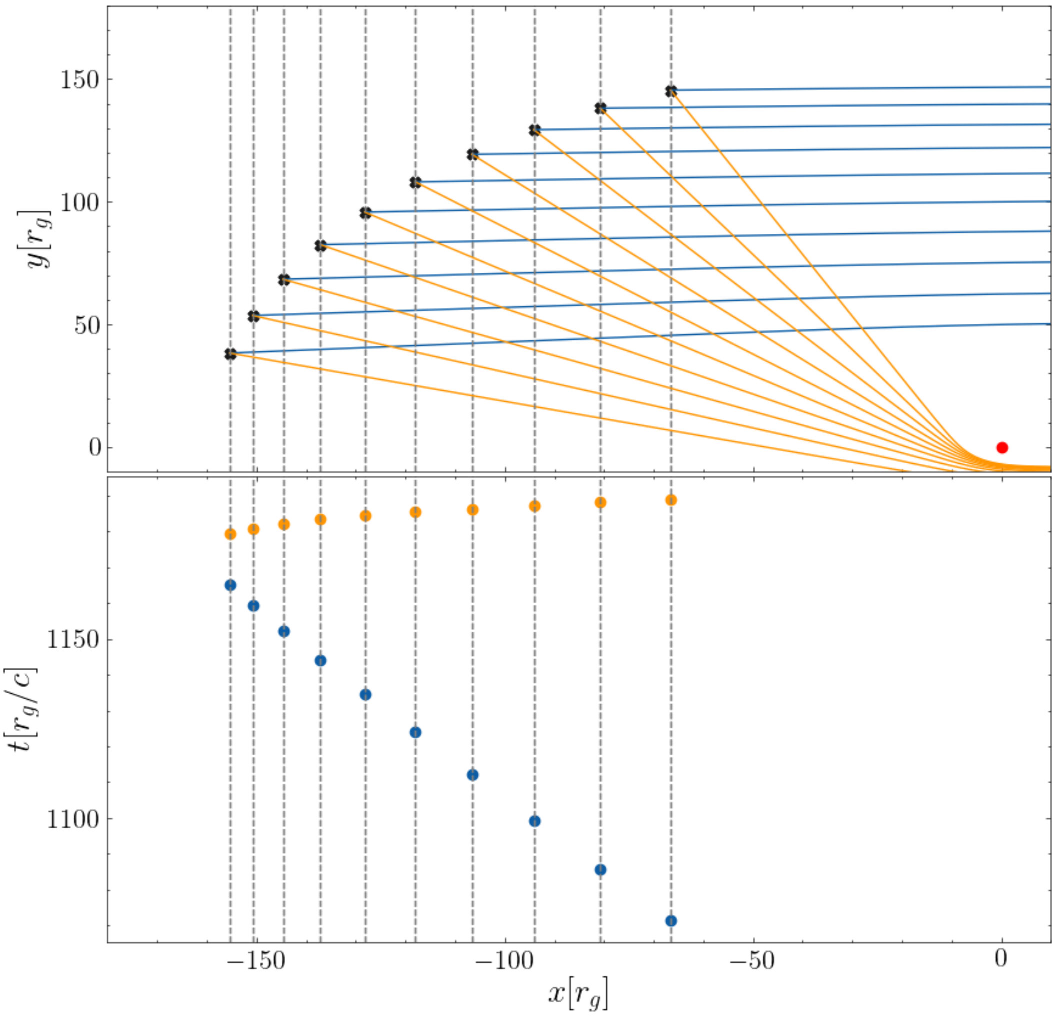

Fig. 4.10: (*Top panel:*) Primary and secondary rays subject to gravitational lensing for a segment of pulsar orbit on the far side of the BH. (*Bottom panel:*) Corresponding photon propagation times for the primary and secondary rays. Evidently the propagation times for the primary and secondary rays differ due to both the different spatial path and the degree of gravitational time delay. Equivalently, the received time profile will be different for the primary and secondary rays. We have set the BH spin to $a = +0.6$.

The modulation of γ means that the apparent pulsar spin frequency changes over the course of the orbit. The implications for this must be considered on both short and long timescales. For the former, the variation in the observed rotation frequency causes the signal in the Fourier domain to be 'smeared' across frequency bins consequently reducing the signal to noise ratio. Indeed, the detection of compact pulsar binaries is known to be very difficult due to this Doppler smearing effect (e.g. Jouteux et al. 2002). To detect such systems computationally expensive acceleration searches e.g. (e.g. Faulkner et al. 2004) which assume some constant value of the pulsar acceleration over the observation period, or higher order jerk searches (e.g. Andersen & Ransom 2018) are required. The magnitude of γ and the rate of change would be especially pronounced in the detection and timing of pulsars close to periastron and may be further complicated by the existence of secondary rays. Correcting for this effect is then essential to be able to first detect MSP-E/IMRBs. Over longer timescales, once the MSP is detected is is then necessary to account for the change is the pulse frequency over the orbital period timescale, especially if we want long timescale observations of these systems to perform tests of relativity and astrophysics. Taking into account these relativistic effects on the apparent pulsar rotation period is essential to accurately model the signal from a pulsar in an extreme gravity environment. The dependence of the net time dilation on the motion of the emitter also emphasizes the necessity to have an accurate description of the pulsar orbital dynamics - accounting for all general relativistic effects e.g. spin-curvature coupling - in modelling the pulsar signal.

4.2.5 Time-frequency signal

Typically, radio pulsar signals are dispersed in time due to the interstellar medium (ISM) and any signal needs correcting to account for this dispersion (e.g. Cordes et al. 2016). The time delay induced by the presence of plasma along the line of sight,

$$\Delta t \propto \mathrm{DM}\nu^{-2} \; , \tag{4.40}$$

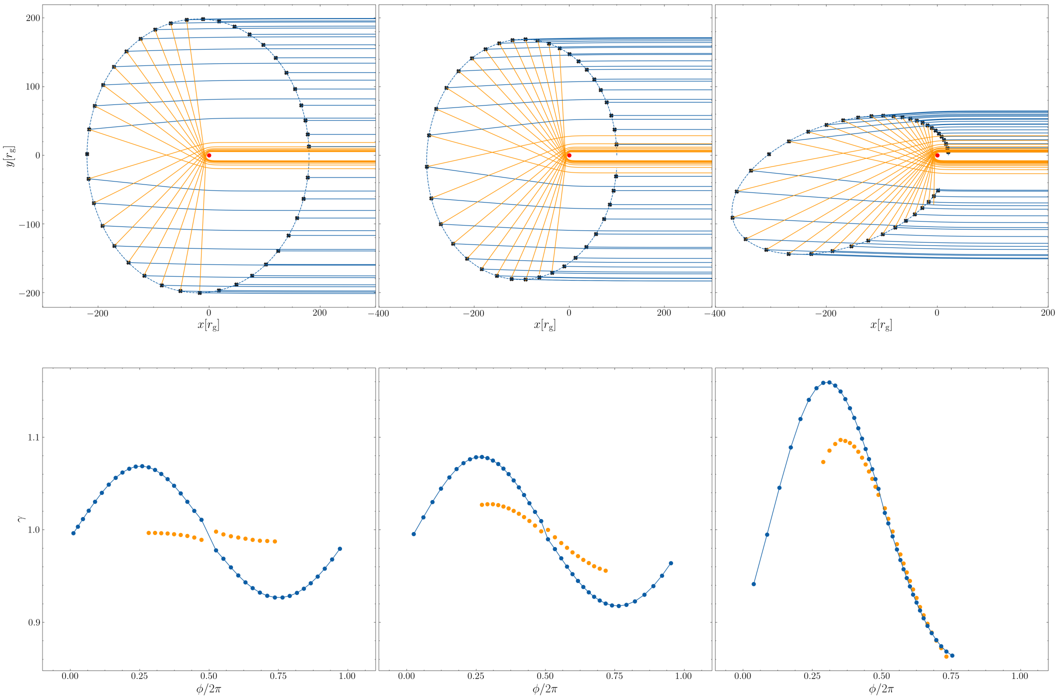

Fig. 4.11: The modulation of γ for a MSP orbiting a BH with $M = 4.31 \times 10^6 M_\odot$ and $a = +0.6$, and semi-major axis $= 200\ r_{\rm g}$ at eccentricities $e = 0.1, 0.5, 0.9$ (left, middle,right columns respectively). More eccentric orbits exhibit larger magnitude modulations due to the increased orbital velocity of the MSP. The γ-shift due to secondary rays exhibits a different profile to that of the primary rays.

for frequency ν and dispersion measure,

$$\mathrm{DM} = \int n_e(l) dl \ , \tag{4.41}$$

where n_e is the free electron number density. Therefore in order to detect the pulsar signal by searching for periodicities in the Fourier domain, one must first correct for the chromatic time delay. During pulsar searches, attempts are made to de-disperse the signal at a number of trial DMs, since the true DM is unknown.

Dispersive effects in the gravitational strong field due to the presence of astrophysical plasma along the ray path are fully accounted for within our framework. All dispersive electromagnetic effects are fundamentally included within the ω_{p}^2 term of the Hamiltonian (Eq. 2.67). Both the primary and secondary rays from the pulsar will be subject to a temporal dispersion. Due to gravitational lensing, the apparent position of the pulsar - the position which lies on the asymptote of the tangent line to the ray that converges at the observer - is distinct from the true pulsar position. Put another way, the observer's line of sight in Minkowski spacetime is distinct from the true light ray path. As a result the apparent region of the plasma that is being probed by the light ray is not the true region. Consequently to properly account for the time delay due to dispersion of the pulsar signal requires correcting for the gravitational bending of the ray path. The primary and secondary rays received from the pulsar will each follow a different spatial path and so be subject to a different dispersive time delay. This is in addition to the time shift induced due to other effects, such as the diverging path length, gravitation and relativistic time dilation, spin and orbital effects etc. This raises the possibility of a confusion problem and additional complexities for both pulsar searches and precision timing.

In addition to temporal dispersion, the combination of strong-field curvature and electron plasma induces a spatial dispersion such that the trajectory followed by the ray after being deflected by the black hole is frequency dependent

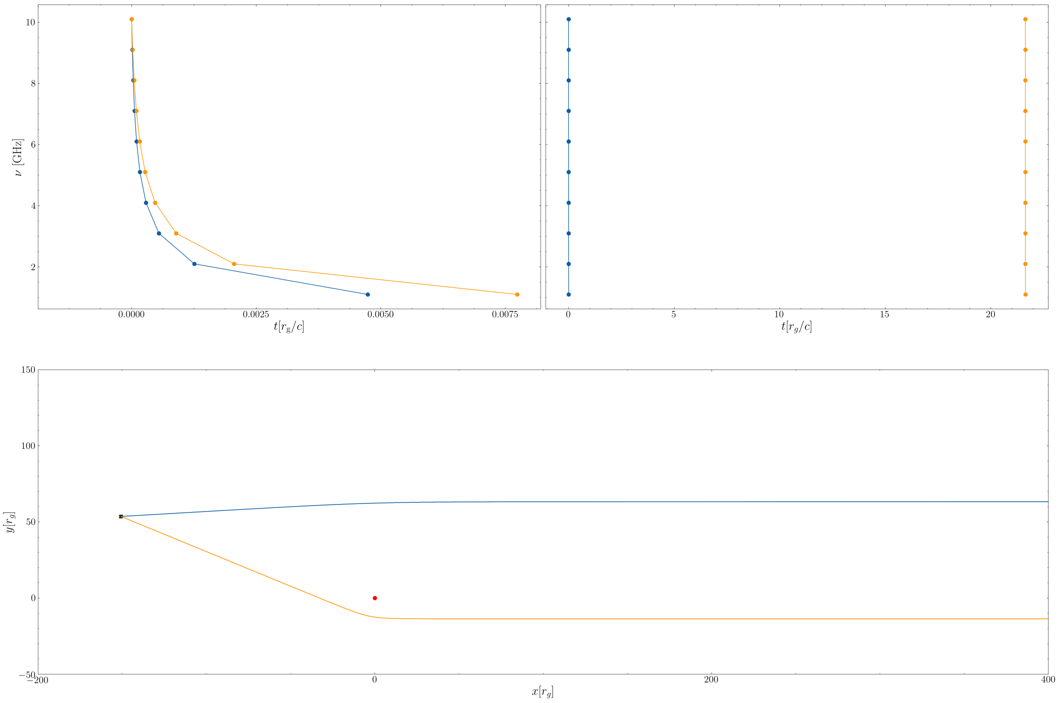

Fig. 4.12: Temporal dispersion at radio frequencies for rays on the far side of a BH mass $M = 4.31 \times 10^6 M_\odot$, $a = 0.6$ surrounded by a plasma with profile $n = n_0 r^{-1.1}$ and $n_0 = 3.5 \times 10^7$ cm^{-3} (Psaltis 2012). In the top left panels the times of the primary and secondary rays have been normalised such that the different $t - \nu$ profile is evident. This is on account of the different spacetime and plasma traversed. The right panel shows the relative delay of the secondary ray bundle with respect to the primary ray.

(see e.g. Fig 2.3). This further complicates the previous discussion on temporal dispersions and has several implications for rays which are gravitationally bent. Firstly, some rays may no longer be visible in specific frequency bins since if the spatial dispersion is sufficiently severe the ray path is bent such that is does not hit the observer's image plane. Moreover, each ray which does reach the observer has followed a different spatial trajectory, a different spacetime geodesic, and encountered a different plasma path integral, analogous to the case for primary/secondary rays. The effect is to further smear the pulse, rendering the pulse undetectable if the smearing is of sufficient magnitude. Any corrections for gravitational light bending are frequency dependent; the apparent position of the pulsar can be related to multiple true positions, depending on the ray frequency, each necessitating a different DM correction to be applied in each frequency bin. The total received signal is then not some function that varies smoothly with the pulsar orbital phase, but instead the convolution of different energy rays emitted at different orbital phases and consequently subject to differing relativistic and line-of-sight effects. This may, depending on the orbital configuration, result in additional difficulties in detecting signals from PSR-EMRB systems.

4.3 Discussion

We have presented the principles and framework for calculating the radio signal from a PSR in an E/IMRB. We restrict our study to extreme/intermediate mass ratio systems and so do not consider PSRs in stellar-mass black hole binaries with finite mass ratios (e.g. Liu et al. 2014). We account for both relativistic and astrophysical effects and the convolution between the two. This includes gravitational and relativistic time dilation and energy shift, gravitational light bending, complex orbital dynamics induced by spin couplings, temporal variation and distortion of the pulse profile due to spin axis precession and relativistic aberration, 2nd order pulses due to gravitational bending, and dispersions (temporal and spatial) induced by the material along the line of sight. We have demonstrated that within our framework we are able to determine the time-frequency behaviour accounting for all these effects. The framework also applies for any orbital configuration, e.g. we are not restricted to orbital motion or beaming in the equatorial plane. The methods used are entirely covariant and general relativistic, rather than working under any post-Newtonian approximation and so are inherently more accurate. Indeed, the post-Newtonian method is an explicitly weak-field method, and the validity of its application to strong-field dynamical regimes is unclear (Will 2011). Whilst working explicitly in the Kerr metric means that we are unable to independently probe either alternative gravitational theories or extensions to Kerr (e.g. bumpy black holes e.g. Vigeland & Hughes 2010), our framework provides the basis for a theoretical timing model which can then be compared with observations for tests of strong field GR. We approximate the PSR body as a perfect sphere. However due to the spin of the PSR the true shape is more oblate. This will ultimately influence the pitch angle of the ray with the neutron star surface. This effect is considered to be minor, but the method could easily be extended to account for this oblateness (see Nättilä & Pihajoki 2018). We neglect the effects of hydrodynamic drag due to the plasma that surrounds that black hole, since at compact radii ($\lesssim 10^4 r_g$) the gravitational and relativistic effects dominate (Psaltis 2012). We also do not take account of any potential Newtonian perturbations on the motion of the pulsar (e.g. Merritt et al. 2011) due to the presence of other masses (e.g. stars, other compact objects etc.) since these factors are likely negligible for the orbital periods considered in this work ($\lesssim$ 0.3 years, Liu et al. 2012). Indeed, the potential for external perturbations to hamper tests of strong-field GR necessitates that an ideal PSR-EMRB systems should have orbital periods on the order of 0.1 years (or better), or else observations should be taken close to periapsis (see discussion in Psaltis et al. 2016). These are precisely the regions where the spacetime curvature and orbital acceleration is greatest, further stressing the importance of a strong-field timing model. We also neglect any influence of gravitational radiation on the orbit or the ray trajectory. The neglect of gravitational radiation is justified since in the extreme mass ratio limit, the timescale for orbital decay due to gravitational wave emission is (Misner et al.

1973),

$$\tau_{GW} \sim \frac{5r^4}{96mM(m+M)} f(e)^{-1} \ , \tag{4.42}$$

for where M is the mass of the black hole, m the pulsar mass and r the orbital separation. The eccentricity function is,

$$f(e) = (1-e^2)^{-7/2} \left(1 + \frac{73}{24}e^2 + \frac{37}{96}e^4\right) \ . \tag{4.43}$$

If we take the PSR orbital period P to be Keplerian, then for a pulsar with mass $1.4 M_{\odot}$ on an eccentric ($e = 0.8$), $P = 0.1$ year orbit around a BH with mass $4.3 \times 10^6 M_{\odot}$,

$$\frac{\tau_{GW}}{P} \sim 10^9 >> 1 \ , \tag{4.44}$$

and so the effects of gravitational radiation can be neglected. Even for smaller radii and more eccentric orbits the spacetime is well approximated as stationary (e.g. $\tau_{GW}/P \sim 10^5$ for $e = 0.9$, $r = 100M$). Whilst the effects of gravitational radiation are then not important for a single orbit, for observations over longer periods of time the effect of gravitational emission on the orbit and hence the timing solution will need to be considered. The PSR may also emit a gravitational wave burst during passage through periastron (Berry & Gair 2013b). The influence of this gravitational radiation on both the PSR trajectory and the photon ToA is not considered here.

In this work we do not address the task of how to use our calculations to perform mock data analysis and extract orbital parameters from simulated PSR-EMRB timing data. This is achievable, for instance, by using a software package such as TEMPO (Hobbs et al. 2006) to determine the parameters of the timing model from the simulated data (e.g. Liu et al. 2014), or/and by performing a Markov Chain Monte Carlo fitting to investigate constraints on the orbital parameters (e.g. Zhang & Saha 2017). In principle, the method outlined in this work can be used to generate time-frequency data which could then be analysed by the aforementioned methods, but this is beyond the scope of this work. Similarly, it may prove possible to fit a relativistic model like one presented here to astrophysical data in order to extract system parameters, analogous to the matched filtering approach commonly used in gravitational wave astronomy, but again we do not consider that here. We also caveat that, due to the high stellar density of the Galactic centre, timing data can be influenced by external Newtonian perturbations (from e.g. stars, stellar mass compact objects Merritt et al. 2011). Any consistent timing solution should therefore provide a method to correct for these gravitational foreground disturbances (e.g. Angélil & Saha 2014; Zhang & Saha 2017). The handling of such perturbations is not explicitly considered in this work, but we restrict our analysis to pulsars on orbits of $P \lesssim 0.1$ years where such perturbations are more likely to be negligible (Liu et al. 2012). The analysis of timing data taken from orbital systems with longer periods would need a method to remove these effects (another possibility is to analyse only data taken close to periapsis, where the magnitude of these perturbations is expected to be less severe).

Whilst we have started the theoretical basis for timing observations of a strong-field PSR, there are a number of further potential developments of this work. With the ray tracing solution, we can then perform general relativistic radiative transfer along the rays (e.g. Fuerst & Wu 2004, 2007; Younsi et al. 2012) so as to determine the effects of line-of-sight material on the beam intensity. Understanding the received intensity and consequent S/N ratio is essential for accurately exploring the prospect of using PSR as probes of strong-field GR. As mentioned, it would also be of interest to investigate how well the weak-field post-Keplerian parameterization can describe strong-field effects (see the following chapter). This is important both for determining the types of PSR we require to test GR and for creating an accurate model to then compare with observations. A coherent $t - \nu$ model which accounts for all relativistic and line of sight effects could then also be potentially used to inform detections; e.g. are acceleration searches necessary for the detection of MSP close to the Galactic centre? As noted by Faucher-Giguère & Loeb (2011), the high stellar density in the Galactic Centre may allow for the creation of some rare binaries (e.g. triple systems). The subsequent dynamics (e.g. Remmen & Wu 2013) and impact on the PSR signal would be another interesting pursuit.

To summarize, accurately modelling the time-frequency behaviour from a radio PSR in the strong-field regime leads to a number of higher-order effects which will influence the photon ToA. These include:

- Consideration of spin curvature coupling can lead to variations of order $\pm 10\mu$s in the photon ToA compared to when spin-curvature coupling is neglected. Lower order estimates to the orbital motion (e.g. pure Keplerian dynamics) will further exacerbate the discrepancy, whilst accurate determination of the orbital motion (i.e. including spin-spin, spin-orbit, spin-curvature couplings) is essential for accurately modelling the frequency modulation.

- Precession of the spin axis in conjunction with relativistic aberration influences both the pulse profile, pulse duration, the pulse arrival time and the pulse intensity. Aperiodicity in the spin precession may introduce additional complications in the detection of pulsars, whilst severe precession could leave the pulsar signal intermittent.

- Gravitational bending causes deviation from a simple Minkowski geodesic which naturally influences the photon ToA. Strong gravitational bending can cause multiple (primary/secondary) pulses to be received by the observer, emitted from a pulsar at approximately the same location. Each ray follows a distinct spacetime path and so suffers different transfer effects, both gravitational (e.g. time dilation) and those due to interaction with material along the line of sight (i.e. temporal dispersion with the DM different for the primary and secondary rays). The interplay of gravitational bending with spatial dispersion further compounds these effects.

- Gravitational and relativistic time dilation causes substantial shift in the observed pulse frequency over the orbit. The magnitude of the dilation varies over the orbit and is more pronounced for more eccentric orbits. Secondary, highly bent rays traverse a different curvature of spacetime and so the frequency modulation is different from that of the primary rays.

- The presence of material along the ray path causes a temporal dispersion in the photon ToA, whilst a coupling with the strong spacetime curvature causes a spatial dispersion of the rays. Since each ray of a given frequency follows a different path - and so is subject to different gravitational and line of sight effects - the ToA will vary.

To conclude, in order to undertake precision tests of GR it is necessary to have a coherent, accurate theoretical model with which to compare observations. In this work we present a framework for calculating the time-frequency behaviour from a pulsar signal in an entirely general relativistic context, including the effects of spin axis precession and nutation, relativistic aberration, relativistic and gravitational time shift, relativistic energy shifts, spatial and temporal dispersion and gravitational light bending. The convolution of these effects will all ultimately influence the photon arrival time. Such a framework is the first step toward the creation of an accurate timing model of a PSR signal in the strong-field regime.

Chapter 5

Post Keplerian methods in the Strong-field

5.1 Introduction

A pulsar timing model is fundamentally a map between the time at which the pulse was received in the observers frame t to the time at which the pulse was emitted in the 'clock frame' τ (i.e. the frame comoving with the pulsar). With a sufficiently accurate timing model it is then possible to infer precision information about the intrinsic system parameters. For the majority of pulsars it is sufficient to take the inertial reference frame of the pulsar as being equivalent to the solar system barycentre. The model is then describe in terms of the usual Keplerian parameters (eccentricity, orbital period, etc.). However the presence of relativistic effects introduce additional 'Post-Keplerian' timing delays. For pulsars in binary systems there are 3 primary relativistic delays

$$t = \tau + \Delta_R + \Delta_S + \Delta_E \ , \tag{5.1}$$

where Δ_R is the Romer delay due to orbital motion of the pulsar, Δ_S is the Shapiro delay due to gravitational time dilation and Δ_E is the Einstein delay, the relativistic time dilation (see Lorimer & Kramer 2012, for further details). The relationship between the timing delays $(\Delta_R, \Delta_S, \Delta_E)$ and the system parameters is based on the 'Post-Keplerian' (PK) approximation (Blandford & Teukolsky 1976; Damour & Deruelle 1986). These binary systems in which the relativistic effects need to be accounted for in the timing model are the most interesting from the perspective of testing fundamental physics and astrophysics; the decay of the orbital period of the Hulse-Taylor binary provided the first evidence for gravitational waves (Weisberg et al. 1981) whilst observations of the remarkable double pulsar system PSR J0737-3039 (Burgay et al. 2003) and the associated relativistic effects have enabled stringent tests of GR.

The PK approximation is derived under the assumption that the gravitational field is weak. GR is subsequently treated perturbatively as an expansion about Newtonian gravity. Whilst this considerably simplifies the previously non-linear equations, such an approximation may not be appropriate for relativistic orbits close to massive black holes. Tests of GR in the solar system which employ the PK framework are undertaken in an environment where typically $\epsilon \sim 10^{-8}$. In binary pulsar systems $\epsilon \lesssim 10^{-6}$. Conversely, for a pulsar at periapsis on a $P = 0.1$ year eccentric ($e = 0.9$) orbit around Sgr A*, $\epsilon = 0.01$. Due to external perturbations on the PSR orbit (Merritt et al. 2010), the cleanest information on the BH parameters will be obtained from the PSR at periapsis, in precisely the region of strongest gravity. Photons propagating from the pulsar to an observer may pass sufficiently close to the BH so as to traverse a spacetime where ϵ approaches unity (see e.g. discussion on the use of pulsars to probe quantum effects and the BH event horizon Estes et al. 2017). It therefore seems reasonable to question the validity of the weak-field approximation in a region where the gravitational potential is $\gtrsim 10^4$ times stronger than the environments in which it is typically applied.

Pulsar timing delays given by the PK approximation in strong-field regimes was partly addressed in Hackmann & Dhani (2018) who investigate the propagation delays (Roemer and Shapiro) from circular orbits in a Schwarzschild spacetime. The influence of the central black hole spin on the measurement of pulsar orbital parameters was investigated in Zhang & Saha (2017), whilst Li et al. (2019) explored the impact of relativistic spin dynamics on the PSR emission. In this work, we further develop these previous studies by deploying our consistent, relativistic framework that we have outlined previously to accurately calculate the pulse ToA from a spinning pulsar orbiting a Kerr BH. We can then compare this 'true' GR solution with the 'approximate' PK solution and so determine the validity of the PK approach for BH parameter estimation at the Galactic centre and the centre of globular clusters.

5.2 Comparison with Post-Keplerian approximation

The core focus here is to compare the fully general relativistic solution using the methods outlined in the previous chapters with the timing delays given by the PK approximation. For a given quantity X we can determine 4 'levels' of solution

1. $X_{\mathrm{PK},i}$ - solution given by the i-th order PK approximation
2. $X_{\mathrm{GEO},a=0}$ - GR solution for zero BH spin ($a=0$) and zero MSP spin (i.e. Schwarzchild geodesic)
3. $X_{\mathrm{GEO},a\neq 0}$ - GR solution for non-zero BH spin and zero MSP spin (i.e. Kerr geodesic)
4. X_{MPD} - GR solution for spinning BH and spinning MSP (i.e. full MPD solution)

We will investigate the difference between each of these levels of solution, defining the respective differences as,

$$\delta_{\alpha,i}(X) = X_{\mathrm{GEO},a=0} - X_{\mathrm{PK},i} \tag{5.2}$$

$$\delta_{\beta}(X) = X_{\mathrm{GEO},a\neq 0} - X_{\mathrm{GEO},a=0} \tag{5.3}$$

$$\delta_{\gamma}(X) = X_{\mathrm{MPD}} - X_{\mathrm{GEO},a\neq 0} \tag{5.4}$$

It is worth taking a moment to consider how we compare different quantities in different spacetimes. For $\delta_\beta X$ and $\delta_\gamma X$, the comparison is straightforward; in all cases we are working in Boyer-Lindquist coordinates, with the Schwarzschild coordinates of the Schwarzschild metric simple being a special ($a=0$) case. However, solutions derived within the post-Keplerian framework are derived from the PK metric which typically uses a different coordinate system. In particular, by writing the Schwarzschild metric in harmonic coordinates (such that $g^{\mu\nu}\Gamma^{\alpha}{}_{\mu\nu} = 0$) where the radial harmonic coordinates r_h is related to the Boyer Lindquist coordinate as,

$$r = r_h + 1 \ , \tag{5.5}$$

and by taking the weak field (large r_h) limit, the metric components become,

$$g_{00} = -1 + 2/r_\mathrm{h} - \frac{1}{2}\left(2/r_\mathrm{h}\right)^2 + \cdots \tag{5.6}$$

$$g_{jk} \ \ = \left(1 + 2/r_\mathrm{h}\right)\delta_{jk} + \tfrac{1}{4}\left(2/r_\mathrm{h}\right)^2\left(\delta_{jk} + n_j n_k\right) + \cdots \tag{5.7}$$

where $n^j = x^j/r_h$ and $n_j = \delta_{jk}n^k$ (Poisson & Will 2014). At first order the metric interval is then

$$ds^2 = -\left(1 - \frac{2}{r_h}\right)dt^2 + \left(1 + \frac{2}{r_h}\right)(d\bar{\rho})^2 \ , \tag{5.8}$$

where $(d\bar{\rho})^2 = dx^2 + dy^2 + dz^2$.This is the first order PK metric and is the one typically used (e.g. Blandford & Teukolsky 1976) for calculating the pulsar timing delays. Explicitly, the second order metric solution is:

$$ds^2 = -\left(1 - \frac{2}{r_h} + \frac{2}{r_h^2}\right)dt^2 + \left(1 + \frac{2}{r_h} + \frac{1}{r_h^2}\right)(d\bar{\rho})^2 \tag{5.9}$$

$$+ \frac{1}{r_h^2} n_j n_k dx^j dx^k \ . \tag{5.10}$$

The primary search area for MSP-E/IMRBs is the Galactic centre. Although no MSPs have yet been detected in this region previous surveys can be shown to be insensitive to the population (Rajwade et al. 2017) and so the development of advanced radio facilities with increased sensitivities e.g. SKA or dedicated search methods e.g. NASA DSN - along with the development of appropriate relativistic search algorithms -should render this population detectable. Subsequently, to use a MSP in the Galactic centre as a precision probe of strong-field GR (e.g. Liu et al. 2012; Psaltis et al. 2016) it is important to time a pulsar that is solely affected by the gravitational field of the central BH. However there do exist astrophysical perturbations to the pulsar orbit e.g. gravitational perturbations due to the presence of other masses (Merritt et al. 2010). For orbits with periods $\lesssim 0.3$ year external perturbations are expected to be negligible (Liu et al. 2012). Observations close to periapsis of some longer, sufficiently eccentric orbits may also be viable. Consequently in this work we will consider eccentric systems with appropriately short orbital periods $\lesssim 0.3$ year. We take the mass of the Galactic centre BH to be $M \sim 4.3 \times 10^6 M_\odot$ (Gillessen et al. 2009). The PK timing delays that we will investigate are,

1. Einstein delay, Δ_E - due to gravitational and relativistic time dilation of the MSP.
2. Roemer delay, Δ_R - due to the orbital motion of the MSP
3. Shapiro delay, Δ_S - due to the gravitational time dilation of light

We will now explore each of these pulsar timing delays in turn

5.2.1 Einstein Delay, Δ_E

The Einstein delay describes the Doppler shift and gravitational time delay (redshift), or the difference between the MSP proper time and the time measured by a distant observer,

$$\Delta_\mathrm{E} = t - \tau \ . \tag{5.11}$$

Determining the Einstein delay from the numerical relativistic solutions is straightforward, since at each integration time step we have the MSP proper time and the observer coordinate time by solving Eq. 3.21. Within the PK approximation, one can derive an analytical expression for the Einstein delay (Blandford & Teukolsky 1976; Zhang & Saha 2017) as,

$$\Delta_E = \frac{Pe}{\pi a_*}(\sin E' - \sin E'_0) + \frac{3}{2}\frac{t}{a_*} \ , \tag{5.12}$$

where a_* is the semi major axis (as distinct from spin parameter a defined in earlier chapters) and E' the eccentric anomaly, an angular parameter given by

$$\cos E'(t) = \frac{1}{e}\left(1 - \frac{r_h(t)}{a_*}\right) \ . \tag{5.13}$$

Evidentially the Einstein delay is then composed of an oscillatory part, of magnitude $\gamma = Pe/\pi a_*$ and a linear term. Rather than computing the analytical evolution of Δ_E by e.g. solving the Kepler equation for E', we employ a different approach. From Eq. 5.8 it follows that,

$$\left(\frac{dt}{d\tau}\right)^2 = \frac{1 + \left(1 + \frac{2}{r_h}\right) v^2}{1 - \frac{2}{r_h}} \ , \tag{5.14}$$

where $v^2 = |d^2\bar{\rho}/d\tau^2|$. At second order,

$$\left(\frac{dt}{d\tau}\right)^2 = \frac{1 + \frac{1}{r_h^2} n_j n_k \frac{dx^j}{d\tau}\frac{dx^k}{d\tau} + \left(1 + \frac{2}{r_h} + \frac{1}{r_h^2}\right) v^2}{1 - \frac{2}{r_h} + \frac{2}{r_h^2}} \ . \tag{5.15}$$

We can express the squared velocity magnitude in terms of BL coordinates by the straightforward coordinate transformation of a general contravariant vector,

$$Y^a = \frac{\partial x^a}{\partial x^b} Y^b \ . \tag{5.16}$$

Explicitly, in conjunction with Eq. 5.5, the fact that $dr_h/dr = 1$ and the transformation between (spherical polar) harmonic and Cartesian coordinates then,

$$v^2 = v_x^2 + v_y^2 + v_z^2 \tag{5.17}$$

$$\begin{aligned} =&(\sin\theta\cos\phi\, u^r + r_h\cos\theta\cos\phi\, u^\theta - r_h\sin\theta\sin\phi\, u^\phi)^2 \\ &+ (\sin\theta\sin\phi\, u^r + r_h\cos\theta\sin\phi\, u^\theta - r_h\sin\theta\cos\phi\, u^\phi)^2 \\ &+ (\cos\theta\, u^r - r_h\sin\theta\, u^\theta)^2 \end{aligned} \tag{5.18}$$

where the u^α terms are the components of the MSP 4-velocity as given by Eq. 3.21. Together this gives us a differential equation for t as determined by the PK metric at first and second order. It is equivalent to the 0-th term of the relativistic solution described by Eq. 3.21. As we integrate the complete relativistic solution numerically, we can then at each integration timestep also compute v and r_h and solve Eq. 5.14. This then gives us t (and hence Δ_E) as given by the PK solution for an MSP which has the same spatial orbital trajectory as described by the full relativistic solution. The Einstein delay given by the respective solutions for a Galactic centre MSP with orbital period $P = 0.1$ years, in the equatorial plane is presented in Fig. 5.1 at eccentricities $e = 0, 7, 0.8, 0.9$. The evolution of the Einstein delay for all the orbits considered has general oscillatory contribution, illustrated by the first term of Eq.

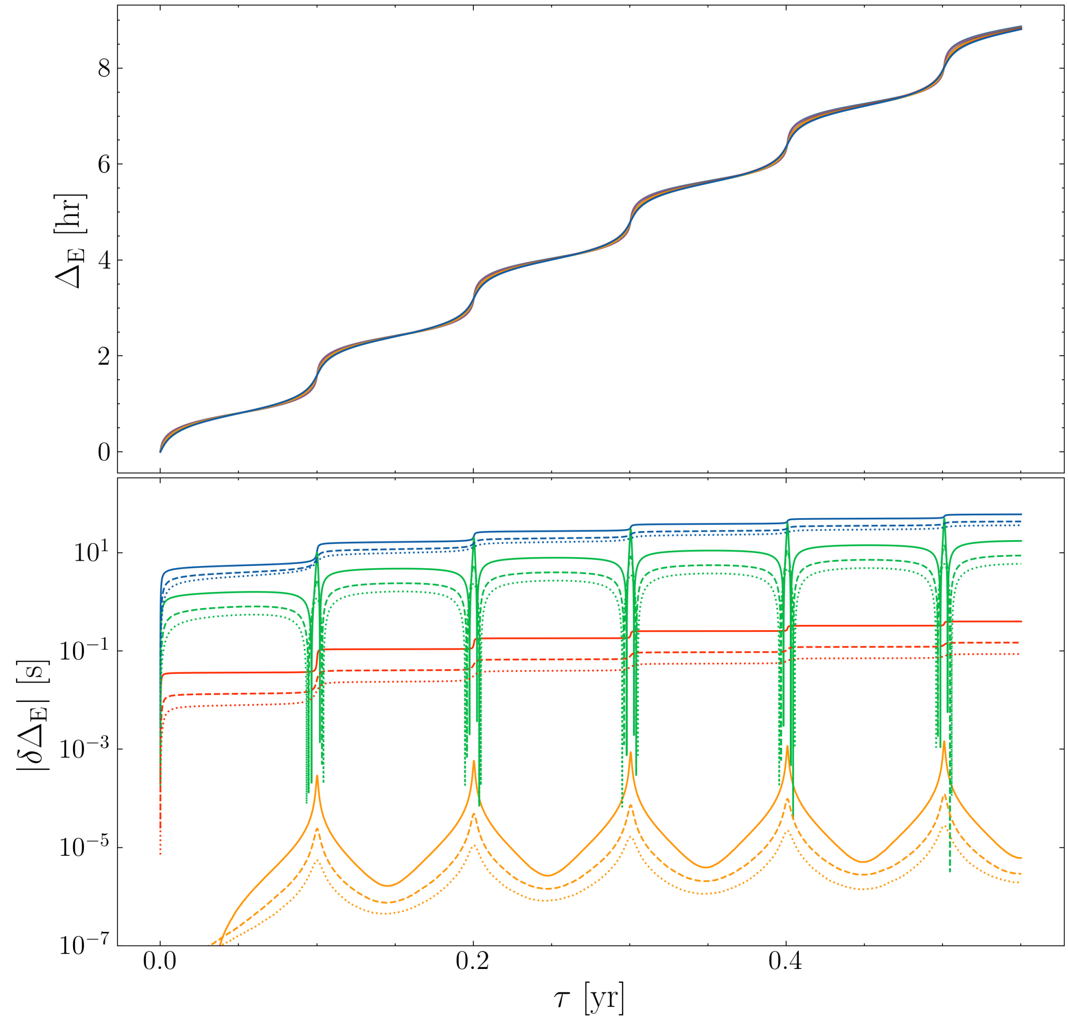

Fig. 5.1: *Top panel:* The Einstein delay given by the 5 solutions (2 PK + 3 GR) from a MSP orbiting the Galactic centre BH in the equatorial plane at a range of difference eccentricities. The BH mass is set as $4.31 \times 10^6 M_\odot$, with spin parameter $a + 0.6$. The delay accumulates up to 2 hrs after one orbital period, with rapid variations as the pulsar goes through periapsis. *Bottom panel:* The differences between the respective solutions $\delta_{\alpha,1}(\Delta_\mathrm{E})$ (blue),$\delta_{\alpha,2}(\Delta_\mathrm{E})$ (red), $\delta_\beta(\Delta_\mathrm{E})$ (green), $\delta_\gamma(\Delta_\mathrm{E})$ (orange) at eccentricities $e = 0.9, 0.8, 0.7$ (solid, dashed, dotted lines respectively)

5.12 and an additional linear term. Rapid variations are observed as the MSP passes through periapsis and is moving at its fastest. After a single orbital period the Einstein delay has accumulated to ~ 2 hrs for all the solutions and all the eccentricities. Variations in the Einstein delay induced by relativistic effects are seen to occur at smaller scales: at the first level, $\delta_{\alpha,1}(\Delta_{\rm E})$ is of the order 10^1 seconds, whilst $\delta_{\alpha,2}(\Delta_{\rm E}) \sim 10^{-2} - 10^{-1}$ seconds, with greater magnitude errors for more eccentric orbits which move faster at periapsis and probe a stronger gravitational field. The variations induced by the BH spin for $a = +0.6$, $\delta_{\beta}(\Delta_{\rm E})$ introduce additional variations in the timing delay on the order of $0.1 - 1$ seconds, again with more eccentric orbits exhibiting larger magnitude variations. The influence of 'switching on' the MSP spin and the associated couplings is particularly interesting. Although subdominant to the $\delta_{\alpha,\beta}$ variations, the MSP spin introduces periodic contributions to the Einstein delay. As before, these corrections peak in magnitude at periapsis and for $e = 0.9$, $\delta_{\gamma}(\Delta_{\rm E}) \sim 1$ ms, whilst for $e = 0.7$ the maximal variations are of magnitude ~ 30 μs. Radio facilities such as FAST or SKA are able to determine pulse ToA to precisions < 100 ns (Hobbs et al. 2014; Stappers et al. 2018), especially for stable MSPs which are free of glitches. Consequently, small variations in the timing residuals $\mathcal{O}$ (μs - ms) will be both detectable and important for a consistent, long-term timing solution.

5.2.2 Propagation Delays: Shapiro and Roemer, Δ_S , Δ_R

In PK timing models for pulsar binaries, the photon propagation time between observer and source is the sum of the Roemer delay ($\Delta_{\rm R}$, i.e. time delay due to the finite speed of light propagating in a flat spacetime) and the Shapiro delay ($\Delta_{\rm S}$, time delay due to first order curvature corrections). This can be seen by decomposing the spacetime geodesic in terms of a Minkowskian (0th order) background plus a higher-order curvature perturbation (see e.g. Carroll 2003) i.e.

$$x^{\mu}(\lambda) = x^{(0)\mu}(\lambda) + x^{(1)\mu}(\lambda) + x^{(2)\mu}(\lambda) \ . \tag{5.19}$$

The background and perturbation tangent vectors are,

$$k^{\mu} \equiv \frac{dx^{(0)\mu}}{d\lambda} \ ; \ l^{\mu} \equiv \frac{dx^{(1)\mu}}{d\lambda} \ ; \ q^{\mu} \equiv \frac{dx^{(2)\mu}}{d\lambda} \ . \tag{5.20}$$

Similarly, we can decompose the metric up to second order as,

$$g_{\mu\nu} = \eta_{\mu\nu} + \epsilon h^{(1)}_{\mu\nu} + \epsilon^2 h^{(2)}_{\mu\nu} \ , \tag{5.21}$$

with contravariant form,

$$g^{\mu\nu} = \eta^{\mu\nu} - \epsilon h^{\mu\nu}_{(1)} + \epsilon^2 H^{\mu\nu}_{(2)} \ , \tag{5.22}$$

where $H^{\mu\nu}_{(2)} = \left(2h_{(1)}{}^{\nu}_{\alpha} h^{\mu\alpha}_{(1)} - h^{\mu\nu}_{(2)}\right)$. Since the perturbations are defined as tensors on the background spacetime, their indices can be raised and lowered via the background metric i.e.

$$h^{\mu\nu}_{(1)} = \eta^{\mu\alpha}\eta^{\nu\beta}h^{(1)}_{\alpha\beta} \ , \tag{5.23}$$

$$h_{(1)}{}^{\nu}_{\alpha} = \eta^{\nu\beta}h^{(1)}_{\beta\alpha} \ , \tag{5.24}$$

Generally the Christoffel symbols for a metric connection are given by,

$$\Gamma^{\mu}{}_{\rho\sigma} = \frac{1}{2}g^{\mu\lambda}\left(\partial_\rho g_{\sigma\lambda} + \partial_\sigma g_{\lambda\rho} - \partial_\lambda g_{\rho\sigma}\right) \ . \tag{5.25}$$

Taking Eqs. 5.21, 5.22, the Christoffel connection can also be decomposed into terms of order i which we write as ${}_{(i)}\Gamma^{\mu}{}_{\rho\sigma}$. Explicitly:

$${}_{(0)}\Gamma^{\mu}{}_{\rho\sigma} = 0 \ , \tag{5.26}$$

$${}_{(1)}\Gamma^{\mu}{}_{\rho\sigma} = \frac{1}{2}\eta^{\mu\lambda}\left(\partial_\rho {h_{\sigma\lambda}}^{(1)} + \partial_\sigma {h_{\lambda\rho}}^{(1)} - \partial_\lambda {h_{\rho\sigma}}^{(1)}\right) \ , \tag{5.27}$$

$$\begin{aligned} {}_{(2)}\Gamma^{\mu}{}_{\rho\sigma} = & \frac{1}{2}\eta^{\mu\lambda}\left(\partial_\rho {h_{\sigma\lambda}}^{(2)} + \partial_\sigma {h_{\lambda\rho}}^{(2)} - \partial_\lambda {h_{\rho\sigma}}^{(2)}\right) \\ & - \frac{1}{2}h^{\mu\lambda}{}_{(1)}\left(\partial_\rho {h_{\sigma\lambda}}^{(1)} + \partial_\sigma {h_{\lambda\rho}}^{(1)} - \partial_\lambda {h_{\rho\sigma}}^{(1)}\right) \ . \end{aligned} \tag{5.28}$$

The perturbed geodesic equation can then be written as,

$$-\frac{d}{d\lambda}\left(k^\mu + l^\mu + q^\mu\right) = \left({}_{(1)}\Gamma^{\mu}{}_{\rho\sigma} + {}_{(2)}\Gamma^{\mu}{}_{\rho\sigma}\right)\left(k^\rho + l^\rho + q^\rho\right)\left(k^\sigma + l^\sigma + q^\sigma\right) \ . \tag{5.29}$$

By collecting terms at each order:

$$\frac{d}{d\lambda}k^\mu = 0 \ , \tag{5.30}$$

$$\frac{d}{d\lambda}l^\mu = -\,{}_{(1)}\Gamma^{\mu}{}_{\rho\sigma}k^\rho k^\sigma \ , \tag{5.31}$$

$$\frac{d}{d\lambda}q^{\mu} = - {}_{(2)}\Gamma^{\mu}{}_{\rho\sigma}k^{\rho}k^{\sigma} - {}_{(1)}\Gamma^{\mu}{}_{\rho\sigma}(k^{\rho}l^{\sigma} + k^{\sigma}l^{\rho}) \ , \tag{5.32}$$

Now, the photon propagation time between observer and source is,

$$\begin{aligned} \Delta_{\text{prop}} &= \int \frac{dx^0}{d\lambda} d\lambda \\ &= \int k^0 d\lambda + \int l^0 d\lambda + \int q^0 d\lambda \\ &= \Delta_{\text{R}} + \Delta_{\text{S}} + \Delta_{\text{S}}^{(2)} \end{aligned} \tag{5.33}$$

where $\Delta_{\text{S}}^{(2)}$ labels the higher (second) order curvature time delay. Within the PK framework, one can derive analytical expressions for the evolution of Δ_{R}, Δ_{S} in terms of the system orbital parameters as (Shapiro 1964; Blandford & Teukolsky 1976; Damour & Deruelle 1986; Zhang & Saha 2017),

$$\Delta_{\text{R}} = \tilde{\alpha}\left(\cos E' - e\right) + \tilde{\beta}\sin E' \ , \tag{5.34}$$

$$\Delta_{\text{S}} = 2\ln\left[\frac{1 + e\cos f}{1 - \sin i \sin\left(\omega + f\right)}\right] \ , \tag{5.35}$$

where i is the inclination with respect to the observer, defined via Eq. 3.36, ω is the angle of periapsis and f the true anomaly, with

$$\tilde{\alpha} = a_{\star}\sin i \sin\omega \ , \tag{5.36}$$

$$\tilde{\beta} = \left(1 - e^2\right)^{1/2} a_{\star}\sin i \cos\omega \ . \tag{5.37}$$

Similar to deriving the Einstein delay in the previous section, we do not use these expressions explicitly but instead proceed via an equivalent route to express the time delays in terms of coordinates rather than orbital parameters. To do this, we first need expressions for l^0, q^0 (k^0 is trivially $= 0$). Explicitly each of the tensors relevant for our calculations are:

$$\eta_{\mu\nu} = \eta^{\mu\nu} = \text{diag}(-1,1,1,1) \tag{5.38}$$

$$h_{\mu\nu} = \text{diag}(-2\Phi, -2\Phi, -2\Phi, -2\Phi) \tag{5.39}$$

$$h^{(2)}_{\mu\nu} = \begin{pmatrix} -2\Phi^2 & 0 & 0 & 0 \\ 0 & \Phi^2(1 + n_1 n_1) & \Phi^2 n_1 n_2 & \Phi^2 n_1 n_3 \\ 0 & \Phi^2 n_1 n_2 & \Phi^2(1 + n_2 n_2) & \Phi^2 n_2 n_3 \\ 0 & \Phi^2 n_1 n_3 & \Phi^2 n_2 n_3 & \Phi^2(1 + n_3 n_3) \end{pmatrix} \tag{5.40}$$

where $\Phi = -1/r_h$ and $n_j = \delta_{jk} n^k$, $n^j = x^j/r_h$.

Now for these metric perturbations the temporal term of the Christoffel connection at first order from Eq. 5.27 is:

$$
\begin{aligned}
{}_{(1)}\Gamma^{0}{}_{\rho\sigma} &= \frac{1}{2}\eta^{0\lambda}\left(\partial_\rho h_{\sigma\lambda}{}^{(1)} + \partial_\sigma h_{\lambda\rho}{}^{(1)} - \partial_\lambda h_{\rho\sigma}{}^{(1)}\right) && (5.41)\\
&= \frac{1}{2}\eta^{00}\left(\partial_\rho h_{\sigma 0}{}^{(1)} + \partial_\sigma h_{0\rho}{}^{(1)} - \partial_0 h_{\rho\sigma}{}^{(1)}\right) , && (5.42)
\end{aligned}
$$

whilst at second order from Eq. 5.28:

$$
\begin{aligned}
{}_{(2)}\Gamma^{0}{}_{\rho\sigma} &= \frac{1}{2}\eta^{0\lambda}\left(\partial_\rho h_{\sigma\lambda}{}^{(2)} + \partial_\sigma h_{\lambda\rho}{}^{(2)} - \partial_\lambda h_{\rho\sigma}{}^{(2)}\right) && (5.43)\\
&\quad - \frac{1}{2}h^{0\lambda}{}_{(1)}\left(\partial_\rho h_{\sigma\lambda}{}^{(1)} + \partial_\sigma h_{\lambda\rho}{}^{(1)} - \partial_\lambda h_{\rho\sigma}{}^{(1)}\right) . && (5.44)
\end{aligned}
$$

Now, both $\eta^{0\lambda}$ and $h^{0\lambda}$ are only non-zero for $\lambda = 0$. Therefore we can write

$$
\begin{aligned}
{}_{(2)}\Gamma^{0}{}_{\rho\sigma} &= \frac{1}{2}\eta^{00}\left(\partial_\rho h_{\sigma 0}{}^{(2)} + \partial_\sigma h_{0\rho}{}^{(2)} - \partial_0 h_{\rho\sigma}{}^{(2)}\right)\\
&\quad - \frac{1}{2}h^{00}{}_{(1)}\left(\partial_\rho h_{\sigma 0}{}^{(1)} + \partial_\sigma h_{0\rho}{}^{(1)} - \partial_0 h_{\rho\sigma}{}^{(1)}\right) .
\end{aligned}
$$

Now, the ∂_0 terms are always $= 0$ since everything we are dealing with here is stationary (i.e. time independent). Therefore

$$
\begin{aligned}
{}_{(2)}\Gamma^{0}{}_{\rho\sigma} &= \frac{1}{2}\eta^{00}\left(\partial_\rho h_{\sigma 0}{}^{(2)} + \partial_\sigma h_{0\rho}{}^{(2)}\right)\\
&\quad - \frac{1}{2}h^{00}{}_{(1)}\left(\partial_\rho h_{\sigma 0}{}^{(1)} + \partial_\sigma h_{0\rho}{}^{(1)}\right) .
\end{aligned}
$$

It is then immediately obvious by comparing with Eqs. 5.39, 5.40 that

$$
{}_{(2)}\Gamma^{0}{}_{\rho\sigma} = 0 . \qquad (5.45)
$$

It follows that the derivatives of the tangent vectors as defined by Eq, 5.32 5.31 are then,

$$
\begin{aligned}
\frac{d}{d\lambda}l^0 &= -\,{}_{(1)}\Gamma^{0}{}_{\rho\sigma}k^\rho k^\sigma && (5.46)\\
&= -2k(\bar{k}\cdot\bar{\nabla}\Phi) , && (5.47)
\end{aligned}
$$

$$
\begin{aligned}
\frac{d}{d\lambda}q^0 &= -\,{}_{(1)}\Gamma^{0}{}_{\rho\sigma}(k^\rho l^\sigma + k^\sigma l^\rho) && (5.48)\\
&= -2\left(l^0(\bar{k}\cdot\bar{\nabla}\Phi) + k^0(\bar{l}\cdot\bar{\nabla}\Phi)\right) && (5.49)\\
&= -2\left(-2k\Phi(\bar{k}\cdot\bar{\nabla}\Phi) + k(\bar{l}\cdot\bar{\nabla}\Phi)\right) && (5.50)\\
&= -2k\left(-2\Phi(\bar{k}\cdot\bar{\nabla}\Phi) + (\bar{l}\cdot\bar{\nabla}\Phi)\right) . && (5.51)
\end{aligned}
$$

We can then integrate each of these over the background path,

$$l^0 = -2k \int (\bar{k} \cdot \bar{\nabla}\Phi) d\lambda \tag{5.52}$$

$$= -2k \int \left(\frac{d\bar{x}}{d\lambda} \cdot \bar{\nabla}\Phi \right) d\lambda \tag{5.53}$$

$$= -2k \int \left(\bar{\nabla}\Phi \cdot d\bar{x} \right) \tag{5.54}$$

$$= -2k \int (d\Phi) \tag{5.55}$$

$$= -2k\Phi \tag{5.56}$$

$$q^0 = -2k \int -2\Phi(\bar{k} \cdot \bar{\nabla}\Phi) d\lambda \tag{5.57}$$

$$= 4k \int \Phi \left(\frac{d\bar{x}}{d\lambda} \cdot \bar{\nabla}\Phi \right) d\lambda \tag{5.58}$$

$$= 4k \int \Phi \left(\bar{\nabla}\Phi \cdot d\bar{x} \right) \tag{5.59}$$

$$= 4k \int \Phi \, (d\Phi) \tag{5.60}$$

$$= 2k\Phi^2 \tag{5.61}$$

where we can set the constant of integration easily since we require $q^0 = 0$ when $\Phi = 0$. With expressions for l^0, q^0 established, we can then write the propagation time between two points $\boldsymbol{r}_1, \boldsymbol{r}_2$ from 5.33 as,

$$\begin{aligned} \Delta_{\text{prop}} &= \int ds - 2 \int \Phi ds + 2 \int \Phi^2 ds \\ &= |\boldsymbol{r}_2 - \boldsymbol{r}_1| + 2 \int \frac{1}{|\boldsymbol{r}|} ds + 2 \int \frac{1}{|\boldsymbol{r}|^2} ds \end{aligned} \tag{5.62}$$

where ds denotes the unperturbed background path. Considering the second integral term (i.e. the Shapiro delay, Δ_{S}), we can parameterize in terms of t such that,

$$\boldsymbol{r} = \boldsymbol{r}_1 + \hat{\boldsymbol{u}} t \ , \tag{5.63}$$

where $\hat{\boldsymbol{u}}$ is the unit vector,

$$\hat{\boldsymbol{u}} = \frac{\boldsymbol{r}_2 - \boldsymbol{r}_1}{|\boldsymbol{r}_2 - \boldsymbol{r}_1|} \ , \tag{5.64}$$

and $t \in [0, |\boldsymbol{r_2} - \boldsymbol{r_1}|]$. With this parameterization, $ds = |\hat{\boldsymbol{u}}|dt$ and so,

$$\begin{aligned} \Delta_\mathrm{S} &= \int \frac{1}{|\boldsymbol{r}_1 + \hat{\boldsymbol{u}}t|} dt \\ &= \int \frac{1}{\sqrt{|\boldsymbol{r}_1|^2 + t^2 + 2t\boldsymbol{r}_1 \cdot \hat{\boldsymbol{u}}}} dt \ . \end{aligned} \tag{5.65}$$

Performing the integral gives,

$$\Delta_\mathrm{S} = \left[\ln\left(t + \boldsymbol{r}_1 \cdot \hat{\boldsymbol{u}} + |\boldsymbol{r}_1 + \hat{\boldsymbol{u}}t|\right)\right]_{t=0}^{t=|\boldsymbol{r}_2 - \boldsymbol{r}_1|} \ , \tag{5.66}$$

and so,

$$\Delta_\mathrm{S} = \ln\left(\frac{|\boldsymbol{r}_2 - \boldsymbol{r}_1| + \boldsymbol{r}_1 \cdot \hat{\boldsymbol{u}} + |\boldsymbol{r}_2|}{\boldsymbol{r}_1 \cdot \hat{\boldsymbol{u}} + |\boldsymbol{r}_1|}\right) \ . \tag{5.67}$$

Using the same parametrization for the quadratic term, it follows that

$$\Delta_\mathrm{S}^{(2)} = \left[\frac{1}{\zeta} \arctan\left(\frac{t + \boldsymbol{r}_1 \cdot \hat{\boldsymbol{u}}}{\zeta}\right)\right]_{t=0}^{t=|\boldsymbol{r}_2 - \boldsymbol{r}_1|} \tag{5.68}$$

$$= \frac{1}{\zeta} \arctan\left(\frac{|\boldsymbol{r}_2 - \boldsymbol{r}_1| + \boldsymbol{r}_1 \cdot \hat{\boldsymbol{u}}}{\zeta}\right) - \frac{1}{\zeta} \arctan\left(\frac{\boldsymbol{r}_1 \cdot \hat{\boldsymbol{u}}}{\zeta}\right) \tag{5.69}$$

with $\zeta = \sqrt{|\boldsymbol{r}_1|^2 - (\boldsymbol{r}_1 \cdot \hat{\boldsymbol{u}})^2}$ Completely, the propagation time along a straight line between two points in the PK framework at second order is then,

$$\Delta_\mathrm{prop} = |\vec{r}_2 - \vec{r}_1| + 2\ln\left(\frac{|\vec{r}_2 - \vec{r}_1| + \vec{r}_1 \cdot \hat{u} + |\vec{r}_2|}{\vec{r}_1 \cdot \hat{u} + |\vec{r}_1|}\right) \tag{5.70}$$

$$= \frac{1}{\zeta} \arctan\left(\frac{|\boldsymbol{r}_2 - \boldsymbol{r}_1| + \boldsymbol{r}_1 \cdot \hat{\boldsymbol{u}}}{\zeta}\right) - \frac{1}{\zeta} \arctan\left(\frac{\boldsymbol{r}_1 \cdot \hat{\boldsymbol{u}}}{\zeta}\right) \ , \tag{5.71}$$

where the first term corresponds to the Roemer delay and the second and third terms to the Shapiro delay at first and second order respectively. A linear decomposition of the propagation time in this way is not generally possible for the relativistic solutions, instead being found by solving Eq. 2.39. Therefore going forward, we will consider the Roemer and Shapiro terms together in terms of the general propagation delay Δ_prop.

To explore the propagation delay according to the PK and relativistic solutions we take a discrete sample of position points of an eccentric orbit. The orbit is calculated by solving the Kerr orbital geodesic equations numerically. The propagation delay between each sample point (i.e. the pulsar emitter)

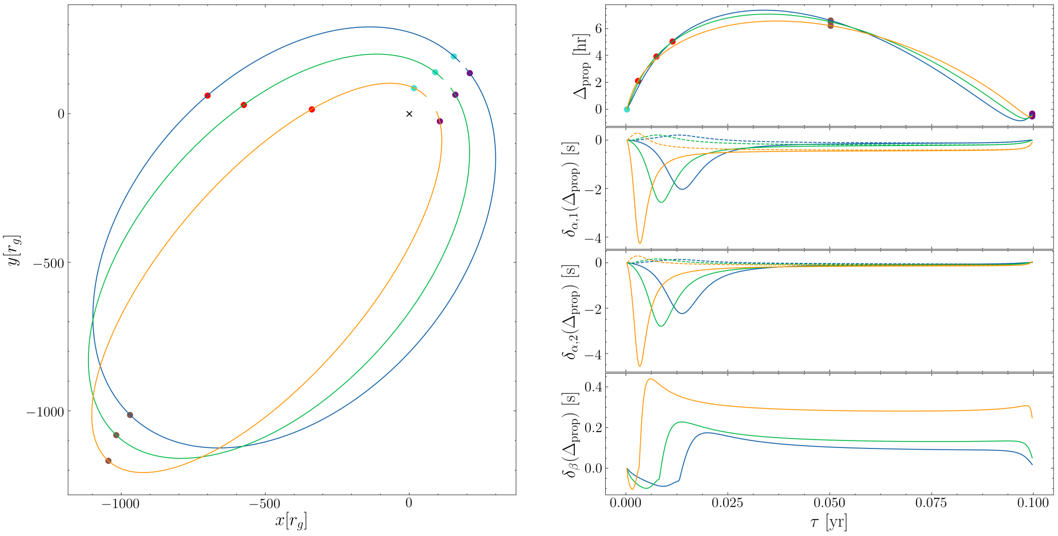

Fig. 5.2: (*Left panel:*) Orbital trajectories of a Galactic centre MSP with $a_* = 825 r_g$, $i = 76°$, $\omega = \Omega = \pi/4$ and eccentricities $e = 0.7, 0.8, 0.9$ (blue, green, orange lines respectively). The scatter points are included as a reference for the right panels and label the initial, final, middle and superior conjunction sample points (turquoise, purple, brown, red respectively) The black cross labels the BH singularity. (*Right panels:*) The propagation timing delay for each of the eccentric orbits, along with the errors between the PK and relativistic solutions ($\delta_{\alpha,i}(\Delta_{\rm prop})$,$\delta_\beta(\Delta_{\rm prop})$).For the middle two panels the dashed lines show the residual when the PK lensing correction is included (see also Fig. 5.4). Significant timing residuals are present between both $\delta_{\alpha,i}(\Delta_{\rm prop})$,$\delta_\beta(\Delta_{\rm prop})$ relative to typical radio pulsar timing precision.

and the image plane of a distant observer (with Boyer Lindquist coordinates $R = 10^4, \Theta = \pi/2, \Phi = 0$) can be calculated via the PK solution (Eq. 5.71) and the relativistic solutions (Eq. 2.39.) Obviously, since the MSP spin does not influence the photon propagation, $\delta_\gamma(\Delta_{\rm prop}) = 0$ (however, the MSP spin does generally influence the orbital evolution of the pulsar which in turn will influence the evolution of $\Delta_{\rm R}$. We will return to this point later.) We consider the orbit of a Galactic centre MSP with semi-major axis $a_* = 825 r_g$, $\omega = \Omega = \pi/4$ and $\iota = 20^\circ$ at eccentricities $e = 0.7, 0.8, 0.9$. The spin parameter is $a = +0.6$. Since the observers image plane is in the positive x-direction, this corresponds to an inclination with respect to the observer of $i = 76^\circ$. The propagation delay, along with the associated orbital trajectory, for this system is shown in Fig. 5.2. Since generally pulsar timing can only detect variations in the light travel time, rather than the absolute travel time itself, we normalise $\Delta_{\rm prop}$ with respect to its initial value. The propagation delay evolves on the scale of hours over the course of the orbit, with more eccentric orbits having a slightly greater magnitude of variation. The error in the PK solutions at first and second order compared to the Schwarzschild relativistic solutions, $\delta_{\alpha,i}(\Delta_{\rm prop})$ evolve over the orbit and reaches an extrema when the pulsar is on the far side of the BH. In this case the photon tray traverses a more strongly curved spacetime and is subject to a greater degree of strong-field time dilation and gravitational lensing, both of which drive the PK solutions away from the relativistic solution. For this orientation, more eccentric orbits have greater extrema than less eccentric orbits since their far side points are at shorter orbital radii. The additional propagation delays induced by the BH spin, $\delta_\beta(\Delta_{\rm prop})$, follow a similar general evolution to $\delta_\alpha(\Delta_{\rm prop})$, with greatest variations found for eccentric orbits on the far side of the BH. Variations here are of the order ~ 0.1 s. Whilst for both $\delta_\alpha(\Delta_{\rm prop})$ and $\delta_\beta(\Delta_{\rm prop})$ are greatest for far side sample points, the error remains significant over the entire orbit, especially given the high timing precision of pulsar timing $(10 - 100$ ns).

Clearly the exact propagation time is going to depend upon the ray path. To first order in the PK solution rays travel in straight lines. Such an approximation may be appropriate for longer orbits and emission on the near side of the BH, but for more compact orbits where the pulsar is on the far side of the BH it is also important to account for the gravitational lensing which is naturally included by the relativistic solution. Lensing introduces two additional timing delays with the PK framework. The first is a geometrical delay Δ_{geo} due to the different spatial path traversed given by Rafikov & Lai (2006),

$$\Delta_{\text{geo}} = 2\left(\frac{\Delta R_{\pm}}{R_E}\right) \ , \tag{5.72}$$

where R_E is the Einstein radius and $\Delta R_{\pm} = |R_{\pm} - R_s|$ for image position $R_{\pm}$ and 'flat space position' R_s (see Rafikov & Lai 2006, for a further explanation of these terms). The second delay is due to a correction to the Shapiro delay since the lensed ray traverses a different gravitational potential than the unlensed ray. Indeed, for edge on orbits Eq. 5.35 diverges when $f = \pi/2$ since this ray path involves going directly through the BH singularity, which is evidently unphysical. At first order within the PK framework, the Shapiro delay is modified due to lensing as (Rafikov & Lai 2006),

$$\Delta_{\text{S,L}} = 2\ln\left[\frac{a_*(1-e^2)}{\sqrt{r_{||}^2 + R_{\pm}^2} - r_{||}}\right] \ , \tag{5.73}$$

where $r_{||}$ is the orbital separation projected along the line of sight. The net propagation delay then becomes

$$\Delta_{\text{prop}} = \Delta_{\text{R}} + \Delta_{\text{S,L}} + \Delta_{\text{geo}} \ . \tag{5.74}$$

The linear weak field description of lensing involves decomposing the ray trajectory into two parts. The first is the radial ray which travels from the image plane to the lensing plane. Upon reaching the lensing plane the ray is deflected and travels again in a straight line towards the emitter (see Fig. 5.3). The total propagation time is then the sum of the propagation time along these two linear trajectories. We can therefore the describe the PK time propagation delay taking in account lensing by evaluating Eq. 5.71 along the two relevant trajectories and taking the sum. The effect of the inclusion of PK lensing corrections on $\delta_{\alpha,i}(\Delta_{\text{prop}})$is shown in Figs. 5.2 and 5.4. The inclusion of lensing corrections significantly improves the PK solution, with the peak magnitude

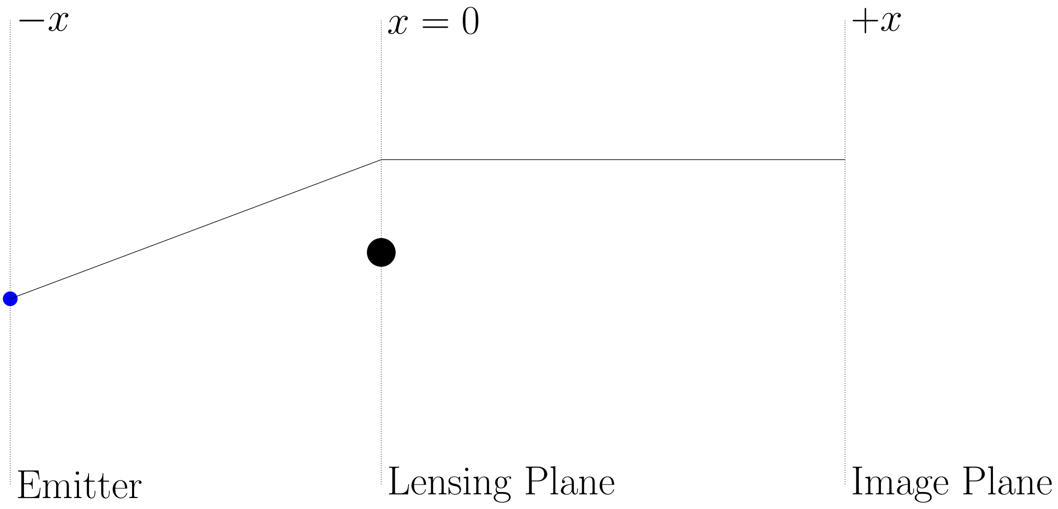

Fig. 5.3: Schematic of weak-field, linear gravitational lensing.

of $\delta_\alpha(\Delta_{\rm prop})$ reducing to $\mathcal{O}(0.1)$ for both the first and second order solutions, with the second order solution generally exhibiting lower magnitudes than the first. However, this error is still far in excess of the timing precisions that can be achieved via pulsar timing. It is also worth noting that whilst lensing is most prominent for points on the far side of the BH with respect to the observer, due to the BH spin the rays are deflected from their Minkowski straight line geodesics even on the near side, if sufficiently close to the BH.

As mentioned previously, the MSP spin will generally couple to the background spacetime and so influence the orbital evolution, driving it away from geodesic motion. These positional variations will in turn influence the evolution of the Roemer delay. The Roemer delay is generally given as,

$$\Delta_{\rm R}(\tau) = \hat{\boldsymbol{O}} \cdot \boldsymbol{x}(\tau) \tag{5.75}$$

where $\hat{\boldsymbol{O}}$ is the position unit vector of the observer and $\boldsymbol{x}(\tau)$ the location of the orbiting pulsar. In this way positional variations will imprint on the pulsar timing residuals. The difference in the Roemer delay between a non-spinning and a spinning pulsar, i.e. $\delta_\gamma(\Delta_{\rm R})$, is presented in Fig. 5.5. Generally the MSP spin-curvature coupling manifests in two ways: an additional component perpendicular to the orbital plane (e.g. Singh et al. 2014) and also a contribution to the precession of periastron (which is itself a PK parameter. See also e.g. Li et al. 2019). We consider the same eccentric systems and observer

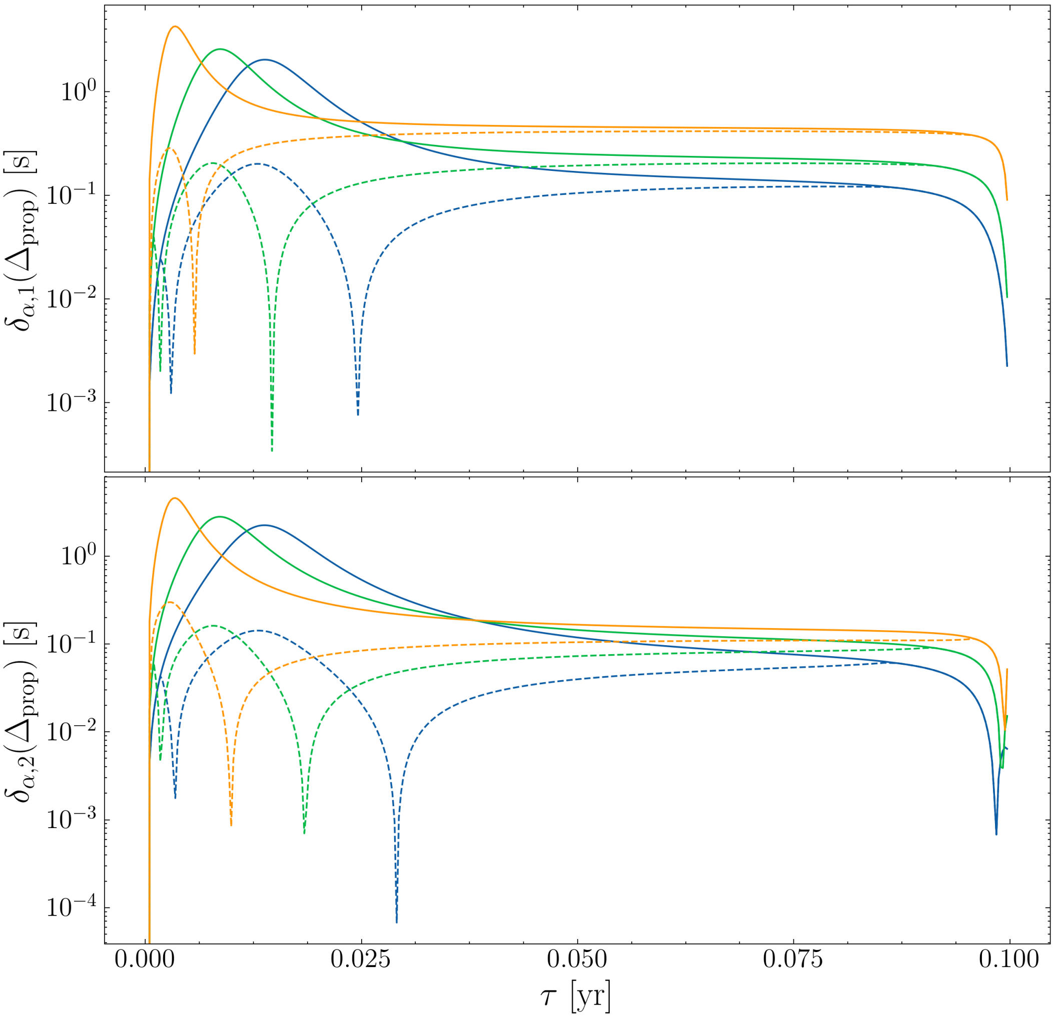

Fig. 5.4: Enhanced view of the two middle right panels of Fig. 5.2. Error between the PK and Schwarzschild propagation delays $\delta_{\alpha,i}(\Delta_{\rm prop})$, for each of the eccentric systems when lensing corrections are included (dashed lines) and without. Lensing significantly improves the solution, but marked residuals remain. The typical magnitude of $\delta_{\alpha,2}(\Delta_{\rm prop})$ are less than $\delta_{\alpha,1}(\Delta_{\rm prop})$, but even in the case where we consider the second order solution with lensing, significant timing discrepancies are present.

orientation as used previously ($a_* = 825 r_g, i = 76^\circ$ etc.). For these orbital parameters, $\delta_\gamma(\Delta_{\rm R})$ varies periodically, with rapid, large magnitude variations as the pulsar goes through periapsis. For the most eccentric systems ($e = 0.9$) the extrema of $\delta_\gamma(\Delta_{\rm R})$ are of magnitude a few μs, whilst for less eccentric systems the magnitude of these variations drops markedly (e.g. $|\delta_\gamma(\Delta_{\rm R})| \sim 0.1 \mu$s for $e = 0.8$.) This is on account of more eccentric orbits probing a stronger gravitational field as they pass through periapsis and so the curvature coupling with the MSP spin becomes more significant. Whilst the magnitude of these spin-induced variations are much smaller than the lower order ($\delta_{\alpha,\beta}$) differences there are a few points to consider. Firstly, for the most eccentric orbits these variations are within the timing precision of the next generation of radio facilities. Consequently, in order to use these systems for precision parameter estimation of the central BH such small variation may need to be included in the residuals timing solution. Moreover, whilst we have focused on systems with $P \sim 0.1$ years, for more compact orbits or different observer orientations this spin induced variation will be more pronounced. For stronger gravitational fields - precisely the region in which we wish to test GR - such effects will be more significant. Since the error between the two solutions grows with time upon repeated periapsis passages, systems which are observed over longer timescales may also need to correct for this effect.

5.3 Discussion

Estimates based on PK frameworks suggest that via pulsar timing the parameters such as the mass and spin of the BH at the Galactic centre can be determined to a precision $\sim 10^{-5} - 10^{-3}$ (Liu et al. 2012; Psaltis et al. 2016). Some authors consider consistent timing campaigns (Liu et al. 2012) whilst others (Psaltis et al. 2016) consider instead dense observations close to periapsis. Both approaches have merit, however observations close to periapsis seems highly desirable for the purposes of minimizing external perturbations (Merritt et al. 2010) and maximizing the value of the gravitational potential ϵ which can be investigated.

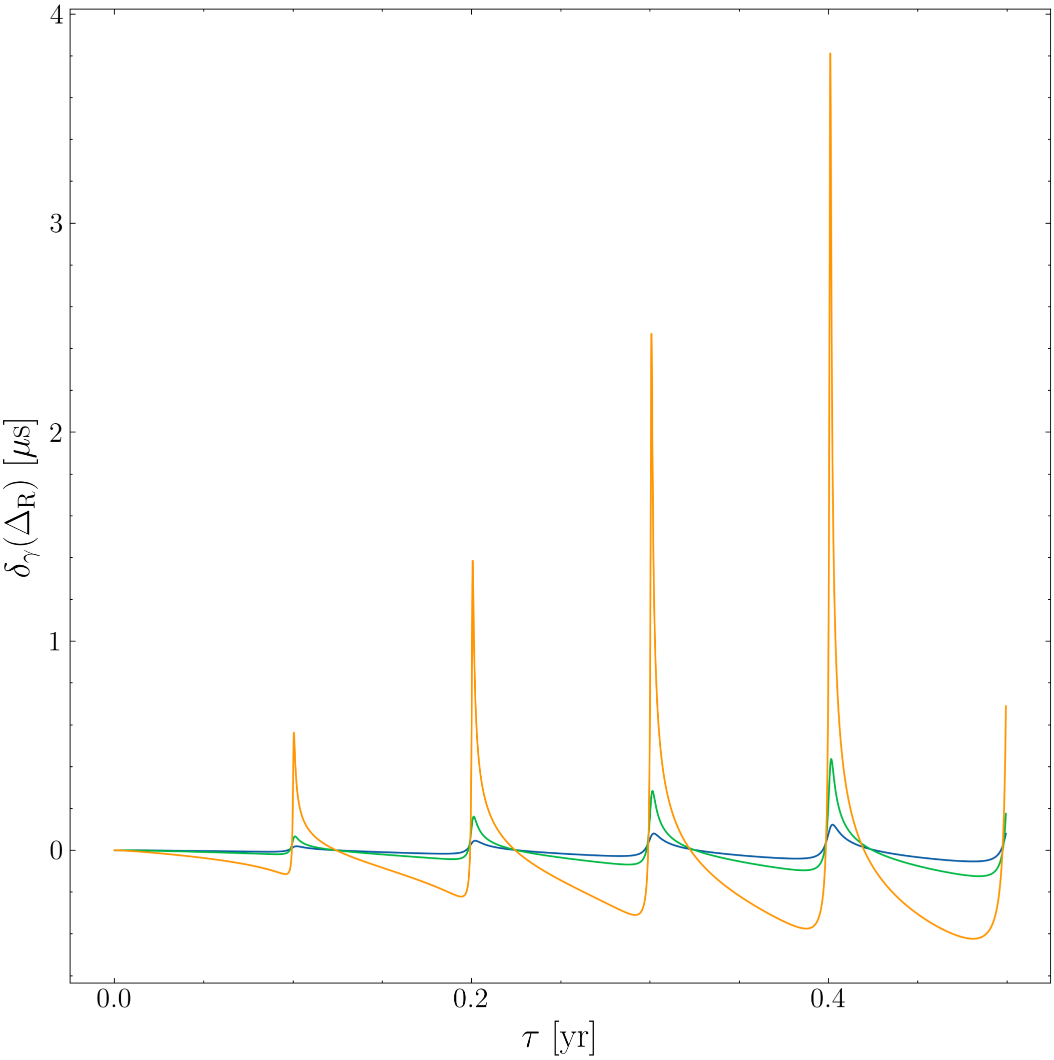

Fig. 5.5: Error in the Roemer delay between the MPD and Kerr solutions. We consider a Galactic centre MSP with $a_* = 825 r_g$, $i = 76°$, $\omega = \Omega = \pi/4$ and eccentricities $e = 0.7, 0.8, 0.9$ (blue, green, orange lines respectively). Rapid, large magnitude variations are observed as the pulsar goes through periapsis, with the most significant discrepancies - $\mathcal{O}(\mu\mathrm{s})$ - for the most eccentric systems which probe the strongest gravitational fields.

However, our results highlight that these regions that are most scientifically attractive (c.f. tests of astrophysics and fundamental physics) are precisely the regions where the accuracy and appropriateness of the PK framework is lacking. Any pulsar timing model is fundamentally a mapping between the proper time of the pulsar and the time recorded by the observer, $\tau \rightarrow t$. In these regions of high spacetime curvature, the convolution of spin, relativistic and gravitational effects become more prominent and the naive PK framework fails to account for these higher-order effects and the $\tau \rightarrow t$ mapping does not hold. In particular:

- For a $P = 0.1$ year orbit at the Galactic centre, the error in the Einstein delay according to the PK framework is of the order $\sim$ 10s of seconds compared to the relativistic (Schwarzschild) solution. This error grows with time; after 5 orbits with eccentricity $e = 0.9$, $\delta_{\alpha}(\Delta_{\rm E}) = 55$s. Higher order corrections in the time delay due to the BH spin and the pulsar spin are of the order 10^{-1} and 10^{-4} seconds respectively (see Fig. 5.1). The most severe errors are seen at periapsis when the pulsar is moving fastest and the gravitational potential is strongest.

- The propagation delay for a similar eccentric Galactic centre system, inclined with respect to the observer at $i = 76°$ varies on the order of hours over the course of a single orbit. The error in the PK solution is $\delta_{\alpha}(\Delta_{\rm prop}) \sim \mathcal{O}(s)$ whilst effects due to the BH spin introduce errors $\delta_{\alpha}(\Delta_{\rm prop}) \sim \mathcal{O}(0.1s)$ (Fig. 5.2). For this particular orbital configuration, these errors are most drastic for the more eccentric orbits and the largest magnitude variations are seen when the pulsar is on the far side of the BH; in this case the photon ray must traverse the most strongly curved spacetime.

- The introduction of first order linear lensing corrections which account for the geometrical time delay $\Delta_{\rm geo}$ and the modified Shapiro delay $\Delta_{\rm S,L}$ dramatically improves the PK propagation solution, reducing $\delta_{\alpha}(\Delta_{\rm prop})$ to $\sim \mathcal{O}(0.1s)$ (see Fig. 5.4) . However, this error is still much greater than typical timing precisions enjoyed by pulsar radio timing. Consequently higher order corrections will be needed for strong field systems if viewed from a sufficiently ‘edge on’ angle. Even for emission on the near side of the BH, the BH spin will cause an additional lensing effect.

- The coupling of the pulsar spin to the background spacetime will cause the orbital dynamics to divert from that of pure geodesic motion. Such a variation on the coordinate variables will manifest in a change in the evolution of the Roemer delay. This effect is small, with $\delta_\gamma(\Delta_{\rm R}) \sim 1\mu$s for a system with $P = 0.1$ years and $e = 0.9$, observer at $i = 76°$, but may still be significant over longer timescales, for more compact systems, or dense observations close to periapsis.

Evidently in the gravitational strong-field there is significant discrepancy between the PK and GR solutions across all of the parameters considered in this work. The timing delay according to the PK solution disagrees with the GR solution by at least a few μs in all parameters, up to discrepancies as larges as a few s and naturally this error is more severe as relativistic effects become more prominent; i.e. for highly spinning BHs, measurements near periapsis or rays which traverse a spacetime which is highly curved. Consequently, whilst the quoted precisions with which the BH parameters can be determined via pulsar timing (e.g. BH mass to precision 10^{-5}) may be achievable, this work suggests that in EMRB systems which probe the strong-field, higher-order relativistic effects should be included in a complete timing model to accurately determine the prospects of using PSRs to test GR. Indeed, the EMRBs discussed in this work are the progenitors of the key LISA target Extreme Mass Ratio Inspirals (EMRIs), where weak-field methods are recognized as being entirely inadequate (Barack & Pound 2019).

The disagreement between the PK and GR solutions in strong-field regimes motivates the necessity of a consistent, relativistic,frequency-dependent timing model (e.g. Kimpson et al. 2019a). In developing this work, it would be highly desirable to use such a strong-field PSR-timing model to generate an accurate, relativistic, set of mock data. The ToAs generated by this relativistic model can then be used for a consistent covariance analysis (e.g. Liu et al. 2012), fed into a pulsar timing software package (e.g. TEMPO2, Hobbs et al. 2006), allowing the current pulsar data analysis algorithms to be assessed in the strong-field (c.f. lack of detections in the Galactic Centre) and allow for quantitative estimates on the precision to which the BH parameters can be recovered. We defer this study for future work. In addition, whilst these results are indicative of the appropriateness or otherwise of a PK timing model for MSP-E/IMRBs, for a more definitive work it is necessary to consider a consistent phase-connected solution. We have also not thoroughly explored the whole parameter space instead just considering some typical example system; determining for what sort of set of orbital parameters relativistic effects start to influence the timing solution would also be a worthwhile enterprise.

Beyond the failure of the PK framework in the strong-field, there also exist additional corrections that will influence the photon ToA and pulse profile, such as spatial and temporal dispersion (Kimpson et al. 2019b) precession of the spin axis and relativistic aberration. Being able to accurately model the photon $t-\nu$ signal in relativistic regimes is essential to maximize the scientific return of the detection of pulsar systems (including conincident multimessenger detections, e.g. Kimpson et al. 2020a), realistically estimate the scientific prospects (e.g. to what precision can we hope to determine the BH mass?) and compare pulsar timing as a GR probe with complementary methods (e.g. Event Horizon telescope, stellar orbits, gravitational wave astronomy). It is worth noting however that the strengths of the PK method lie beyond the timing accuracy; the advantage of PK is their computational simplicity and the straightforward way in which deviations from GR can be incorporated. The numerical methods discussed in this work are naturally much more computationally demanding than the analytical PK solutions, however it is conceptually straightforward to develop the numerical approach beyond the GR solution and include beyond GR effects via the use of some alternative (non-Kerr) metric e.g. the quasi-Kerr metric of Glampedakis & Babak (2006) and used in e.g. Kimpson et al. (2020b).

In addition to correctly modelling strong-field PSR-EMRBs, another important consideration is the best environment to attempt to use PSRs to undertake precision, strong-field GR tests. Whilst much of the cited literature focuses on the Sgr A* BH, owing to its high mass-to-distance ratio, observations of the Galactic centre are made all the more difficult since it is not a clean environment. Material along the line of sight can cause scattering which results in temporal smearing of the pulse profile, whilst ionized gas can decrease the received flux density. Indeed, since the GC pulsar population is expected to be dominated by MSPs, such environmental effects mean that previous GC searches have been insensitive to the pulsar population (Macquart & Kanekar 2015; Rajwade et al. 2017). Perhaps unsurprisingly then, only one pulsar - the magnetar PSR J1745-29 (Kennea et al. 2013) - has been detected within 10' of Sgr A*.

Whilst the GC remains an important target, potentially more fruitful hunting grounds are globular clusters and dwarf elliptical galaxies. These systems have exceptionally high stellar densities - up to 10^6 stars per cubic parsec in the central regions (Freire 2013). Due to the effects of mass segregation and dynamical friction, heavy objects like neutron stars are expected to sink to the centre of these stellar clusters. It is observed that per unit mass there are up to 10^3 more pulsars in globular clusters than in the Galactic disk (Freire 2013). Millisecond pulsars are thought to evolve from low mass X-ray binaries and globular clusters are known hosts of abundant LMXB populations. Consequently MSPs comprise a significant fraction of the globular cluster pulsar population (Camilo & Rasio 2005; Ransom 2008). Some notable clusters are Terzan 5 with 37 pulsars (Cadelano et al. 2018a) and 47 Tucanae which is known to host 25 pulsars, all of which have spin periods less than 8ms (Freire et al. 2017). Observations of X-ray emission from globular clusters led to the first suggestion that globular clusters could host central BHs of intermediate mass ($10^3 - 10^5 M_\odot$ Silk & Arons 1975; Colbert & Miller 2006; Lin et al. 2018). Moreover, extrapolation to the low-mass end of the "M-σ

relation" (Ferrarese & Merritt 2000; Gebhardt et al. 2000) also suggests that globular clusters should host IMBHs (Sadoun & Colin 2012; Graham & Soria 2019). Suggestive evidence for IMBHs is put forth via observational radiative accretion signatures (Ulvestad et al. 2007, e.g.) and stellar kinematics (e.g. Gebhardt et al. 2002; van der Marel & Anderson 2010; Feldmeier et al. 2013), but other studies dispute this as evidence for IMBH (e.g. Miller-Jones et al. 2012; Baumgardt 2017). For a complete review and discussion on the current observational evidence for IMBH, see Mezcua (2017).

If globular clusters and dwarf galaxies do host IMBH, then the large stellar densities and expected pulsar population make these ideal, clean environments to search for PSR-BH systems from the perspectives of testing GR. As discussed, there is expected to be a large fraction of MSP which are highly desirable from the perspective of precision astronomy, given their enhanced spin period (i.e. the clock is more precise) and their long term stability (i.e. the clock is more accurate) owing to the lack of glitches - indeed the canonical pulsars are dominated by timing noise and rotational instability, whilst MSP timing models are white noise dominated (Verbiest et al. 2008) and so stand most to gain from the increased sensitivity of the next generation of radio telescopes. Moreover, whilst pulsars in globular clusters are more distant and so more faint, they are also localised in central regions, making it easier for deep radio observations, whilst the increased sensitivity of the next generation of radio telescopes will make it easier to detect their flux.

5.4 Conclusion

In summary, we have calculated the Einstein delay and the propagation delays for a typical MSP-E/IMRB system using a fully general relativistic method which accounts for both strong-field curvature effects on the photon spacetime trajectory and the impact of extended spinning body dynamics on the pulsar orbital motion. We have then compared this with the the linear, weak-field PK solution which is typically used in pulsar studies. We have shown that there exists a significant discrepancy between the post-Keplerian timing delays and the fully general relativistic solutions in strong-field regimes of gravity. Accounting for this discrepancy is essential for both detecting MSP-E/IMRB systems and using them as probes of strong-field GR.

Chapter 6

Gravitational Radiation from Pulsar Systems

We have seen how there is a huge scientific return from electromagnetic radio observations of an MSP-E/IMRB. An alternative avenue for investigating these systems is through gravitational radiation. The measurement of this radiation provides a complementary channel for precision tests of GR and astrophysics. Due to the time variation of the mass quadrupole moment of the gravitational field, a compact object in an elliptical orbit around a massive BH will emit gravitational radiation, which in turn causes the orbit to slowly decay and circularize (Peters 1964). These systems which continuously emit gravitational radiation and have an associated inspiral motion are know as Extreme Mass Ratio Inspirals (EMRIs, Babak et al. 2017; Berry et al. 2019). EMRIs are a major class of target for the future observations by the next generation of space-based gravitational wave detectors such as the Laser Interferometer Space Antenna (LISA, Amaro-Seoane et al. 2007). EMRIs are particularly prized scientific targets for the same reasons as MSP-EMRBs; precision measurements in the strong-field regime, although in addition EMRIs inhabit a highly dynamical spacetime.

The typical orbital periods considered for MSP-EMRBs (~ 0.1 years) are not sufficiently short to continuously radiate gravitational radiation in the LISA frequency band ($\sim$ mHz). Moreover, whilst there is a large degree of uncertainty in the expected EMRI rate - with a variance over 3 orders of magnitude from a few per year up to many 1000s (Babak et al. 2017) - EMRIs which are detected by LISA are expected to primarily consist of systems in which the smaller compact object is a BH rather than a neutron star. This is simply due to BHs typically having larger masses than NSs, which leads to both stronger GW signals and an increased effectiveness of mass segregation during EMRI formation, although the expected rate of NS in EMRIS can be significantly increased should they form in situ, close to the central massive black hole (Aharon & Perets 2016). Consequently whilst a coincident, multimessenger, electromagnetic and gravitational detection of an 'MSP-EMRI' is possible, it remains unlikely. However, a MSP in an E/IMRB will emit a burst of radiation as it passes through periapsis (Rubbo et al. 2006; Yunes et al. 2008; Berry & Gair 2013b). The coincident observation of the continuous electromagnetic MSP timing signal and the burst gravitational radiation from a MSP-EMRB offers a unique apparatus for multimessenger astronomy in strong-field environments. In addition, the continuous pulsar electromagnetic signal may aid in the detection of the accompanying gravitational radiation. Moreover, the burst gravitational radiation may in turn influence the received radio timing signal. Whilst burst waveforms are typically considered less informative than continuous EMRI waveforms, a multimessenger observation of a pulsar and GW burst may compound the potential scientific return.

In this work we explore the potential for the detection of burst gravitational radiation from typical MSP-EMRBs, of the sort typically considered for precision tests of strong-field GR (e.g. Liu et al. 2012). We calculate the gravitational burst waveforms and signal-to-noise ratio (SNR) of a MSP-EMRB for generic orbits (i.e not restricted to e.g. equatorial plane, circular motion, spin-alignment). Firstly the waveforms are constructed via the semi-relativistic numerical kludge (NK) approach (Babak et al. 2007; Berry & Gair 2013b) where we account for the relevant spin-spin, spin-orbit and spin-curvature couplings on the orbit via the described MPD framework. With the time-domain waveforms determined, it is then possible to calculate the burst SNR via Fourier methods from a MSP-EMRB, and explore the prospects for their detection and the synergy between electromagnetic and gravitational wave observations. In addition, the GW emission might have an impact on the pulsar timing signal and so we explore the implications for the detection and modelling of MSP-EMRBs.

This chapter is organized as follows.In Section 6.1 we then review the methods for mapping the orbital motion to the gravitational waveforms and determine the waveforms for typical MSP-EMRBs that are used as radio timing GR probes. In Section 6.2 we go on calculate the burst SNR of these systems for the most recent LISA configuration and noise model. Discussion and concluding remarks are made in Section 6.3.

6.1 Constructing the Waveforms

The generation of sufficiently accurate waveforms from compact objects around a massive BH companion is currently a major enterprise in order to realise the scientific potential of LISA-EMRIs (e.g. Chua & Gair 2015; van de Meent 2017; Pound 2017a; Barack & Pound 2019). Via perturbation theory in the extreme mass ratio limit, waveforms accurate to first-order can be calculated accounting for the self-force or back-reaction effects of the GW radiation on the orbit. In order to accurately track the orbit over the large number of cycles that are expected to be observable with ERMIs ($\sim 10^4$), calculations accurate to second order are required and work in this area is ongoing (Pound 2017b; Moxon & Flanagan 2018). Given both the theoretical complexity and computational cost of calculating consistent waveforms in this way, alternative 'fast- yet-accurate' models have been developed by a number of authors (e.g. Barack & Cutler 2004; Babak et al. 2007; Chua et al. 2017). For our purposes, we adopt the Numerical Kludge (NK) approach of Babak et al. (2007). The GW 'recipe' within the NK framework has two primary ingredients. First the orbital trajectory of the object is specified. Typically the motion is described as that of a test body following a geodesic on a Kerr background spacetime.

However, as discussed this neglects the extended nature of real astrophysical pulsars and the associated spin couplings. For this work we go beyond the point-particle geodesic approximation and consider generic orbits of extended objects around a Kerr BH, specifying the orbital trajectory via the MPD equations outlined in the preceding section which properly account for the dynamical spin effects. Once the orbital motion has been specified, the Boyer-Lindquist coordinates of the background curved spacetime are mapped to flat-space spherical polar coordinates. The waveform can then be constructed from the well-known expressions for gravitational waves from flat-space trajectories (e.g. Misner et al. 1973).

Naturally the NK approach is not self-consistent; the gravitational radiation is generated assuming a flat background spacetime whilst the orbital motion instead assumes a curved Kerr geometry (with, in our case, associated relativistic spin couplings). However it does exhibit a remarkable agreement with the more computationally expensive perturbative methods. Specifically, the overlap between the NK and the more intensive, accurate waveforms is $> 95\%$ across most of the parameter space. Babak et al. (2007) offer the rule of thumb that NK waveforms are appropriate as long as the periapsis distance is greater than $\sim 5r_g$. Since we are concerned with pulsars on typical orbits that will be used for radio timing tests of GR, we will exclusively deal with orbits $r_p > 5r_g$. However, it is worth noting that this rule of thumb was considered for orbits which continually emit in the LISA frequency range and so need to be tracked over a large number of cycles. For single bursting passages it seems reasonable that the NK approach could be pushed below this limit.The numerical kludge approach is also applied to eccentric orbits in Berry & Gair (2013b).

6.1.1 Time domain waveforms

Within the NK framework, gravitational waves are described as a perturbation ($h_{\mu\nu}$) on a background flat (Minkowski, $\eta_{\mu\nu}$) spacetime,

$$g_{\mu\nu} = \eta_{\mu\nu} + h_{\mu\nu} \tag{6.1}$$

The trace-reversed metric perturbation is in turn given by,

$$\bar{h}^{\mu\nu} \equiv h^{\mu\nu} - \frac{1}{2}\eta^{\mu\nu}\eta^{\mu\nu}h_{\mu\nu} \; . \tag{6.2}$$

Within the Lorentz or Hilbert gauge ($\bar{h}^{\mu\alpha}_{,\alpha} = 0$) we then have the Einsteinian wave-equation,

$$\Box\bar{h}^{\mu\nu} = -16\pi T^{\mu\nu} \; , \tag{6.3}$$

with 3-space solution,

$$\bar{h}^{jk}(t, \mathbf{x}) = 4\int \frac{T^{jk}(t - |\mathbf{x}-\mathbf{x}'|, \mathbf{x}')}{|\mathbf{x}-\mathbf{x}'|} d^3x' \; , \tag{6.4}$$

where $(t, \mathbf{x})$ is the location of the observer and $\mathbf{x}'$ an integration variable (Misner et al. 1973). It can be shown that to octupole order that (Bekenstein 1973; Press 1977)

$$\bar{h}^{jk} = \frac{2}{r}\left[\ddot{I}^{jk} - 2n_i\ddot{S}^{ijk} + n_i\dddot{M}^{ijk}\right] \; , \tag{6.5}$$

where n_i is the radial unit vector pointing to the observer and I^{jk}, S^{ijk}, M^{ijk} are the mass quadrupole, current quadrupole and mass octupole respectively, given in the flat-spacetime approximation as

$$I^{jk} = \mu x_p'^{j} x_p'^{k} \; , \tag{6.6}$$

$$S^{ijk} = v^i I^{jk} \; , \tag{6.7}$$

$$M^{ijk} = x_p'^{i} I^{jk} \; , \tag{6.8}$$

where $(t_p, \mathbf{x}_p)$ is the location of the orbiting body and $v^i \equiv dx'^i/dt'_p$. In order to calculate the second and third derivatives of the multipole moments necessary for calculating Eq. 6.5 we use a numerical finite difference scheme (Fornberg 1988).

If we take the transverse traceless (TT) gauge ($h_{\mu 0} = 0, h_{ij,j} = 0,\; h_{kk} = 0$) then the waveform received by the observer is given as,

$$h^{jk}_{TT} = \frac{1}{2}\begin{pmatrix} 0 & 0 & 0 \\ 0 & h_+ & h_\times \\ 0 & h_\times & -h_+ \end{pmatrix} \tag{6.9}$$

where h_+ and $h_\times$ are the 'plus' and 'cross' polarisations where,

$$h_+ = h^{\Theta\Theta} - h^{\Phi\Phi} \ , \tag{6.10}$$

$$h_\times = 2h^{\Theta\Phi} \ , \tag{6.11}$$

and,

$$\begin{aligned}
h^{\Theta\Theta} &= \cos^2\Theta \left[h^{xx}\cos^2\Phi h^{xy}\sin 2\Phi + h^{yy}\sin^2\Phi\right] + h^{zz}\sin^2\Theta \\
&\quad - \sin 2\Theta \left[h^{xz}\cos\Phi + h^{yz}\sin\Phi\right] \\
h^{\Phi\Theta} &= \cos\Theta \left[-\frac{1}{2}h^{xx}\sin 2\Phi + h^{xy}\cos 2\Phi + \frac{1}{2}h^{yy}\sin 2\Phi\right] \\
&\quad + \sin\Theta \left[h^{xz}\sin\Phi - h^{yz}\cos\Phi\right] \\
h^{\Phi\Phi} &= h^{xx}\sin^2\Phi - h^{xy}\sin 2\Phi + h^{yy}\cos^2\Phi \ .
\end{aligned}$$

Example burst time-domain waveforms from a pulsar going through periapsis at the Galactic centre are presented in Figure 6.1. Variations in the orbital parameters naturally influence the resultant waveform; e.g. more eccentric orbits have a more localised burst with greater amplitudes whilst for more circular orbits the waveform is more extended. This will have implications for the SNR and detectability of GW bursts from MSP-EMRBs. The target pulsars have typical orbital periods of ~ 0.1 year and so over a year of observation there will be multiple GW bursts as the PSR repeatedly passes through periapsis, as presented in Fig. 6.2. As the observer angle changes, so too does the wave amplitude, particularly for the $h_\times$ mode.

Before proceeding further, as a sanity check it is desirable to compare our numerical kludge waveforms with some accurate, analytical template. For the specific case of circular and equatorial orbits, in the distant limit, it is possible to derive exact analytical expressions for the $h_{+,\times}$ waveforms as,

$$h_+(t,r,\theta,\phi) = 2\frac{\mu}{r}\frac{M}{r_0}(1+\cos^2\theta)\cos[2\omega_0(t-r_*)+2(\phi_0-\phi)] \ , \tag{6.12}$$

$$h_\times(t,r,\theta,\phi) = 4\frac{\mu}{r}\frac{M}{r_0}\cos\theta\sin[2\omega_0(t-r_*)+2(\phi_0-\phi)] \ , \tag{6.13}$$

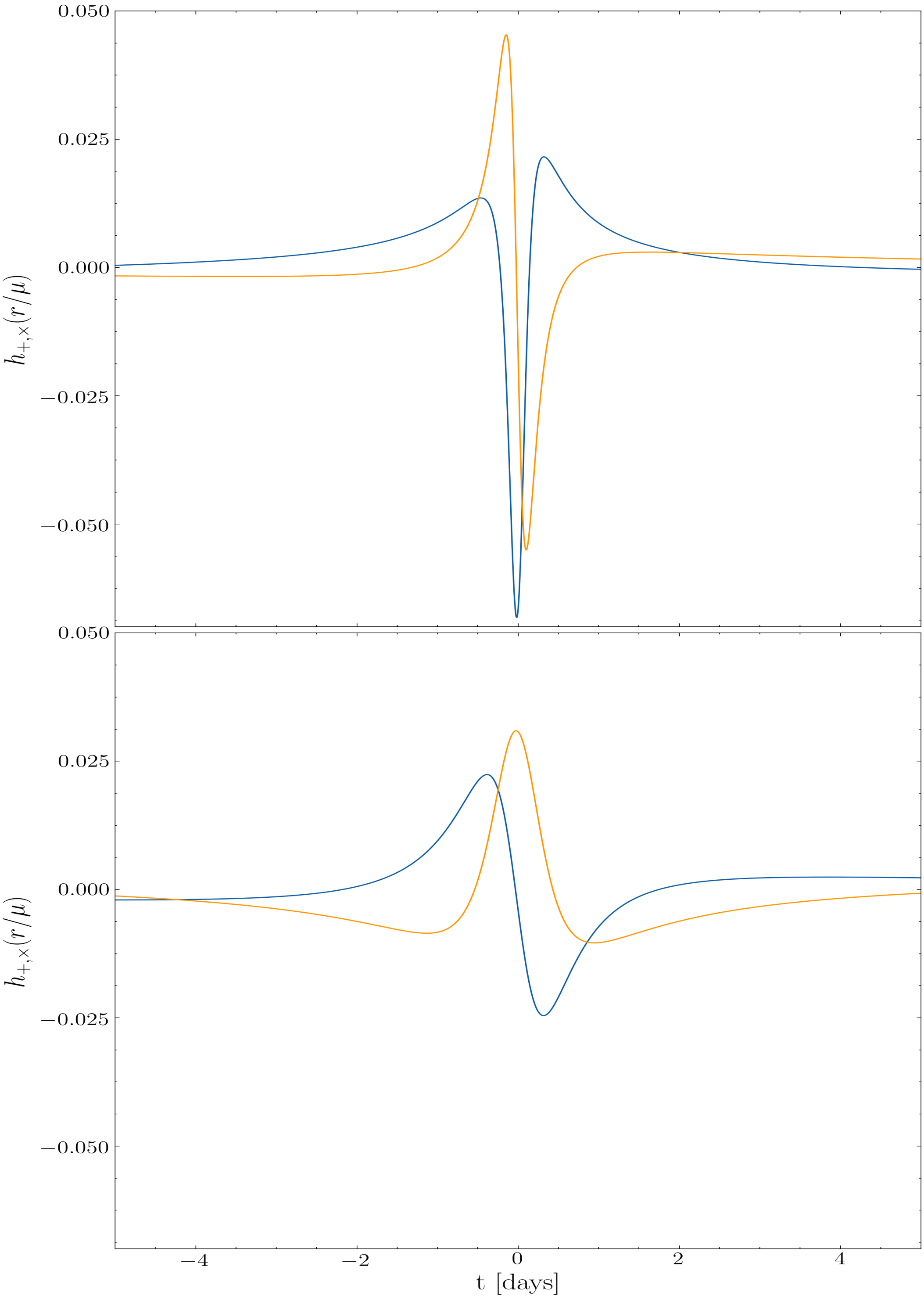

Fig. 6.1: *Top panel:* An example gravitational burst waveform from a $1.4M_\odot$ mass object with orbital parameters $a = 0.6$, $e = 0.9$, $P = 0.1$ years, $\iota = 15$ degrees, $\Omega = 0$ radians and the observer is situated at $\Theta = \Phi = 0$. The BH has mass $4.3 \times 10^6 M_\odot$ and spin parameter $a = 0.6$. Both the $+$ (blue) and $\times$ (orange) polarisations are presented. *Bottom panel:* As top panel but for $a = 0.85$, $e = 0.8$, $\iota = 25$, $\Omega = 3\pi/4$. The observer angles and orbital period are unchanged from the first case. The waveform is more extended compared to the more eccentric case, and the amplitude is reduced.

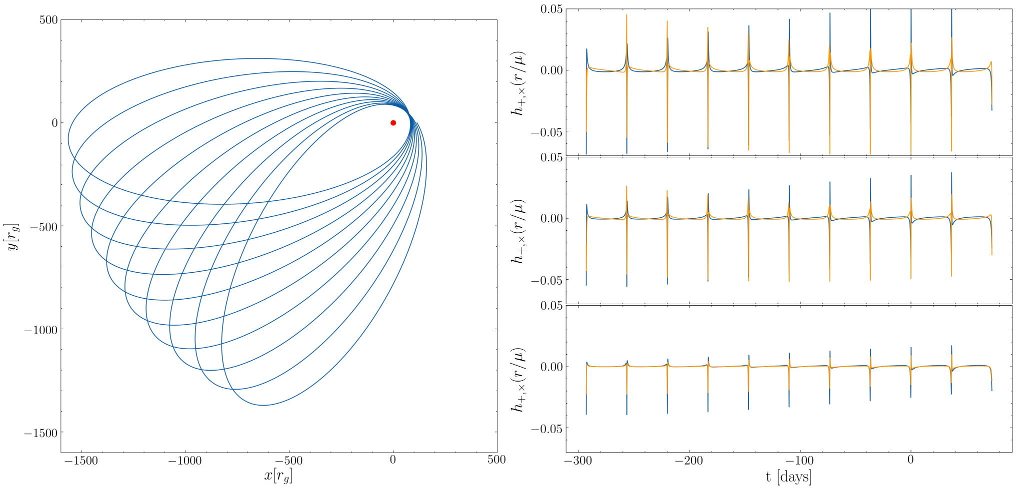

(a) **(b)**

Fig. 6.2: Orbital system of a 1.4 $M_\odot$ mass MSP with orbital parameters $a = 0.6$, $e = 0.9$, $P = 0.1$ years, $\iota = 15$ degrees, $\Omega = 0$ radians (i.e. as in Fig. 6.1), observed over over 10 orbits (i.e. 1 year observation) *(a)* Orbital trajectory in the $x - y$ plane (solid blue line) a around a spinning black hole. Precession of apsis is clearly visible. *(b)* Waveforms for $\Theta = 0, \pi/4, \pi/2$ (top,middle,bottom panels respectively). The waveforms amplitude decreases with increasing Θ. Again, both the + (blue) and × (orange) polarisations are presented.

for tortoise coordinate r_*, orbital angular velocity ω_0 and orbital radius r_0. (Gourgoulhon et al. 2019). Turning 'off' the relativistic spin couplings of the MPD formalism, we can then also describe a circular, equatorial orbital geodesic numerically and generated the associated waveforms. Following Babak et al. (2007); Chua et al. (2017),we define the overlap between two waveforms as,

$$\mathcal{O} = (\hat{a}|\hat{b}) \tag{6.14}$$

where $\hat{a}$ denotes a normalized unit vector such that

$$(\hat{a}|\hat{a}) = (\hat{b}|\hat{b}) = 1 \tag{6.15}$$

and $(\hat{a}|\hat{b})$ denotes an inner product. The inner product is defined with respect to the noise power spectral density $P_n(f)$, which are both described in the next section. Identical waveforms have $\mathcal{O} = 1$ whilst for completely anti-correlated signals $\mathcal{O} = -1$ and $\mathcal{O} = 0$ for orthogonal signals. To check the accuracy of our MPD + NK approach, we take the circular, equatorial orbit with $r = 6r_g$ and $\Theta = 0$ (c.f. Fig 3 of Gourgoulhon et al. 2019) around a non-spinning ($a = 0$) BH and generate the gravitational waveform numerically. The trajectory and waveform are presented in Figure 6.3. To the eye the numerical and analytical waveforms are completely overlaid and cannot be resolved. More quantitatively, in double precision $\mathcal{O} = 1 - 3 \times 10^{-16}$, i.e. the waveforms are identical to machine precision. This is especially encouraging since the $r = 6\,r_g$ regime around the BH is explicitly the strong field regime.

6.2 Signal to Noise ratio

In order to establish whether the burst gravitational radiation from MSP-EMRB system is detectable, it is necessary to calculate the burst signal to noise ratio (SNR), ρ. The general inner product is defined,

$$(a|b) = 2\int_0^\infty \frac{\tilde{a}^*(f)\tilde{b}(f) + \tilde{b}^*(f)\tilde{a}(f)}{P_n(f)} df \ , \tag{6.16}$$

where f is the frequency and $P_n(f)$ is the noise power spectral density (PSD, Cutler & Flanagan 1994). The gravitational wave signal recorded by the detector is a linear combination of the two polarisation modes, corrected for the

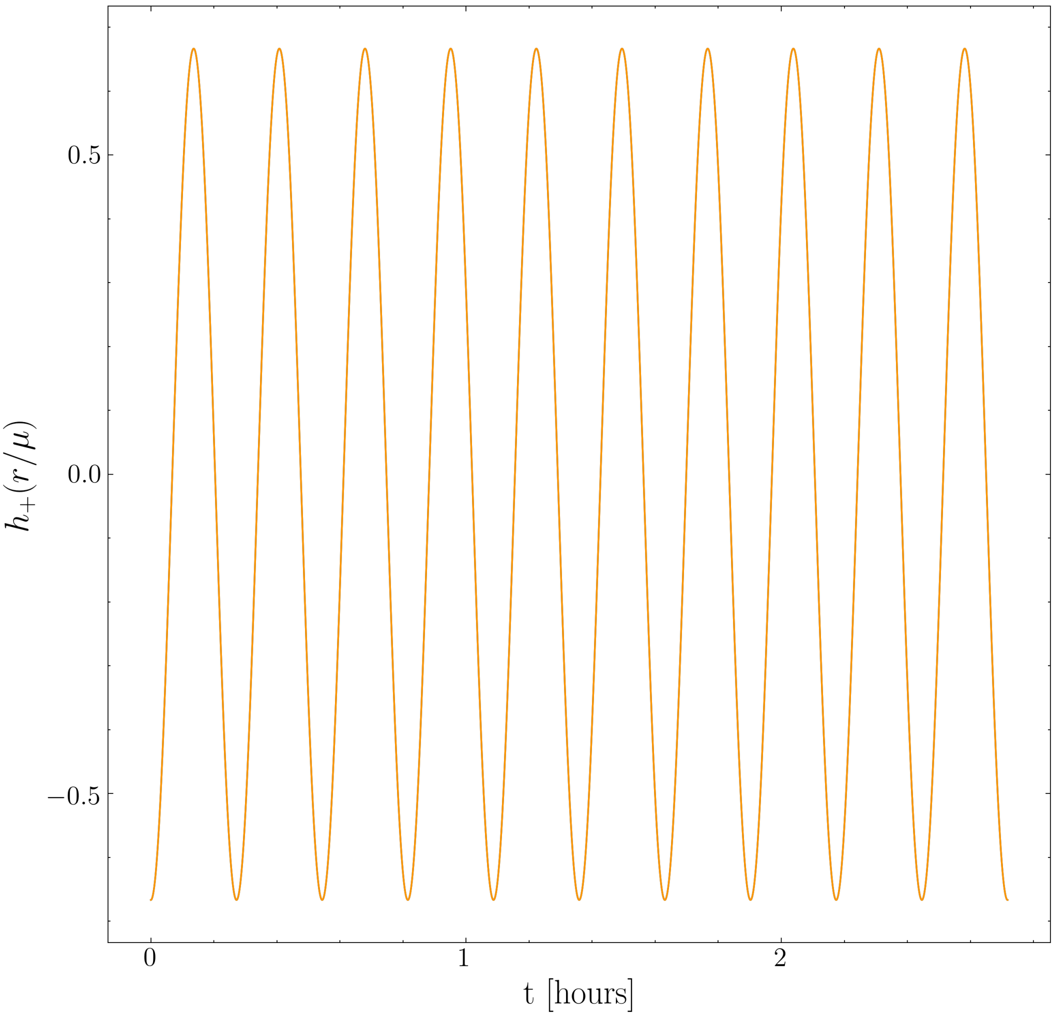

Fig. 6.3: The gravitational waveforms in the time domain from equatorial circular orbital motion ($r = 6r_g$ and $\Theta = 0$) around a non-spinning ($a = 0$, Schwarzchild) BH. Both the NK and analytical solutions are presented, but cannot be resolved due to the high degree of overlap, $\mathcal{O} = 0.9999999999999997$.

the response functions $F_{+,\times}$ of the LISA instrument,

$$\tilde{h}(f) = F_{+}(\Theta, \Phi, \Psi, f)\tilde{h}_{+}(f) + F_{\times}(\Theta, \Phi, \Psi, f)\tilde{h}_{\times}(f) \ , \tag{6.17}$$

where Ψ is the polarisation angle. Denoting the sky and polarisation average as $\langle\rangle$, the averaged GW signal is given by

$$\langle \tilde{h}(f)\tilde{h}^{*}(f) \rangle = \mathcal{R}(f) \left(|\tilde{h}_{+}(f)|^2 + \tilde{h}_{\times}(f)|^2 \right) \ , \tag{6.18}$$

where $\mathcal{R}$ is the instrument response function averaged over the sky (Θ, Φ) and polarization angle (Ψ):

$$\mathcal{R}(f) = \langle F_{+}(f)F_{+}^{*}(f) \rangle = \langle F_{\times}(f)F_{\times}^{*}(f) \rangle \ , \tag{6.19}$$

see Robson et al. (2019) for details. Consequently, the effective SNR used in this work is given by,

$$\rho^2 = 4 \int_{0}^{\infty} \frac{|\tilde{h}_{+}(f)|^2 + |\tilde{h}_{\times}(f)|^2}{S_n(f)} df \ , \tag{6.20}$$

where

$$S_n(f) = \frac{P_n(f)}{\mathcal{R}(f)} \ . \tag{6.21}$$

This definition is also used for the study of GW from Galactic Centre objects in Gourgoulhon et al. (2019).

6.2.1 LISA Noise Model

The instrument response function does not have a closed form expression, but can be well fit as (Robson et al. 2019),

$$\mathcal{R}(f) = \frac{3}{10} \frac{1}{1 + 0.6(f/f_{*})^2} \ , \tag{6.22}$$

and f_{*} is the LISA transfer frequency. However, instead of this form we use the exact response function as given by Robson et al. (2018). The LISA noise PSD is given by

$$P_n(f) = \frac{P_{\rm OMS}}{L^2} + 2(1 + \cos^2(f/f_{*}))\frac{P_{\rm acc}}{(2\pi f)^4 L^2} \ , \tag{6.23}$$

for LISA arm length L. The optical metrology noise,

$$P_{\rm OMS} = (1.5 \times 10^{11} \ {\rm m})^2 \left[1 + \left(\frac{2 \ {\rm mHz}}{f} \right)^4 \right] \ {\rm Hz}^{-1} \ , \tag{6.24}$$

Parameter	Value
α	0.171
β	292
γ	1680
κ	1020
f_k	2.15 mHz
A	$1.8 \times 10^{44}/N$
L	2.5 Gm
f_*	19.09 mHz

Table 6.1: LISA instrumental specifications used in this work. The parameters describing the Galactic confusion noise $S_c(f)$ are taken from Robson et al. (2019) for a 1 year timescale. We set the number of channels to be $N = 2$ and the transfer frequency is defined $f_* = c/(2\pi L)$.

and the acceleration noise is,

$$P_{\rm acc} = (3 \times 10^{-15}\ \mathrm{m\ s^{-2}})^2 \left[1 + \left(\frac{0.4\ \mathrm{mHz}}{f}\right)^2\right] \left[1 + \left(\frac{f}{0.4\ \mathrm{mHz}}\right)^4\right] \mathrm{Hz}^{-1}\ . \tag{6.25}$$

In addition to the instrumental noise, there is also an additional non-stationary noise contribution from the population of compact galactic binaries. This noise can be well described by the parametric function (Cornish & Robson 2017)

$$S_c(f) = A f^{-7/3} e^{-f^{\alpha} + \beta f \sinh(\kappa f)} \left[1 + \tanh(\gamma(f_k - f))\right] \mathrm{Hz}^{-1} \tag{6.26}$$

For our bursting sources we use with fit parameters relevant for observation times less than 6 months, given in Robson et al. (2019) The characteristic strain is defined,

$$h_c^2 = f(S_n(f) + S_c(f)) \tag{6.27}$$

The fundamental LISA instrumental specifications used in this work, along with the relevant fit parameters are summarised in Table 6.1

6.2.2 Windowing

In transforming the GW signal from the time domain to the frequency domain we are necessarily performing a Fourier transform on a finite signal. As a consequence the signal in the frequency space exhibits spectral leakage; extra components in the frequency regime, due to the fact that the time series is not exactly zero valued at the edges of the time interval T over which the Fourier transform takes place.

To counter the effects of spectral leakage we first multiply our GW time series with a window function which tapers the signal to zero outside of the interval T. For this work we adopt the Nuttal window with continuous first derivative (Nuttall 1981):

$$w[n] = a_0 - a_1 \cos\left(\frac{2\pi n}{N}\right) + a_2 \cos\left(\frac{4\pi n}{N}\right) - a_3 \cos\left(\frac{6\pi n}{N}\right) \ , \tag{6.28}$$

where N is the window length, $0 \leq n \leq N$ and $(a_0, a_1, a_2, a_3) = (0.355768, 0.487396, 0.144232, 0.012604)$. Whilst other choices of window function are available, the Nuttal window is both computationally inexpensive to evaluate and exhibits good performance for the parameter space explored in this work (see e.g. Appendix A of Berry & Gair 2013b). The effects of the Nuttal window on the frequency spectra of a particular MSP-BH system are presented in Fig. 6.4

6.2.3 SNR of a Astrophysical MSP-EMRB

We are now in a position to calculate the GW SNR from a typical radio MSP-EMRB. We are concerned here with MSP-EMRB systems which have orbital parameters which render them useful from the perspective of testing strong-field GR via radio PSR timing (e.g. Liu et al. 2012; Psaltis et al. 2016). Typically the principal search area discussed for these systems is the Galactic centre. Whilst this region is an important target, globular clusters and dwarf spheroidal galaxies provide alternative, cleaner search grounds, without the typical problems of the Galactic centre c.f. scattering and dispersion (e.g. Rajwade et al. 2017). With the exception of the Small and Large Magellanic clouds, no extragalactic pulsars have currently been detected (Noori et al.

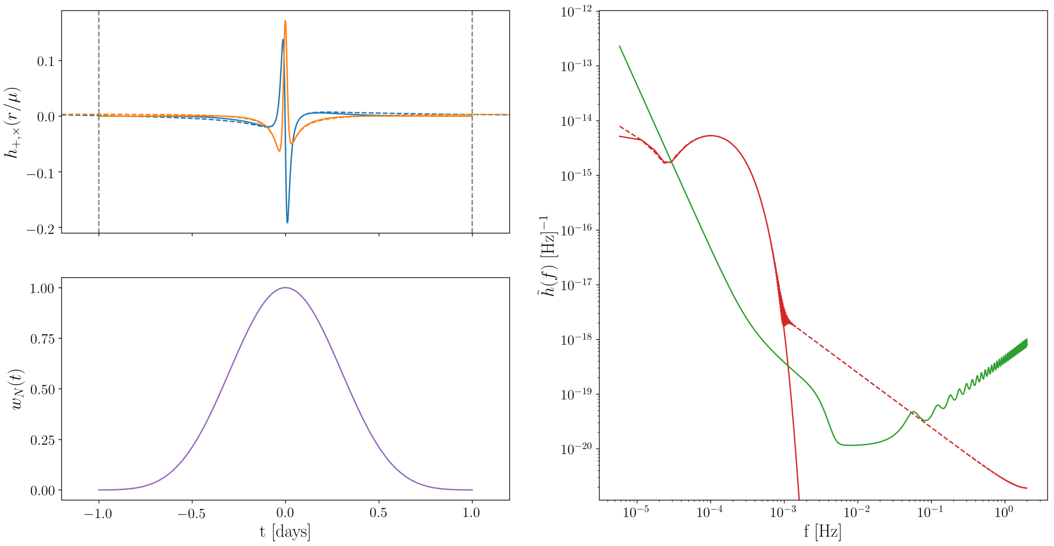

Fig. 6.4: *Left panel, top:* The time domain gravitational waveform from a MSP orbiting the Galactic Centre BH with orbital period $P = 0.01$ years, $e = 0.9$, $\iota = 30\,\text{deg}$, $\Omega = \pi/2$, $a = 0.6$, $\Theta = \Phi = 0$. The '+' (blue) and '×' (orange) polarisations are shown, with no window (coloured, dashed) and after being windowed by the Nuttal function (coloured, solid). The vertical grey dashed lines indicate the width of the Nuttal window. *Left panel, bottom:* The Nuttal window in the time domain. *Right panel:* The LISA noise curve (green) $\sqrt{S_n(f)}$ (not the characteristic strain h_c, Eq. 6.27) as described by Eq. 6.21. The oscillations at higher frequencies result from the confusion noise due to unresolved Galactic binaries. The red lines are the waveform in the frequency domain $\sqrt{\tilde{h}_+(f)^2 + \tilde{h}_\times(f)^2}$ both with windowing (solid) and without (dashed).

2017), nor have we detected MSPs sufficiently close to Sgr A* for appropriate tests of GR. However, with the advanced sensitivity of the next generation of radio telescopes (e.g. FAST/SKA), and the development of more sophisticated search algorithms - appropriate for the strong-field, relativistic environments that these systems inhabit - there is a real possibility to detect and time MSPs both in the Galactic centre and in external regions (e.g. globular clusters). Indeed, it is expected that SKA will be able to detect PSRs of the Local Group (Keane et al. 2015). Moreover, long integrations of a specific target - in contrast to wide field search sky imaging - may also allow these systems to be detected. It is therefore prudent to consider not just the GC, but also nearby globular clusters and dwarf spheroidal galaxies. We now explore the GW SNR from MSP-EMRBs in each of these environments in turn.

Galactic Centre

Typically studies looking at using MSP-EMRBs to test GR have focused on systems at the Galactic centre. Due to the proximity of the central massive BH this target is highly appealing, but for strong-field GR tests there are some requirements on the sort of orbit, as we have discussed in the previous chapters. To avoid external Newtonian perturbations (Merritt et al. 2011) contaminating a 'clean' GR test, it is necessary for consistent timing campaigns to observe orbits with $P < 0.1$ years (Liu et al. 2012). Alternatively, dense timing campaigns close to periapsis (Psaltis et al. 2016) of some longer, eccentric orbit may also mitigate these external perturbations. MSP-EMRBs are expected to retain significant eccentricities since during their formation they are scattered by two body interactions (see e.g. Amaro-Seoane & Preto 2011; Amaro-Seoane 2018, for a comprehensive review of the formation mechanisms of extreme mass ratio binaries) or else supernova kicks (e.g. Bortolas & Mapelli 2019) on to eccentric orbits, and have not had sufficient time to circularize due to GW emission. Eccentric orbits are highly appealing since the periapsis approach scales with the eccentricity as

$$r_p \propto \frac{1}{1+e} \,, \tag{6.29}$$

and so more eccentric orbits will probe stronger gravitational fields, as well as being less susceptible to external Newtonian perturbations. Eccentric orbits are similarly useful for GW bursts, since the GW burst strength scales with the periapsis approach (Berry & Gair 2013b).

For MSP-BH systems at the Galactic centre we set the Galactic centre BH mass to be $4.31 \times 10^6 M_\odot$ and at a distance 8.33 kpc (Gillessen et al. 2009), with spin parameter $a = 0.6$. The spectra of 3 Galactic centre MSP-EMRB systems with orbital periods $P = 0.01, 0.05, 0.1$ years and $e = 0.9$ are presented in Fig. 6.5. The MSP mass is set to be $1.4 M_\odot$, whilst we have set $\iota = 30\,\text{deg}$, and the longitude of the ascending node to be $\Omega = \pi/2$, with the observer located in the Galactic plane at $\Theta = \pi/2, \Phi = 0$, assuming the spin axis of the central black hole is perpendicular to the Galactic plane (see Fig. 3.1). It is immediately evident, as expected, that those systems with shorter orbital periods and hence closer periapsis passages will exhibit stronger signals. Decreasing the orbital period from $P = 0.1$ years to $P = 0.01$ causes a corresponding shift in the frequency spectra to the region where LISA has greatest sensitivity (towards $\sim$ mHz). The SNR from each of these systems is $\rho = 22, 0.25, 0.03$ for $P = 0.01, 0.05, 0.1$ years respectively. The SNR will be influenced not only by the orbital period, but also secondary factors such as the eccentricity, system orientation with respect to the BH and the observer (ι, Θ) and the BH spin. The exploration of this parameter space is shown in Fig. 6.6. It can be seen that the major factors which influence the SNR are the orbital period and the eccentricity, with the influence of secondary factors such as system orientation or BH spin causing smaller deviations. As expected, short period, highly eccentric systems corresponds to the greatest SNR values. Typically in GW data analysis, for a system to be detectable, it requires that the SNR is greater than ~ 10. For this limit, only those systems at the Galactic centre with orbital periods less than ~ 0.02 years and eccentricities $e \sim 0.9$ might emit gravitational burst radiation which is detectable. The exact physical interpretation of SNR here warrants further exploration. The output of a GW detector like LIGO or LISA consists of a superposition of the detector noise

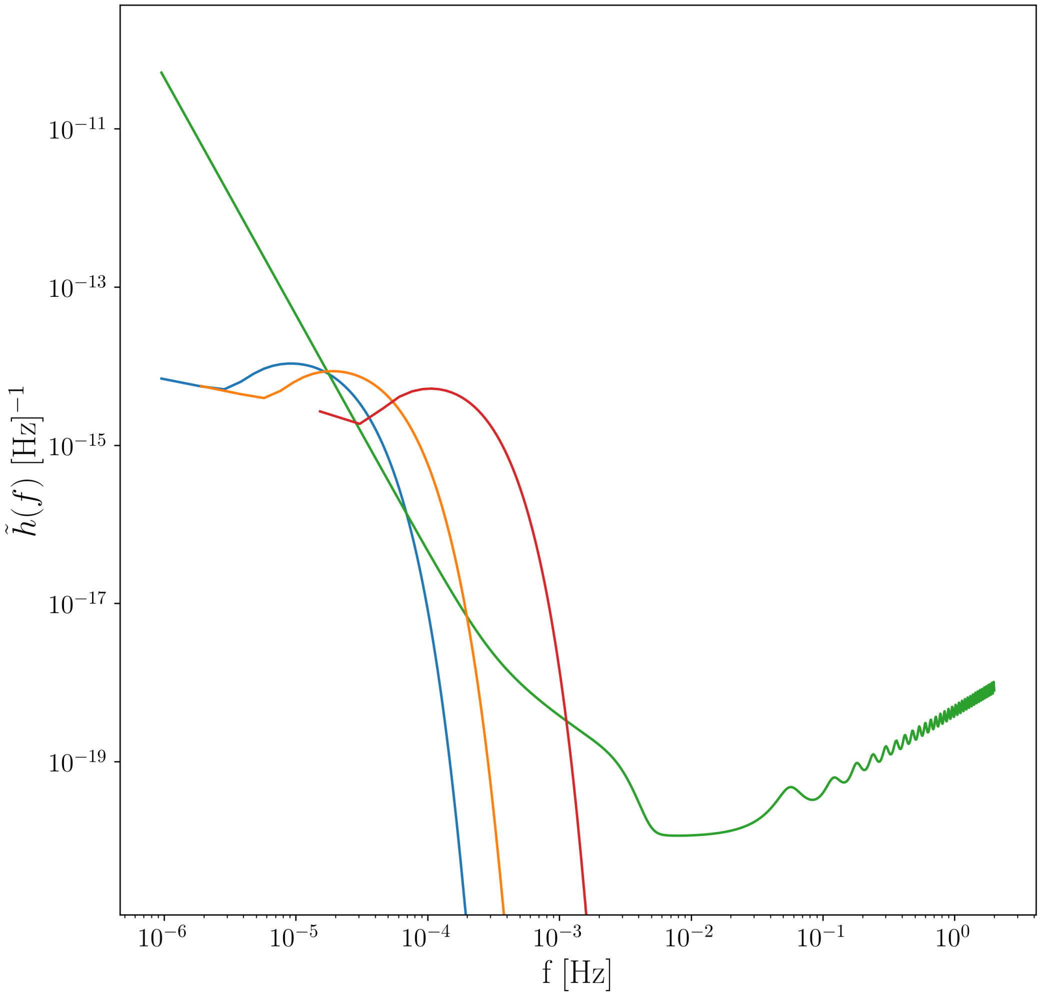

Fig. 6.5: The frequency spectra of 3 MSP-EMRB systems at the Galactic centre with eccentricity $e = 0.9$ and orbital periods $P = 0.01, 0.05, 0.1$ (red, orange, blue respectively). The inclination angle is $\iota = 30\,\mathrm{deg}$ and we have set the MSP mass to be $1.4M_\odot$. The SNR of each of these systems is $\rho = 22, 0.25, 0.03$ respectively.

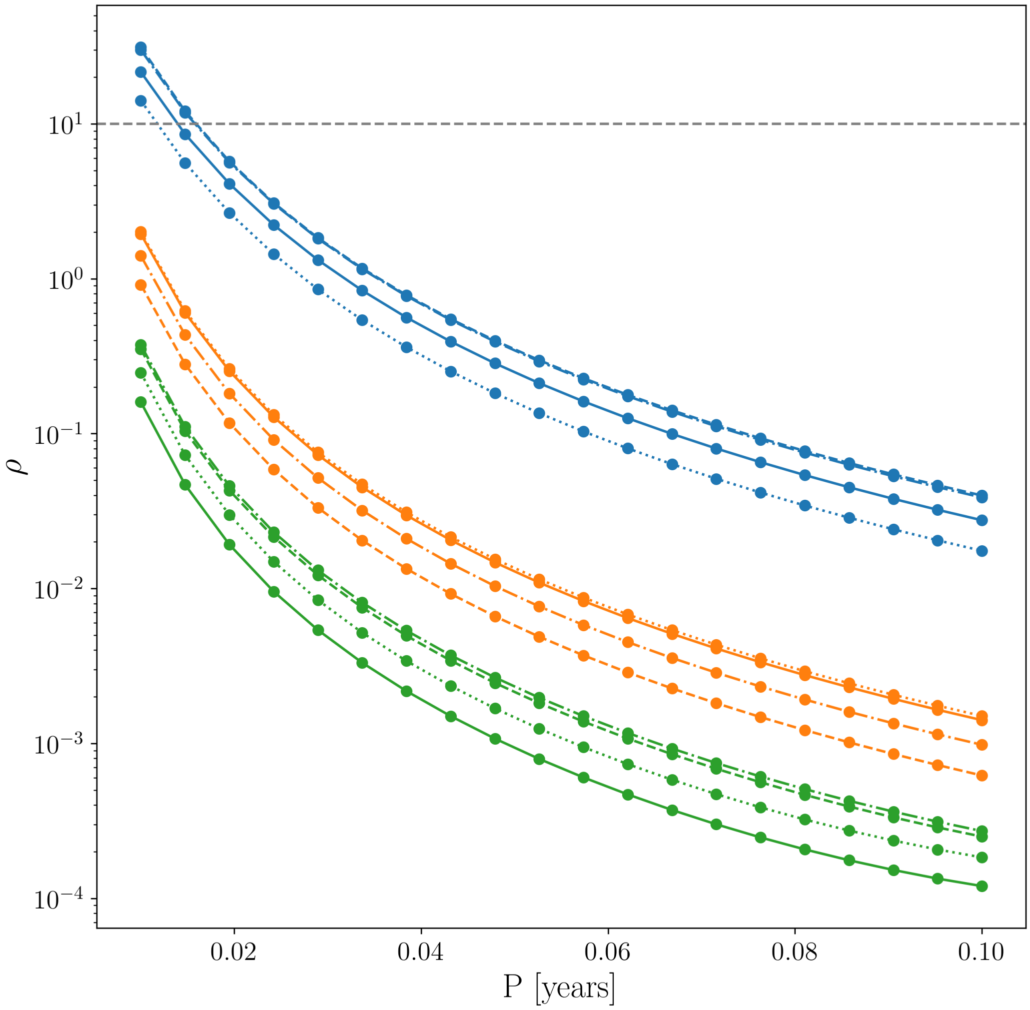

Fig. 6.6: The signal to noise ratio of Galactic centre MSP-BH systems at $e = 0.9, 0.8, 0.7$ (blue, orange, green respectively) at inclinations $\iota = 0, 30, 60, 80$ deg. More eccentric orbits with shorter orbital periods have greater values of ρ, whilst the SNR is also weakly dependent on how face on the orbit is to the observer. The grey horizontal line denotes $\rho = 10$, a typical cutoff for the minimal detection SNR in GW astronomy. However, given the presence of an accompanying EM beacon, the detection could be pushed below this threshold.

$n(t)$ and the gravitational wave signal $h(t)$,

$$s(t) = h(t) + n(t) \tag{6.30}$$

The aim of GW data analysis is then to try and extract $h(t)$. In standard, blind GW astronomy (i.e. no continuous EM counterpart) for continuously radiative sources (e.g. LIGO/Virgo BH-BH mergers, LISA EMRIs) high values of ρ are desirable since this governs both the probability of detection and the precision with which the system parameters can ultimately be determined. In order to maximise the SNR and to combat the weak instantaneous GW signal, typical GW sources are observed for a large number of cycles to allow the signal to build up above the noise. LISA EMRIs in particular are expected to spend a large number of cycles radiating in the LISA frequency band; 1 year of observation would be required to detect a $1M_{\odot}$ object in a circular orbit at $r = 50$ around a Schwarzschild BH at the Galactic centre (Fig. 7, Gourgoulhon et al. 2019). Typical bursting sources with large amplitudes such as cosmic strings (e.g. Aasi et al. 2014) are searched for by simply looking for an excess of power, which shows above the instrument noise. Eccentric compact objects orbiting the Galactic centre typically do not have a continuous inspiral emission, but are instead bursting sources. Consequently, these systems are only detectable if the bursting GW amplitude is sufficiently large, requiring a large mass compact object with a close periapsis passage. As a result, BHs with masses of 10s of $M_{\odot}$ at 10s of r_g are typically considered as the primary sources, whilst the detection of signals from lower mass ($\sim 1M_{\odot}$) pulsars or white dwarfs with longer orbital periods is less likely.

However, MSPs acting as a BH companion and a GW source provide a unique advantage over other types compact objects (white dwarfs, BHs) in that they have a continuous electromagnetic beacon. As a consequence, if a pulsar is observed via radio timing around the Galactic centre, it would be possible to derive a precision prediction of the expected gravitational waveform and the expected time at which this waveform would be received by an observer. Electromagnetically dark bursting waveforms are typically poorly modelled and not amenable to matched filtering methods, whilst GW burst from MSP sources would have exceptionally well modelled waveforms. With this information known apriori it would be possible to detect GW signals via matched filtering methods which is usually not possible for dark bursting sources. As a consequence, whilst the SNR as given by Eq. 6.20 are a useful standard metric for quantifying the strength of the GW signal, since the expected signal is well-known apriori it may prove possible to detect bursting signals at SNRs that are typically though of as being undetectable. Once the waveform has been detected using a EM-informed template, one could then further refine the waveform model to match the observations for parameter estimation. Clearly there will be some lower limit at which point the noise is completely dominant over the signal and no GW can be detected, even when the expected signal is known. However, for the Galactic centre pulsars that are typically considered for radio timing tests of GR these signals should be detectable via matched filtering, even for longer orbits.

Stellar Clusters

In addition to the Galactic centre, there exist other potential hunting grounds for MSP-EMRBs which can be used via radio timing for strong-field tests of GR. As discussed, consilient strands of evidence suggest that IMBH could reside in globular clusters (Mezcua 2017), although some of this evidence is disputed and definitive ‘smoking-gun’ evidence for IMBH is still lacking. Nevertheless, if the centre of globular clusters do host IMBH, then these regions would be ideal places to search for MSP-EMRBs without the additional complications raised due to scattering of the MSP radio pulse, as is expected for observations of the Galactic centre. As discussed, the centre of globular clusters have remarkably high stellar densities ($\sim 10^6$ stars per cubic parsec, Freire 2013) and indeed the number of pulsars per unit mass is a factor of 10^3 greater than in the Galactic disk on account of these high stellar densities allowing dynamical effects like mass segregation to be more efficient. Since MSPs are thought to evolve from low mass X-ray binaries (LMXBs) and globular clusters are known hosts of abundant LMXB populations, MSPs make up a significant fraction of the globular cluster pulsar population (Camilo & Rasio 2005; Ransom 2008). For example, the globular cluster of the MW bulge, Terzan 5 is known to host at least 37 MSPs (Cadelano et al. 2018b), whilst M28 has ~ 8 MSPs out of a total PSR population of 12.

For the purposes of this work investigating the gravitational waveforms from astrophysical MSP-EMRBs, we take 47 Tucane ('47 Tuc') as our example globular cluster. Indeed, 47 Tuc is known to host a substantial pulsar population (25 pulsars, all of which have spin periods less than 8ms, Pan et al. 2016) and it has been suggested -based on dynamical pulsar signatures- that at the core of 47 Tuc there also exists an intermediate mass black hole of mass $\sim 2.2 \times 10^3 M_{\odot}$ (Kızıltan et al. 2017b,c) although this interpretation has been disputed (Mann et al. 2019). The existence or otherwise of a IMBH in the centre of 47-Tuc is not an issue here - we just take 47 Tuc as a representative example of the sorts of globular clusters that could host MSP-EMRB.

Since the expected mass of the central BH is 'intermediate' ($\sim 10^3 M_{\odot}$), in order to probe the gravitational strong field, the orbital periods of MSP in globular clusters systems are required to be shorter than those for the Galactic centre. An MSP in 47 Tuc with a 0.01 day orbital period and an eccentricity $e = 0.9$ around a central IMBH of mass $\sim 2.2 \times 10^3 M_{\odot}$ would probe a gravitational potential of strength $\epsilon \sim 0.02$ as it passes through periapsis. Whilst no MSP-IMRB with an appropriately short orbital period has yet been detected, there remain real questions about whether our current PSR search algorithms are sophisticated enough to detect these weak signals from such relativistic systems in strong-field environments, when the signal is subject to a slew of general relativistic effects (Psaltis et al. 2016). Similar to MSP-EMRB in the Galactic centre, the lack of MSP-IMRB detections in globular clusters is then likely due to inappropriate and insufficient observational methods. Going forward we set the BH mass as $\sim 2.2 \times 10^3 M_{\odot}$ and leave the spin parameter unchanged from the Galactic centre case, $a = 0.6$. An advantage of 47 Tuc is that it is closer than the Galactic centre; we set the observer to be at a

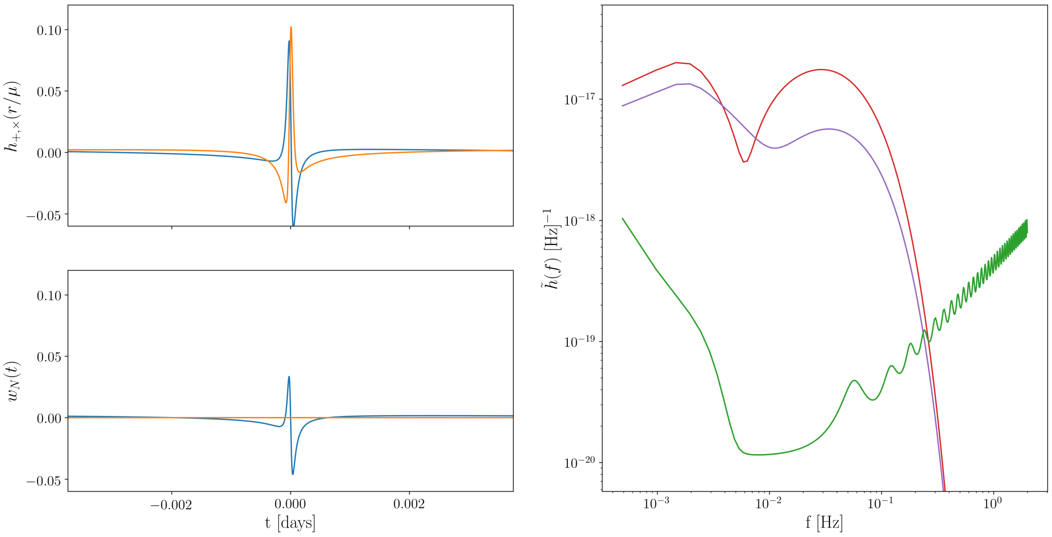

Fig. 6.7: Waveforms in the time *(left-side)* and frequency *(right-side)* domain for a MSP-IMRB going through periapsis in 47 Tuc. The orbital period is $P = 0.01$ days with $e = 0.9$, $\iota = 0\,\mathrm{deg}$ and $\Omega = \pi/2$. The BH parameters are $M_{\rm BH} = 2.2 \times 10^3 M_\odot$, $a = 0.6$. The observer is at $r_{\rm obs} = 4$ kpc, $\Phi = 0$, with latitude $\Theta = 0$, (top left time waveform, red line frequency waveform) and $\Theta = \pi/2$ (bottom left time waveform, purple line frequency waveform). again for the time waveforms the blue and orange lines denote the $h_+, h_\times$ GW polarisations respectively. In the frequency spectra the green line is the LISA noise curve $\sqrt{S_n(f)}$ (not the characteristic strain h_c, Eq. 6.27) as described by Eq. 6.21.

distance of 4.0 kpc.

The time and frequency spectra of a MSP on an $P = 0.01$ day, $e = 0.9$ orbit in this 47-Tuc system is shown in Fig. 6.7. Since the orientation of the BH spin axis with respect to the observer is unknown astrophysically, we consider the two limiting cases; one where the observer location is the in the equatorial plane with respect to the BH spin axis, i.e. $\Theta = \pi/2$ and the other where the observer lies along the BH axis such that $\Theta = 0$. We set the MSP to orbit in the equatorial plane ($\iota = 0$). In the $\Theta = 0$ case, $\rho = 396$, whilst when $\Theta = \pi/2$ the SNR is reduced to $\rho = 144$. These SNRs are markedly higher than those calculated for the Galactic centre, even before exploring the full parameter space. This is on account of the fact that the systems are much closer and the signal occupies a different frequency regime on account of the different central BH masses and orbital periods. Whilst MSPs on sufficiently short orbits in globular clusters have not yet been discovered, less the existence of IMBH, this suggests that if these systems do exist they offer fertile grounds for multimessenger strong field astronomy, without the complications of radio scattering and with increased SNRs due to their proximity and waveform frequencies. We can also explore the parameter space analogous to how we did in the Galactic centre case. The results are presented in Fig. 6.8. We can see that the SNR is strongest for more eccentric systems; all systems with $e = 0.9$ and $P < 0.1$ days have $\rho > 100$. For these high eccentricities, ρ starts to drop off as P becomes very short due to the shift of the signal to a different part of the frequency spectrum where LISA is less sensitive. The SNR depends much more strongly on the system orientation than for Galactic centre systems, with greater values of ρ for face-on systems.

Given that we have considered a nearby system, it is also interesting to investigate the detection prospects for a more distant, extragalactic system. Dwarf spheroidal galaxies are old clusters and also have exceptionally high densities in their central regions. For example M32, a satellite of Andromeda, has an remarkable measured stellar density in the central parsec of $3 \times 10^7 M_{\odot}\text{pc}^{-3}$ (Lauer et al. 1992). M32 is also thought to harbour a massive BH at its core of mass $\sim 3 \times 10^6 M_{\odot}$ (van der Marel et al. 1997; Bender et al. 1996; Verolme et al. 2002; van den Bosch & de Zeeuw 2010). This combination of a massive BH in an old, dense stellar environment suggests that MSP-EMRBs should also be present in these systems. If the radio emission could be detected then these systems could also potentially be used for strong-field GR tests via radio timing. Whilst additional difficulties arise due to the distance of these sources (M32 is at a distance of 763 kpc) and the commensurate faintness of the radio signal, there are compensatory advantages due to an expected lack of scattering. Again, target searches looking specifically for these systems with specialist search techniques for relativistic systems may prove fruitful. Indeed, whilst searches of nearby M32 did not definitely detect any pulsars, several single pulse events were detected which could be attributed to pulsar emission (Rubio-Herrera et al. 2013).

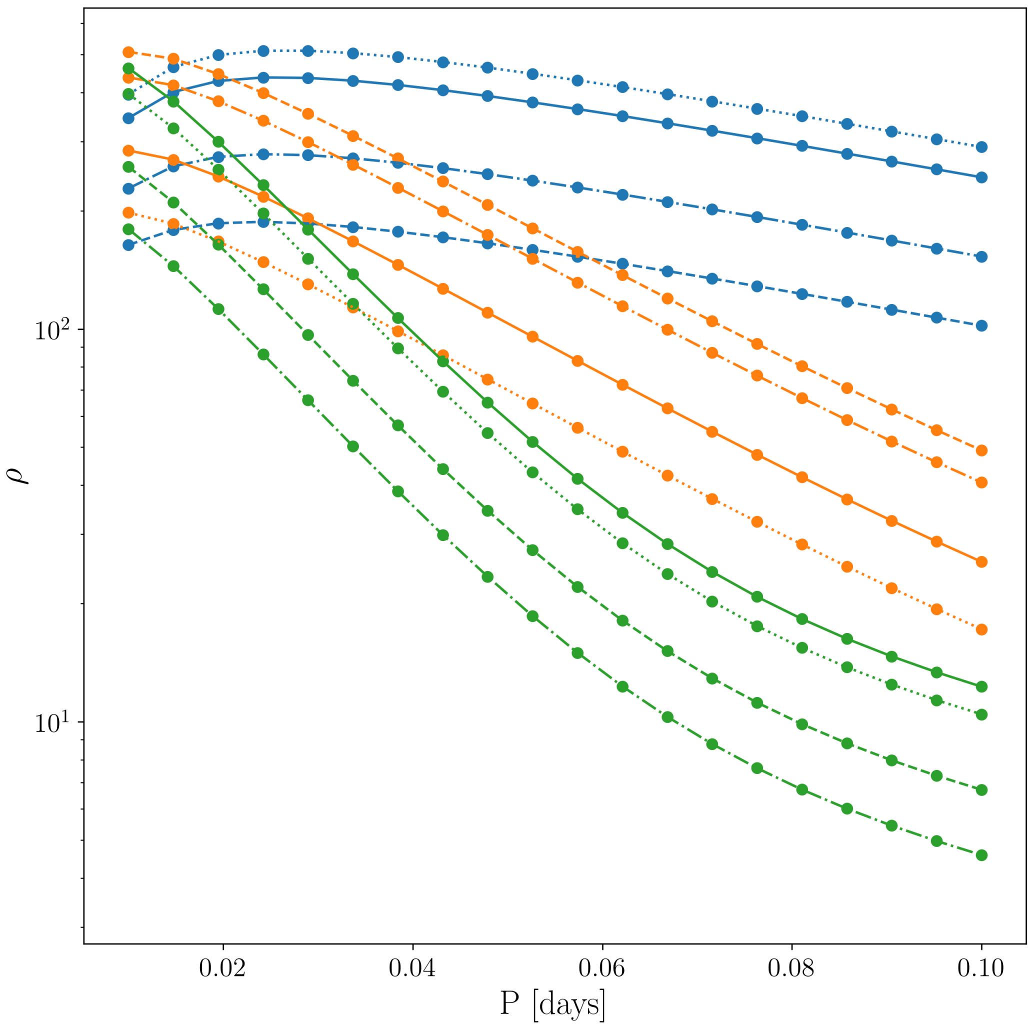

Fig. 6.8: The signal to noise ratio of MSP-BH systems in 47-Tuc at $e = 0.9, 0.8, 0.7$ (blue, orange,green respectively) at inclinations $\iota = 0, 30, 60, 80\,\mathrm{deg}$. Typically, shorter period orbits have greater SNRs, though this trend is less strong for more eccentric systems. The influence of the system orientation with respect to the observer is much stronger than for the Galactic centre systems, with face on observations corresponding to greater signal strengths.

For this work we take as M32 as our archetypal dwarf galaxy. Similar to when we were considering globular clusters and 47 Tuc, the orientation of the BH spin axis with respect to the observer is uncertain and so we again consider the two extremal cases where $\Theta = 0, \pi/2$. The BH mass is set as $3 \times 10^6 M_{\odot}$ and the observer at a distance of 763 kpc. For an orbital period of $P = 0.01$ years, $e = 0.9$, and a favorable system orientation ($\iota = 0$, $\Theta = 0$) the SNR is only $\rho = 0.3$. Naturally, those systems which are less favorably aligned have even lower SNRs. This low SNR of the GW is due to the same reason that radio pulsars are difficult to detect for these systems; they are simply very distant. In order to detect burst gravitational radiation would require orbital periods shorter than what we have considered here. For instance, if we take the same system but shorten the orbital period to $P = 0.001$ years $\rho = 14$. However such systems pass through periapsis at only $\sim 5 r_{\rm g}$ and their existence is unlikely, although not impossible. Alternatively, since these are regions of high stellar density it is possible that exotic systems could forms such as a neutron star binary orbiting the massive central black hole i.e a extreme mass ratio hierarchical triple system (e.g. Remmen & Wu 2013). The increased mass of the effective orbiter (i.e. 2 vs 1 neutron stars) would increase the resulting GW signal. Whilst the dynamics and resulting waveforms would be much more complicated in this triple case, a first order approximation to the SNR can be obtained since the NS separation is much smaller than the orbital radius and so we can approximate the the double NS system as equivalent to a single object of mass $2 \times 1.4 = 2.8 M_{\odot}$. Such a system again with $P = 0.001$ would have an SNR of $\rho \sim 30$. Again, we grant that the formation and detection of such a system may be unlikely, however it is not completely unphysical and the huge scientific returns that could be returned from a multimessenger observations of a triple system in the gravitational strong field make the possibility of detecting such a system at least worth some consideration.

6.3 Discussion and Conclusions

Through this work we have shown that in addition to MSP-EMRBs being used as strong-field GR probes through radio timing, with LISA it will be possible to detect bursting gravitational radiation from these systems as the MSP passes through periapsis. It is important to note that the gravitational waveforms have not been calculated in a self-consistent way - we have used a Numerical Kludge approach rather than a fully perturbative treatment. However, we are primarily concerned here with showing that GW bursts from typical MSP-EMRBs are detectable rather than calculating explicitly consistent waveforms. In addition, the NK approach is known to give strong agreement in the parameter space we have considered, and indeed we observe a high degree of overlap ($= 1$) between our NK waveforms and those for which exact analytical solutions exist. We are therefore confident that the SNRs calculated in this work are at least reasonable approximations to the true burst SNRs.

In order to use MSPs as strong-field probes, it is important to have as 'clean' and environment as possible (c.f. complications from hydrodynamic drag, Psaltis 2012 or Newtonian perturbers, Merritt et al. 2010). Whilst the burst gravitational radiation is scientifically useful in and of itself, it also has the danger of acting as a potential noise source from the perspective of MSP radio timing. The gravitational radiation may influence the timing signal via two main channels. The first is via the effective perturbation that the gravitational wave introduces to the background spacetime metric which may in turn affect the geodesic of the photon ray emitted by the MSP. The second is by the GW emission influencing the MSP orbital motion. Both these points can be quickly addressed: GWs are transverse waves and so even for EM and GW radiation emitted coincidentally at periapsis, the photon ray will not be affected by the gravitational burst radiation. For the second point, due to the extreme mass ratio and the orbital periods considered for this work the orbital constants (e.g. E, L) do not meaningfully evolve over the burst duration and so will not impact either the PSR radio timing or - indeed - the calculated waveform

SNRs (see e.g. Eq. 4.44). The lack of influence of the gravitational burst radiation on either the photon path or the orbital dynamics is advantageous from the perspective of radio pulsar timing and multimessenger astronomy since it means that the two messenger signals are entirely separate and will not influence each other. Therefore when calculating a PSR timing model the influence of this gravitational radiation will have no influence on the timing residuals.

From these results, the most attractive target in terms of multimessenger strong-field astronomy is perhaps not the Galactic centre, but instead the centre of nearby globular clusters, such as 47 Tuc. MSP-EMRBs in globular systems would have shorter orbital periods and are also typically less distant in comparison to e.g. the Galactic centre. As a consequence the SNRs for the systems considered in this work were typically highest for globular cluster type systems, uncertainties in the system orientation (c.f BH spin axis, orbital inclination etc.) notwithstanding. In addition to their higher GW burst SNRs, MSP-EMRB in globular clusters are also appealing from the perspective of MSP radio timing; globular clusters are known to host large populations of MSPs whilst radio observations do not suffer from line of sight effects due to astrophysical plasma causing scattering (and temporal broadening of the pulse profile, e.g. Wucknitz 2015) and spatial dispersion. Moreover, since stars in globular clusters do not have a strong prograde/retrograde rotation preference, there is an even probability of detecting MSPs on a retrograde orbit, which would introduce additional interesting dynamical effects and imprints on the GW waveforms which we have not considered here. In addition to Globular clusters hosting sizable NS populations, there also exist numerous Globular clusters in the Galaxy which naturally increases the expected event rate. Globular clusters as MSP-EMRB targets do have their own drawbacks however, most notably that that the existence or otherwise of IMBH in the cores of these systems is far from well established. However, if a MSP on an appropriate orbit in a nearby globular cluster could be detected then the combination of simultaneous EM and GW multimessenger observations could firmly establish the existence - or otherwise - of IMBH, as well as probing other key questions of fundamental physics.

In addition to globular clusters, observations of the Galactic centre remain a highly attractive target. In contrast to the centre of globular clusters, the existence of a massive nuclear BH associated with the Sgr A* radio source is well established (Boehle et al. 2016; Gravity Collaboration et al. 2018a). To briefly review the discussion of the previous chapters, the Galactic centre is also a region of high stellar density and is observed to host a collection of young massive OB stars, indicating a high rate of star formation. This observational evidence in conjunction with theoretical considerations of the historical star formation rate and the Galactic initial mass function suggests that the Galactic centre should host a large population of neutron stars (Wharton et al. 2012). However despite numerous searches of the Galactic centre (e.g. Bates et al. 2011) no radio pulsars have been detected. Originally this dearth of detections was explained as being due to scattering due to astrophysical plasma along the line of sight causing pulse temporal smearing. Since PSR typically have steep radio spectra, searches are typically carried out at low radio frequencies. Unfortunately, at lower frequencies the scattering becomes more pronounced, hindering detections at the usual frequencies. However, even deep searches at higher frequencies (e.g. Macquart et al. 2010) returned no detections. Moreover, the detection in 2013 of the magnetar SGR J1745-29 in the inner parsec of the Galactic centre (Kennea et al. 2013; Mori et al. 2013) indicates that the scattering towards the Galactic centre is less than expected and that previous searches should have detected pulsars in the Galactic centre. Such a tension has been dubbed the 'missing PSR problem' (Dexter & O'Leary 2014). However, it was subsequently demonstrated Macquart & Kanekar (2015); Rajwade et al. (2017) that if the Galactic centre pulsar population is composed primarily of MSPs then previous surveys were insensitive to the signals from this population. Moreover, as we have shown in the preceding sections if these MSP-EMRB inhabit the strong gravitational field regime, then their dynamics and signals will be subject to strong field relativistic effects which current search methods may be not sufficiently sophisticated to detect. The hypothesis of a MSP GC population is not proposed merely as a solution to the missing PSR problem; there exists independent reasons to think that MSPs exist in this region. Firstly, as noted, the Galactic centre is a region of high stellar density. Consequently any pulsars would be subject to multiple close interactions, spinning up their rotation rate. Indeed, in the Globular cluster 47 Tuc - which is also a region of high density - 90% of the pulsars have spin periods less than 30 ms. This is in contrast to the total pulsar population where only $\sim$ 14% of puslar have such short spin periods (see also Fig. 1.1). Secondly, the Galactic centre is known to have an overabundance of X-ray transients (Hailey et al. 2018) which appear to be LMXB. As in globular clusters, the presence of a LMXB population is typically correlated with increased MSP numbers, given LMXB as a mechanism for the formation and spin up of MSPs. Finally, the well known Fermi γ-ray excess is best explained via a population of MSPs (Yuan & Zhang 2014; Bartels et al. 2016), rather than a signal due to dark matter annihilation. If MSP-EMRB in the Galactic centre do exist and can be detected and used for strong field tests of GR (e.g. Liu et al. 2012; Psaltis et al. 2016), then this work illustrates that GW burst radiation should also be detectable, allowing another opportunity for strong field multimessenger astronomy.

As opposed to the two Galactic cases we have considered, the detection of GW burst radiation from extragalactic sources such as M32 is rather unlikely. This is simply on account of the distance to such sources reducing both the MSP radio signal and the GW signal. The SNR only becomes appreciable for more unlikely orbital configurations, for example short orbital periods in conjunction with some complex hierarchical triple system. Whilst such an instance may be more unlikely, it is not completely unphysical since the increased stellar density and associated two body interactions might allow for the formation of such exotic systems. However we do suggest that observational efforts are best concentrated on Galactic sources.

Beyond detecting these bursts, it is also of scientific interest to use them for parameter estimation of the central BH. Via standard blind GW astronomy, a GW burst from a 10 $M_{\odot}$ object at the Galactic centre is expected to be scientifically informative for appropriately short ($\lessapprox 10r_{\rm g}$) orbits, in the best case providing mass and spin estimations of the central BH to one part in 10^4 (Berry & Gair 2013b). Due to their increased distance, for bursts from extragalactic sources the periapsis approach needs to be correspondingly shorter in order for these signals to be scientifically useful. Given this constraint these signals are also expected to be relatively rarer than Galactic ones. In the best case parameters estimation of the central BH for extragalactic sources (e.g. M32) is expected to be at the $0.1 - 1\%$ level (Berry & Gair 2013a).

These quoted uncertainties in the inferred parameters are derived with an uninformative prior, since in typical GW astronomy for burst sources there are few constrains on the source parameters. For a set of inferred parameters $\bar{\boldsymbol{\theta}}$, the associated uncertainty, in the limit of high SNR, is given by,

$$\sqrt{\langle (\Delta \bar{\theta}^i)^2 \rangle} = \sqrt{\bar{\Sigma}^{ii}} \tag{6.31}$$

where for an uninformed prior $\bar{\boldsymbol{\Sigma}}$ is the inverse of the Fisher information matrix, $\bar{\boldsymbol{\Gamma}}$ (see e.g. Cutler & Flanagan 1994). However, in the presence of an accompanying, coincident radio signal we would have good estimates via a timing solution for some of the system parameters. In the case where the parameter has some Gaussian prior with a variance-covariance matrix $\bar{\boldsymbol{\Sigma}}_{\mathbf{0}}$ then the variance-covariance of the posterior is

$$\bar{\boldsymbol{\Sigma}} = (\bar{\boldsymbol{\Gamma}} + \bar{\boldsymbol{\Sigma}}_{\mathbf{0}}^{-1})^{-1} \tag{6.32}$$

and so *apriori* information will immediately improve the parameter estimation precision. Moreover, as noted in Cutler & Flanagan (1994), whilst apriori information can have a significant effect on the parameters to which the priors apply, it also aids the other parameters due to correlations. Electromagnetic pulsar timing observations would give constraining priors on a range of system parameters. Firstly, the BH mass and spin can be estimated via a pulsar timing solution. In the best case, over long timescales, these precisions are expected to be of the order $10^{-5} - 10^{-3}$ or better (Liu et al. 2012). Naturally even weaker constrains would be useful as a Bayesian prior. In addition estimates of the quadrupole moment of the central BH can also be made (Psaltis et al. 2016). For pulsars - which are neutron stars - we immediately have a constrained estimate of the mass which is further improved as the timing solution is refined. Given the mass it is then possible to break the mass-distance degeneracy for bursts, and in any case the source distance will also be constrained independently through the host environment of the pulsar (e.g Galactic centre, 47 Tuc etc.). If the pulsar is observed for a sufficiently long time prior to receiving the GW burst we would also have good estimates of the coordinates of the orbital trajectory and quantities such as the orbital energy, angular momentum and Carter constant. Quantitative estimates of the improvement in the parameter uncertainty by using priors determined by radio pulsar timing observations require more involved calculations which are beyond the scope of this paper and we defer them for a future work. Furthermore, whilst the preceding discussion was focused on a single GW burst event, for bound orbiting systems multiple bursts would be observed on a timescale set by the orbital period, which would likely further improve the attainable measurement precision.

An MSP-EMRB would be a unique gravitational wave source, given the presence of a continuous electromagnetic counterpart. Typical GW detection involves comparing a large number (covering the parameter space) of templates of the theoretical signal with the real noisy data. Such an approach would be unable to detect burst radiation from compact objects which are electromagnetically dark (e.g. BH, WD) over the sorts of orbital periods and timescales considered in this work. The presence of an EM beacon in the PSR beam is therefore a powerful tool for detecting gravitational radiation from these systems. Approaching the system from the other side - i.e. the from the perspective of EM radio timing rather than GW astronomy - the potential to detect an accompanying gravitational radiation signal in conjunction with the radio

MSP timing signal would enable true multimessenger precision astronomy in these strong-field regimes. The extent to which such observations could be used as a scientific apparatus c.f. parameter estimation from multimessenger observations has not been explored in this work but would be an interesting further development. For instance, given the detection of a MSP-EMRB and the associated EM and GW emission, to what precision can e.g. the BH spin be determined? We defer the investigation on the use of MSP-EMRB EM + GW burst waveforms for parameter estimation for a future work, but simply note here that the simultaneous electromagnetic and gravitational signals would provide a unique astronomical probe of strong-field black hole spacetimes. It is also worth noting here that we have not explored the full orbital parameter space and the influence on the SNR, but instead just considered 3 major representative cases and briefly inspected the influence of system orientation. A full exploration of the parameter space we again defer for a future work. For the typical orbital periods considered in this work $P \sim 0.1$ year we have shown that radiation reaction self force effects can be neglected. As discussed this is advantageous from the perspective of MSP radio timing as a strong-GR probe since it means that the system remains ‘clean’ and the gravitational radiation does not act as a noise source in the MSP timing residuals. However for shorter orbital periods with smaller periapsis distances the self-force backreaction will start to influence the orbital dynamics and burst waveform. Consistent modelling of Extreme Mass Ratio Inspirals (EMRIs) accounting for self force effects to second order is currently a major theoretical challenge (see discussion in Barack & Pound 2019). The resolution of this problem is key if EMRIs are to be detected with LISA and realise their scientific potential as precision strong-field probes.

Chapter 7

Beyond - GR signatures

The analysis within this thesis so far has taken place assuming that GR is the correct description of reality, and so the background spacetime is described by a solution to the Einstein field equations i.e. a Kerr BH. However, as discussed, definitive proof of the 'Kerr Hypothesis' - that astrophysical BHs are indeed described by the Kerr solution - is still lacking. Within GR, it is possible for astrophysical BHs to be some horizonless object (a 'naked singularity', e.g. Harada et al. 2002), or else some exotic dark compact object such as a boson star (Ruffini & Bonazzola 1969; Liebling & Palenzuela 2012) or a gravastar (Mazur & Mottola 2001). In addition, should gravity in the strong-field regime be fundamentally described by some theory beyond classical GR (e.g. Psaltis et al. 2008), then the Kerr Hypothesis naturally fails. An important further consideration of this work, therefore, is the observational signatures from a strong-field MSP-BH system when the background spacetime deviates from the Kerr solution.

An axisymmetric curved spacetime can be described by a multipole expansion, where the multipole moments are given as a series of scalars, the mass moment M_l and the current moment S_l. A key feature of Kerr BHs in GR is the satisfaction of the No Hair Theorem (NHT, Israel 1967, 1968; Carter 1971); higher order multipole moments of the spacetime ($l \geq 2$) are determined by the two lowest order moments the BH mass ($M = M_0$) and the spin ($J = S_1$)

as,

$$M_l + iS_l = M(ia)^l \ , \tag{7.1}$$

recalling that $a = J/M$. Since the spacetime is completely determined by the lowest order moments, once the mass and spin of the BH are determined, an independent measurement of the next order moment, the quadrupole moment (M_2) would then provide a direct challenge to the NHT and the Kerr Hypothesis. Whilst its validity would provide another success for GR and rule out alternative theories for which the NHT does not hold, its violation would point to errors in the foundations of relativity, immediately refute the Kerr Hypothesis and may guide the way to alternative theories of gravity. Consequently, being able to accurately determine the observational signature of a non-Kerr quadrupole moment is an essential enterprise.

The relativistic spin-orbital dynamics of a MSP around a massive Kerr BH have been investigated by a variety of authors (Singh et al. 2014; Saxton et al. 2016; Li et al. 2019) - in addition to the work undertaken in the preceding chapters of this thesis - taking GR to be the correct description of the underlying astrophysics. In this Chapter we build on previous investigations to investigate the relativistic orbital spin dynamics of a pulsar around a massive black hole with an arbitrary mass quadrupole moment. In the extreme mass ratio limit, the MSP mass can be neglected and the orbital and spin dynamics of the MSP are determined by the background spacetime and the interaction of the MSP spin dipole moment with this background metric via the MPD equations (Chapter 3). In turn, the spacetime is described by the quasi-Kerr metric of Glampedakis & Babak (2006), which describes a stationary, axisymmetric spacetime with a quadrupole moment that deviates slightly from the Kerr value. We determine the effect on the astrophysical observables and discuss the implications for PSR timing in an E/IMRB system and the results for both astrophysics and fundamental physics.

7.1 Equations of motion

7.1.1 Quasi-Kerr Metric

The spacetime of a spinning BH with an arbitrary mass quadrupole moment can be described by the quasi-Kerr metric of Glampedakis & Babak (2006). Within this metric, the quadrupole moment $Q(=M_2)$ is given by,

$$Q = -M(a^2 + \epsilon M^2) \tag{7.2}$$

where ϵ is some parameter which quantifies the deviation from the Kerr quadrupole moment ($Q_K = -J^2/M$). The use of the quasi-Kerr metric, rather than a more general multipolar expansion of an axisymmetric vacuum spacetime, is motivated by the prior that that astrophysical BHs are in fact most likely Kerr BHs. This enables one to effectively perform a null hypothesis test of the question ‘Are astrophysical BHs described by the Kerr solution?’ (i.e. the Kerr hypothesis) whilst remaining agnostic on the source of the metric perturbation itself. The quasi-Kerr metric retains axisymmetry and stationarity and is Ricci flat up to quadrupole order (i.e. it is a solution to the Einstein Field equations). In the $\epsilon \rightarrow 0$ limit it also smoothly reduces to the pure Kerr solution.

The perturbed metric can be written in a covariant form as,

$$g_{\mu\nu} = {g^{\mathrm{K}}}_{\mu\nu} + \epsilon h_{\mu\nu} \ , \tag{7.3}$$

for Kerr metric ${g^{\mathrm{K}}}_{\mu\nu}$ (see Eqs. 2.2 - 2.6) and perturbation $h_{\mu\nu}$. To linear order in ϵ, the contravariant form is simply,

$$g^{\mu\nu} = g^{\mathrm{K}\mu\nu} - \epsilon h^{\mu\nu} \ . \tag{7.4}$$

Only the diagonal components of the perturbation are non-zero. The contravariant components in Boyer-Lindquist coordinates are,

$$h^{tt} = \frac{(1-3\cos^2\theta)\mathcal{F}_1(r)}{1-2/r} \ , \tag{7.5}$$

$$h^{rr} = \left(1 - \frac{2}{r}\right)(1-3\cos^2\theta)\mathcal{F}_1(r) \ , \tag{7.6}$$

$$h^{\theta\theta} = -\frac{(1 - 3\cos^2\theta)\mathcal{F}_2(r)}{r^2} \ , \tag{7.7}$$

$$h^{\phi\phi} = -\frac{(1 - 3\cos^2\theta)\mathcal{F}_2(r)}{r^2\sin^2\theta} \ , \tag{7.8}$$

where

$$\mathcal{F}_1(r) = -\frac{5(r-1)}{8r(r-2)}\left(2 + 6r - 3r^2\right) - \frac{15r(r-2)}{16}\ln\left(\frac{r}{r-2}\right) \ , \tag{7.9}$$

$$\mathcal{F}_2(r) = \frac{5}{8r}\left(2 - 3r - 3r^2\right) + \frac{15}{16}\left(r^2 - 2\right)\ln\left(\frac{r}{r-2}\right) \ . \tag{7.10}$$

With the relevant metric established, the equations of motion are specified via the covariant MPD equations, Eq. 3.19 - 3.21.

It is worth pausing to consider the regime of validity of the quasi-Kerr metric. Since any multipole expansion degenerates for $r \to 0$, it is important to consider how the metric breaks down on horizon scales. In Johannsen & Psaltis (2010) this limit is considered via the definition of a critical radius r_c below which the metric is no longer valid. This critical radius is a function of both the BH spin a and the perturbation parameter ϵ and defines the radius at which higher order terms $(\epsilon^2, \epsilon a)$ can no longer be neglected compared to the first order ϵ terms. Whilst these terms cannot be calculated explicitly in the quasi-Kerr metric, by comparing the quadrupole correction terms, order ϵ in the quasi-Kerr metric to the respective elements in the Kerr metric to quadrupole order, a regime of validity can be established. The cut-off r_c is subsequently defined as the radius at which the quadrupole correction reaches 50 % of the diagonal -r element, g_{rr}, which is the element most affected by the linear correction. In the case where $|\epsilon| = 1$ and $a = 1$, $r_c \sim 3r_g$ (Johannsen & Psaltis 2010). Whilst this regime is important for horizon ray tracing (e.g. Psaltis 2012) or GW inspirals (e.g. Carson & Yagi 2020), for our purposes we will be dealing exclusively with regions $> r_c$ and so the metric remains valid throughout the region in which we apply it.

7.1.2 MPD Formalism with arbitrary quadrupole

The MPD formalism described in Chapter 3 is explicitly covariant. Whilst previously the numerical determination of the spin-orbit evolution of the pulsar was calculated using the Kerr metric ${g^{\mathrm{K}}}_{\mu\nu}$, the same procedure can be followed where the background metric is the quasi-Kerr metric of Eq. 7.3, albeit with increased algebraic complexity. Further complications exist since the perturbed spacetime is no longer Petrov type D (Berti et al. 2005) and in general the perturbative quadrupole terms render the Hamiltonian inseparable in the coordinate variables. As a consequence a constant of integration - the Carter Constant (Carter 1968) - is lost. Only for the special case of equatorial orbits does the Hamiltonian for the quasi-Kerr metric regain separability and an equivalent Carter constant be defined. To proceed, we therefore restrict our analysis to the equatorial plane. The mapping described in Chapter 3 between constants of motion (i.e. specifying the initial conditions) and orbital parameters was particular to the case of a Kerr metric. This mapping needs to be updated for the general case of an arbitrary quadrupole moment in order to allow a correct description of the sorts of orbits we want to model. For equatorial orbits, the Hamilton-Jacobi equation for the quasi-Kerr metric is trivially separable and it follows that the radial 4-velocity is given as,

$$\begin{aligned}(u^r)^2 = V(r) = \left[(r^2+a^2)E - aL\right]^2 - \Delta\left[r^2 + (L-aE)\right] \\ -\epsilon r^4 \left(1-\frac{2}{r}\right)\left((\mathcal{F}_3 - \mathcal{H}_3)\frac{L^2}{r^2} + \mathcal{F}_3\right)\end{aligned}$$

where

$$\mathcal{F}_3 = -\frac{5(r-1)\left(2+6r-3r^2\right)}{8r(r-2)} - \frac{15r(r-2)}{16}\ln\left(\frac{r}{r-2}\right) \tag{7.11}$$

$$\mathcal{H}_3 = \frac{5\left(2-3r-3r^2\right)}{8r} + \frac{15\left(r^2-2\right)}{16}\ln\left(\frac{r}{r-2}\right) \; . \tag{7.12}$$

Collecting terms is is evident that we can write,

$$V(r) = f(r)E^2 - 2g(r)EL - h(r)L^2 - d(r) \; , \tag{7.13}$$

where

$$f(r) = r^4 + a^2 r(r+2) \tag{7.14}$$

$$g(r) = 2ar \tag{7.15}$$

$$h(r) = r(r-2) - \epsilon \left[2\mathcal{F}_3 r - 2\mathcal{H}_3 r - \mathcal{F}_3 r^2 + \mathcal{H}_3 r^2\right] \tag{7.16}$$

$$d(r) = r^2\Delta - \epsilon \left[2\mathcal{F}_3 r^3 - \mathcal{F}_3 r^4\right] \tag{7.17}$$

Eq 7.13 is of the same form as the base construction in Schmidt (2002) and so we can proceed in an analogous way to Chapter 3 and defining the energy and angular momentum as,

$$E = \sqrt{\frac{\kappa\rho + 2\epsilon\sigma - 2D\sqrt{\sigma\left(\sigma\epsilon^2 + \rho\epsilon\kappa - \eta\kappa^2\right)}}{\rho^2 + 4\eta\sigma}} \tag{7.18}$$

$$L_z = -\frac{g_1 E}{h_1} + \frac{D}{h_1}\sqrt{g_1^2 E^2 + \left(f_1 E^2 - d_1\right) h_1} \tag{7.19}$$

where, as before,

$$\kappa \ \equiv d_1 h_2 - d_2 h_1 \tag{7.20}$$

$$\varepsilon \equiv d_1 g_2 - d_2 g_1 \tag{7.21}$$

$$\rho \equiv f_1 h_2 - f_2 h_1 \tag{7.22}$$

$$\eta \equiv f_1 g_2 - f_2 g_1 \tag{7.23}$$

$$\sigma \ \equiv g_1 h_2 - g_2 h_1 \tag{7.24}$$

and

$$(f_n, g_n, h_n, d_n) \equiv (f(r_n), g(r_n), h(r_n), d(r_n)) \tag{7.25}$$

with $D = \pm 1$ to denote prograde and retrograde orbits and r_1 denotes the periapsis radius and r_2 the apoapsis. With the orbital constants specified, the initialization of p^μ is given by $p^\mu = m u^\mu$ where Glampedakis & Babak (2006),

$$u^t = \frac{1}{r^2}\left((r^2 + a^2)\frac{\mathcal{P}}{\Delta} - a(aE - L)\right) - \epsilon\left(1 - \frac{2}{r}\right)^{-1}\mathcal{F}_3 E \tag{7.26}$$

$$
\begin{aligned}
(u^r)^2 =& \frac{1}{r^4}\Big(\mathcal{P}^2 - \Delta(r^2 + (L - aE)^2) \\
& - \epsilon r^4 \left(1 - \frac{2}{r}\right) ((\mathcal{F}_3 - \mathcal{H}_3)\frac{L^2}{r^2} + \mathcal{F}_3)\Big)
\end{aligned}
$$

$$u^\theta = 0 \tag{7.27}$$

$$u^\phi = \frac{1}{r^2}\left(\frac{a\mathcal{P}}{\Delta} - aE + L\right) - \epsilon \frac{\mathcal{H}_3 L}{r^2} \tag{7.28}$$

This framework of mapping the geometric orbital parameters to the initial conditions on p^μ is fundamentally an approximation since it does not include spin effects of the MSP. As a consequence the orbital parameters are not constant as they would be for a weak-field Keplerian orbit, but vary in time (see e.g. Singh et al. 2014). Nevertheless, these variations are typically small and so this mapping framework provides a decent first-order approximation to the sorts of orbits that we want to model. It is also worth noting that even in the case where the underlying metric is separable (e.g. Johannsen 2013) chaotic motion can occur should the orbital motion depart from being equatorial.

7.2 Spin-Orbit Dynamics of a MSP

We take as our canonical MSP a NS with mass $1.4 M_\odot$ and spin period 1 ms. We will consider BHs of both 'intermediate' mass ($M = 10^3 M_\odot$) and 'supermassive' ($M = 10^6 M_\odot$). Since the spin of astrophysical BHs is not well observationally constrained we set the BH spin at an intermediate value of $a = \pm 0.6$. We will consider different orbital parameters, $\Xi = (\mathcal{P}, e)$, and explore the effects induced by the quadrupole moment and the spin couplings. We define $\delta_\epsilon X$ as the quadrupole-induced difference on a general quantity X and similarly $\delta_\lambda X$ as the difference the quantity induced by the MSP spin, i.e.

$$\delta_\epsilon X = X(\epsilon, \Xi) - X(0, \Xi) \tag{7.29}$$

$$\delta_\lambda X = X(\lambda, \Xi) - X(0, \Xi) \tag{7.30}$$

7.2.1 Orbital Dynamics

The BH quadrupole moment modifies the background spacetime, whilst the MSP spin couplings alter the interaction of the MSP spin with this background field. As a consequence, the orbital trajectory of the MSP exhibits different behaviour compared to the pure Kerr geodesic case. The influence of a non-Kerr quadrupole moment ($\epsilon = 0.1$) on the spatial coordinate variables is presented in Figure 7.1 for a system with a supermassive BH with spin parameter $a = 0.6$ orbited by a MSP in the equatorial plane with semi-major axis $= 50\, r_{\rm g}$, at different eccentricities. The influence of the quadrupole has two clear types of modification on the orbital trajectory, which are most apparent by examining the behaviour of the ϕ coordinate variable. The first is a longer timescale secular drift, which causes a precession of the orbital orientation (the angle of pericentre). In addition to this secular behaviour, there is also a short timescale, periodic feature as the MSP passes through periapsis. These periodic features are strongest for more eccentric orbits, since these systems have shorter periapsis passages. There is a large magnitude in the quadrupole-induced variation in the r and ϕ coordinate variables, with a fractional difference of order 1%. In absolute terms, these spatial differences are of the order $0.1 r_{\rm g}$. The $\delta_{\epsilon} r$ and $\delta_{\epsilon} \phi$ evolution is out of phase by $\pi/4$; the maxima of $\delta_{\epsilon} \phi$ occur as the MSP passes through periapsis whilst the maxima of $\delta_{\epsilon} r$ occurs when $\delta_{\epsilon} \phi$ is changing most rapidly.

For the same system, we can also examine the spin-induced variation in the MSP coordinate position working in Cartesian coordinates, rather than spherical-polar Boyer Lindquist coordinates (Figure 7.2). Recall that the two coordinate systems are mapped via the standard spherical polar relation as,

$$x = m \sin\theta \cos\phi \tag{7.31}$$

$$y = m \sin\theta \sin\phi \tag{7.32}$$

$$z = r \cos\theta \tag{7.33}$$

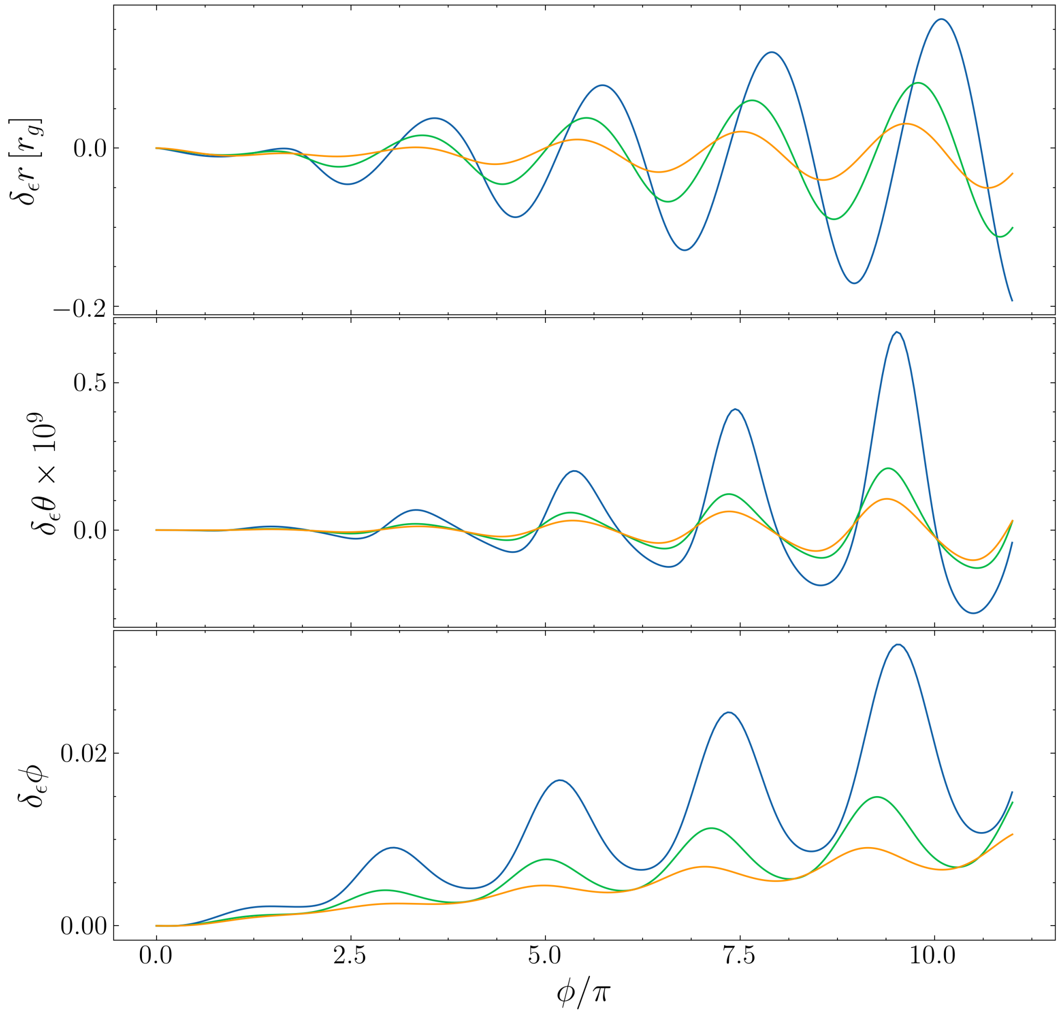

Fig. 7.1: Variation ($\delta x = x_{\epsilon=0.1} - x_{\epsilon=0.0}$) induced in the coordinate variables due to a non-Kerr quadrupole moment $\epsilon = 0.1$. The BH has $M = 4.3 \times 10^6 M_\odot$, $a = 0.6$ and the MSP has semi-major axis $= 50 r_g$, inclination $i = 0$ and eccentricities $e = 0.2, 0.4, 0.6$ (orange, green, blue respectively). More eccentric orbits exhibit greater magnitude deviations induced by ϵ on account of their closer periapsis passage. The $\delta_\epsilon \theta$ changes are smaller than the corresponding changes in $r - \phi$ since we are initialised in the orbital plane.

for $m = \sqrt{r^2 + a^2}$. Again we observe short timescale periodic features as the MSP passes through periapsis, with the effect being stronger for more eccentric orbits. The spin couplings cause a variation not just in the vertical coordinate $z-$direction (e.g. Singh et al. 2014), but also variations in the in-plane $x - y$ motion. Across the considered parameter space, typical variations are of magnitude $\mathcal{O}(10)$ km. Whilst this lengthscale is small compared to the gravitational lengthscale r_g, a 10 km variation is equivalent to a light travel time of $\sim 30 \mu s$ which is readily detectable via radio pulsar timing. The astrophysical implications of these spin couplings will be further explored later. Whilst we have just considered here the particular case of a BH with mass $\sim 10^6 M_{\odot}$, the magnitude of the spin-curvature coupling is independent of the BH mass.

In addition to the spatial evolution of the MSP, we can also consider the time evolution i.e. the ratio of the proper time τ to the coordinate time t. The nature of MSPs as relativistic precision clocks means that this difference can be directly measured, and indeed the difference in the rate at which the MSP 'ticks' due dynamical redshift is a key component of pulsar timing models (the 'Einstein delay'). This ratio is given by the 0-th component of the MSP 4-velocity ($u^0 = dt/d\tau$). The evolution of u^0 is shown in Figure 7.3, for a BH with $M = 10^3 M_{\odot}$, $a = 0.6$ along with the quadrupole and spin ($\epsilon - \lambda$) induced corrections. The $\epsilon - \lambda$ induced variations in u^0 exhibit the same general behaviour as the variations induced in the spatial coordinates; δu^0 displays periodic oscillations, with the frequency set by the orbital frequency of the system (extrema of δu^0 at periapsis), and more eccentric orbits displaying greater magnitude variations. The corrections due to the quadrupole moment, $\mathcal{O}(10^{-4})$, are greater than those due to the spin couplings, $\mathcal{O}(10^{-6})$.

7.2.2 Spin Dynamics

Since generally the MSP spin axis is not aligned with the orbital angular momentum axis, the spin vector s^{μ} evolves with time and the spin axis exhibits precession and nutation. This spin evolution in turn influences the MSP orbital dynamics (e.g. Eq. 3.19 - Eq. 3.21). In a Newtonian description, the spin

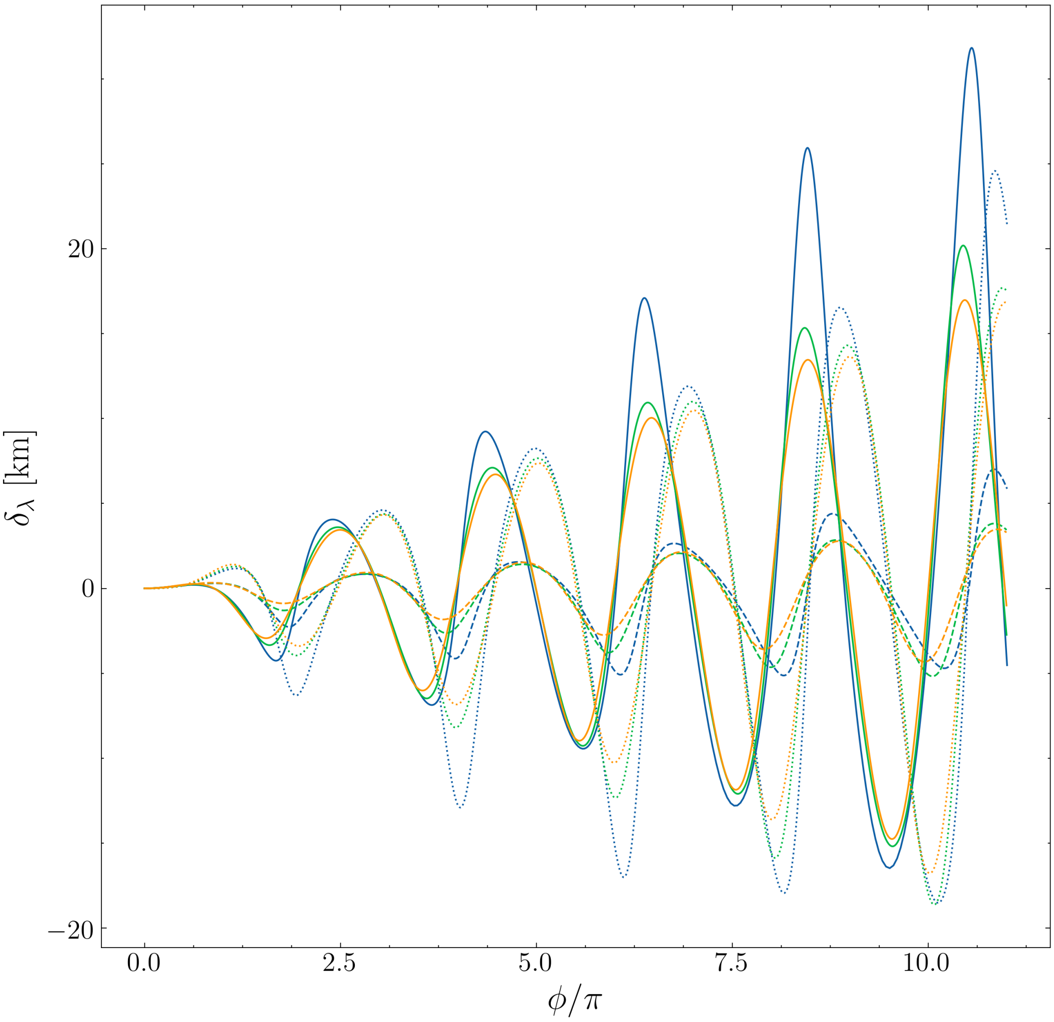

Fig. 7.2: Difference in the x, y, z coordinate variables (solid, dotted, dashed lines respectively) between a fast-spinning and non-spinning MSP, on a background quasi-Kerr spacetime with $\epsilon = 0.1$. The eccentricities are $e = 0.2, 0.4, 0.6$ (orange, green, blue respectively), with semi-major axis $= 50r_{\rm g}$, inclination $i = 0$ whilst the BH mass $M = 4.3 \times 10^6 M_\odot$, $a = 0.6$. Periodic variations are seen as the MSP passes through periapsis, with greater magnitude variations for more eccentric orbits.

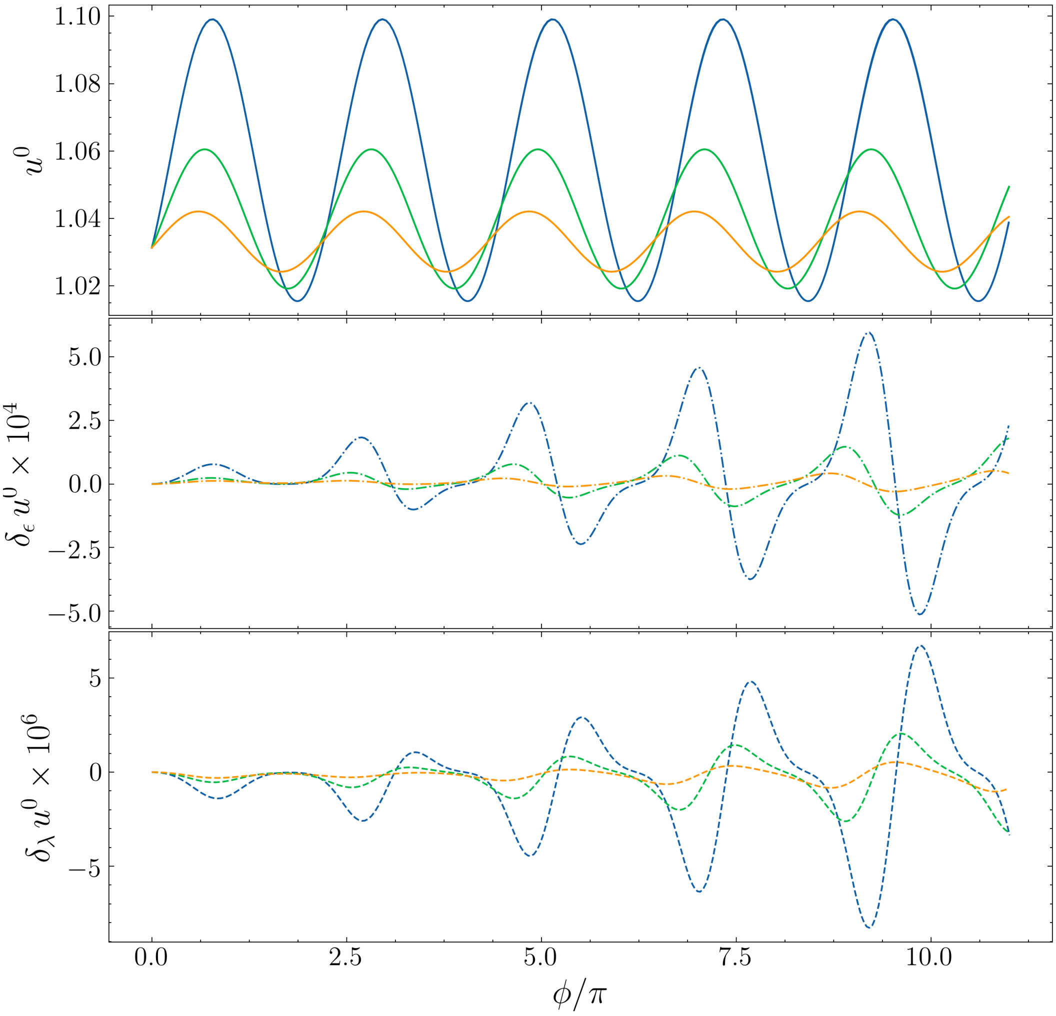

Fig. 7.3: The 0-th component of the MSP 4-velocity (top panel) for an MSP with orbital parameters, semi-major axis= $50r_{\rm g}$, $\iota = 0$, $e = 0.2, 0.4, 0.6$ (blue, orange, green respectively) around a BH of mass $M = 10^3 M_\odot$ and $a = 0.6$. Middle panel shows the corrections due to a non-Kerr quadrupole moment of $\epsilon = 0.1$ and the bottom panel shows the corrections due to the MSP spin couplings on a background quasi-Kerr spacetime.

3-vector $\boldsymbol{s}_1$ of an object of mass m_1 in a binary system with another object of mass m_2, spin vector $\boldsymbol{s}_2$ is given by (Kidder 1995),

$$\dot{\boldsymbol{s}}_1 = \frac{1}{r^3}\left[(\boldsymbol{L} \times \boldsymbol{s}_1)\left(2 + \frac{3}{2}\frac{m_1}{m_2}\right) - \boldsymbol{s}_1 \times \boldsymbol{s}_2 + 3\,(\hat{\boldsymbol{n}} \cdot \boldsymbol{s}_2)\,(\hat{\boldsymbol{n}} \times \boldsymbol{s}_1)\right] \tag{7.34}$$

where $\hat{\boldsymbol{n}}$ is the unit vector between the two bodies and $\boldsymbol{L}$ is the usual orbital angular momentum. The first term $(\boldsymbol{L} \times \mathbf{s}_1)$ describes the spin-orbit coupling and the other terms describe the spin-spin couplings. In a general relativistic context, the geodetic precession velocity of a gyroscope can be generally represented as (e.g. O'Connell 1969),

$$\Omega = \Omega_{\rm DS} + \Omega_{\rm LT} + \Omega_{\rm Q} \tag{7.35}$$

where $\Omega_{\rm DS}$, $\Omega_{\rm LT}$, $\Omega_{\rm Q}$ are the de Sitter (precession due to the BH mass), Lense-Thirring (due to the BH spin) and quadrupole contributions respectively. Via the MPD formalism on our quasi-Kerr spacetime we can consistently describe both the geodesic and spin coupling effects simultaneously.

Recall from Chapter 4 that the orientation of the spin axis can be described by the two Euler angles, $\theta_{\rm spin}$, which relates to the nutation and $\phi_{\rm spin}$ which describes the precession. These angles are given in the laboratory frame as,

$$\theta_{\rm spin} = \text{atan2}\left(\sqrt{S_x^2 + S_y^2}, S_z\right) \tag{7.36}$$

$$\phi_{\rm spin} = \text{atan2}\,(S_y, S_x) \tag{7.37}$$

where $S_{x,y,z}$ are the Cartesian components of the spin vector, related to s_μ as (see e.g. Eq.3.20, Eq. 3.11),

$$S_x = s_1 \sin(\theta)\cos(\phi) + s_2 r \cos(\theta)\cos(\phi) - s_3 r \sin(\theta)\sin(\phi) \tag{7.38}$$

$$S_y = s_1 \sin(\theta)\sin(\phi) + s_2 r \cos(\theta)\sin(\phi) + s_3 r \sin(\theta)\cos(\phi) \tag{7.39}$$

$$S_z = s_1 \cos(\theta) - s_2 r \sin(\theta) \tag{7.40}$$

The spin evolution in time of an MSP orbiting (equatorial, semi-major axis $= 50 r_{\rm g}$) an IMBH ($M = 10^3 M_\odot$, $a = +0.6$) are illustrated in Figs. 7.4, 7.5, over 5 orbits, along with corrections induced by spin couplings and the BH quadrupole moment, where initially $\theta_{\text{spin}} = \phi_{\text{spin}} = \pi/4$. For an MSP on a Kerr geodesic, θ_{spin} is described by Eq. 7.35 i.e. the nutation is governed solely by geodesic effects determined by the background spacetime. In this case θ_{spin} exhibits rapid, periodic variations as the MSP passes through periapsis. More eccentric orbits display greater magnitude variations in θ_{spin}, whilst also being more constrained in time. The introduction of a BH quadrupole with $\epsilon = 0.1$ induces additional contributions, with $\delta_\epsilon \theta_{\text{spin}} \sim \mathcal{O}(10^{-4})$. These contributions are periodic, with the periodicity set by the MSP orbital frequency. Since the strength of the quadrupole interactions is governed by the distance of the MSP from the central BH, more eccentric orbits (with closer periapsis distances) exhibit the largest magnitude variations. These large magnitude oscillations decay more rapidly than oscillations from less eccentric orbits and as a consequence $\delta_\epsilon \theta_{\text{spin}}$ can be greater at certain orbital phases for less eccentric systems. The spin-induced variations in θ_{spin} follow the same general pattern with rapid, periodic perturbations as the MSP passes through periapsis, albeit with a different time profile. In addition the λ-perturbations display a secular, long timescale behaviour due to the drastic change in θ_{spin} as the MSP comes out of periapsis. This is unlike the ϵ perturbations whereby $\delta_\epsilon \theta_{\text{spin}} \rightarrow\sim 0$ after the MSP has gone through periapsis. These spin-induced variations for the systems considered here are typically an order of magnitude smaller than those due to the quadrupole moment.

The precession of the spin axis $\phi_{\text{spin}}(\tau)$, follows the same general behaviour as θ_{spin} with rapid, large amplitude, periodic variations as the MSP goes through periapsis. However, there is also an additional secular contribution that causes ϕ_{spin} to generally increase with time. Moreover, the rapid change in ϕ_{spin} at periapsis is not oscillatory in the same way that θ_{spin} is, but can instead be seen to be a rapid 'jump'. The $\epsilon - \lambda$ induced variations also display the same general behaviour as in the θ_{spin} case, with $\delta_\epsilon \phi_{\text{spin}} \sim \mathcal{O}(10^{-3})$ and $\delta_\lambda \phi_{\text{spin}} \sim \mathcal{O}(10^{-5})$. However, this time the ϵ-corrections exhibit an additional secular contribution, whilst the λ-corrections are periodic.

For the same system in a retrograde orbit ($a = -0.6$), the evolution of the time component of the spin vector, s^0, is displayed in Fig. 7.6, along with the variations induced by the quadrupole moment of the BH. This variation in s^0 is a strong-field relativistic phenomenon, since this component would remain constant in the usual PN formulation (see discussion of this issue in Li et al. 2019). The exact physical meaning of the temporal component of the spin vector s_0 is not well understood, although it can be shown to have some relation to the difference in the centre of mass and the centre of momentum. In addition, from the SSC (Eq. 3.7) it can be shown by dividing by u^0 that the time component of the covariant form of the spin vector is

$$s_0 = -\left(s_1 \frac{dr}{dt} + s_2 \frac{d\theta}{dt} + s_3 \frac{d\phi}{dt} \right) \tag{7.41}$$

which describes the spatial components of a spin vector (i.e. the 3-vector) as measured by a static observer. Since u^0 is related to the relativistic time dilation, s_0 may also be related to the relativistic aberration of light. From Fig. 7.6 we can see that for each of the eccentric orbits s^0 oscillates with rapid variations as the MSP goes through periapsis. The presence of the quadrupole moment induces an additional variation in s^0 on the scale of $\sim 1\%$.

7.3 Astrophysical/Observational Implications

7.3.1 Radio Pulsar Timing

There are expected to be large populations of MSPs at the centre of the Galaxy (Wharton et al. 2012; Rajwade et al. 2017) whilst Globular clusters are also known to harbour large numbers of MSPs (Hui et al. 2010; Pan et al. 2016). The detection of an MSP with a BH companion in the centre of these stellar clusters is a major target for advanced radio facilities such as the SKA (Combes 2015) or the NASA Deep Space Network (Majid et al. 2019; Pearlman et al. 2019). Whilst these systems are scientifically rich, they also inhabit the gravitational strong field and so radio timing in these regimes encounters additional challenges not experienced by standard weak-field pulsar observations (see e.g. Kimpson et al. 2019a). We will now discuss the implications of the spin-orbital dynamics for strong-field pulsar astronomy.

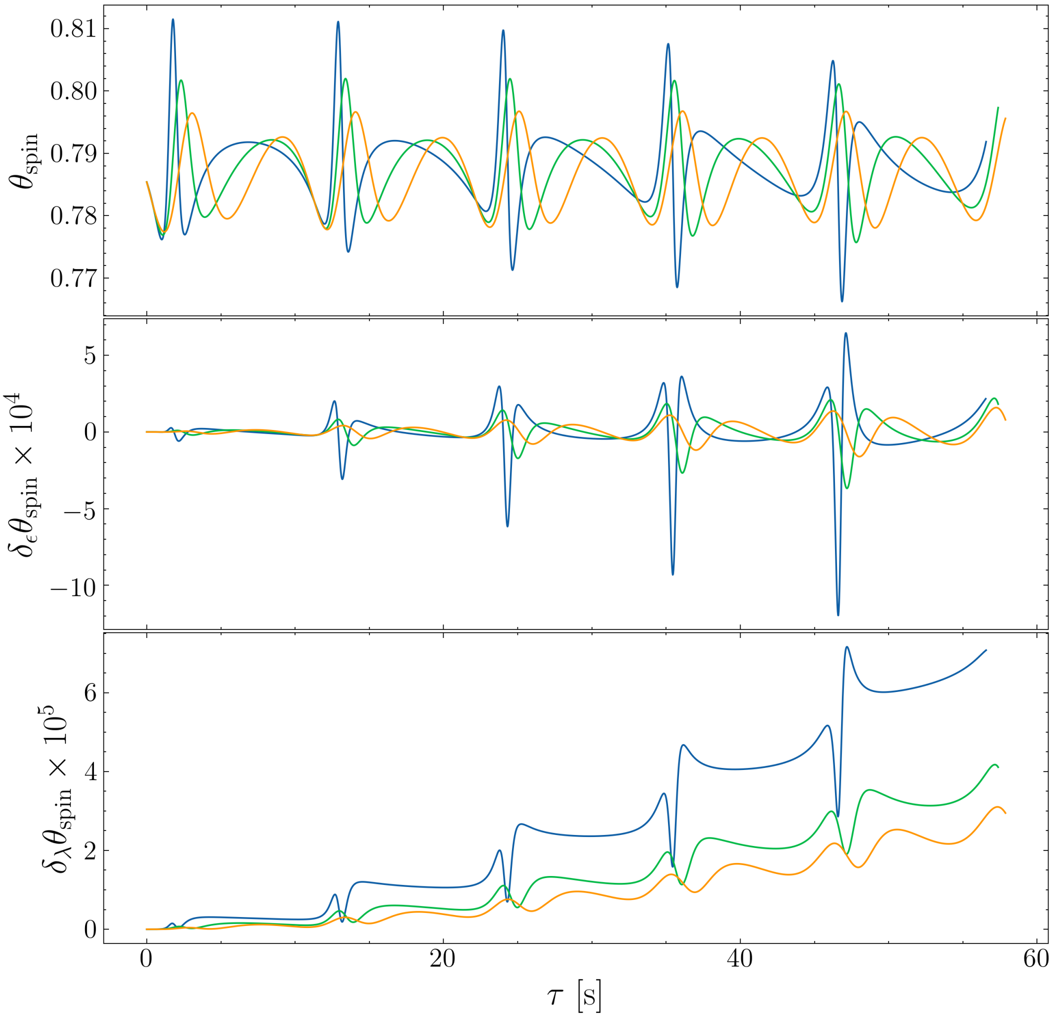

Fig. 7.4: *Top panel:* The nutation of the MSP spin axis due to geodetic and spin coupling effects for a MSP with spin period 1 ms, semi-major axis $50 r_{\rm g}$ around a BH with $M = 10^3 M_\odot, a = +0.6$, and eccentricities $e = (0.6, 0.4, 0.2)$ (blue, green,orange). Rapid variations are seen as the MSP passes through periapsis, with larger magnitude oscillations for more eccentric orbits. *Middle panel:* Quadrupole induced corrections to the nutation. These are periodic and maximal when the MSP is closest to the BH. *Bottom panel:* Spin-induced corrections to the nutation. These again are periodic and also display a secular behaviour.

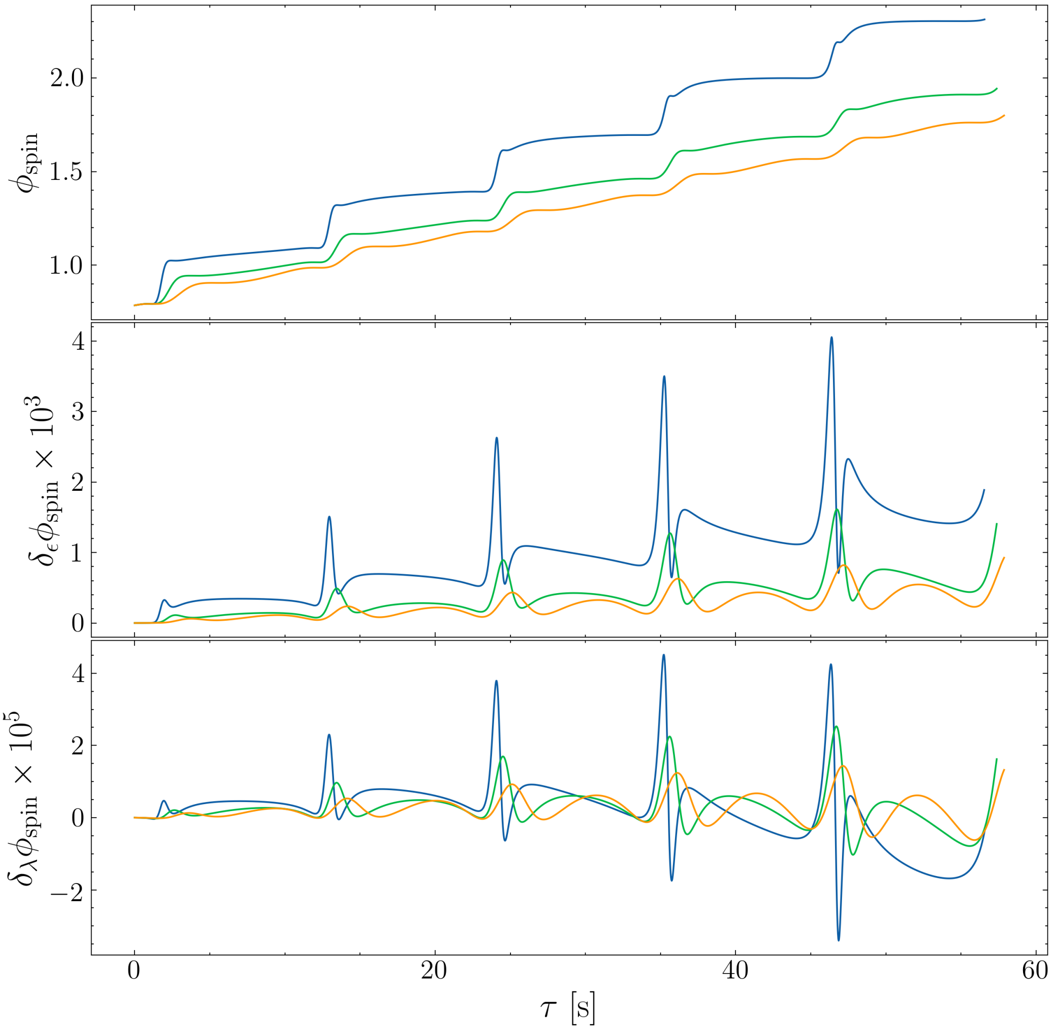

Fig. 7.5: As Fig. 7.4, but for the precession of the MSP spin axis. The precession exhibits rapid 'jumps' as the MSP goes through periapsis which causes a general secular, step-wise increase in the precession angle. The corrections due to $\epsilon-\lambda$ effects exhibit the same general behaviour as in the nutation.

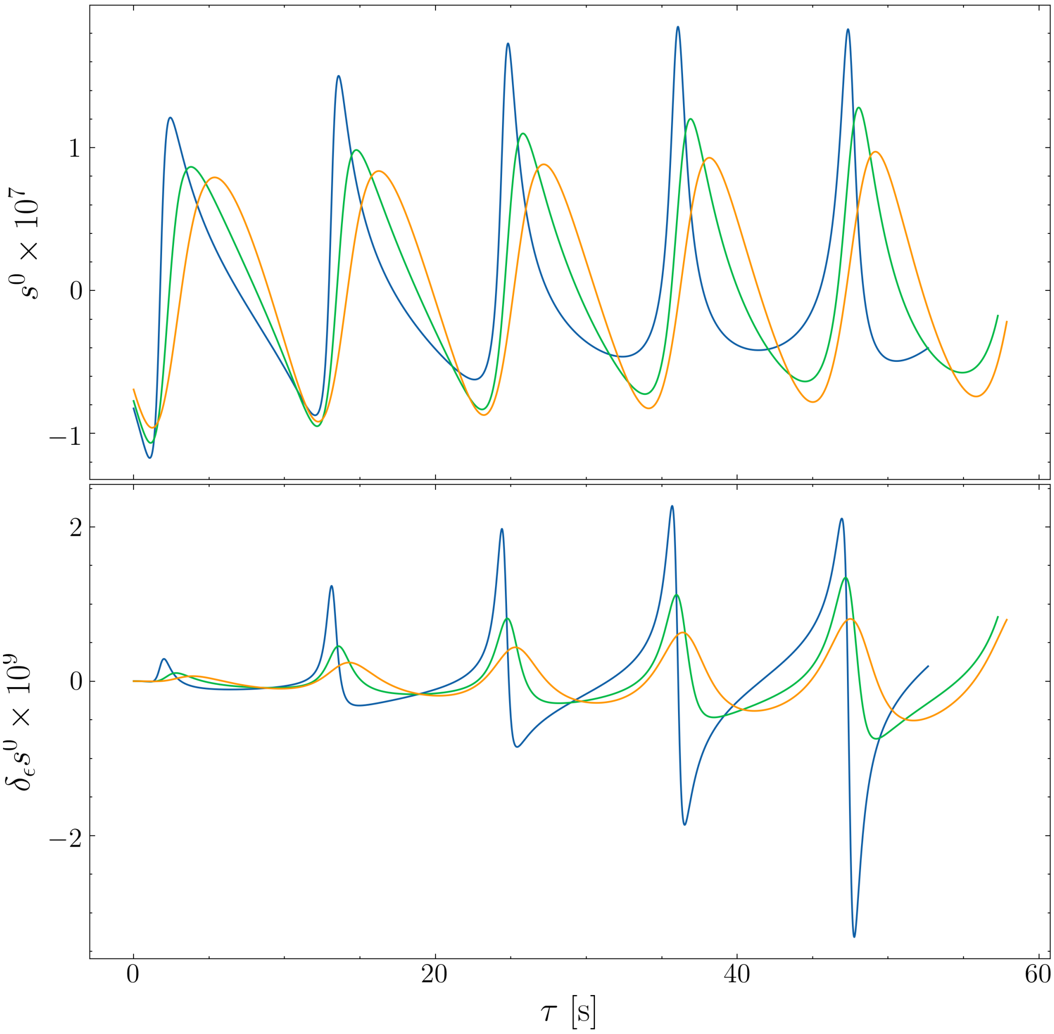

Fig. 7.6: *Top panel:* Time evolution of s^0 due to the breaking of the spacetime rotational symmetry as a consequence of the MSP spin. Rapid variations in s^0 are seen as the MSP passes through periapsis, with greater amplitude oscillations for more eccentric systems. *Bottom panel:* The difference in s^0 induced by a quadrupole moment $\epsilon = 0.1$ as compared to the Kerr ($\epsilon = 0$) case. The quadrupole moment induces a relative error on the order of 1%. The BH has parameter $M = 10^3 M_\odot, a = -0.6$.

Implications of Orbital Dynamics

The orbital motion of the MSP is determined by the background spacetime, and the dynamical spin interaction of the MSP with this gravitational field. Consequently, as we have shown, the quadrupole moment of the central massive BH and the spin couplings of the MSP will lead to variations in the coordinate position of the MSP. In turn, the variation in the coordinate variables of the MSP (e.g. Fig. 7.1) compared to the geodesic case will manifest observationally in the radio MSP timing solution. Firstly the additional $\epsilon - \lambda$ contributions will cause pericentre angle ω and the projected semi-major axis $x = a \sin i / c$ to exhibit a secular evolution (see e.g. Wex & Kopeikin 1999). The magnitude of this effect is sub-dominant to the effect of the BH mass and spin and so as noted in Wex & Kopeikin (1999) these secular effects may not be a useful may to actually measure the BH quadrupole. However, when constructing a complete MSP timing solution over longer time scales and several orbital periods it will be import to include the contributions of the spin couplings and the BH quadrupole to the orbital precession rate.

Rather than secular effects, the periodic effects induced by the quadrupole moment of the MSP have been identified as a more fruitful avenue for measuring the BH quadrupole moment. In particular, the periodic variations in the MSP coordinate position will manifest in changes in the Roemer delay of the pulsar. The Roemer delay is given by

$$\Delta_{\mathrm{R}} = \frac{1}{c} \hat{\boldsymbol{K}} \cdot \boldsymbol{x} \tag{7.42}$$

where $\hat{\boldsymbol{K}}$ is the position unit vector of the observer and $\boldsymbol{x}$ the position vector of the MSP. Variations in the Roemer delay induced by the quadrupole will manifest in the MSP TOA residuals. The Roemer delay for a MSP-BH system is shown in Fig 7.7, along with the residuals induced by both the quadrupole moment and the MSP spin couplings. We consider a Galactic Centre-like MSP-BH system with BH mass $4.31 \times 10^6 M_{\odot}, a = +0.6$, and set the MSP to have eccentricity $e = 0.9$ and consider 3 orbital periods $P = 0.1, 0.05, 0.01$ years. We set the observer at an orientation $\Theta = \pi/4$. For all these systems the Romer delay is a periodic function which varies on the scale of $\sim$ hours. The presence of a quadrupole moment $\epsilon = 0.1$ leaves the background gravitational field anisotropic and introduces a periodic timing residual. For $P = 0.1$ years, this quadrupole-induced residual $\delta_{\epsilon}\Delta_{\rm R}$ is of the order 1 seconds, whilst when $P = 0.01$ years, $\delta_{\epsilon}\Delta_{\rm R}$ is of the order of tens of seconds. Both of these residuals are well within the purview of MSP radio timing precision; the SKA is expected to enjoy timing precision in the range 10-100 ns (Liu et al. 2011; Stappers et al. 2018). In addition to the quadrupole-induced residuals, the spin couplings also introduce additional periodic variations. The potential degeneracy between these two effects will be briefly discussed later in Section 7.3.1. These spin residuals are of the order 100's μs for $P = 0.01$ years and $\sim 10\mu$s for $P = 0.1$ years. Again this is well within typical radio pulsar timing precision and so for a consistent, accurate, phase connected timing solution for precision parameter estimation of the system parameters it will be important to account for these spin effects. We have solely considered here a quadrupole moment of $\epsilon = 0.1$. If this quadrupole moment is smaller then naturally the magnitude of $\delta_{\epsilon}\Delta_{\rm R}$ will decrease whilst the magnitude of $\delta_{\lambda}\Delta_{\rm R}$ will remain unchanged. As a consequence the spin couplings could become a substantial fraction of the Roemer residuals. This again highlights the importance of a general covariant timing solution that can be applied to strong field environments for eccentric MSPs, especially if we want to use these systems for precision tests of strong-field GR; since the $\delta_{\lambda}\Delta_{\rm R}$, $\delta_{\epsilon}\Delta_{\rm R}$ follow the same general time evolution, with periodic signatures as the MSP passes through periapsis, unmodelled spin effects could imitate a non-Kerr quadrupole leading to a confusion problem for certain orbital parameters. Further, the influence of the quadrupole and spin couplings are most pronounced for close periapsis passages. Since eccentric orbits are the most desirable from the perspective of testing strong field GR, probing the quadrupole and reducing the influence of external perturbations, this is an influence that needs to be accounted for.

As noted in Fig. 7.3, due to the motion of the pulsar and the associated relativistic time dilation, pulsar signals also suffer a timing delay known as the

Einstein delay, $\Delta_{\rm E}$. This delay quantifies the difference between the coordinate t and proper τ times of the pulsar, i.e.

$$\Delta_{\rm E} = t - \tau \tag{7.43}$$

Given the nature of a pulsar as a highly accurate clock, if the intrinsic rotation period of the pulsar can be established, the Einstein delay can in turn be calculated. The Einstein delay is a relativistic effect that is naturally induced through a geodesic description of the pulsar's motion. In addition, there are further contributions that arise from the quadrupole and spin. The Einstein delay for the Galactic centre systems described above is presented in Fig. 7.8. The Einstein delay accumulates over ~ 5 orbital phases to ~ 4.5 hrs for the system with $P = 0.01$ years and up to 9 hrs for the system with $P = 0.1$ years, with rapid increases as the pulsar passes through periapsis, and a general secular evolution otherwise. The quadrupole moment induces an error in the timing solution of the Einstein delay on the order of $0.1 - 1$ s, with MSP systems with shorter orbital periods most drastically affected ($\delta_{\epsilon}\Delta_{\rm E}$ peaks at $\sim$ 6s for $P = 0.01$ year). The error introduced due to the spin couplings is again subdominant to the quadrupole moment, of the order $1 - 10\mu$s. Both the quadrupole and spin residuals follow the same general profile, with periodic rapid variations as the MSP passes through periapsis. As noted for the Roemer delay this could introduce additional complications to consistently model the MSP timing signal accounting for both spin couplings and the (unknown) quadrupole moment.

Implications of Spin Dynamics

Pulsar emission is not isotropic, but beamed. The misalignment between the magnetic axis $\boldsymbol{B}$ and the spin axis $\boldsymbol{S}$ is what causes the observed pulsed emission. The evolution of the spin axis can strongly influence the radio timing observations. Precession and nutation of the spin axis will directly influence the photon arrival times in addition to affecting the pulse profile, intensity and observed pulse frequencies (Li et al. 2019; Kimpson et al. 2019a; Kocherlakota et al. 2019). The characteristic change in the pulse frequency due to spin precession has also been suggested as a mechanism for measuring

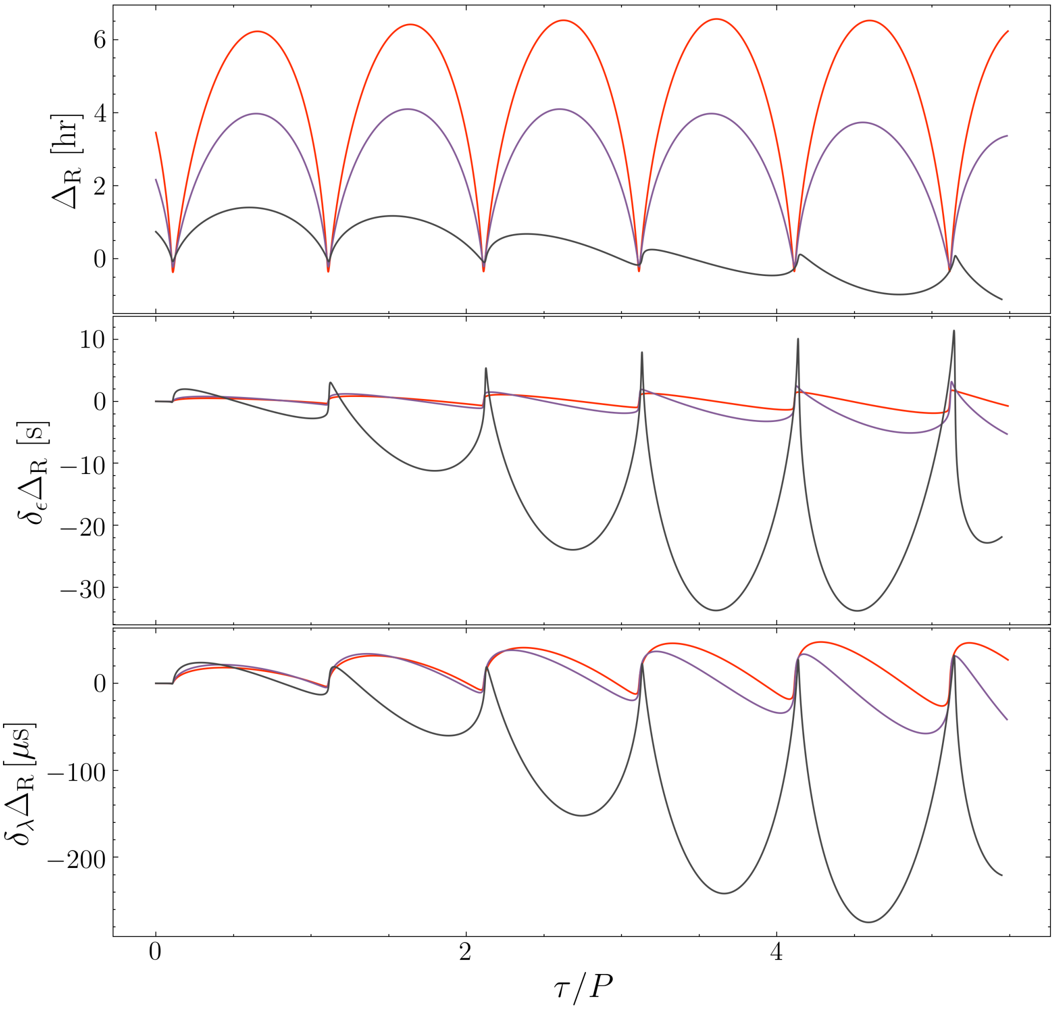

Fig. 7.7: *Top panel:* Romer Delay of an MSP orbiting the Galactic centre Sgr A* BH with $e = 0.9$ and orbital period $P = 0.1, 0.05, 0.01$ years (red, purple, black lines respectively). The distant observer is located at $\Theta = \pi/4$. The Roemer delay varies periodically due to the eccentric orbital motion of the MSP. *Middle panel:* The quadrupole-induced difference in the Roemer Delay (i.e. the timing residuals). MSPs with shorter orbital periods have greater timing residuals due to the quadrupole, but even for the longest period systems considered here the difference is of order 1s, easily withing pulsar radio timing precisions. *Bottom panel:* The timing residuals in the Roemer delay induced by spin couplings. Note the similar profile with the quadrupole-induced residuals.

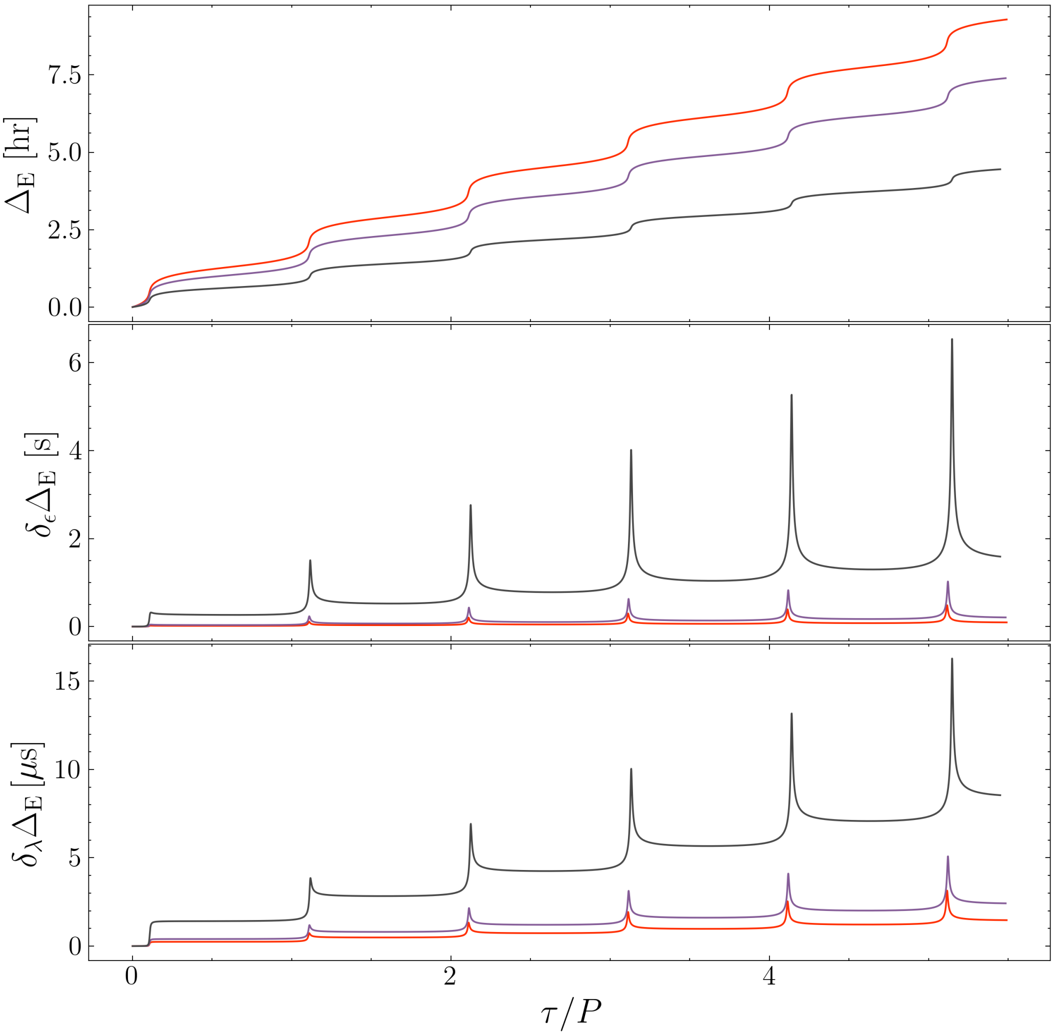

Fig. 7.8: *Top panel:* Einstein delay of a Galactic Centre MSP with orbital period P=$0.1, 0.05, 0.01$ years and eccentricity $e = 0.9$. The Einstein delay accumulates to ~ 9 hrs for the longer period system and ~ 4.5 hrs for the shorter period system. *Middle panel:* Residuals in the timing solution to the Einstein delay due to the BH quadrupole moment with $\epsilon = 0.1$. *Bottom panel:* Timing residuals in the Einstein delay due to the MSP spin couplings.

the spin parameter of the central black hole and establishing the validity or otherwise of the Cosmic Censorship Conjecture (Kocherlakota et al. 2019). The influence of the pulsar spin axis orientation on the pulsar timing signal and the profile shape was described in Section 4.2.2. We now briefly review the main results and further explore the influence of the BH quadrupole and the MSP spin couplings.

To explore the impact of the spin dynamics on the MSP radio timing we consider the evolution of the pulsar radiation axis in terms of a rotating vector model. If $\psi, \chi(\tau)$ define the polar and azimuthal angles of the radiation beam about the pulsar spin axis (we do not consider the time evolution of the polar angle), then the evolution of the magnetic axis 3-vector is related to the spin axis as,

$$\boldsymbol{B}(\tau) = \boldsymbol{R}_{\mathrm{z}}(\phi_{\mathrm{spin}}(\tau))\boldsymbol{R}_{\mathrm{y}}(\theta_{\mathrm{spin}}(\tau)) \begin{pmatrix} \sin\psi\cos\chi(\tau) \\ \sin\psi\sin\chi(\tau) \\ \cos\psi \end{pmatrix} \tag{7.44}$$

where $\boldsymbol{R}_{z,y}$ are the 3-space rotation matrices about the coordinate z and y axes respectively. We label the observer direction by the vector $\boldsymbol{O}$. This vector can be considered as the vector which is tangent to the asymptote that converges at the observer in a flat spacetime. Recall from Chapter 4 that the 'pitch angle' ω between the radiation vector and the observer vector is then defined via,

$$\cos\omega = \hat{\boldsymbol{B}} \cdot \hat{\boldsymbol{O}} \tag{7.45}$$

for unit vectors $\hat{\boldsymbol{B}}, \hat{\boldsymbol{O}}$. We define the pulse arrival time (i.e. the time centre of the pulse profile) to occur when the pitch angle is at a minimum, subject to bounds on the value of the pitch angle (the beam will not be 'seen' if the pitch angle is $\pi/2$ for example). For example, if in an orthonormal basis the observer is in direction $\hat{\boldsymbol{O}} = (1, 0, 0)$, then the pitch angle is minimized and the centre of the pulse intersects with the observer's line of sight when the radiation vector points in the same direction, $\hat{\boldsymbol{B}} = (1, 0, 0)$. This gives us the condition that the pulse arrival time occurs when the beam phase $\chi(\tau)$ obtains some critical value χ_c, at which $\partial_\tau \omega = 0$. Now, since the pulsar spin timescale (~ 1 ms) is much shorter than the precession and nutation timescales of the spin axis, we can employ a two timescale approximation and neglect the evolution of $\theta_{\rm spin}, \phi_{\rm spin}$ over the MSP rotation period. If we specify that the polar angle of the radiation beam with respect to the spin axis is $\psi = \pi/4$, and the observer is at $\Theta = \pi/4, \Phi = 0$ then then the critical phase angle is:

$$\chi_c = \arccos \left[\frac{\cos\phi_{\rm spin}\cos\theta_{\rm spin} - \sin\theta_{\rm spin}}{\sqrt{\cos^2\phi_{\rm spin}\cos^2\theta_{\rm spin} + \sin^2\phi_{\rm spin} + \sin^2\theta_{\rm spin} - \cos\phi_{\rm spin}\sin 2\theta_{\rm spin}}} \right] \tag{7.46}$$

From this equation we can see that both the precession ($\phi_{\rm spin}$) and the nutation ($\theta_{\rm spin}$) contribute to the critical phase angle. The extra phase angle than must be traversed in order to reach the centre of the pulse profile ($\delta\chi_c$, i.e. the variation in the value and evolution of χ_c such that $\delta\chi_c = \chi_c(\tau) - \chi_c(0)$) will directly influence the observed pulse frequency. In this way, variations in the spin axis can directly imprint on the pulsar timing solution. Naturally, for variations of sufficient magnitude the spin axis variation would be so severe that the minimum of ω would be greater than the beam width and so no emission would be observed. A difference in the critical phase value is related to a timing delay as,

$$\Delta t = \frac{P_s}{2\pi}\delta\chi_c \tag{7.47}$$

for MSP spin period P_s. The pulse timing delay due to the time evolution of the pulsar spin axis is shown in Figure 4.6. The BH quadrupole and the MSP spin couplings can then further imprint on the pulsar timing solution, since both of these effects influence the precession and nutation of the MSP spin axis. The additional variation in the timing delay due to these effects is shown in Fig. 7.9. The presence of a non-Kerr quadrupole induces an additional timing delay as the MSP passes through periapsis, of the order of $\sim 100's$ ns. Whilst this timing delay is less than those induced by the quadrupole for e.g. the Roemer or Einstein delays, it is at the limit of MSP timing precision and the residuals also have a distinctive characteristic profile that may leave them important for real astrophysical systems. The residuals induced by the spin for the system considered here are of the order a few ns, which are unlikely to be detectable via radio timing. Naturally as the orbital radius decreases and these systems spend more time in the strong field regime the manifestation of the spin axis evolution and the contributions from the spin couplings will become more important, but we restrict ourselves here to more astrophysically likely orbital configurations.

The preceding discussion dealt with the timing delay due to the shift of the centroid of the pulse profile. In addition, the nutation of the spin axis will influence the pulse profile by modifying the observed pulse width. The beam width can be defined as,

$$w = \chi_1 - \chi_2 \tag{7.48}$$

where χ_1, χ_2 correspond to the beam phase at the edges of the emission cone, where $\omega = \pm\gamma$, for beam half opening angle γ. Taking the observer to be at $\Theta = \pi/4$, and under the assumption that the precession angle ϕ does not significantly influence the beam width, then it follows that:

$$w = 2\cos^{-1}\left(\frac{1.41\cos\gamma\csc\psi - \cos\theta\cot\psi - \sin\theta\cot\psi}{\cos\theta - \sin\theta}\right) \tag{7.49}$$

The evolution of the pulse width, along with the corrections induced by the quadrupole moment and the MSP spin couplings are shown in Fig. 7.10, for a MSP orbiting a 47-Tuc like IMBH, with $a = -0.6$ and semi major axis $= 200r_\mathrm{g}$. It can be seen that the pulse width varies due to the nutation of the spin axis on the order of $\sim 4\%$. The corrections to the pulse width due to the $\epsilon - \lambda$ effects are smaller, of order 10^{-4} and 10^{-5} respectively for $\epsilon = 0.1$. Whilst these are small absolute numbers, the nature of MSP timing requires stacking and folding multiple pulse profiles. It is this method which leaves pulse timing so particularly sensitive; for example the pulsar PSR J0437-4715 has a spin period measured as $P_s = 5.757451924362137$ ms (Verbiest et al. 2008), which is a measurement to a precision $\sim 10^{-15}$. Consequently, even small variations in the pulse profile can prove important.

Additional comments

The timing residuals caused by the BH quadrupole and the MSP spin also raise the potential for a confusion problem: can an observer distinguish the

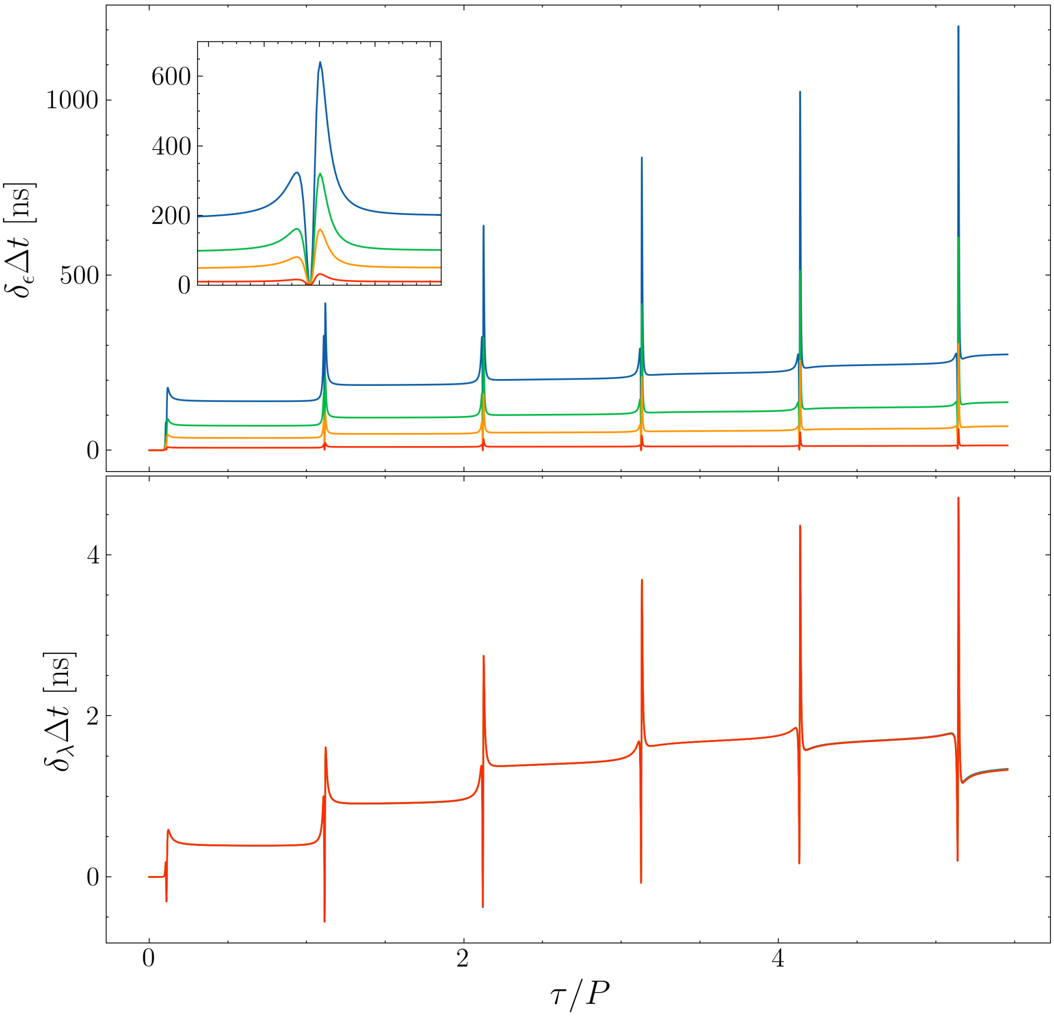

Fig. 7.9: *Top panel:* The timing residuals induced by the BH quadrupole, $\epsilon = 0.01, 0.05, 0.1, 0.2$ (red, orange, green, blue respectively) for the MSP-IMBH system described above, with $e = 0.9$. The additional precession and nutation induced by the BH quadrupole leads to timing delays of the order 100's ns, with a characteristic profile as the MSP passes through periapsis. *Bottom panel:* Residuals due to the spin couplings, which are of the order a few ns, which are likely beyond the timing precision of radio facilities. Systems with shorter orbital periods will exhibit stronger spin couplings and the associated timing delays.

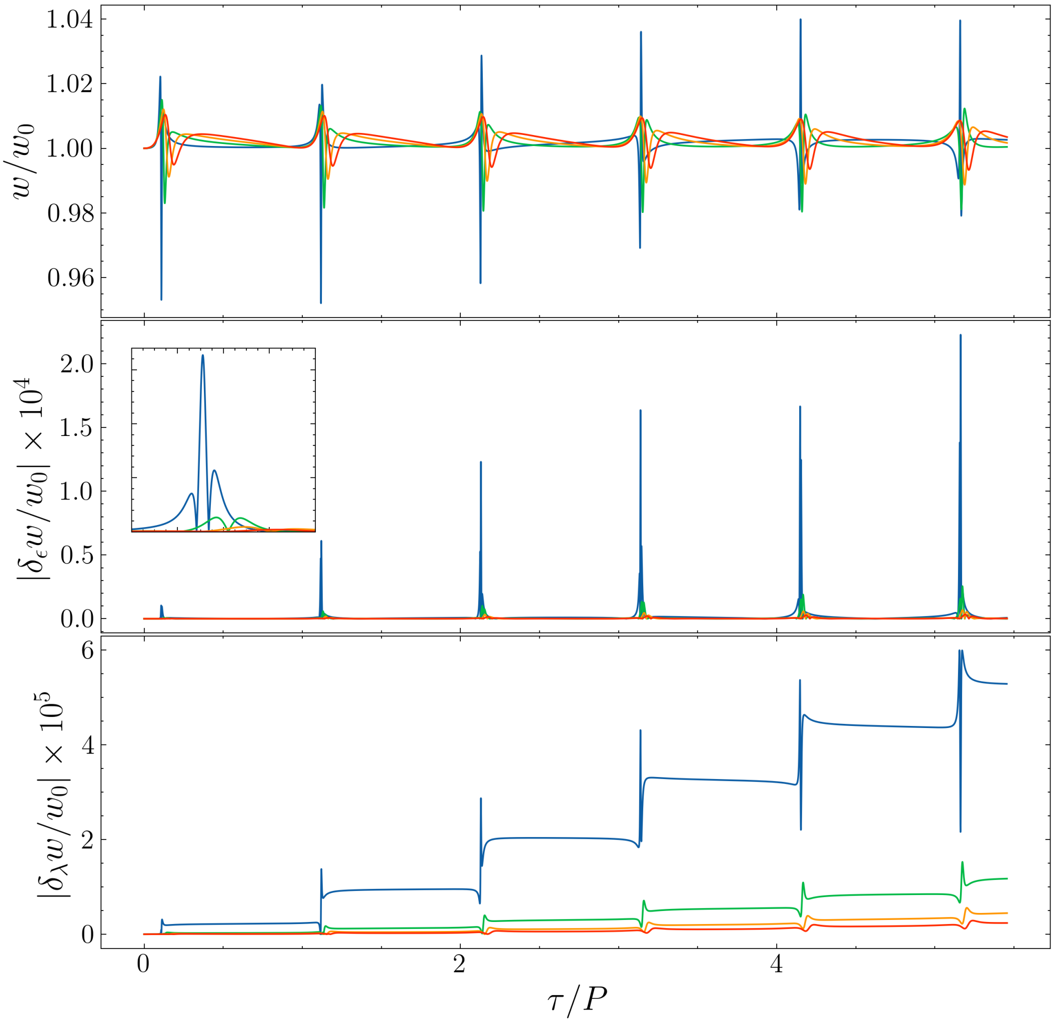

Fig. 7.10: *Top panel:* Change in the pulsar beam width for a MSP initially with $\theta_{\rm spin} = \pi/6, \phi_{\rm spin} = 0$, $\psi = \pi/12$, semi-major axis $= 200 r_{\rm g}$ when in a retrograde orbit about an IMBH with $M = 2.2 \times 10^3 M_\odot$, $a = -0.6$, eccentricities $e = 0.9, 0.8, 0.7, 0.6$ (blue, green, orange, red respectively). For $e = 0.9$, the pulse width changes by $\sim 4\%$, for $e = 0.6$ the change is $\sim 1\%$. *Middle panel:* Variation in w/w_0 induced by the BH quadrupole $\epsilon = 0.1$. Rapid variations with distinctive structure are seen as the MSP passes through periapsis. *Bottom panel:* Variations in w/w_0 induced by the MSP spin.

behaviour of e.g. a non-Kerr metric with some set of orbital/pulsar parameters with the Kerr metric for some different orbital/pulsar parameters? Moreover, the $\epsilon - \lambda$ residuals exhibit similar profiles (e.g. Figs. 7.7, 7.8, 7.9), with rapid, periodic variations at periapsis. This introduces a further uncertainty for the observer: is this variation due to the spin couplings or the BH quadrupole moment? For the example systems considered in this work with $\epsilon = 0.1$, the quadrupole variations are typically larger than the spin variations. In this case the spin couplings introduce an effective uncertainty into the quadrupole residuals. Self-force effects due to the mass of the MSP itself perturbing the background spacetime (see Barack & Pound 2019) could also influence the timing signal, leading to an additional confusion source. From this it is clear that it is essential to understand and model the effect of spin couplings on pulsar ToAs in a relativistic setting. Furthermore, we have not fully explored the astrophysically relevant parameter space - instead considering just typical example systems - and for different orbital parameters or smaller values of ϵ the spin effects will become comparable. We have also not explored the influence of the BH spin parameter on the PSR timing signal (e.g. Zhang & Saha 2017) or considered systems with a MSP and a stellar mass BH (e.g. Oscoz et al. 1997). Additionally, exploring the influence of the $\epsilon - \lambda$ on the gravitational burst waveforms that are expected from these systems (e.g. Berry & Gair 2013b; Kimpson et al. 2020a) would be an interesting further development of this work.

Moving from the time to the frequency domain, the $\epsilon - \lambda$ effects are also generally important since they intrinsic additional frequencies that must be accounted for in the Fourier analysis, particularly with regards to the evolution of the spin axis. Whilst a single isolated pulsar would exhibit one characteristic frequency set by the spin period, a MSP in the gravitational strong field would have multiple peaks in the frequency spectra. As noted in Kocherlakota et al. (2019), this multi-peaked frequency spectra may provide a further method to extract the BH parameters.

7.3.2 E/IMRI Waveform Modelling

Waveform modelling from ∼stellar mass compact objects inspiraling in to much more massive BHs (Extreme/intermediate Mass Ratio Inspirals, E/IMRIs) is currently an essential research area (van de Meent 2017; Barack & Pound 2019). The detection of gravitational radiation from these systems with LISA will allow precision tests of the dynamical strong field. The eccentric systems considered in this work are particularly relevant as LISA E/IMRI sources; unlike the BH-BH binaries detected by LIGO, E/IMRIs are expected to retain significant eccentricities upon entering the LISA frequency band (Amaro-Seoane 2018) and so accounting for this eccentricity is key to both inform the detection of these systems, and subsequent precision parameter estimation. In addition to eccentricity, the $\epsilon - \lambda$ effects will also introduce additional variations that may need to be accounted for for accurate E/IMRI waveform modelling. E/IMRI systems are expected to be observed for a large $\sim 10^4$ number of cycles at compact radii and so small perturbations can lead to significant shifts in the waveform, especially as the orbiter goes through periapsis. Whilst the dominant contributions to the waveform come from the 0th and 1st order moments, higher order effects will prove important for accurate waveform modeling; it is know for example in circular systems that spin effects leading a to a dephasing of the waveform (Warburton et al. 2017). The convolution between the eccentricity, spin and quadrupole effects and the subsequent impact on the gravitational waveform would be an interesting further study, though beyond the scope of this paper.

7.4 Conclusion

In this work we have explored the orbital-spin dynamics of a MSP in an eccentric orbit around a massive BH with an arbitrary mass quadrupole via the MPD framework. The inclusion of the BH quadrupole and the MSP spin couplings lead to perturbations in the orbital and spin evolution of the MSP. For astrophysical systems such as pulsars at the Galactic centre or the centre of globular clusters, these effects will imprint on both the pulsar timing solution (detectable with radio telescopes such as FAST, SKA, DSN) and the gravitational waveform (detectable with mHz GW detectors such as LISA). Further development of this work would be interesting, for example constructing a fully consistent, phase-connected solution to consistently model the pulsar TOAs via a relativistic pulsar timing model (e.g. Kimpson et al. 2019a) accounting for not just the pulsar dynamics but also the photon ray geodesic (Shapiro delay, gravitational lensing, spatial and temporal dispersion etc.) This would then allow for a much greater understanding of the observational consequences of the effects described in this work.

Chapter 8

Future Work

The strong-field pulsar timing framework derived in this thesis is numerically straightforward to implement computationally and highly parallelisable. The mathematical formulation is also not limited to regimes where the gravitational field is weak, instead being generally applicable. The natural extension of this work is the development of these methods to simulate the radio time-frequency signal from an MSP orbiting a massive BH in the gravitational strong-field. Such an enterprise would provide accurate, self-consistent, relativistic synthetic timing data from an MSP at the Galactic centre or the centre of globular clusters. In turn, with this properly calculated synthetic data in hand, it is possible to thoroughly evaluate current pulsar search techniques when applied to regions like the Galactic centre and develop more advanced methods as needed. Moreover, the ability to generate relativistic pulsar timing models across a broad orbital parameter space would permit direct comparison with observations and the appraisal of current pulsar parameter estimation pipelines e.g. TEMPO (Hobbs et al. 2006). Whilst this work has examined the lowest-order modifications to GR and the influence on the strong-field pulsar timing signal, it would be highly desirable to explore higher-order variations, the influence of a central exotic compact object (e.g. a boson star) instead of a BH, and - ideally - the construction of a theory-independent formulation. As noted by Faucher-Giguère & Loeb (2011), the high stellar density in the Galactic centre may allow for the creation of some rare binaries (e.g. triple systems). The subsequent dynamics (e.g. Remmen &

Wu 2013) and impact on the MSP timing signal would be a further interesting pursuit. Further extensions include correcting for the non-spherical, oblate shape of the pulsar (e.g. Nättilä & Pihajoki 2018), which may in turn be used to inform the neutron star equation of state. Whilst Newtonian perturbations (e.g. Merritt et al. 2011) for sufficiently short orbital period systems are unlikely, it may prove prudent to also extend current methods for filtering out a Newtonian foreground (e.g. Angélil & Saha 2014) to the relativistic regimes in the Galactic centre. When examining the influence of astrophysical plasma on the pulsar light ray, we assumed a specific form for the density profile and took the plasma as being cold. Both of these assumptions could be further refined to more accurately describe the true astrophysical scenario. Similarly, we neglected the effects of hydrodynamic drag from the plasma on the pulsar orbit since it is expected that at compact radii relativistic effect will dominate (Psaltis 2012); the precision with which pulsar timing measurements can be made means that the even a small influence of drag could imprint on the timing solution and so this effect should be explored. Moreover, we have implicitly assumed a conal-like model for the pulsar radio beam - other models (e.g. a fan-beam model Saha & Dyks 2017) do exist and may influence our conclusions.

If we also consider burst gravitational radiation from MSP-BH systems, it would be highly desirable to build upon the work in this thesis by obtaining quantitative estimates of the improvement in parameter estimation uncertainty by coincident multimessenger GW burst and EM radio observations. In the case where one measurement is much better than the other one will not gain much, but in the case where the measurement uncertainties are comparable it may prove possible to split degeneracies and get significant improvements. Moreover, in this work I have considered only single bursting events; since these pulsars systems are on bound orbits one would expect repeated bursts which may improve the parameter estimation precision. Analogous to the exploration of a potential deviation of GR via the No Hair Theorem, it would also be of interest to investigate the influence of a non-Kerr quadrupole moment on the burst gravitational waveform. For waveform modelling of Extreme Mass Ratio Inspirals, a key factor is the presence of the gravitational self-force. The influence of the gravitational self-force on the pulsar signal may also be a fruitful development of this work and potentially provide an empirical resolution of the current mathematical challenges of constructing the self-force to sufficiently high ($\sim$ second order) accuracy (see e.g. Barack & Pound 2019). If we can detect a pulsar in a bound orbit around a massive black hole, the nature of pulsars as relativistic clocks allows us to map the worldline of the smaller compact object. With the worldline measured, it may then be possible to measure the deviation due to the self-force. This in turn could be used to inform or verify any second order self force model.

Bibliography

Aasi, J., Abadie, J., Abbott, B. P., et al. 2014, Phys. Rev. Lett., 112, 131101

Abbott, B. P., Abbott, R., Abbott, T. D., et al. 2016, Phys. Rev. Lett., 116, 061102

Abbott, B. P., Abbott, R., Abbott, T. D., et al. 2017a, Phys. Rev. Lett., 119, 161101

Abbott, B. P., Abbott, R., Abbott, T. D., et al. 2017b, Phys. Rev. Lett., 118, 221101

Ackermann, M., Ajello, M., Albert, A., et al. 2017, ApJ, 840, 43

Adámek, K., Novotný, J., Dimoudi, S., & Armour, W. 2019, arXiv e-prints, arXiv:1911.01353

Agol, E. 2000, ApJ, 538, L121

Aharon, D. & Perets, H. B. 2016, ApJ, 830, L1

Amaro-Seoane, P. 2018, Living Reviews in Relativity, 21, 4

Amaro-Seoane, P., Gair, J. R., Freitag, M., et al. 2007, Classical and Quantum Gravity, 24, R113

Amaro-Seoane, P. & Preto, M. 2011, Classical and Quantum Gravity, 28, 094017

Andersen, B. C. & Ransom, S. M. 2018, ApJ, 863, L13

Angélil, R. & Saha, P. 2014, MNRAS, 444, 3780

Aschenbach, B. 2010, MmSAI, 81, 319

Audet, C. & Dennis, J. 2006, SIAM Journal on Optimization, 17, 188

Babak, S., Fang, H., Gair, J. R., Glampedakis, K., & Hughes, S. A. 2007, Phys. Rev. D, 75, 024005

Babak, S., Gair, J., Sesana, A., et al. 2017, Phys. Rev. D, 95, 103012

Baker, J., Bellovary, J., Bender, P. L., et al. 2019, arXiv e-prints, arXiv:1907.06482

Bambi, C. 2011, Modern Physics Letters A, 26, 2453

Bambi, C., Jiang, J., & Steiner, J. F. 2016, Classical and Quantum Gravity, 33, 064001

Barack, L. & Cutler, C. 2004, Phys. Rev. D, 69, 082005

Barack, L. & Cutler, C. 2007, Phys. Rev. D, 75, 042003

Barack, L. & Pound, A. 2019, Reports on Progress in Physics, 82, 016904

Barausse, E., Hughes, S. A., & Rezzolla, L. 2007, Phys. Rev. D, 76, 044007

Bartels, R., Krishnamurthy, S., & Weniger, C. 2016, Phys. Rev. Lett., 116, 051102

Bates, S. D., Johnston, S., Lorimer, D. R., et al. 2011, MNRAS, 411, 1575

Baumgardt, H. 2017, MNRAS, 464, 2174

Bekenstein, J. D. 1973, ApJ, 183, 657

Bender, R., Kormendy, J., & Dehnen, W. 1996, ApJ, 464, L123

Berry, C., Hughes, S., Sopuerta, C., et al. 2019, BAAS, 51, 42

Berry, C. P. L. & Gair, J. R. 2013a, MNRAS, 433, 3572

Berry, C. P. L. & Gair, J. R. 2013b, MNRAS, 429, 589

Berti, E., White, F., Maniopoulou, A., & Bruni, M. 2005, MNRAS, 358, 923

Bertotti, B., Iess, L., & Tortora, P. 2003, Nature, 425, 374

Bin-Nun, A. Y. 2010, Phys. Rev. D, 82, 064009

Blandford, R. & Teukolsky, S. A. 1976, ApJ, 205, 580

Boehle, A., Ghez, A. M., Schödel, R., et al. 2016, ApJ, 830, 17

Bortolas, E. & Mapelli, M. 2019, MNRAS, 485, 2125

Bower, G., Chatterjee, S., Cordes, J., et al. 2019, BAAS, 51, 438

Bozza, V. & Mancini, L. 2009, The Astrophysical Journal, 696, 701

Bozza, V. & Mancini, L. 2012, ApJ, 753, 56

Bramante, J. & Linden, T. 2014, Phys. Rev. Lett., 113, 191301

Broderick, A. & Blandford, R. 2003, MNRAS, 342, 1280

Broderick, A. E., Fish, V. L., Doeleman, S. S., & Loeb, A. 2009, ApJ, 697, 45

Broderick, A. E., Fish, V. L., Doeleman, S. S., & Loeb, A. 2011, ApJ, 735, 110

Broderick, A. E. & Loeb, A. 2005, MNRAS, 363, 353

Burgay, M., D'Amico, N., Possenti, A., et al. 2003, Nature, 426, 531

Burrows, D. N., Kennea, J. A., Ghisellini, G., et al. 2011, Nature, 476, 421

Cadelano, M., Ransom, S. M., Freire, P. C. C., et al. 2018a, ApJ, 855, 125

Cadelano, M., Ransom, S. M., Freire, P. C. C., et al. 2018b, ApJ, 855, 125

Camilo, F. & Rasio, F. A. 2005, in Astronomical Society of the Pacific Conference Series, Vol. 328, Binary Radio Pulsars, ed. F. A. Rasio & I. H. Stairs, 147

Campitiello, S., Celotti, A., Ghisellini, G., & Sbarrato, T. 2019, arXiv e-prints, arXiv:1907.00986

Carroll, S. 2003, Spacetime and Geometry: An Introduction to General Relativity (Benjamin Cummings)

Carson, Z. & Yagi, K. 2020, Phys. Rev. D, 101, 084050

Carter, B. 1968, Physical Review, 174, 1559

Carter, B. 1971, Phys. Rev. Lett., 26, 331

Chaibi, W., Geiger, R., Canuel, B., et al. 2016, Phys. Rev. D, 93, 021101

Chennamangalam, J. & Lorimer, D. R. 2014, MNRAS, 440, L86

Chicone, C., Mashhoon, B., & Punsly, B. 2005, Physics Letters A, 343, 1

Chua, A. J. K. & Gair, J. R. 2015, Classical and Quantum Gravity, 32, 232002

Chua, A. J. K., Moore, C. J., & Gair, J. R. 2017, Phys. Rev. D, 96, 044005

Colbert, E. J. M. & Miller, M. C. 2006, in The Tenth Marcel Grossmann Meeting. On recent developments in theoretical and experimental general relativity, gravitation and relativistic field theories, 530

Combes, F. 2015, Journal of Instrumentation, 10, C09001

Cordes, J. M., Shannon, R. M., & Stinebring, D. R. 2016, ApJ, 817, 16

Cornish, N. & Robson, T. 2017, in Journal of Physics Conference Series, Vol. 840, Journal of Physics Conference Series, 012024

Cutler, C. & Flanagan, É. E. 1994, Phys. Rev. D, 49, 2658

d'Ambrosi, G., Satish Kumar, S., & van Holten, J. W. 2015, Physics Letters B, 743, 478

Damour, T. & Deruelle, N. 1986, Ann. Inst. Henri Poincaré Phys. Théor., Vol. 44, No. 3, p. 263 - 292, 44, 263

De Felice, F. & Preti, G. 1999, Class. Quantum Grav., 16, 2929

Debney, G. C., Kerr, R. P., & Schild, A. 1969, Journal of Mathematical Physics, 10, 1842

Desvignes, G., Caballero, R. N., Lentati, L., et al. 2016, MNRAS, 458, 3341

Dexter, J. 2016, MNRAS, 462, 115

Dexter, J. & O'Leary, R. M. 2014, ApJ, 783, L7

Dixon, W. G. 1964, Il Nuovo Cimento, 34, 317

Dixon, W. G. 1974, Philosophical Transactions of the Royal Society of London A: Mathematical, Physical and Engineering Sciences, 277, 59

Doeleman, S. S., Weintroub, J., Rogers, A. E. E., et al. 2008, Nature, 455, 78

Dokuchaev, V. I. 2014, General Relativity and Gravitation, 46, 1832

Dolan, S. R. 2018, arXiv e-prints, arXiv:1801.02273

Eatough, R., Lazio, T. J. W., Casanellas, J., et al. 2015, Advancing Astrophysics with the Square Kilometre Array (AASKA14), 45

Estes, J., Kavic, M., Lippert, M., & Simonetti, J. H. 2017, ApJ, 837, 87

Event Horizon Telescope Collaboration, Akiyama, K., Alberdi, A., et al. 2019, ApJ, 875, L1

Everitt, C. W. F., Muhlfelder, B., DeBra, D. B., et al. 2015, Classical and Quantum Gravity, 32, 224001

Falcke, H., Goss, W. M., Matsuo, H., et al. 1998, ApJ, 499, 731

Faucher-Giguère, C.-A. & Loeb, A. 2011, MNRAS, 415, 3951

Faulkner, A. J., Stairs, I. H., Kramer, M., et al. 2004, MNRAS, 355, 147

Feldmeier, A., Lützgendorf, N., Neumayer, N., et al. 2013, A&A, 554, A63

Ferrarese, L. & Merritt, D. 2000, ApJ, 539, L9

Filipe Costa, L. & Natário, J. 2014, arXiv e-prints, arXiv:1410.6443

Filippenko, A. V. & Ho, L. C. 2003, ApJ, 588, L13

Fletcher, R. & Reeves, C. M. 1964, The Computer Journal, 7, 149

Fomalont, E. & Reid, M. 2004, New Astronomy Reviews, 48, 1473

Fonseca, E., Demorest, P., Ransom, S., & Stairs, I. 2019, BAAS, 51, 425

Fornberg, B. 1988, Mathematics of Computation - Math. Comput., 51, 699

Fragione, G., Pavlík, V., & Banerjee, S. 2018, MNRAS, 480, 4955

Frail, D. A., Diamond, P. J., Cordes, J. M., & van Langevelde, H. J. 1994, ApJ, 427, L43

Freire, P. C. C. 2013, in IAU Symposium, Vol. 291, Neutron Stars and Pulsars: Challenges and Opportunities after 80 years, ed. J. van Leeuwen, 243–250

Freire, P. C. C., Ridolfi, A., Kramer, M., et al. 2017, MNRAS, 471, 857

Frenkel, J. 1926, Zeitschrift für Physik, 243, 262

Froeschle, M., Mignard, F., & Arenou, F. 1997, in ESA Special Publication, Vol. 402, Hipparcos - Venice '97, ed. R. M. Bonnet, E. Høg, P. L. Bernacca, L. Emiliani, A. Blaauw, C. Turon, J. Kovalevsky, L. Lindegren, H. Hassan, M. Bouffard, B. Strim, D. Heger, M. A. C. Perryman, & L. Woltjer, 49–52

Fuerst, S. V. & Wu, K. 2004, Astron. Astrophys., 424, 733

Fuerst, S. V. & Wu, K. 2007, Astron. Astrophys., 474, 55

Gair, J. R., Babak, S., Sesana, A., et al. 2017, in Journal of Physics Conference Series, Vol. 840, Journal of Physics Conference Series, 012021

Gair, J. R., Tang, C., & Volonteri, M. 2010, Phys. Rev. D, 81, 104014

Gebhardt, K., Bender, R., Bower, G., et al. 2000, ApJ, 539, L13

Gebhardt, K., Rich, R. M., & Ho, L. C. 2002, ApJ, 578, L41

Generozov, A., Stone, N. C., Metzger, B. D., & Ostriker, J. P. 2018, Monthly Notices of the Royal Astronomical Society, 478, 4030

Genzel, R., Eisenhauer, F., & Gillessen, S. 2010, Reviews of Modern Physics, 82, 3121

Gillessen, S., Eisenhauer, F., Trippe, S., et al. 2009, ApJ, 692, 1075

Glampedakis, K. & Babak, S. 2006, Classical and Quantum Gravity, 23, 4167

Gourgoulhon, E., Le Tiec, A., Vincent, F. H., & Warburton, N. 2019, arXiv e-prints, arXiv:1903.02049

Graham, A. W. & Soria, R. 2019, MNRAS, 484, 794

Gravity Collaboration, Abuter, R., Accardo, M., et al. 2017, A&A, 602, A94

Gravity Collaboration, Abuter, R., Amorim, A., et al. 2018a, A&A, 615, L15

Gravity Collaboration, Abuter, R., Amorim, A., et al. 2018b, A&A, 618, L10

GRAVITY Collaboration, Abuter, R., Amorim, A., et al. 2020, arXiv e-prints, arXiv:2004.07187

Greene, J. E., Peng, C. Y., Kim, M., et al. 2010, ApJ, 721, 26

Gültekin, K., Richstone, D. O., Gebhardt, K., et al. 2009, ApJ, 698, 198

Hackmann, E. & Dhani, A. 2018, ArXiv e-prints

Hailey, C. J. & Mori, K. 2017, in AAS/High Energy Astrophysics Division #16, AAS/High Energy Astrophysics Division, 109.12

Hailey, C. J., Mori, K., Bauer, F. E., et al. 2018, Nature, 556, 70

Harada, T., Iguchi, H., & Nakao, K. 2002, Progress of Theoretical Physics, 107, 449

Harding, A. K. 2013, Frontiers of Physics, 8, 679

Hessels, J. W. T., Ransom, S. M., Stairs, I. H., et al. 2006, Science, 311, 1901

Hobbs, G., Dai, S., Manchester, R. N., et al. 2014, arXiv e-prints, arXiv:1407.0435

Hobbs, G. B., Edwards, R. T., & Manchester, R. N. 2006, MNRAS, 369, 655

Hui, C. Y., Cheng, K. S., & Taam, R. E. 2010, The Astrophysical Journal, 714, 1149

Iorio, L. 2018, Universe, 4, 59

Israel, W. 1967, Physical Review, 164, 1776

Israel, W. 1968, Communications in Mathematical Physics, 8, 245

Istomin, Y. N. 1991, Soviet Astronomy Letters, 17, 301

Johannsen, T. 2013, Phys. Rev. D, 88, 044002

Johannsen, T. & Psaltis, D. 2010, ApJ, 716, 187

Johnston, S., Kramer, M., Lorimer, D. R., et al. 2006, MNRAS, 373, L6

Jouteux, S., Ramachandran, R., Stappers, B. W., Jonker, P. G., & van der Klis, M. 2002, A&A, 384, 532

Kaspi, V. M. 2018, in IAU Symposium, Vol. 337, Pulsar Astrophysics the Next Fifty Years, ed. P. Weltevrede, B. B. P. Perera, L. L. Preston, & S. Sanidas, 3–8

Kato, Y., Miyoshi, M., Takahashi, R., Negoro, H., & Matsumoto, R. 2010, MNRAS, 403, L74

Keane, E., Bhattacharyya, B., Kramer, M., et al. 2015, Advancing Astrophysics with the Square Kilometre Array (AASKA14), 40

Kennea, J. A., Burrows, D. N., Kouveliotou, C., et al. 2013, ApJ, 770, L24

Kerr, R. P. 1963, Phys. Rev. Lett., 11, 237

Kidder, L. E. 1995, Phys. Rev. D, 52, 821

Kim, C. & Davies, M. B. 2018, Journal of Korean Astronomical Society, 51, 165

Kimpson, T., Wu, K., & Zane, S. 2019a, MNRAS, 486, 360

Kimpson, T., Wu, K., & Zane, S. 2019b, MNRAS, 484, 2411

Kimpson, T., Wu, K., & Zane, S. 2020a, MNRAS, 495, 600

Kimpson, T., Wu, K., & Zane, S. 2020b, MNRAS

Kızıltan, B., Baumgardt, H., & Loeb, A. 2017a, Nature, 542, 203

Kızıltan, B., Baumgardt, H., & Loeb, A. 2017b, Nature, 542, 203

Kızıltan, B., Baumgardt, H., & Loeb, A. 2017c, Nature, 542, 203

Kleihaus, B., Kunz, J., & Schneider, S. 2012, Phys. Rev. D, 85, 024045

Kocherlakota, P., Joshi, P. S., Bhattacharyya, S., et al. 2019, MNRAS, 490, 3262

Kramer, M., Backer, D. C., Cordes, J. M., et al. 2004, New Astron. Rev., 48, 993

Krolik, J. H., Hawley, J. F., & Hirose, S. 2005, ApJ, 622, 1008

Krone-Martins, A., Delchambre, L., Wertz, O., et al. 2018, A&A, 616, L11

Kulkarni, A. K., Penna, R. F., Shcherbakov, R. V., et al. 2011, MNRAS, 414, 1183

Lauer, T. R., Faber, S. M., Currie, D. G., et al. 1992, AJ, 104, 552

Lazarus, P., Karuppusamy, R., Graikou, E., et al. 2016, MNRAS, 458, 868

Lazio, T. J. W. & Cordes, J. M. 1998, ApJ, 505, 715

Li, K. J., Wu, K., & Singh, D. 2019, MNRAS, 485, 1053

Liebling, S. L. & Palenzuela, C. 2012, Living Reviews in Relativity, 15, 6

Lin, D., Strader, J., Carrasco, E. R., et al. 2018, Nature Astronomy, 2, 656

Liu, K., Eatough, R. P., Wex, N., & Kramer, M. 2014, Mon. Not. R. Astron. Soc., 445, 3115

Liu, K., Verbiest, J. P. W., Kramer, M., et al. 2011, MNRAS, 417, 2916

Liu, K., Wex, N., Kramer, M., Cordes, J. M., & Lazio, T. J. W. 2012, Astrophys. J., 747

Liu, X. J., Bassa, C. G., & Stappers, B. W. 2018, MNRAS, 478, 2359

Lorimer, D. & Kramer, M. 2012, Handbook of Pulsar Astronomy, Cambridge Observing Handbooks for Research Astronomers (Cambridge University Press)

Lorimer, D. R. 2008, Living Rev. Relativ., 11, 8

Lu, K.-X., Huang, Y.-K., Zhang, Z.-X., et al. 2019, ApJ, 877, 23

Lützgendorf, N., Kissler-Patig, M., Gebhardt, K., et al. 2013, A&A, 552, A49

Lyne, A. & Graham-Smith, F. 2012, Pulsar Astronomy, 4th edn., Cambridge Astrophysics (Cambridge University Press)

Macquart, J.-P. & Kanekar, N. 2015, ApJ, 805, 172

Macquart, J. P., Kanekar, N., Frail, D. A., & Ransom, S. M. 2010, ApJ, 715, 939

Majid, W. A., Prince, T. A., Pearlman, A. B., Kocz, J., & Horiuchi, S. 2019, in AAS/High Energy Astrophysics Division, AAS/High Energy Astrophysics Division, 112.80

Manchester, R. N. 2015, International Journal of Modern Physics D, 24, 1530018

Manchester, R. N., Hobbs, G. B., Teoh, A., & Hobbs, M. 2005, AJ, 129, 1993

Mann, C. R., Richer, H., Heyl, J., et al. 2019, ApJ, 875, 1

Marrone, D. P., Moran, J. M., Zhao, J.-H., & Rao, R. 2007, ApJ, 654, L57

Mashhoon, B. & Singh, D. 2006, Phys. Rev. D, 74, 124006

Mathisson, A. 1937, Acta Phys. Pol., 6, 163

Mazur, P. O. & Mottola, E. 2001, arXiv e-prints, gr

Mehrgan, K., Thomas, J., Saglia, R., et al. 2019, arXiv e-prints, arXiv:1907.10608

Merritt, D., Alexander, T., Mikkola, S., & Will, C. M. 2010, Phys. Rev. D, 81, 062002

Merritt, D., Alexander, T., Mikkola, S., & Will, C. M. 2011, Phys. Rev. D, 84, 044024

Mezcua, M. 2017, International Journal of Modern Physics D, 26, 1730021

Miller-Jones, J. C. A., Wrobel, J. M., Sivakoff, G. R., et al. 2012, ApJ, 755, L1

Misner, C., Thorne, K., & Wheeler, J. 1973, Gravitation, Gravitation No. pt. 3 (W. H. Freeman)

Möller, C. 1949, Annales de l'institut Henri Poincaré, 11, 251

Mori, K., Gotthelf, E. V., Zhang, S., et al. 2013, ApJ, 770, L23

Mościbrodzka, M., Gammie, C. F., Dolence, J. C., Shiokawa, H., & Leung, P. K. 2009, ApJ, 706, 497

Moxon, J. & Flanagan, É. 2018, Phys. Rev. D, 97, 105001

Muno, M. P., Lu, J. R., Baganoff, F. K., et al. 2005, ApJ, 633, 228

Narayan, R., Yi, I., & Mahadevan, R. 1995, Nature, 374, 623

Nättilä, J. & Pihajoki, P. 2018, A&A, 615, A50

Nelder, J. A. & Mead, R. 1965, The Computer Journal, 7, 308

Nobili, A. M. & Anselmi, A. 2018, Phys. Rev. D, 98, 042002

Nocedal, J. & Wright, S. 2006, Numerical optimization, 2nd edn., Springer series in operations research and financial engineering (New York, NY: Springer)

Noori, H. A., Roberts, M. S. E., Champion, D., et al. 2017, in Journal of Physics Conference Series, Vol. 869, Journal of Physics Conference Series, 012071

Nuttall, A. 1981, IEEE Transactions on Acoustics, Speech, and Signal Processing, 29, 84

Obukhov, Y. N., Silenko, A. J., & Teryaev, O. V. 2009, Phys. Rev. D, 80, 064044

O'Connell, R. F. 1969, Ap&SS, 4, 119

Oscoz, A., Goicoechea, L. J., Mediavilla, E., & Buitrago, J. 1997, MNRAS, 285, 413

Özel, F., Psaltis, D., & Narayan, R. 2000, ApJ, 541, 234

Pachner, J. 1970, Canadian Journal of Physics, 48, 970

Pan, Z., Hobbs, G., Li, D., et al. 2016, MNRAS, 459, L26

Papapetrou, A. 1951, Proceedings of the Royal Society of London A: Mathematical, Physical and Engineering Sciences, 209, 248

Pearlman, A. B., Majid, W. A., Prince, T. A., et al. 2019, in AAS/High Energy Astrophysics Division, AAS/High Energy Astrophysics Division, 112.105

Penrose, R. 1979, in General Relativity: An Einstein centenary survey, ed. S. W. Hawking & W. Israel, 581–638

Perera, B. B. P., Stappers, B. W., Lyne, A. G., et al. 2017, MNRAS, 468, 2114

Peters, P. C. 1964, Physical Review, 136, 1224

Pirani, F. A. E. 1956, Acta Physica Polonica, 15, 389

Pitkin, M. 2018, Journal of Open Source Software, 3, 538

Plyatsko, R. & Fenyk, M. 2016, Phys. Rev. D, 94, 044047

Poisson, E. & Will, C. 2014, Gravity: Newtonian, Post-Newtonian, Relativistic (Cambridge University Press)

Pound, A. 2017a, Phys. Rev. D, 95, 104056

Pound, A. 2017b, Phys. Rev. D, 95, 104056

Press, W., Flannery, B., Teukolsky, S., & Vetterling, W. 1992, Numerical Recipes in FORTRAN 77: Volume 1, Volume 1 of Fortran Numerical Recipes: The Art of Scientific Computing (Cambridge University Press)

Press, W. H. 1977, Phys. Rev. D, 15, 965

Psaltis, D. 2008, Living Reviews in Relativity, 11, 9

Psaltis, D. 2012, ApJ, 759, 130

Psaltis, D., Perrodin, D., Dienes, K. R., & Mocioiu, I. 2008, Phys. Rev. Lett., 100, 119902

Psaltis, D., Wex, N., & Kramer, M. 2016, ApJ, 818, 121

Pu, H.-Y., Yun, K., Younsi, Z., & Yoon, S.-J. 2016, ApJ, 820, 105

Quataert, E. & Gruzinov, A. 2000, ApJ, 545, 842

Rafikov, R. R. & Lai, D. 2006, ApJ, 641, 438

Rafikov, R. R. & Lai, D. 2006, The Astrophysical Journal, 641, 438

Rajwade, K. M., Lorimer, D. R., & Anderson, L. D. 2017, MNRAS, 471, 730

Ransom, S. M. 2008, in IAU Symposium, Vol. 246, Dynamical Evolution of Dense Stellar Systems, ed. E. Vesperini, M. Giersz, & A. Sills, 291–300

Raynaud, R., Guilet, J., Janka, H.-T., & Gastine, T. 2020, Science Advances, 6, eaay2732

Remillard, R. A. & McClintock, J. E. 2006, ARA&A, 44, 49

Remmen, G. N. & Wu, K. 2013, MNRAS, 430, 1940

Ricarte, A. & Dexter, J. 2015, MNRAS, 446, 1973

Rios, L. & Sahinidis, N. 2009, Journal of Global Optimization, 56

Robson, T., Cornish, N., & Chang, L. 2018, LISA sensitivity calculator, https://github.com/eXtremeGravityInstitute/LISA_Sensitivity

Robson, T., Cornish, N. J., & Liug, C. 2019, Classical and Quantum Gravity, 36, 105011

Rosquist, K., Bylund, T., & Samuelsson, L. 2009, International Journal of Modern Physics D, 18, 429

Rubbo, L. J., Holley-Bockelmann, K., & Finn, L. S. 2006, in American Institute of Physics Conference Series, Vol. 873, Laser Interferometer Space

Antenna: 6th International LISA Symposium, ed. S. M. Merkovitz & J. C. Livas, 284–288

Rubio-Herrera, E., Stappers, B. W., Hessels, J. W. T., & Braun, R. 2013, MNRAS, 428, 2857

Ruffini, R. & Bonazzola, S. 1969, Phys. Rev., 187, 1767

Sadoun, R. & Colin, J. 2012, MNRAS, 426, L51

Saha, L. & Dyks, J. 2017, MNRAS, 467, 2529

Saxton, C. J., Younsi, Z., & Wu, K. 2016, Mon. Not. R. Astron. Soc., 461, 4295

Schmidt, W. 2002, Classical and Quantum Gravity, 19, 2743

Shapiro, I. I. 1964, Phys. Rev. Lett., 13, 789

Shcherbakov, R. V. & Huang, L. 2011, MNRAS, 410, 1052

Siegel, E. R., Hertzberg, M. P., & Fry, J. N. 2007, MNRAS, 382, 879

Silk, J. & Arons, J. 1975, ApJ, 200, L131

Singh, D. 2005, Phys. Rev. D, 72, 084033

Singh, D., Wu, K., & Sarty, G. E. 2014, Mon. Not. R. Astron. Soc., 441, 800

Sjouwerman, L. O., Lindqvist, M., van Langevelde, H. J., & Diamond, P. J. 2002, A&A, 391, 967

Smits, R., Tingay, S. J., Wex, N., Kramer, M., & Stappers, B. 2011, A&A, 528, A108

Stappers, B. W., Keane, E. F., Kramer, M., Possenti, A., & Stairs, I. H. 2018, Philosophical Transactions of the Royal Society of London Series A, 376, 20170293

Stovall, K., Creighton, T., Price, R. H., & Jenet, F. A. 2012, ApJ, 744, 143

Synge, J. 1960, Relativity: The General Theory, North-Holland series in physics No. v. 1 (North-Holland Publishing Company)

Tan, C. M., Bassa, C. G., Cooper, S., et al. 2018, ApJ, 866, 54

The LIGO Scientific Collaboration, the Virgo Collaboration, Abbott, R., et al. 2020, arXiv e-prints, arXiv:2009.01075

Tomsick, J. A., Bellm, E., Fuerst, F., et al. 2015, ArXiv e-prints, arXiv:1501.03534

Torczon, V. 1997, SIAM J. on Optimization, 7, 1–25

Tulczyjew, W. 1959, Acta Phys. Pol., 18, 393

Ulvestad, J. S., Greene, J. E., & Ho, L. C. 2007, ApJ, 661, L151

van de Meent, M. 2017, Journal of Physics: Conference Series, 840, 012022

van den Bosch, R. C. E. & de Zeeuw, P. T. 2010, MNRAS, 401, 1770

van den Bosch, R. C. E., Greene, J. E., Braatz, J. A., Constantin, A., & Kuo, C.-Y. 2016, ApJ, 819, 11

van der Marel, R. P. & Anderson, J. 2010, ApJ, 710, 1063

van der Marel, R. P., de Zeeuw, P. T., Rix, H.-W., & Quinlan, G. D. 1997, Nature, 385, 610

Verbiest, J. P. W., Bailes, M., van Straten, W., et al. 2008, ApJ, 679, 675

Verolme, E. K., Cappellari, M., Copin, Y., et al. 2002, MNRAS, 335, 517

Vigeland, S. J. & Hughes, S. A. 2010, Phys. Rev. D, 81, 024030

Volonteri, M. 2010, A&A Rev., 18, 279

Wang, Y., Creighton, T., Price, R. H., & Jenet, F. A. 2009a, ApJ, 705, 1252

Wang, Y., Jenet, F. A., Creighton, T., & Price, R. H. 2009b, ApJ, 697, 237

Warburton, N., Osburn, T., & Evans, C. R. 2017, Phys. Rev. D, 96, 084057

Weisberg, J. M., Taylor, J. H., & Fowler, L. A. 1981, Scientific American, 245, 74

Wex, N. & Kopeikin, S. M. 1999, Astrophys. J., 514, 388

Wharton, R. S., Chatterjee, S., Cordes, J. M., Deneva, J. S., & Lazio, T. J. W. 2012, Astrophys. J., 753

Will, C. M. 2011, Proceedings of the National Academy of Sciences, 108, 5938

Will, C. M. 2014, Living Rev. Relativ., 17, 4

Wolfe, P. 1971, SIAM Review, 13, 185

Wrobel, J. M., Miller-Jones, J. C. A., Nyland, K. E., & Maccarone, T. J. 2018, ArXiv e-prints

Wucknitz, O. 2015, arXiv e-prints, arXiv:1501.04510

Yagi, K. & Stein, L. C. 2016, Classical and Quantum Gravity, 33, 054001

Younsi, Z., Wu, K., & Fuerst, S. V. 2012, Astron. Astrophys., 545

Yuan, Q. & Zhang, B. 2014, Journal of High Energy Astrophysics, 3, 1

Yunes, N., Sopuerta, C. F., Rubbo, L. J., & Holley-Bockelmann, K. 2008, ApJ, 675, 604

Zhang, F. & Saha, P. 2017, ApJ, 849, 33